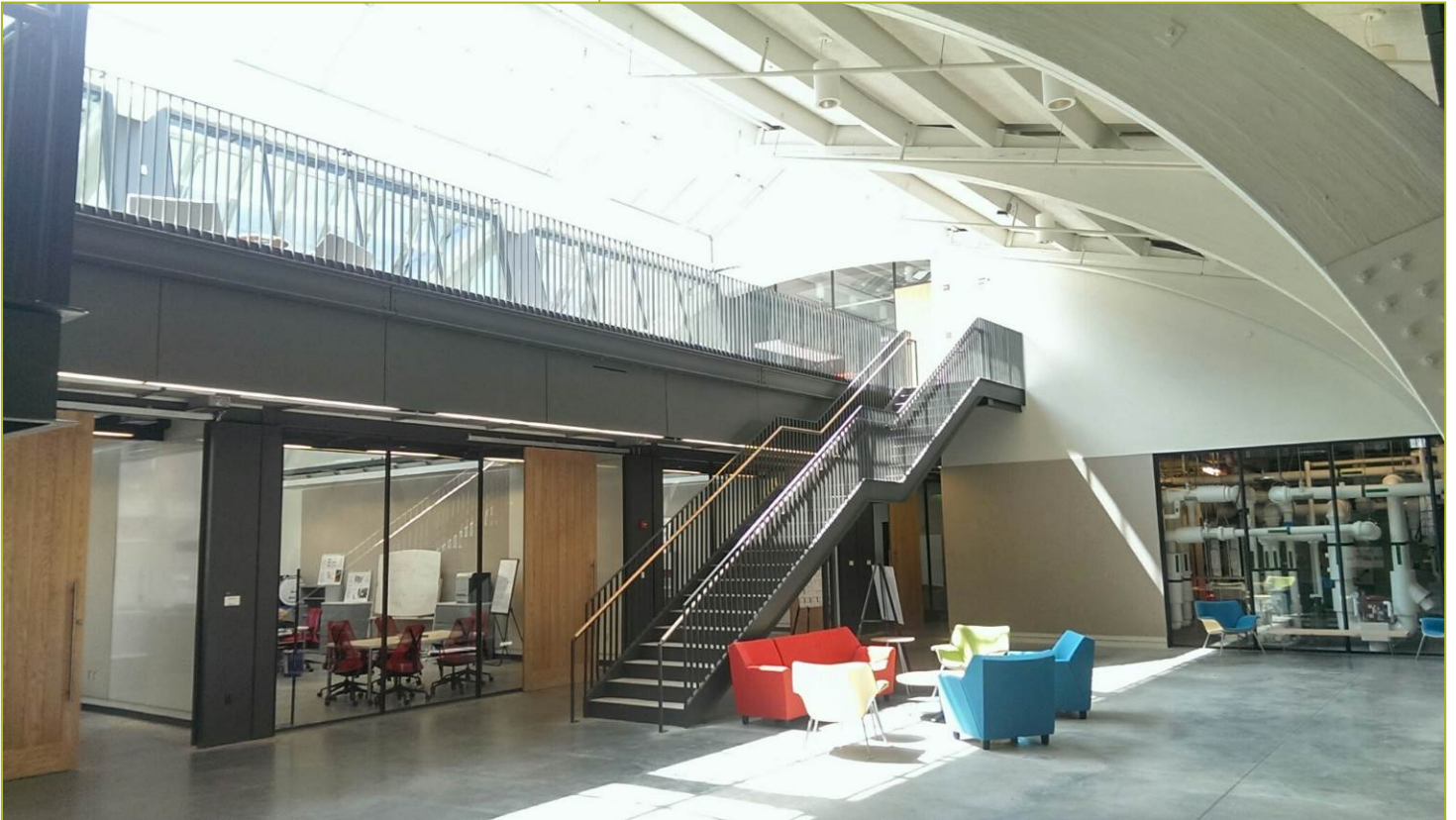


Title: Whole Building Diagnostic & Decision Support

Report Date: January 2013

Report Author(s): (See Report)



CBEI was referred to as the Energy Efficiency Buildings HUB at the time this report was developed.



Report Abstract

CBEI conducted research to develop and demonstrate a library of diagnostics decision support tools that can enable cost effective diagnostics solutions for existing buildings. This report describes early results in successfully developing and demonstrating the effectiveness of diagnostics and decision support tools for subsystem diagnostics (RTU, DX, AHU-VAV and building envelope subsystems) and fault prioritization.

Contact Information for Lead Researcher

Name: James E. Braun

Institution: Purdue University

Email address: jbraun@purdue.edu

Phone number: 765-494-9157

Acknowledgement

This material is based upon work supported by the Consortium for Building Energy Innovation (CBEI) sponsored by the U.S. Department of Energy under Award Number DE-EE0004261.

Disclaimer

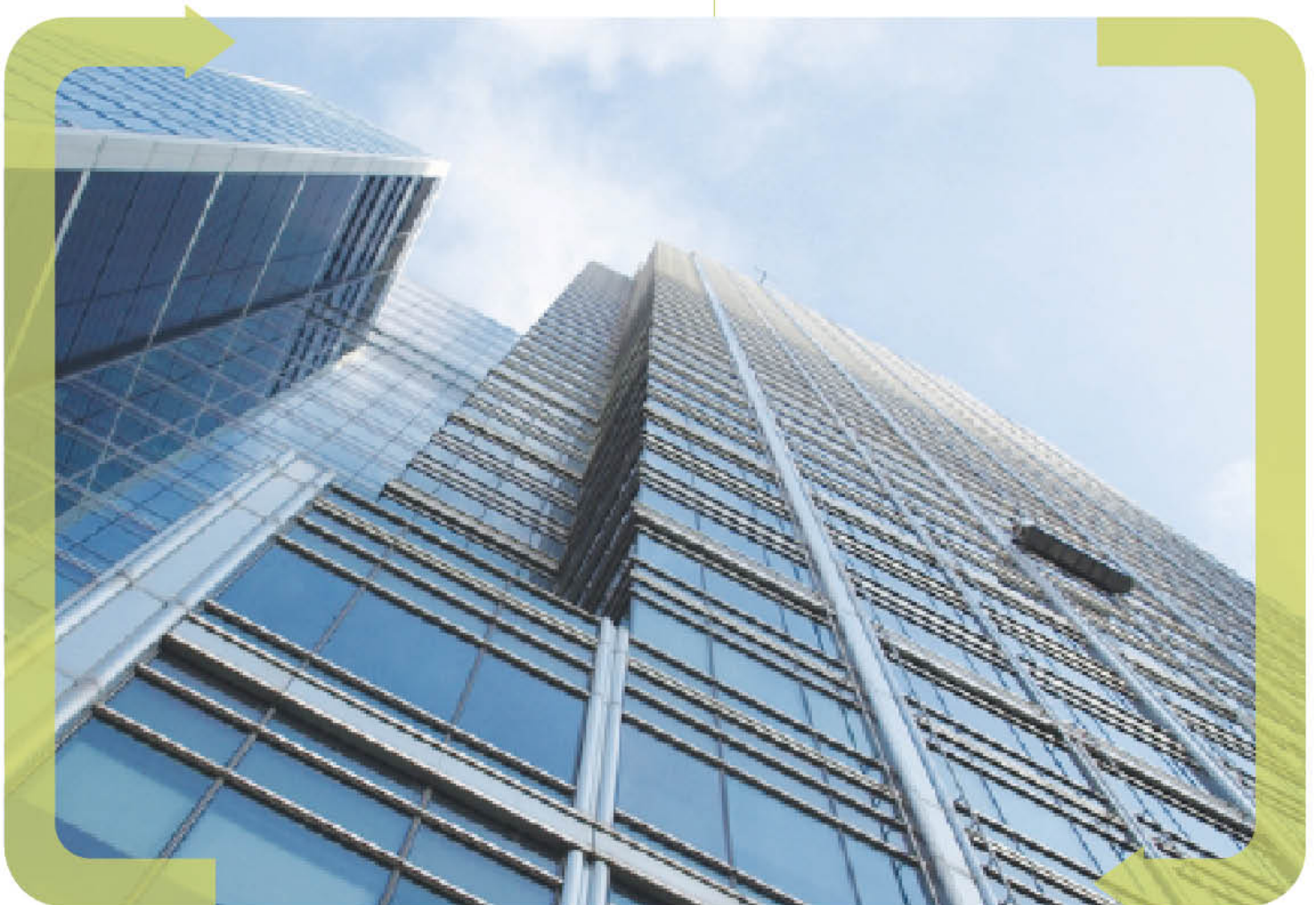
This report was prepared as an account of work sponsored by an agency of the United States Government. Neither the United States Government nor any agency thereof, nor any of their employees, makes any warranty, express or implied, or assumes any legal liability or responsibility for the accuracy, completeness, or usefulness of any information, apparatus, product, or process disclosed, or represents that its use would not infringe privately owned rights. Reference herein to any specific commercial product, process, or service by trade name, trademark, manufacturer, or otherwise does not necessarily constitute or imply its endorsement, recommendation, or favoring by the United States Government or any agency thereof. The views and opinions of authors expressed herein do not necessarily state or reflect those of the United States Government or any agency thereof.



Budget Period 2 Subtask 4.3 Annual Report

Whole Building Diagnostic & Decision Support

1 February 2012 - 31 January 2013



Authors: Bayer Material Science (Amy Wylie), Drexel University (Adam Regnier, Jin Wen), Purdue University (Jim Braun, Andrew Hjortland, Woohyun Kim), United Technologies Research Center (Trevor Bailey, Mikhail Gorbounov, Ritesh Khire, Ashutosh Tewari)



Subtask 4.3: Whole Building Diagnostic & Decision Support

Deliverable #19: Demonstration of easy-to-use tools and cost effective technologies for operators to continuously diagnose and optimize performance during extended operation of AERs.

Brief Summary: The team has demonstrated a number of diagnostic and decision support tools that can enable cost effective whole building decision support for building operators. For rooftop units (RTUs) Purdue has developed and demonstrated virtual sensors as a means of realizing a robust and low-cost approach to monitoring, detecting, and diagnosing faults. Existing data and laboratory tests were used to assess the diagnostic methods for refrigerant and air-side faults, including faulty economizer operation, heat exchanger fouling, faulty refrigerant charge, compressor problems, etc. A video demonstration was created that demonstrates a diagnostic system for refrigerant charge and condenser fouling faults. For AHU-VAV systems, Drexel has developed and demonstrated a diagnostic approach that utilizes pattern matching and principle component analysis methods and that does not require any fault data training and requires only 10-15 days fault-free training data (for each season). The method was tested using data from three different buildings for winter, summer, and shoulder seasons. Bayer demonstrated the application of two building envelope diagnostic techniques to the Building 101. UTRC developed and demonstrated fault prioritization tools for the design and operational phases of a building. The tool chains use a generic model based approach that can quantify the impacts of various faults on energy consumption as a means of prioritizing corrective actions.

Executive Summary

HVAC systems in buildings are responsible for 14% of primary energy consumption and 32% of all electricity generated in the U.S. For office buildings, HVAC energy consumption represents about 48% of the total primary energy usage (Pérez-Lombard et al., 2008). Furthermore, energy use in the built environment is projected to grow at an average rate of 1.5% annually. Previous studies have indicated that energy consumption in commercial buildings is as much as 30% higher than expected due to the presence of faults (Katipamula and Brambley 2005). Automated fault detection and diagnosis (AFDD) can reduce this additional energy consumption, improve comfort conditions, and reduce costs for service.

The goal of this project is to develop and demonstrate a library of diagnostics decision support tools that can enable cost effective diagnostics solutions for existing buildings. Whole building diagnostic and decision support tools should robustly maintain building energy performance at an optimal level following commissioning of retrofitted buildings. In Budget Period 2 (BP2), the project teams have focused on two select building types: 1) buildings that employ packaged rooftop air conditioners (RTU) and 2) buildings that utilize built-up air-handling units (AHU) with variable-air-volume (VAV). These building types were selected to be representative of the 10-county EEB-HUB region. The specific goals for BP2 were: 1) develop, evaluate and implement sub-system diagnostics solutions as both embedded and add-on solutions and 2) develop and evaluate whole building decision support tools and systems for corrective action prioritization by building decision makers (including facility operators and sub-system service providers). The Purdue team focused on RTU and DX equipment, the Drexel team addressed AHU-VAV systems, Bayer studied faults for envelope systems and the UTRC addressed whole building decision support tools and systems. In subsequent years, the library will expanded to include tools that cover all of the representative equipment, envelopes, and systems within buildings for the EEB-HUB region and whole building demonstrations of the diagnostic implementations will be performed.

In BP2, the team members have successfully developed and demonstrated the effectiveness of diagnostics and decision support tools for subsystem diagnostics (RTU, DX, AHU-VAV and building envelope subsystems) and fault prioritization. These tools can enable cost effective diagnostics solutions for existing buildings. Both existing literature and our study have demonstrated that these developed tools can help to reduce the HVAC system energy consumption by up to 30 percent. Therefore, this subtask directly support the Hub’s goal of “... reduce annual energy use in the commercial buildings sector in Greater Philadelphia by 20 percent by 2020.”

The following sections provide a quick overview of the major accomplishments by the UTRC, Purdue, Drexel, and Bayer teams.

A. Fault Prioritization Tool Chain (UTRC team)

A.1 Fault Prioritization Tool Chain for Design Phase (UTRC, Export Controlled - ECCN: EAR99)

Identifying critical failure modes affecting building performance (such as energy consumption) is important, as it can lead to actions to eliminate them, if possible, or can be used for designing a suitable monitoring and diagnostic system. Typically, expert judgment is used to guess critical faults, which leads to over instrumented, complex, and expensive building performance monitoring and diagnostic systems. In this BP2, we demonstrated a tool chain that uses a building performance simulation (BPS) tool to perform failure mode effect analysis and also developed a systematic process to identify and prioritize critical faults.

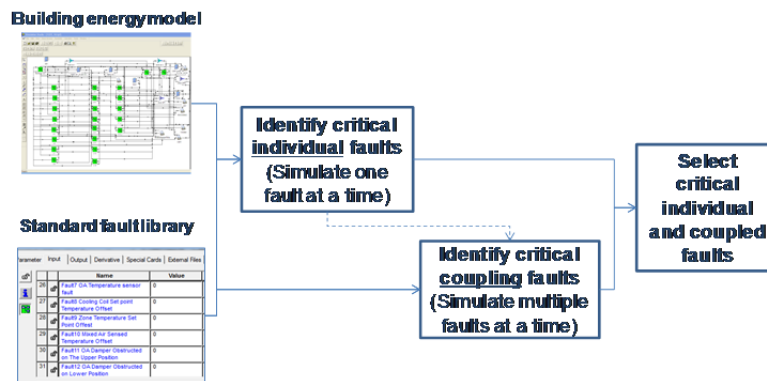


Figure 1 Systematic process to identify and prioritize critical faults

The current state-of-the-art building performance simulation (BPS) tools do not provide the ability to model and simulate faults occurring in buildings. In BP2, we developed a building system fault modeling library in TRNSYS, and demonstrated its applicability by conducting failure mode effect analysis on building 101. The fault model library is now readily deployable, generic, and scalable to any building size. The library includes both abrupt and degradation faults.

We also developed and demonstrated a process for quantifying the impact of individual as well as fault couplings. We demonstrated both the process and the use of the fault library on building 101. The findings show that a stuck outside damper appears to be one of the most important faults and causes significant increase in energy consumption in both summer and winter seasons. In addition, it has been shown that fault couplings can boost the effect of faults that are individually not significant, which is not intuitive: e.g. in summers, not shutting down heating and a stuck heating valve in the AHU are

individually insignificant. However, if these two faults happen at the same time, their effect is significant. Such findings are not always intuitive.

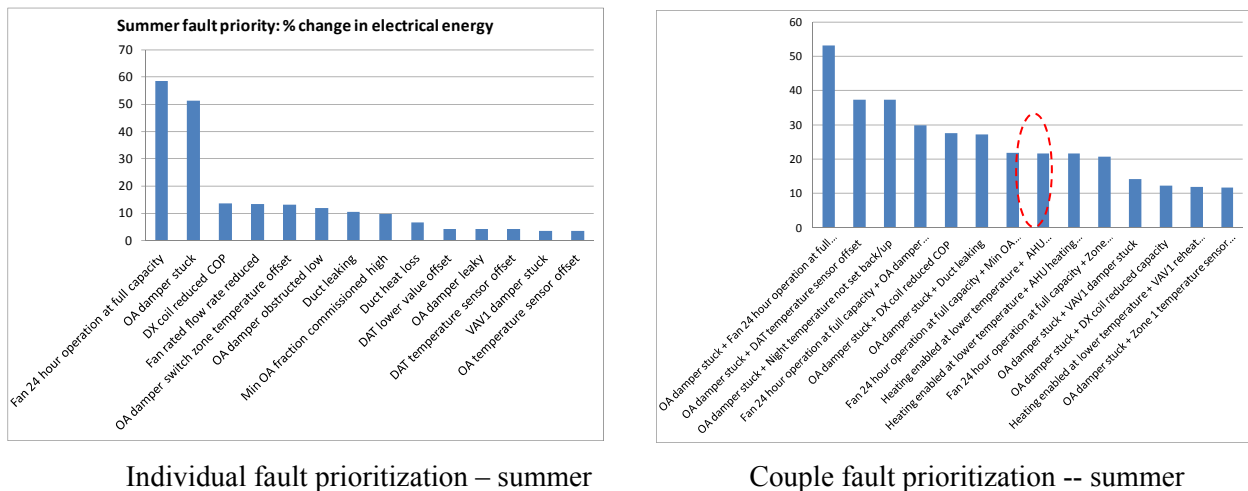


Figure 2 Fault prioritization for summer season

A.2 Fault Impact Assessment Tool Chain for Operation Phase (UTRC, Export Controlled - ECCN: EAR99)

Assessing the energy impacts of ongoing faults in an operational HVAC system provides valuable information to the facility manager for efficient resource allocation. This information becomes even more critical in large commercial building where several faults may coexist at a given time. In the BP2, UTRC developed a reusable tool chain to assess the impacts of HVAC component faults on energy consumption. This tool chain is intended to assist building managers in making critical building operation decisions. The scalability of our approach can be attributed to specialized data driven models (Graphical Models), which form the basic building blocks of the tool chain. These data-driven models do not require detailed building or equipment specific information and can be learned using limited operational data, while still being accurate enough to obtain energy impacts under different fault conditions.

Our approach works by decomposing the HVAC system into smaller subsystems and learning graphical models on those. Figure 1 shows the models for the *Economizer* and the *Heat Exchanger* subsystems. A fault in the upstream subsystem is propagated (as shown on figure below) to downstream subsystems to assess the overall energy impact of the fault.

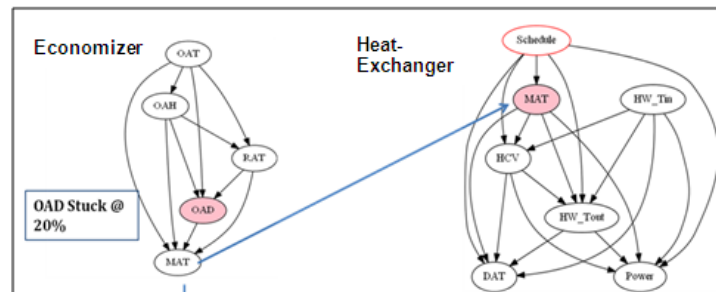


Figure 3 Data-driven graphical models for HVAC subsystems and the fault propagation scheme

As a proof of concept, the data driven graphical models were used to estimate energy impacts of faults such as *AHU outside air damper stuck* and *Heating coil valve stuck* in the building-101 simulation environment. In Figure 4, we compare the excess energy consumption due to a stuck damper, estimated using the proposed method with that obtained from a detailed TRNSYS model for building 101, along with the baseline (no-fault) energy consumption. Clearly, the proposed fault assessment method does a reasonably good job of estimating the energy consumption under fault conditions, when compared with the TRNSYS model.

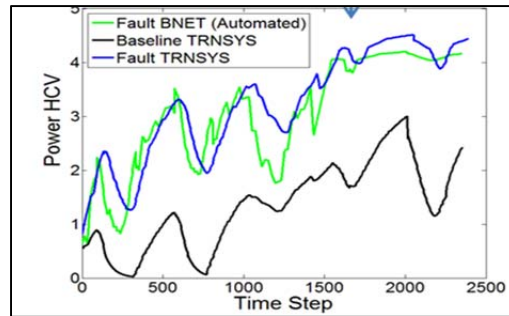


Figure 4 Benchmarking the energy impact based on the proposed approach with that of detailed TRNSYS model

A.3 RTU laboratory and field testing (UTRC, Export Controlled - ECCN: EAR99)

The experimental data are needed for development of a robust diagnostics methodology as well as for its validation and demonstration. Experimental data were generated by UTRC in well controlled environmental laboratory tests and also in more realistic field conditions. The Carrier 7.5 ton RTU 48HCDD08 (Figure 5) was used for refrigerant charge diagnostics testing with 70%, 75%, 80%, 85%, 100%, 140% charge levels. RTU testing conditions are shown in Table 1.



Lab RTU



Field RTU

Figure 5. Tested RTU systems

Table 1. RTU testing conditions in the lab

Testing Matrix						
Charge, %	IA flow, cfm	OA TDB, °F	IA TDB, °F	IA TWB, °F	Circuit	Total Tests
140%/100%/85%/80%/75%/70%	2930/2250	85/95/105/115	80/75	67	2 and 1	100

The Carrier 10 ton RTU 50PG-C12-D-60-S4 installed on a UTRC building rooftop was used for field testing. The RTU has no heating function, has an interlocked modulating outside-air and return-air dampers with a damper position. The experimental data with variable charge, condenser flow and damper position were generated for the state-of-the-art RTU in field conditions. Table 2 contains operating ranges for the conducted tests for 70%, 80%, 90%, 85%, 100% and 120% charge level; Condensed flow restriction for 0%, 30%, 43%, 56% and damper position 0, 25%, 50%, 75%, 100%. All the tests have been done except the case of 120% charge and 56% condenser air reduction because of cold ambient conditions in October of 2012.

Table 2. RTU testing conditions in field tests

Refrigerant charge levels	70%, 80%, 90%, 100%, and 120% of normal charge
Condenser air flow rate reduction	0%, 30%, 43%, and 56% of normal flow
Outside-air damper opening	0%, 25%, 50%, 75%, and 100%

The detailed data from lab and field tests were transferred to Purdue University team for diagnostics method validation.

B. RTU AFDD (Purdue University)

The primary goal of this work was to develop and demonstrate automated fault detection and diagnostic (AFDD) implementations for rooftop air conditioners (RTUs) having fixed speed compressors and a DX system with a variable stage compressor. In order of realize a cost-effective solution, virtual sensors are employed that utilize a model and low cost measurements in order to provide outputs that would be expensive to measure directly. Specific accomplishments include: 1) laboratory and field testing to generate data for normal and faulty performance of RTUs; 2) assessment of the impacts of faults on system performance and operating costs, which is important for setting fault diagnostic thresholds; 3) development and validation of a number of virtual sensors; 4) development of an active method of diagnosing economizer faults for RTUs; 5) development of an interface for presenting diagnostic information; and 6) development of video demonstrations for RTU diagnostics.

B.1 Typical Fault Impacts for Cooling Equipment

Figure 6 shows the effects of refrigerant charge level on cooling capacity and estimated annual operating costs for a number of different cooling systems determined from laboratory measurements and modeling. The impact of charge varies with system. However, in general, charge has a relatively small impact if it is within about 10% of the rated value. The impact increases dramatically for units that are undercharged by 20% or more. The impacts of air-side fouling for both the evaporator and condenser were also determined from laboratory measurements. The impacts are relatively small if the air flows are within 10% of the nominal air flow. This data is useful for establishing necessary accuracy for virtual sensors that can estimate refrigerant charge and air flow from other measurements.

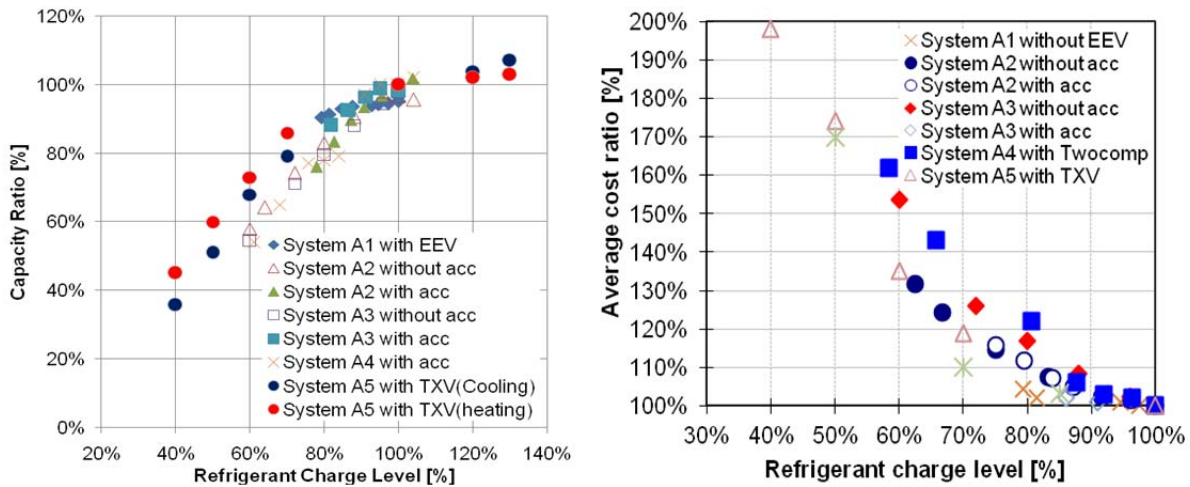


Figure 6. Capacity and annual cost ratios for different systems based on the refrigerant charge

B.2 Example Virtual Sensors

Figure 7a shows performance of a virtual refrigerant charge (VRC) sensor for laboratory data. In general, charge predictions are within 10%, which is adequate based on the relatively small fault impacts within this range. The VRC only requires four externally mounted temperature sensors to estimate the refrigerant charge at any given operating condition.

Figure 7b shows accuracy of a virtual compressor power (VCP) sensor for a system that was tested with a variety of different faults, including evaporator and condenser air-side fouling, low and high refrigerant charge, liquid line restrictions, compressor valve leakage, and the presence of a non-condensable gas in the refrigerant. Overall, this approach provides very accurate estimates of compressor power regardless of the faults present. Three temperature measurements are necessary to provide VCP sensor outputs.

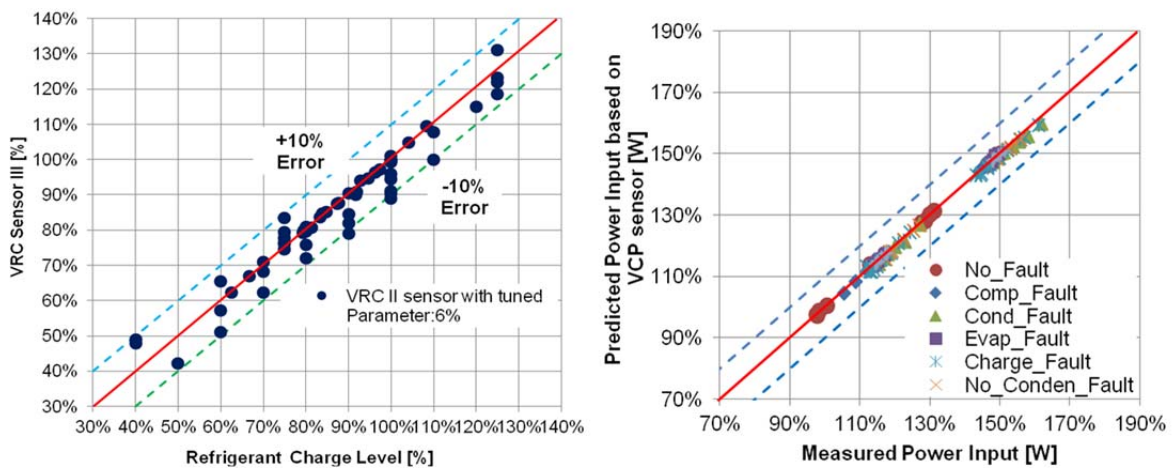


Figure 7. a) Performance of VRC sensor based on tuned parameters; b) Performance of VCP sensor under no fault and fault conditions

In addition to compressor power, refrigerant mass flow rate is an important measurement for monitoring equipment performance and enabling fault detection and diagnostics. However, a traditional mass flow meter is expensive to purchase and install. Three different virtual refrigerant mass flow (VRMF) sensors were developed and evaluated in this study that use mathematical models to estimate flow rate using low cost measurements: 1) compressor map for refrigerant mass flow rate, 2) energy-balance method that employs the VCP sensor, 3) semi-empirical correlations for thermostatic expansion valves (TXV) that are based on an orifice equation. Differences between the three VRMF sensors can be used within a diagnostic system to isolate compressor faults since the accuracy of the energy balance model and expansion device models are independent of compressor flow faults. Figure 3.34

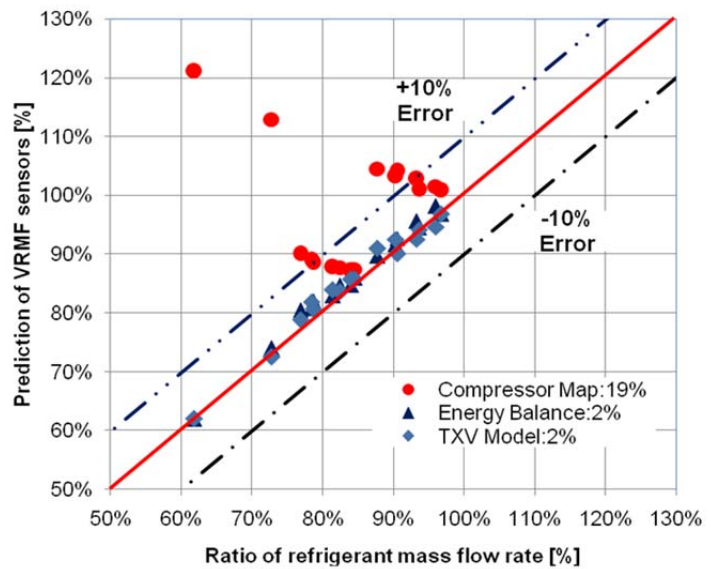


Figure 8. Comparison of VRMF sensor outputs with compressor flow fault

Figure 8 shows example comparisons of the three VRMF sensors with mass flow measurements. With a simulated compressor valve leakage fault, the refrigerant mass flow rate is reduced compared to normal operation. As a result, the compressor map over-predicts refrigerant mass flow rate, whereas the other VRMF sensors provide accurate flow estimates.

Virtual sensors were also developed and evaluated for evaporator and condenser air flow, which can be employed for isolating heat exchanger fouling. The different virtual sensors developed in this study were evaluated using both laboratory and field data for a number of different systems.

B.3 RTU Economizer Diagnostics

An active method for diagnosing common economizer faults is under development and some initial assessments have been made. Laboratory test data was obtained for a range of ambient conditions and damper openings for method development and evaluation. One of the challenges in performing diagnostics for RTU economizers is that some portion of the exhaust air from the economizer can be recirculated to the intake as depicted in Figure 9a. This implies that a separate outdoor air temperature sensor would not be an accurate representation for the ventilation air temperature. An even more challenging issue is that the mixed air conditions are often highly non-uniform because of a small mixing chamber and so a single-point measurement is not accurate. Figure 9b shows highly non-uniform temperature conditions for a 60% open damper determined through the laboratory testing. In order to realize a cost-effective measurement for mixed and ventilation air, an approach was developed for correcting single-point measurements that correlates the effect of damper position on the average temperatures for the cross section. This virtual sensing approach improves diagnostic performance with no additional sensor costs.

The diagnostic method being developed for economizers uses virtual sensors for outdoor-air fraction (OAF) and other temperature performance indices as inputs and employs rules for expectations for these outputs with open and closed damper positions. Active testing would be employed to initiate open and

closed damper positions when it is clear that faults exist and during an unoccupied period. A Bayesian classifier is used to isolate individual faults using rules established for a list of commonly occurring faults.

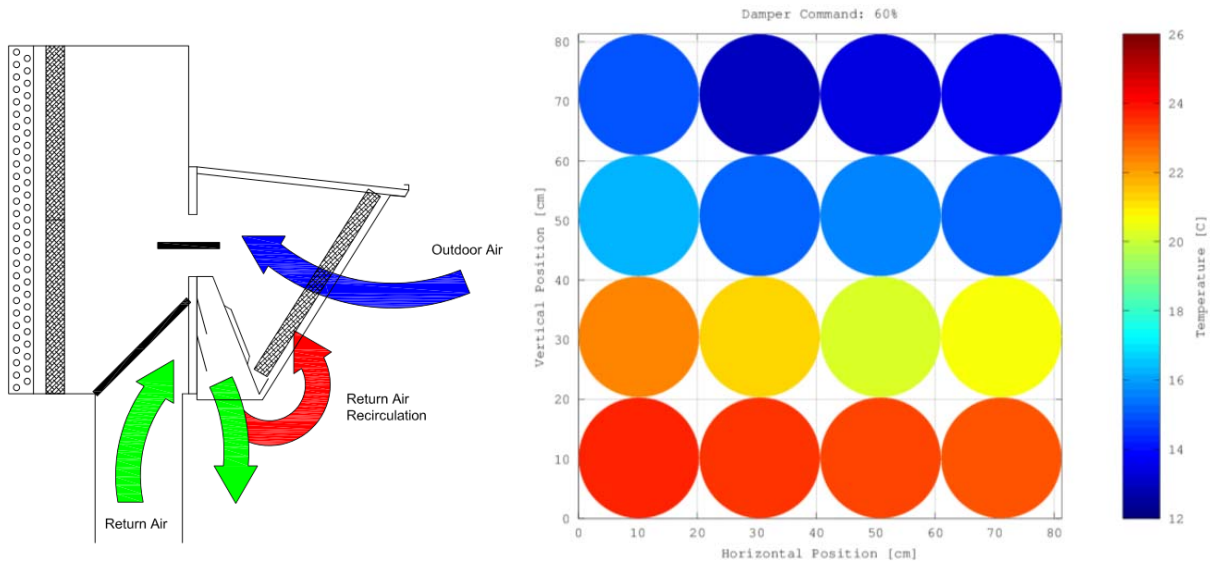


Figure 9. a) Return-air recirculation present in the packaged air-conditioner economizer hood; b) Non-uniform mixed-air temperature distribution at the evaporator inlet position with the outdoor-air damper 60% open. The color scale ranges from outdoor-air temperature (blue) to return-air temperature (red)

B.4 RTU Embedded Diagnostics Demonstration

An implementation for embedded diagnostics applied to a laboratory RTU has been developed using the structure shown on Figure 10. In the preprocessor block, transient input and output measurements are filtered out using a steady-state detector. Once measurements are collected, a fault detection step is used to determine if a fault has occurred. The FDD detection uses three types of virtual sensors; sensor level, component level, and system level. Sensor level means that real measurements (e.g., refrigerant pressure) are replaced with virtual sensors using lower cost measurements (e.g., refrigerant saturation temperature). Component level virtual sensors utilize component models with low-cost input measurements (e.g., a compressor map). System level virtual sensors provide outputs for quantities that could not be determined solely using component level information, including overall refrigerant charge, cooling or heating capacity, and COP. The outputs of the virtual sensors are processed by a fault detection classifier which compares outputs from the virtual sensors to expected values associated with normal behavior to evaluate whether a fault is present. The fault diagnosis block determines the cause of the fault from a list of possibilities. Once, the existence of fault has been detected and identified, a decision block recommends the proper maintenance needed based upon economic considerations.

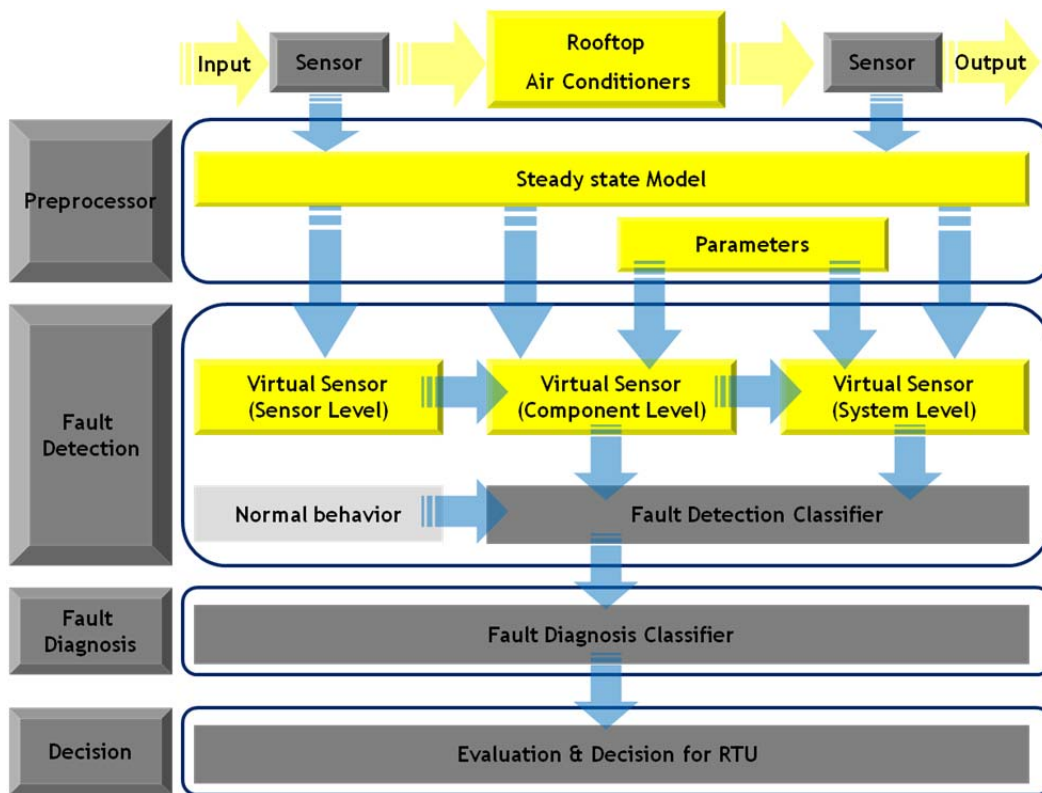


Figure 10. FDD block diagram for RTUs

Initial video demonstrations have been developed for the laboratory RTU that illustrate refrigerant charge and condensing fouling fault diagnostics. Figure 11 shows the interface that displays virtual sensor outputs along with capacity and COP impacts. The virtual refrigerant charge and condenser air flow sensors only require six temperature inputs: evaporating, condensing suction line, liquid line, condenser air inlet and condenser air outlet temperature. For this particular demonstration, 75% refrigerant charge was used to simulate an undercharged condition, whereas the condenser air flow was normal. The capacity and COP ratio indicate 95% and 96% of normal performance for the current operation. The results demonstrate that the impact of refrigerant charge on performance is relatively small for 75 % of the rated charge at this operating condition.

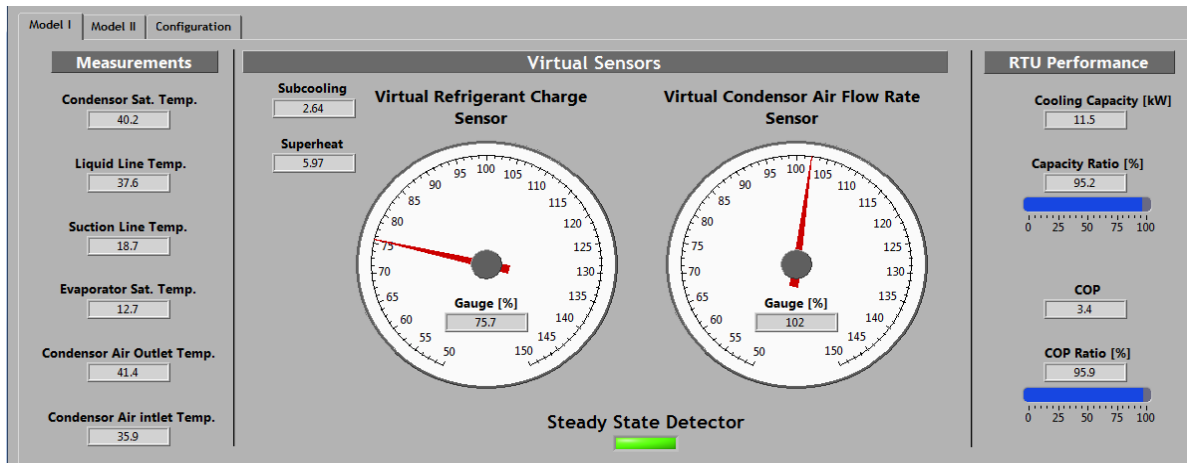


Figure 11. 75% refrigerant charge level & 0% condenser fouling level demonstration

C. AHU-VAV Fault Diagnosis (Drexel team)

During budget period two (BP2), the Drexel team worked to complete the following deliverables in an effort to advance AFDD for AHUs toward widespread commercialization. Briefly, these three areas can be summarized as follows:

- Completion of the Dynamic Fault Simulation Testbed for AHU-VAV systems
- Development and demonstration of the Pattern Matching Principle Component Analysis (PMPCA) Fault Detection Method
- Investigation of fault incidence and associated energy impacts via engagement with local industry and experimental data

C.1 Dynamic Fault Simulation Testbed for AHU-VAV systems

The dynamic fault simulation testbed (Figure 12) allows for the simulation of 51 discrete faults during any seasonal operating condition specified by the user. Nearly all of these 51 faults can also be adjusted so different severities can be tested as well. This testbed can now be used for comparison and analysis of AFDD strategies for this EEB HUB project, to identify the most effective AFDD methods as well as individual strengths and weaknesses of the methods. Both the fault free and fault simulation capabilities of this testbed have been experimentally validated using ASRHAE 1312 experimental data and data obtained from NIST 6964 experiments and simulations. Additionally, the testbed is being shared with other researchers as part of a “beta test”, so that it can help extend the research in this field beyond the scope of the HUB activities.



Figure 12. The dynamic fault simulation testbed

C.2 Development and demonstration of the Pattern Matching Principle Component Analysis (PMPCA) Fault Detection Method

The Drexel team developed a novel fault detection technology for typical AHU systems. This data-driven technology utilizes machine learning techniques, including pattern matching and principle component analysis methods. The following figure demonstrates the operation structure of this methodology.

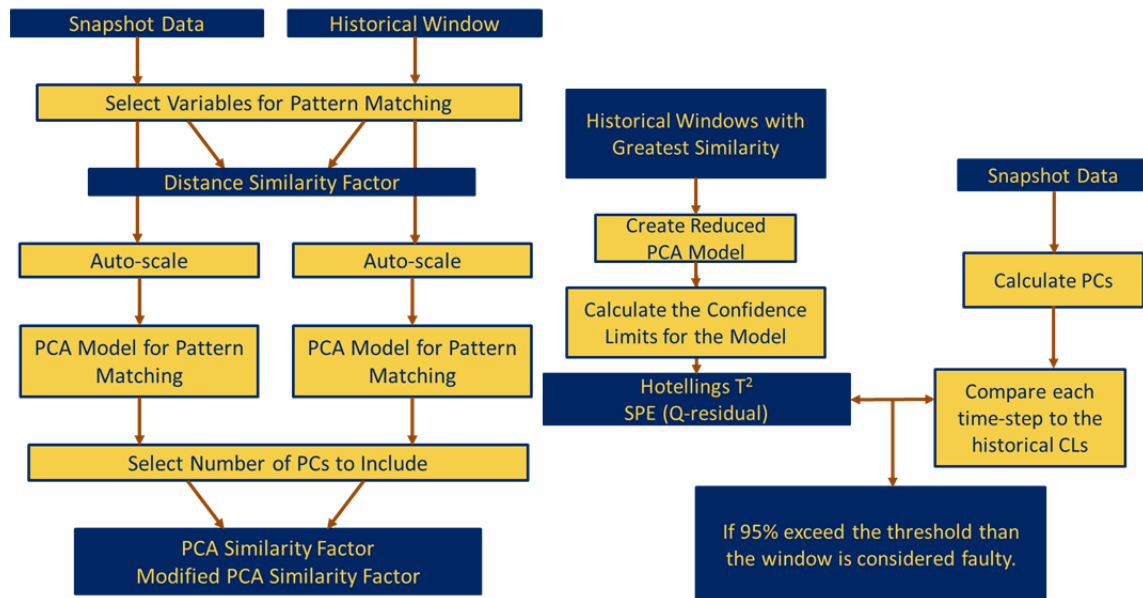


Figure 13. Operation flowchart of the PMPCA method

This approach does not require any fault data training and requires only 10-15 days of fault-free training data (for each season). No requirement for customization for different AHU applications is needed.

In BP 2, various factors that affect the efficacy of this technology were investigated to optimize the performance of the technology:

Data Scaling / Preprocessing – The raw process data from the BMS arrives in many different units and magnitudes. In order to prepare this data for analysis, it must be scaled to even out the impact of the different variables. To do this, a few different methods were tested.

Window Size – The length of the snapshot window and the historical windows must be the same for the purpose of the pattern matching methods. However, the optimal duration needs to be estimated. Shorter windows capture a specific operating condition more effectively, but also result in less data being used in the analysis, so a balance must be struck.

Number of Historical Windows Required – Increasing the number of historical windows used to create the PCA model can result in a more robust model, but this can also result in the use of less similar windows in the model creation that could skew the model.

Window Movement Rates – The rates at which the snapshot and historical windows need to be sampled were studied to consider the trade-off between accuracy and speed.

Impact of Data Normality – The use of PCA requires an underlying assumption that the data is Gaussian. This assumption is met to varying degrees by different training data and snapshot windows. The effect upon the results of the data normality was examined in this project.

Historical Data Requirements – The quantity and quality of historical data plays a key role in the ability to perform accurate fault detection.

Principal Component Retention – PCA-based methods are widely applied across many different fields in the literature, and a number of different component retention methods have been proposed. A number of these different methods have been investigated herein.

These different variables, and the way they impact the efficacy of the PMPCA technology were all explored and summarized in Section 4.5.

Three datasets as described below were used to evaluate the efficacy of the PMPCA technology:

- Small office building experimental data from winter, summer, and shoulder seasons
- Medium-sized office building experimental data from winter months
- Small office building simulation data from the developed virtual testbed

The developed data-driven PMPCA method was shown to detect nearly 90% of the AHU faults from the three datasets described above, with an overall false-alarm rate of less than 1% (details are presented in tables provided in Section 4.5).

Understanding the true strengths and weakness of the PMPCA method requires the context of other existing or proposed AFDD methodologies. Our literature review indicates that there are multiple papers that propose different AFDD techniques. The difficulty with finding benchmarks to compare with is primarily due to the limited testing of the methods that is typically reported. None of the papers identified in the literature provide overall false alarm rates or overall fault detection rates, so there are no widely available benchmarks against which to compare.

The second aspect of evaluating diagnostic methods pertains to the potential for commercialization of the method. To that end, a set of requirements were developed to help with the evaluation process:

- Minimizing the customization required for different systems;
- Trained using solely fault-free data from normal operation;
- Computationally efficient enough for online monitoring;

- Robust enough to maintain accuracy throughout all operating conditions;
- Able to detect abrupt as well as slowly-occurring degradation faults;
- Able to detect both process faults as well as sensor faults;

Using these criteria, many of the methods proposed, while insightful, may not be ready for commercialization. The PMPCA method is qualitatively compared with the one reported by Wall et al. (2011), which was tested using some of the same ERS data utilized in this study. Based on the performance data reported by Wall et al. (2011), the two methods (PMPCA method and the Wall et al. method) performed similarly, both effectively detecting the abnormalities in the data in a manner that corresponds to the severity of the fault. Two potential difficulties with the Wall et al. method are the potential difficulty calibrating a threshold for the log-likelihood at which point a fault should be flagged, and the potential for a very high false alarm rate that is often observed in clustering FDD algorithms.

C.3 Investigation of fault incidence and associated energy impacts via engagement with local industry and experimental data

An investigation of the energy implications of AHU faults, combines analysis of experimental data with interviews conducted with local industry stakeholders. The primary intent of the interviews was to gain further insight into fault occurrence probabilities, as they are observed in the field. This type of information is essential for prioritizing the efforts of AHU diagnostic research, and also allows for increased accuracy when estimating the energy impacts and economic benefits of AFDD for AHUs. Beyond this primary goal of informing our fault incidence estimates, the interview process also provided feedback from industry regarding their needs and desires for effective AFDD.

The ASHRAE 1312 data are also used to assess the energy impact of faults that typically occur in an AHU system. By simultaneously running two identical AHUs side-by-side with the same loads, it is possible to calculate the difference in energy consumption when one is artificially injected with various faults. Using the experimental data from three seasons (summer, winter, and shoulder season), it is found that the fault daily energy impact ranges from 10% up to more than 600%. Faults related to the cooling coil valve have the highest energy impact for all three seasons. For such a small AHU (3000 cubic feet per minute design supply air flow rate), the daily utility cost wasted by faults ranges from 1 dollar up to nearly 300 dollars.

D. Envelope Fault Diagnostics (Bayer team)

Analyzing building envelope faults helps to effectively address air leakage in and out of the building. This in turn helps to ensure acceptable indoor air quality and reduced energy consumption for heating or cooling. Many techniques have been developed to measure the air flow across the building envelope and characterize the envelope faults. Some of the commonly used techniques are: Tracer Gas Test, Blower Door Test, Theatrical Smoke Test and Infrared (IR) Thermography.

Two of the four techniques, IR Thermography and Blower Door Testing, were chosen to be conducted on the EEB HUB headquarters (Building 101). A report was generated for each test to diagnose and characterize faults in the Building 101 envelope. While the Blower door test helped analyze air leakage through the building envelope via HVAC penetrations and windows, the IR thermography test helped to identify the spots in the envelope which accounted for maximum heat loss through the envelope. Bayer generated a report that explains the objectives, advantages and disadvantages of each of four techniques mentioned above, obtained results from the Blower Door Test from another task, oversaw completion of the IR Thermography Test, and summarized the testing results.

The IR Thermography Test detected cracks in window frames on the west side of the building which were a source of air infiltration. This was confirmed through the Blower Door Test which indicated an air leakage of 18cfm through the large arched windows. Both the IR Thermography as well as the Blower Door Test indicated that effective sealing of air gaps at points of penetrations in the exterior walls can help reduce energy consumption. Thus, the results of the two tests complement each other and help to identify and analyze the faults in the building envelope. These faults, when addressed effectively, can contribute to significant reduction in energy consumption of the building.



Figure 14. Heat loss through cracks in window frames

TABLE OF CONTENTS

LIST OF TABLES 18

LIST OF FIGURES 21

1. INTRODUCTION..... 26

2. FAULT PRIORITIZATION TOOL CHAIN..... 26

 2.1 FAULT PRIORITIZATION TOOL CHAIN FOR DESIGN PHASE..... 26

 Introduction 26

 Objective and Motivation 26

 Literature Survey 27

 Methodology 28

 Demonstration and Results 31

 Concluding remarks and future work 34

 2.2. FAULT IMPACT ASSESSMENT TOOL CHAIN FOR OPERATION PHASE..... 35

 Introduction 35

 Methodology 35

 Demonstration and Results..... 40

 Concluding Remarks and Future Work 41

3. RTU FAULT DIAGNOSIS 42

 3.1. INTRODUCTION 42

 3.1.1. Background/Need 42

 3.1.2. Objectives 42

 3.1.3. Literature Review 43

 3.2. RTU LABORATORY AND FIELD TESTING FOR OFFLINE ANALYSIS (UTRC)..... 46

 3.2.1. Laboratory Testing..... 46

 3.2.2. Field Testing 50

 3.3. RTU FDD ASSESSMENTS USING OFFLINE DATA 62

 3.3.1. Impact of Faults on Performance and Costs Using Offline Data 62

 3.3.2. Development and Assessment of Virtual Sensors Based on Existing Laboratory Data 69

 3.3.3. Assessments of Virtual Sensors using UTRC RTU Data 81

 3.4. EMBEDDED AFDD (AUTOMATED FAULT DETECTION AND DIAGNOSIS) FOR RTU 94

 3.4.1. System descriptions and test conditions for refrigerant charge, heat exchanger fouling, economizer, and supply fan faults..... 94

 3.4.2. Virtual sensor (refrigerant charge, refrigerant mass flow rate, and air flow rate) assessments for RTU..... 95

 3.4.3. Structure for a Diagnostic Decision System based on Virtual Sensors 99

 3.4.4. Economizer Fault Detection and Diagnosis 106

 3.4.5. Impact of faults on system performance for AFDD demonstration RTU 135

 3.4.6. Develop user interface for initial diagnostic demonstration..... 137

 3.5. AFDD FOR BUILDING 101 DX SYSTEMS 142

 3.5.1. System descriptions of Building 101 DX/AHU systems..... 142

 3.5.2. Virtual sensors developments/assessments for Building 101 DX systems..... 142

 3.5.3. Initial demonstration of virtual sensor for Building 101 DX systems..... 147

 3.6. CONCLUSIONS 149

 3.7. FUTURE STUDIES 150

4. AHU-VAV FAULT DIAGNOSIS..... 151

4.1 INTRODUCTION	151
4.2. BACKGROUND AND BRIEF REVIEW OF RELEVANT LITERATURE	152
AFDD for AHU-VAV: Pattern Matching PCA Method	152
AHU Fault Energy Impact Literature	157
4.3. DYNAMIC AHU-VAV FAULT SIMULATION TESTBED	158
Testbed Overview and Functionality	158
VAV Fault Model Development and Available Data	158
Model Validation	161
Other Modeled Faults	162
4.4. FAULT DETECTION USING THE PATTERN MATCHING PCA (PMPCA) METHOD	162
Method Overview	164
4.4.4 Method Development and Optimization for AHUs	170
4.5. PATTERN MATCHING PCA DEMONSTRATIONS	171
Demonstration Overview	171
Base Case & Input Methodology	172
Method Refinement	178
Discussion of Results	187
4.6. RECOMMENDATIONS FOR CONTINUING PMPCA INVESTIGATION	188
Testing with Additional Data (Online and Offline)	188
Final Tuning of the Method	188
4.7. DIAGNOSTIC METHOD ASSESSMENTS AND COMPARISON	189
4.8. ENERGY IMPLICATIONS OF AHU-VAV FAULTS	190
Experimental Data	190
Preliminary Expert Interviews	202
4.9. CONCLUSIONS AND RECOMMENDATIONS	203
5. ENVELOPE FAULT DIAGNOSTICS	205
5.1 INTRODUCTION	205
5.2 LITERATURE REVIEW	206
Tracer Gas Test	206
Blower Door Test	207
Theatrical Smoke Test	208
Infrared Thermography	208
5.3. ENVELOPE FAULT CHARACTERIZATION METHODS AND RESULTS	209
Conduct IR thermography test on Bldg. 101	209
Summary	212
5.4. SUMMARIZE BLOWER DOOR TESTING RESULTS FOR BLDG. 101	213
Obtain test summary report from appropriate person	213
Generate summary of results to identify air leaks through the envelope in Bldg. 101	213
5.5. PRESSURE TESTS	215
5.6. SUMMARY	221
6. CONCLUSIONS AND FUTURE STUDY	223
REFERENCE	225
APPENDIX 1	233
APPENDIX 2	234
APPENDIX 3	248

LIST OF TABLES

<u>Table</u>	<u>Page</u>
Table 2.1 Generic fault model types with illustrative examples	29
Table 3.1 Summary of fault incidence analysis	46
Table 3.2 Summary of fault impact analysis.....	46
Table 3.3 Tested conditions in 2012	51
Table 3.4 Additional sensors.....	52
Table 3.5 Air speed data from air balancing report	53
Table 3.6 operating ranges	59
Table 3.7 Data set	62
Table 3.8 System Specifications	63
Table 3.9 Test Conditions	63
Table 3.10 System Specifications	66
Table 3.11 Test Conditions	66
Table 3.12 System descriptions for air conditioner	70
Table 3.13 Test conditions for air conditioners	70
Table 3.14 System descriptions for system A-5	74
Table 3.15 Test conditions for laboratory test data for system A-5	74
Table 3.16 Specification of system	81
Table 3.17 Testing conditions.....	81
Table 3.18 System specification for RTU system.....	86
Table 3.19 testing condition for RTU system.....	86
Table 3.20 System specification	94
Table 3.21 Test conditions.....	94
Table 3.22 Calculation for threshold for Bayes classifier.....	105
Table 3.23 FDD response to compressor valve leakage based on Bayes classifier	105
Table 3.24 FDD responses to 1) low refrigerant charge, 2) condenser fouling, and 3) liquid line restriction faults based on Bayes classifier	105
Table 3.25 Economizer cooling states along with damper position, compressor status, and heating coil status for each state	110

Table 3.26 Outdoor-air economizer performance test conditions for outdoor-air temperature, indoor-air temperature, outdoor-air damper position, and supply fan speed.....	113
Table 3.27 Outdoor-air economizer test measurements.....	114
Table 3.28 Fault detection results for normal data and various types of faults.....	130
Table 3.29 Types of economizer faults with Bayesian classifier class.....	133
Table 3.30 Residual response to stuck damper fault.....	134
Table 3.31 Summary of economizer residual responses.....	134
Table 3.32 Bayesian classifier training data.....	134
Table 3.33 Results of applying the fault diagnostics approach to normal operation data.....	135
Table 3.34 Results of applying the fault diagnostics approach to stuck damper fault data.....	135
Table 3.35 System specification of DX system 2 & 3.....	142
Table 4.1 VAV terminal unit fault summary.....	159
Table 4.2 Baseline results using ASHRAE 1312 ERS data (summer).....	174
Table 4.3 Baseline results using UTRC data.....	178
Table 4.4 Baseline results using simulation data (summer).....	179
Table 4.5 Results with reduced window durations using UTRC data.....	180
Table 4.6 Results with extended window durations using UTRC data.....	181
Table 4.7 Results of reduced number of historical windows using UTRC data.....	181
Table 4.8 Results of reduced number of historical windows using ERS data.....	182
Table 4.9 Results of increased number of historical windows using ERS data.....	183
Table 4.10 Results of reduced pc retention variance using ERS data.....	186
Table 4.11 Results of linear test for pc retention using ERS data.....	187
Table 4.12 Energy comparison of A and B systems at the ERS under fault free conditions.....	194
Table 4.13 Summer fault energy impacts (airstream).....	195
Table 4.14 Spring fault energy impacts (airstream).....	195
Table 4.15 Winter fault energy impacts (airstream).....	198
Table 4.16 Primary system efficiency assumptions.....	198
Table 4.17 Summer fault energy impacts (building energy).....	199
Table 4.18 Spring fault energy impacts (building energy).....	199
Table 4.19 Winter fault energy impacts (building energy).....	200
Table 4.20 Utility cost estimates (Philadelphia, 2012).....	200
Table 4.21 Summer fault impacts (daily cost).....	201

Table 4.22 Spring fault impacts (daily cost) 201

Table 4.23 Winter fault impacts (daily cost)..... 202

Table 5.1 Summary of the findings..... 213

Table 5.2 Analysis results whole building depressurization test 217

LIST OF FIGURES

<u>Figure</u>	<u>Page</u>
Figure 2.1 Various faults modeled in the library	28
Figure 2.2: Integrated fault modeling interface.....	29
Figure 2.3 Overall process for fault prioritization	30
Figure 2.4: Performance measures defined for individual and coupled faults.....	31
Figure 2.5 Building 101 and TRNSYS model	31
Figure 2.6: Summer prioritization based on change in electrical energy (performance measure) for individual and coupling faults.....	33
Figure 2.7: Winter prioritization based on change in boiler energy (performance measure) for individual and coupling faults.....	34
Figure 2.8: Illustration of Backward Fault Injection (BFI) approach for the energy impact assessment of the component faults.....	36
Figure 2.9: Fault impact assessment process used in operation phase.....	36
Figure 2.10 A Graphical model (right) for the Economizer (left) of an Air Handling Unit. The Grey and white nodes represents the discrete and continuous variables respectively	37
Figure 2.11 Comparison of the sensitivity of the discrete (red) and mixed (blue) graphical models in terms of their prediction accuracy.	38
Figure 2.12 Illustration of a functional test to generate good quality data for graphical model learning.....	39
Figure 2.13 Fault propagation capability for operation based models data	39
Figure 2.14 Fault impact analysis process	40
Figure 2.15 Comparison of automated fault impact assessment process with the TRNSYS model, for fault energy impact analysis.....	41
Figure 3.1 The selected RTU (AC24F) on UTRC campus.....	51
Figure 3.2 Static profile from air balancing report	53
Figure 3.3 Dampers of AC24F.....	54
Figure 3.4 Supply-air speed vs. outside-air damper position.....	54
Figure 3.5 Air flows vs. outside-air damper opening.....	55
Figure 3.6 A custom-built air sampling tree	55
Figure 3.7 Air sampling tree on AC24F	56
Figure 3.8 Mixing-air temperature.....	57
Figure 3.9 Charge adjustment.....	57
Figure 3.10 Measurements of speed of air entering the first-circuit condenser.....	58

Figure 3.11 Comparison of air side and refrigerant side energy	59
Figure 3.12 Air side thermal capacity vs. condenser flow reduction	60
Figure 3.13 Subset of data from tests of cooling season of 2012	60
Figure 3.14 Cooling capacity of the same set of data	61
Figure 3.15 Capacity ratio for existing test data based on the refrigerant charge	64
Figure 3.16 Annual cost ratios for all test data as a function of refrigerant charge	65
Figure 3.17 Capacity ratio for RTU and split air conditioners based on indoor air flow rate.....	67
Figure 3.18 Capacity ratio for RTU and split air conditioners based on outdoor air flow rate.....	67
Figure 3.19 Cost ratio for RTU and Split air conditioner based on indoor air flow rate	68
Figure 3.20 Cost ratio for RTU and Split air conditioner based on outdoor air flow rate	68
Figure 3.21 Performance of VRC sensor model 1 based on default parameters	71
Figure 3.22 Performance of VRC sensor model 1 based on tuned parameters.....	71
Figure 3.23 Performance of VRC sensor model 3 based on tuned parameters.....	72
Figure 3.24 Performance of VCP sensors for system C-5 under no fault and multi fault condition	74
Figure 3.25 Performance of VRMF 1 based on compressor map	75
Figure 3.26 Performance of VRMF sensor II based on an energy balance	76
Figure 3. 27 Diagram of TXV.....	77
Figure 3.28 Performance of VRMF sensors III based on TXV model under no fault and fault conditions	78
Figure 3.29 Comparison of VRMF sensor outputs for system C-5 with compressor flow fault	79
Figure 3.30 Predicted condenser air flow from an energy balance versus expected value for system C-580	
Figure 3.31 Predicted evaporator air flow from an energy balance versus expected value for system C-5	81
Figure 3.32 Performance of VRC sensor model 1 based on default parameters for UTRC laboratory data	82
Figure 3.33 Performance of VRC sensor model 1 based on tuned parameters for UTRC laboratory data83	
Figure 3.34 Performance of VRC sensor model 3 based on tuned parameters for UTRC laboratory data83	
Figure 3.35 Performance of VCP sensor for UTRC laboratory data	84
Figure 3.36 Performance of VRMF sensor I based on compressor map for UTRC laboratory data	84
Figure 3.37 Performance of VRMF sensor II based on energy balance for UTRC laboratory data.....	85
Figure 3.38 Performance of VRMF sensor III based on TXV model for UTRC laboratory data	86
Figure 3.39 Charging results based on manufacturers' charging method under no heat exchanger blocking	87

Figure 3.40 Charging results based on manufacturers’ charging method under heat exchanger blocking88

Figure 3.41 Performance of VRC sensor model I based on tuned parameters under no condenser fouling
..... 89

Figure 3.42 Performance of VRC sensor model I based on tuned parameters under condenser fouling89

Figure 3.43 Performance of VRC sensor model III based on tuned parameters under no condenser fouling
..... 90

Figure 3.44 Performance of VRC sensor model III based on tuned parameters under condenser fouling90

Figure 3.45 Performance of VCP sensors under normal and faulty conditions..... 91

Figure 3.46 Performance of VRMF sensors based on model I and II under normal and faulty conditions
..... 92

Figure 3.47 Performance of VRMF sensors based on models II and III under normal and faulty conditions
..... 92

Figure 3.48 Performance of VAF sensors for condenser under normal refrigerant charge level 93

Figure 3.49 Performance of VAF sensors for condenser under different refrigerant charge levels 93

Figure 3.50 Schematic of RTU system..... 95

Figure 3.51 Performance of VRC sensor model 1 based on tuned parameters for RTU system. 96

Figure 3.52 Performance of VRC sensor model 3 based on tuned parameters for RTU system. 96

Figure 3.53 Predicted condenser air flow from an energy balance versus expected value. 97

Figure 3.54 Predicted evaporator air flow from an energy balance versus expected value based on fan
setting..... 98

Figure 3.55 Performance of VCP sensor under no fault and fault conditions 98

Figure 3.56 Comparison of three VRMF sensor outputs for RTU unit 99

Figure 3.57 FDD block diagram for RTUs 100

Figure 3.58 Virtual sensor classifications for air conditioner..... 101

Figure 3.59 Example of virtual sensor interactions for air conditioning equipment..... 101

Figure 3.60 Overall fault interactions for air conditioning equipment 104

Figure 3.61 Packaged air-conditioner ventilation configuration when supplying 100% outdoor-air.. 107

Figure 3.62 Packaged air-conditioner ventilation configuration when outdoor-air damper is fully closed
..... 107

Figure 3.63 Economizer control sequence for dry-bulb economizers with increasing outdoor-air
temperature 108

Figure 3.64 Simulated effects of a stuck open outdoor-air damper in the summer during a day. 111

Figure 3.65 Return-air recirculation present in the packaged air-conditioner economizer hood..... 115

Figure 3.66 Outdoor-air temperature grid for three different damper positions. Temperature measurements at the bottom of the grid are warmer than the rest of the thermocouples due to return-air recirculation. 116

Figure 3.67 Outdoor-air temperature grid for three different damper positions when barometric relief vents were forced closed..... 117

Figure 3.68 Corrected single-point outdoor-air temperature model fit..... 119

Figure 3.69 Non-uniform mixed-air temperature distribution at the evaporator inlet position with the outdoor-air damper 60% open. The color scale ranges from outdoor-air temperature (blue) to return-air temperature (red) 120

Figure 3.70 Predicted supply fan temperature rise model results 122

Figure 3.71 Corrected single-point mixed-air temperature model fit. 123

Figure 3.72 OAF response to different outdoor-air damper positions under different outdoor-air temperatures..... 124

Figure 3.73 Outdoor-air fraction model fit. 125

Figure 3.74 FDD Overall Flow Chart 126

Figure 3.75 Histogram of fault-free economizer operation when outdoor-air damper is at 60% and outdoor-air temperature at 12.78 °C. Note that the M1 matches closely with the expected behavior, which makes the p-value close to 1. 128

Figure 3.76 Histogram of the outdoor-air fraction metric, M1, with a 20% difference between the controlled and actual damper position at an outdoor-air temperature of 12.78 °C. A clear deviation exists between the current and normal operation, signifying an economizer fault. 129

Figure 3.77 Histogram of the outdoor-air fraction metric, M1, when a -2.0 °C sensor bias is applied to the outdoor-air temperature sensor. 129

Figure 3.78 OAE active diagnostics using only dry-bulb temperature sensors and control of the outdoor-air damper position (Fernandez 2009). 131

Figure 3.79 Capacity and COP ratio based on different refrigerant charge levels..... 136

Figure 3.80 Capacity and COP ratio based on the different fouling level. 136

Figure 3.81 75% refrigerant charge level & 0% condenser fouling level demonstration..... 137

Figure 3.82 100% refrigerant charge level & 0% condenser fouling level demonstration 138

Figure 3.83 Condenser status of RTU system (left side: normal & right side: 50% blocking) 138

Figure 3.84 100% refrigerant charge level & 70% condenser fouling level demonstration 139

Figure 3.85 Implementation and demonstration of an automated FDD system for RTU under normal condition 140

Figure 3.86 Implementation and demonstration of VRC sensor under normal condition 141

Figure 3.87 Implementation and demonstration of an automated FDD system for RTU under normal condition 141

Figure 3.88 Implementation and demonstration of VRC sensor under normal condition 142

Figure 3.89 VRC sensor outputs based on default parameters for condensing unit #3A..... 143

Figure 3.90 VRC sensor outputs based on default parameters for condensing unit #3A..... 143

Figure 3.91 VRMF sensor outputs based on energy balance for DX unit 2A 144

Figure 3.92 Performance of VAF sensors based on energy balance for DX unit 2A & 2B. 144

Figure 3.93 Accuracy of predicted power based on compressor map for DX unit 3 circuit 1..... 145

Figure 3.94 Evaluation of VRMF sensor based on energy balance in relation to compressor map for DX unit 3 circuit 1 146

Figure 3.95 VRC sensor outputs based on default parameters for DX unit 3 circuit 1..... 147

Figure 3.96 VRC sensor outputs based on default parameters for DX unit 3 circuit 2..... 147

Figure 3.97 Performance of VRC, VRMF, and VAF sensor for DX unit 1. 148

Figure 3.98 Example of demonstration for DX2A unit 148

Figure 4.1. VAV terminal unit reheat coil stuck open valve fault 161

Figure 4.2 VAV terminal unit reheat coil valve 10% leaking fault 162

Figure 4.3 AHU schematic 163

Figure 4.4 AHU operational modes 166

Figure 4.5: pattern matching algorithm schematic..... 168

Figure 4.6: Fault Detection Algorithm Schematic 169

Figure 4.7: ERS experimental setup 173

Figure 5.1 Heat loss through wall cracks 210

Figure 5.2 Heat loss through building soffit 211

Figure 5.3 Heat loss through cracks in window frames 212

Figure 5.4 Three fan blower door 216

Figure 5.5 Location for blower door fans and pressure taps..... 217

Figure 5.6 Historical test data for non-residential building in terms of ACH 50..... 218

Figure 5.7 Fire control dampers initially sealed with self-adhering duct mask 219

Figure 5.8 Outdoor air intake unmasked..... 220

Figure 5.9 Large arched windows on the west side of the building..... 221

1. Introduction

HVAC systems in buildings are responsible for 14% of primary energy consumption and 32% of all electricity generated in the U.S. For office buildings, HVAC energy consumption represents about 48% of the total primary energy usage (Pérez-Lombard et al., 2008). Furthermore, energy use in the built environment is projected to grow at an average rate of 1.5% annually. Previous studies have indicated that energy consumption in commercial buildings is as much as 30% higher than expected due to the presence of faults (Katipamula and Brambley 2005). Automated fault detection and diagnosis (AFDD) can reduce this additional energy consumption, improve comfort conditions, and reduce costs for service.

The goal of this project is to develop and demonstrate a library of diagnostics decision support tools that can enable cost effective diagnostics solutions for existing buildings. Whole building diagnostic and decision support tools should robustly maintain building energy performance at an optimal level following commissioning of retrofitted buildings. In Budget Period 2 (BP2), the project teams have focused on two select building types: 1) buildings that employ packaged rooftop air conditioners (RTU) and 2) buildings that utilize built-up air-handling units (AHU) with variable-air-volume (VAV). These building types were selected to be representative of the 10-county EEB-HUB region. The specific goals for BP2 were: 1) develop, evaluate and implement sub-system diagnostics solutions as both embedded and add-on solutions and 2) develop and evaluate whole building decision support tools and systems for corrective action prioritization by building decision makers (including facility operators and sub-system service providers). The Purdue team focused on RTU and DX equipment, the Drexel team addressed AHU-VAV systems, Bayer studied faults for envelope systems and the UTRC addressed whole building decision support tools and systems. In subsequent years, the library will be expanded to include tools that cover all of the representative equipment, envelopes, and systems within buildings for the EEB-HUB region and whole building demonstrations of the diagnostic implementations will be performed.

The following sections provide a detailed description of the major accomplishments by the UTRC, Purdue, Drexel, and Bayer teams.

2. Fault Prioritization Tool Chain

2.1 Fault Prioritization Tool Chain for Design Phase

Introduction

It has been widely reported that degraded and poorly controlled building systems can use up to 30% more energy (Katipamula and Brambley 2005). Building performance simulation (BPS) tools have become increasingly important with the growing strive to reduce energy use in building sector. Among other diverse applications, BPS tools can play significant role in facilitating energy retrofit analysis, supporting retro-commissioning activities and act as design support tool when designing sensor network to be used for continuous commissioning.

At the same time, current state of the art tools do not provide a standard and scalable capability to model and simulate faults occurring in buildings. With exception of few (e.g. EnergyPlus fault models, Basarkar et al. 2011) BPS tools assume non faulty operation of the building system.

Objective and Motivation

The objective of this work is to develop a scalable model based approach for evaluating impact of various building faults, and extend it to prioritize building energy failure sources. Due to lack of scalable

approach, expert judgment is currently used to guess critical building faults. Although this approach may work for handful of faults, it does not provide any quantitative measure of fault impact (e.g. kWh or \$ wasted), and provides very little economic input for design of FDD system (i.e. does the fault impact warrant FDD system investment). Also, expert judgment typically fails to capture and prioritize coupling effect when multiple faults occur together. As we will show in this report, coupling effect can be significant even though individually faults may be insignificant.

Thus, a readily deployable and generic fault modeling capability is required if BPS tools are to be employed in above mentioned applications. Also, a systematic process is needed to explore both individual and coupling fault impact. This was also a motivation behind the work presented in this report. Our objective is to develop a generic model based approach that can be used for quantification of various faults and fault severities impact on energy consumption and develop a systematic process that uses this capability for fault prioritization. In this report, we present a fault modeling library developed in TRNSYS and demonstrate its applicability in a systematic process for fault prioritization.

We note that although the library is demonstrated for fault prioritization at design stage in this report, it has applications in other FDD areas as well, such as prognosis and real time fault impact assessment.

Literature Survey

Building Faults

There were a few attempts in the literature to provide lists of most common faults in building systems (e.g. ANNEX 25 1996, Lee et al. 1997, ASHRAE 1043-RP, 1999, Siegel, 2002, Li, 2009). The faults could be of different types as reported by Haves (1977): abrupt – which happen suddenly, and degradation – which develop over time.

In this report, we have derived an extensive list of different fault types that translate to more than 200 faults for complete air handling system and pertinent building zones, based on in-house building expert brainstorming and Wen and Li (2011). Both abrupt and degradation faults were considered.

BPS for Fault modeling

BPS tools have been increasingly used in building design. However, their use in operational phase has been restricted due number of limitations, one of which is their inability to directly account for imperfections in building systems that could possibly lead to misspredictions of performance.

Few isolated studies were reported in which BPS tools were used for fault simulation. Examples include: reverse control and leaky damper faults in HVACSIM+ by Dexter (1995), sensor offset and damper and valve mechanical blockage in MATLAB SIMULINK by Glass et al. (1995), cooling coil fouling and valve leakage in HVACSIM + by Haves et al. (1996) and economizer operation faults in DOE-2 by Katipamula et al. (1999). The faults were simulated perturbing relating parameters to mimic faults. Although this approach can lead to accurate prediction of the change in system performance, it heavily relies on expert judgments of the modeler and thus is not readily reusable for other buildings and available to other modelers. More reusable fault model developments in ENERGYPLUS have been reported by Basarkar et al. (2011).

In addition, the reported studies consider only individual fault effects on degradation of building performance. The coupling effect has not been part of above studies. As we show in this report, building faults could show significant coupling effect when occurring simultaneously, which could as well cause difficulties in designing fault detection and diagnostic algorithms. Hence, a systematic approach to explore both individual and coupling faults is required, which is addressed in this report.

Methodology

Fault Model Library

To simulate different faults, we have developed a generic and scalable fault model library. Currently, the fault library is developed in TRNSYS (TRNSYS, v17), and is reusable and expandable to any building size. The library development resulted in a new TRNSYS environment. It is an extension of the commercially available tool that enables simulation of faults. TRNSYS graphical user interface is extended so, the faults can be modeled in TRNSYS Studio. We also developed a fault manager in TRNSYS, which is used to manage fault simulation and is also intended to serve as an interface to other simulation tools (such as optimization and/or uncertainty quantification tools).

The following inputs are needed to use the newly developed TRNSYS environment:

- TRNSYS textual input file (dck file);
- new TRNSYS environment (new .dlls and proformas in correct folders).

Although TRNSYS allows for high modeling flexibility, passing information from one component model to another without following the working fluid or signal flow is not recommended if consistency of fault propagation has to be assured.

The steps to simulate faults are as follows:

- import dck file into TRNSYS Studio;
- create (or Copy from ‘Template’) Fault Manager Component in the new TRNSYS project file;
- create links between Fault Manager and components in which faults are introduced;
- inject faults using the fault prioritization process discussed later run fault simulation.

ECONOMIZER	PID CONTROLLER	HEATING COIL	PLENUM	BOILER	DX COIL	SCHEDULE	FAN	PUMP
OA DAMPER STUCK	UNSTABLE CONTROLLER	DIRTY COIL		BOILER REDUCED EFFICIENCY	SENSOR OFFSET	AMPLITUDE CHANGE	WORN/LOOSE FAN BELTS	MOTOR FAILING
RA DAMPER STUCK	INVERSE CONTROL	DAMPER STUCK	DUCT LEAK	BOILER REDUCED CAPACITY	REDUCED CAPACITY		INLET OBSTRUCTED	IMPELLER FAILING
EA DAMPER STUCK	SET POINT OFFSET	DAMPER LEAKY		TEMPERATURE SENSOR READING OFFSET	REDUCED COP		24 HOUR OPERATION	INLET OBSTRUCTED
OA DAMPER LEAKY	STUCK ACTUATOR	DAMPER OBSTRUCTED AT LOWER POSITION	DAMANGED INSULATION					
RA DAMPER LEAKY	LEAKY ACTUATOR	DAMPER OBSTRUCTED AT HIGHER POSITION						
EA DAMPER LEAKY	ACTUATOR OBSTRUCTED HIGH	VALVE STUCK						
AMBIENT AIR TEMPERATURE SENSOR OFFSET	ACTUATOR OBSTRUCTED LOW	VALVE LEAKY						
COOLING COIL SET POINT TEMPERATURE OFFSET	MAX VALUE COMMISSIONED HIGH POSITION	VALVE OBSTRUCTED AT LOWER POSITION						
ZONE TEMPERATURE SET POINT OFFSET	MAX VALUE COMMISSIONED LOW POSITION	VALVE OBSTRUCTED AT HIGHER POSITION						
MIXED AIR TEMPERATURE SENSOR OFFSET	SENSOR READING OFFSET							
OA DAMPER OBSTRUCTED HIGH								
OA DAMPER OBSTRUCTED LOW								
MIN OA FRACTION OFFSET								

Figure 2.1 Various faults modeled in the library

We have identified three generic types of fault models (as illustrated in

Table 2.1):

1. Continuous fault/ continuous variable: Fault where the transition from faulty to non-faulty state happens in continuous manner and which can take any value from a given continuous range (e.g. sensor temperature offset).
2. Discrete fault/ discrete variable: Fault where the transition from faulty to non-faulty state does not happen in continuous manner and which can only take value(s) from a discrete range (e.g. changing sign of proportional gain in PID controller).
3. Discrete fault/ continuous variable: Fault where the transition from faulty to non-faulty state does not happen in continuous manner and which can take any value from a given continuous range (e.g. actuator being stuck).

Table 2.1 Generic fault model types with illustrative examples

Continuous fault/ continuous variable	Discrete fault/ discrete variable	Discrete fault/ continuous variable
T_SET_ZONE=T_SET_ZONE+FAULT	IF (FAULT.NE.0.)THEN Kc=-Kc ENDIF	IF (FAULT.NE.0) THEN FRAC_OA=FAULT ENDIF

In the current implementation of the library, each fault is represented by a single parameter (an example is given in Figure 2.2). The same parameter is used to indicate the presence of a fault, as well as to provide information about the intensity and characteristics of the fault. For all the parameters representing faults, value ‘0’ specifies non faulty condition. Any other value is used to characterize the fault. This notion is natural for most of faults of the first type (

Table 2.1) for which the change from faulty to non faulty condition happens by continuously changing a corresponding parameter. However, for the other two types, for which this transition is not, faulty condition is limited to values not-equal to ‘0’.

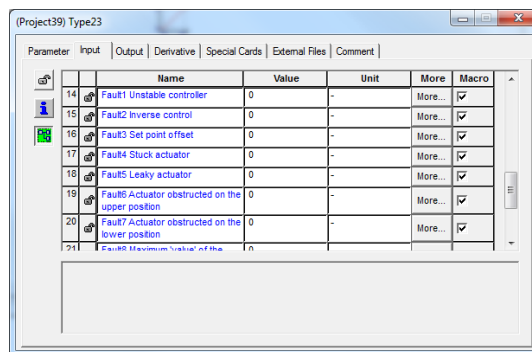


Figure 2.2: Integrated fault modeling interface

Performance measure for fault coupling prioritization has been defined as an additional change in building energy consumption over the additive change when two faults are introduced, and is determined as follows:

$$F(AB) = [E(\text{faults A\&B introduced}) - E(\text{Baseline})] - [F(A) + F(B)]$$

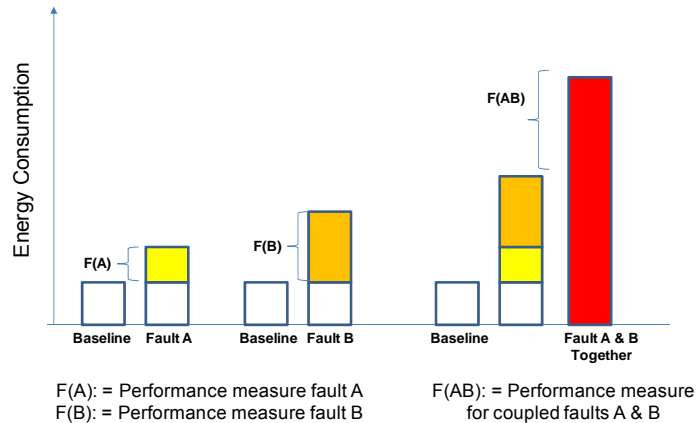


Figure 2.4: Performance measures defined for individual and coupled faults

The fault prioritization is based on the impact on the above defined performance measures. The fault with higher performance measure is ranked higher. Same rationale is applied to coupling effect prioritization. Next, we illustrate our methodology with a case study.

Demonstration and Results

Building Description

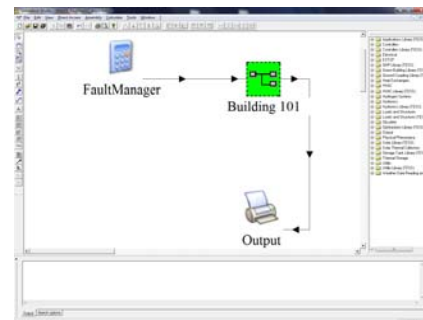


Figure 2.5 Building 101 and TRNSYS model

For the demonstration purposes, we selected a mid-sized office building in the Philadelphia Navy Yard, called Building 101 (Figure 2.5). Overall building is 61700 ft², and is equipped with 3 AHUs and number of VAV boxes with reheat coils. Each AHU contains an economizer, a heating coil (served by boiler), and DX cooling coil. We have developed a TRNSYS model for a part of building 101, as shown in Figure 2.5. Our TRNSYS model included one AHU (called AHU3), 8 VAVs, and all 10 zones served by the modeled part of the HVAC system.

As stated earlier, we evaluated the individual fault impact by injecting one fault at a time, followed by two faults (coupled faults) at a time evaluation. For simplicity, the time variation in fault intensities has not been considered in this study even though the library does not pause such limitation. We simulated one week each from summer and winter seasons, and prioritized faults for each seasons. Next, we discuss the results from summer prioritization. For the discussion purposes, we only illustrate approximately top 15-20 faults in each category.

Fault Prioritization: Summer conditions

Figure 2.6 shows the results of fault prioritization for summer conditions. For summer conditions, we have used the building electric energy consumption as the performance measure. We can see from Figure 2.6 that 24 hour operation and OA damper stuck are top two faults, resulting in approximately 59% and 51% increase in electrical energy consumption, respectively. This result matches building experts' judgment/intuition. However, our methodology has helped quantify the magnitude of energy impact of each fault, which is building system dependent and thus rarely intuitive. Knowledge of top individual faults is very useful to building energy manager, as either they can be eliminated or appropriate diagnostic packages can be deployed to monitor them. Also, the magnitude of the energy impact can also be used to perform economic assessment of such diagnostic package deployment.

Figure 2.6 also shows the prioritization of coupling faults, when two faults occur together. We point to an interesting result marked by red dotted oval. In summer, not shutting down the heating alone does not have significant impact on the performance measure. The same applies to having the heating water valve in AHU heating coil being stuck. However, if these two faults happen at the same time, their effect is significant. For building 101, their coupled effect can be upwards of 20% increase in energy consumption. The heating will work against cooling and increase discharge air temperature from AHU. Occupant comfort does not necessary need to be decreased if it could be provided by higher air flow through each VAV.

This result illustrates that the energy impacts estimated by our methodology for two faults occurring together are not as intuitive to the expert, as the individual faults. The methodology ensures that all key faults and couplings are captured, and nothing is left for intuition. Interestingly, the corrective action to suppress a coupling effect only involves fixing one of the faults. The energy manager can incorporate this information when prioritizing corrective actions.

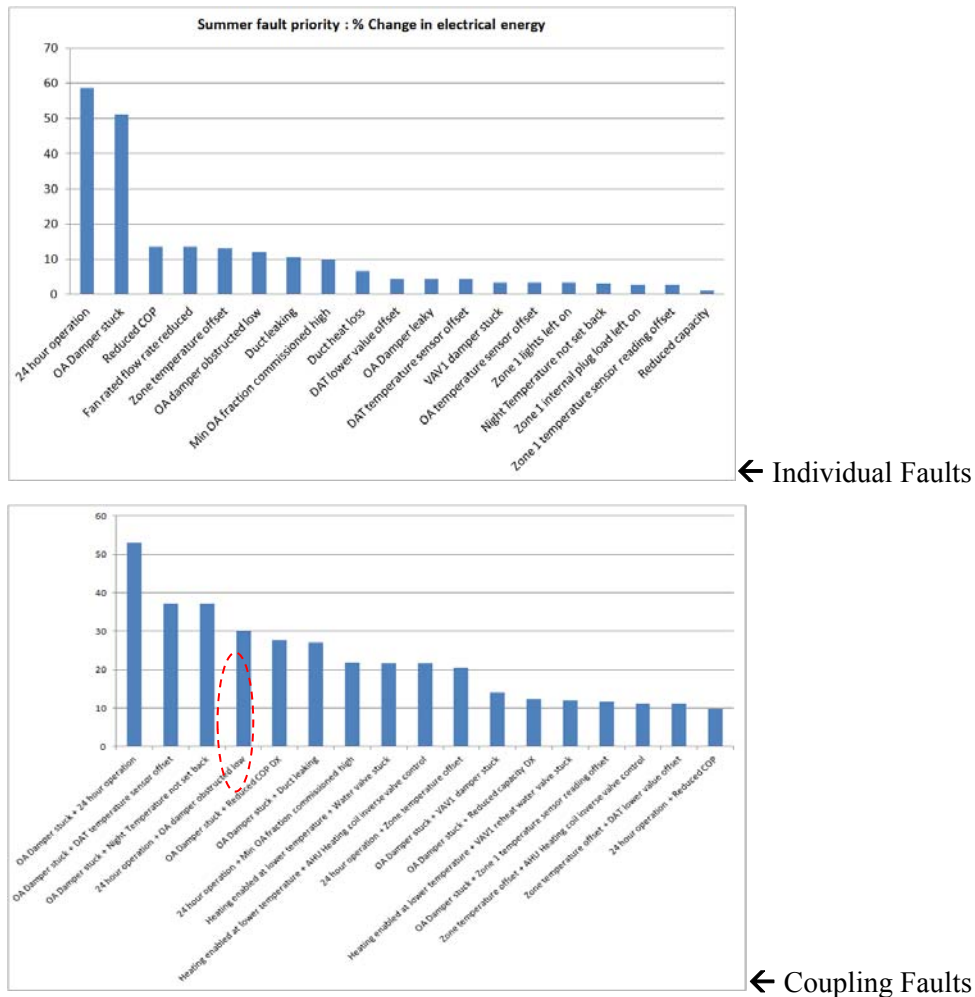


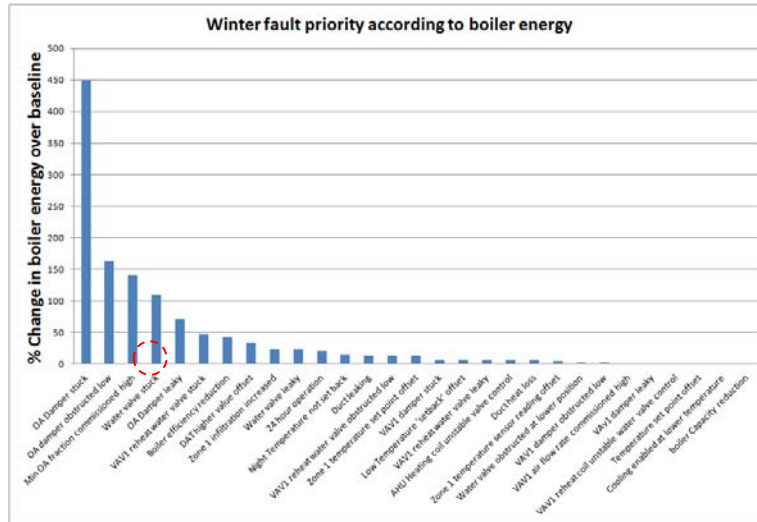
Figure 2.6: Summer prioritization based on change in electrical energy (performance measure) for individual and coupling faults

Fault Prioritization: Winter conditions

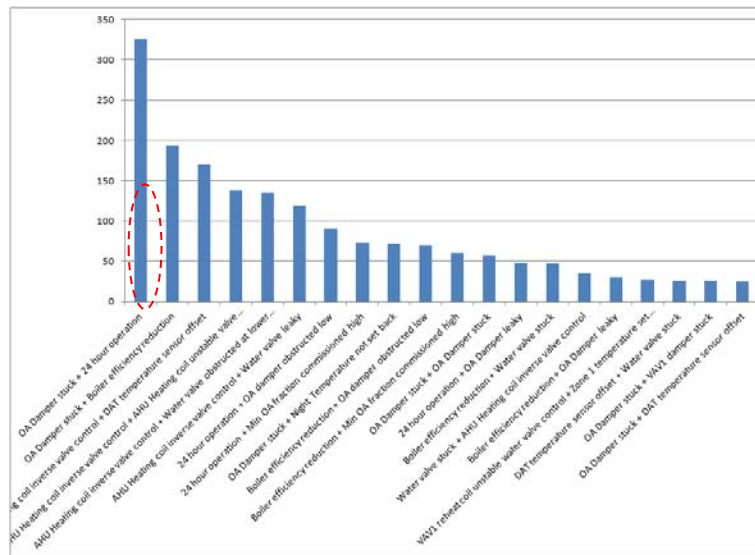
Figure 2.7 shows the results of fault prioritization for winter conditions, where we use the change in boiler energy consumption as the performance measure. We can observe from Figure 2.7 that OA damper stuck is the top most fault for Building 101, resulting in approximately 400% energy consumption. Also, many other damper faults rank among top ten, e.g. damper obstructed and leaky.

In comparison to OA damper stuck, inverting the sign of the proportional gain (K_p) in PID control for AHU heating coil valve has negative impact on energy consumption. Under this fault, the energy consumption reduces by 35% (and therefore not seen in Figure 2.7). In addition, faults such as DAT value offset and AHU heating coil valve being leaky, have only 20% increase above the baseline energy consumption. However, if any of the latter faults happen together with inverse K_p sign, the coupling

impact energy increase to above 100% over the baseline, which is very significant. As such, these coupling results are not intuitive as well, and demonstrate the benefit of our methodology.



← Individual Faults



← Coupling Faults

Figure 2.7: Winter prioritization based on change in boiler energy (performance measure) for individual and coupling faults

Concluding remarks and future work

We have develop a generic model based approach that can be used for quantification of various faults and fault severities impact on energy consumption and develop a systematic process that uses this capability for fault prioritization. In this report, we present a fault modeling library developed in TRNSYS and demonstrate its applicability in a systematic process for fault prioritization. Fault library

extends to BPS capability by enabling modeling and simulation of imperfections in the system in a well managed way (via fault manager). The added capability extends to both abrupt and degradation faults.

By extending this capability for fault prioritization process, we demonstrated that individual, as well as couplings are important. Through a mid-sized office building case study, non-intuitive complex coupling of faults has been demonstrated. The coupling effect can boost the effect of individual faults significantly.

Including occupant comfort as additional performance indicator to limit the study only to the faults that could go undetected and cause significant energy performance degradation. Coupling the impact of the fault to the probability of its occurrence to determine the risks. Study the implementation of the reduced order model so the higher order couplings can be analyzed.

2.2. Fault Impact Assessment Tool Chain for Operation Phase

Introduction

This project has developed and demonstrated a library of diagnostics decision support tools that can enable cost effective diagnostics solutions for existing buildings. The aim is to develop a suite of smart, component-embedded diagnostic tools that can ultimately be integrated to support building energy management. Specifically, we have developed a reusable tool chain to prioritize equipment faults based on their impact on energy consumption. This tool chain is intended to assist building managers in making critical building operation decisions. The aforementioned tool chain relies on a specific type of data driven models (Graphical Network Models) to assess fault energy impact. These data-driven models can be learned using limited operational data, while still being accurate enough to obtain energy impacts under different fault conditions. As a proof of concept, the data driven graphical models were successfully used to estimate energy impacts of faults such as *AHU outside air damper stuck* and *Heating coil valve stuck* in building-101 simulation environment.

Methodology

Backward Fault Injection based Fault Impact Assessment

The proposed method for fault impact assessment is based on an approach that we refer as *Backward Fault Injection* (BFI). In BFI approach, which is illustrated in, as soon as a fault is detected in an operational component, we project the fault in the immediate history to assess its energy impact. This backward projection is carried out by injecting the fault using a Graphical Network Model while keeping some of the exogenous variables (Outside air Humidity, Temperature etc.) the same as in the recorded history. Thereafter, Graphical Network model allows one to estimate the energy consumption under the fault condition as shown by the dotted red curve in Figure 2.8. The solid red curve shows the energy consumption recorded in fault free state. The excess energy consumption under the fault can be assessed to be the area between the two curves.

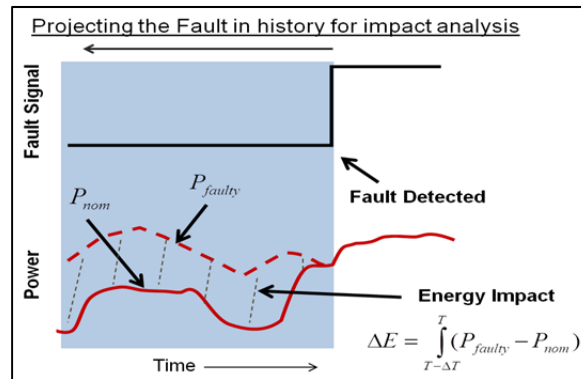


Figure 2.8: Illustration of Backward Fault Injection (BFI) approach for the energy impact assessment of the component faults.

Figure 2.9 outlines the entire process energy impact assessment of a fault. Once a fault is detected, the approach for quantifying its energy impact consists of three steps 1) Seeding the fault in the immediate history on a finite time horizon, (2) estimating the energy consumption under the faulty condition, and 3) Using the difference between the estimated energy and the measured nominal energy consumption to quantify the energy impact of the fault. The data driven Graphical Network models that form the backbone of the proposed method are discussed in greater details in the next section.

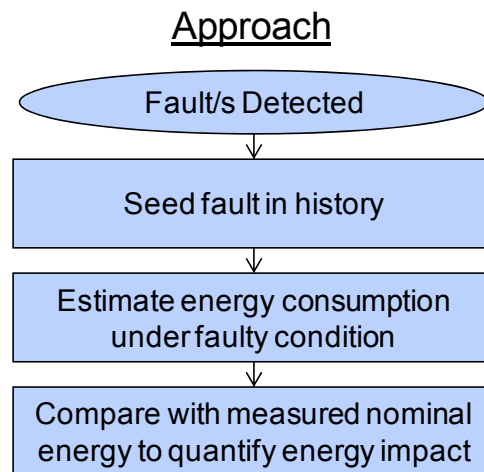
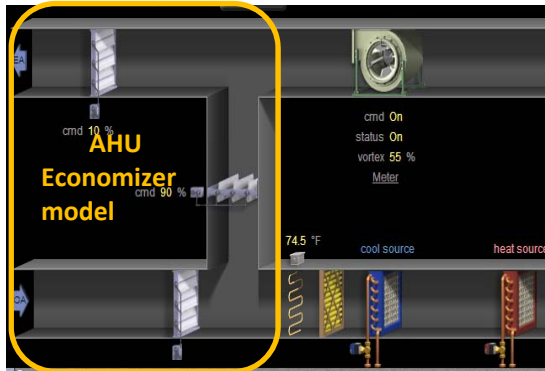


Figure 2.9: Fault impact assessment process used in operation phase

Graphical Models

Figure 2.10 shows a Graphical Network Model for the Economizer of an AHU. The nodes represent the variables that are pertinent to the Economizer and the arrows indicate causality between them. The

cause and effect relationship, encoded by the arrow, may have different strengths. The strength of influence is captured probabilistically between the parent (causes) nodes and the child (effect) node. Such graphical models enable one to estimate the most likely value (and the associated uncertainty) of a certain variable of interest given the other variables. For example, to estimate the Mixed Air Temperature (MAT) when the Outside Air Damper (OAD) is stuck at certain position, one queries the graphical model by supplying values for OAD, OAT, RAT and the schedule (day/night mode) (These inputs are referred as *evidence* in graphical model literature). As the output, we get the expected value of MAT under the supplied evidence with uncertainty bounds.



Fault = OA Damper Stuck

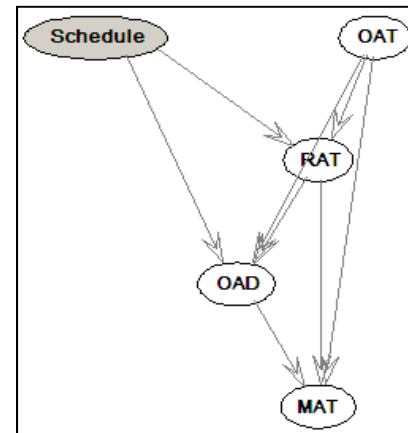


Figure 2.10 A Graphical model (right) for the Economizer (left) of an Air Handling Unit. The Grey and white nodes represents the discrete and continuous variables respectively

Graphical Model Selection

One way to categorize graphical models is based on the data-type they can handle. Historically, *discrete graphical models* have been developed extensively because the domains in which they were used (insurance, fraud detection etc.) had predominantly discrete variables. The applicability of discrete models in other domains, which have significantly more continuous variables, is contingent upon the discretization of continuous variables. Even though discretization allows one to build a discrete graphical model in inherently continuous domains such as HVAC systems, it comes at a price.

- The resulting model becomes sensitive to the discretization policy employed. If discretization is not done right, the impact on the model output can be adverse.
- Number of parameters that are needed to be learned increases significantly. As a result, the data requirements for learning a high fidelity data-driven model increases.
- The applicability of model becomes questionable outside the range in which the model is learned.

An ideal scenario, keeping in mind the above mentioned shortcomings, is to develop graphical models that can directly work with continuous data. There have been some proposals in this regard (Lauritzen (1992)) that aim at learning mixed graphical models with the ability to handle both the discrete and continuous variable in a single model. UTRC has also been funding research in the area of *Mixed*

Graphical Models. The models used in this project were developed in a separate ongoing project in the UTRC.

To illustrate the benefit of using mixed graphical models over the discrete counterpart, for modeling the HVAC components, we take the example of the Economizer shown in figure 10. Figure 11 shows the sensitivity of the two models on the size of data used for learning. The goodness of a model is quantified by the Root Mean Squared Error (RMSE) in the estimation of MAT on an out of sample (never seen) dataset. The robustness of mixed graphical model to fewer data samples is apparent from figure 11. Even under very low data conditions, we obtained mixed graphical models with acceptable accuracy. On the contrary, discrete graphical models showed a more pronounced sensitivity to the size of the data used for model learning. As availability of adequate ground truth (training data) is always a concern in data driven modeling, the mixed graphical model clearly provides a more reliable option for building the graphical network models.

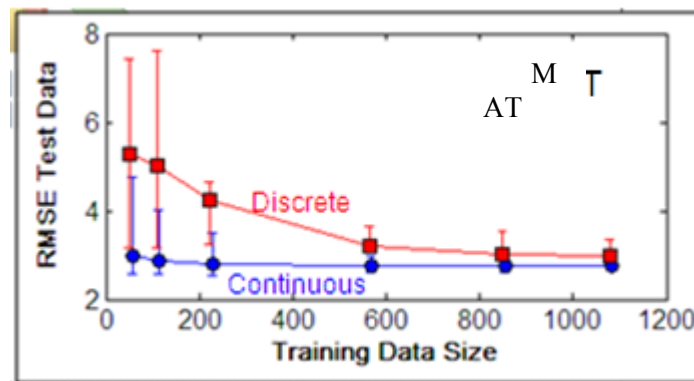


Figure 2.11 Comparison of the sensitivity of the discrete (red) and mixed (blue) graphical models in terms of their prediction accuracy.

Model Training / Commissioning

In data-driven modeling, the onus of learning a good model is primarily on the availability of a reliable representative dataset (training data) generated by the system that needs to be modeled. This is also true for the mixed graphical network models that have been used in the proposed fault impact assessment method. A good training dataset is not just devoid of measurement errors but also is representative of all the conditions that the system is expected to see. Clearly, in systems with multiple variables procuring a training dataset that has comprehensively spanned the input space is quite challenging. UTRC has developed a methodology that allows one to generate such dataset by employing certain functional tests during the commissioning phase of the component. A functional test is defined as an experiment in which all the variables that can be explicitly controlled (OAD position, HCV position etc.) are spanned in their range while simultaneously recording the other variables. The dataset generated by such functional test, contains more information about the underlying system compared to a dataset obtained by simply recording the data from a component in regular operation. Figure 12, illustrates the concept of functional tests for the heat-exchanger graphical model, where the Heat Coil Valve (HCV) position is spanned in its entire range in a systematic manner.

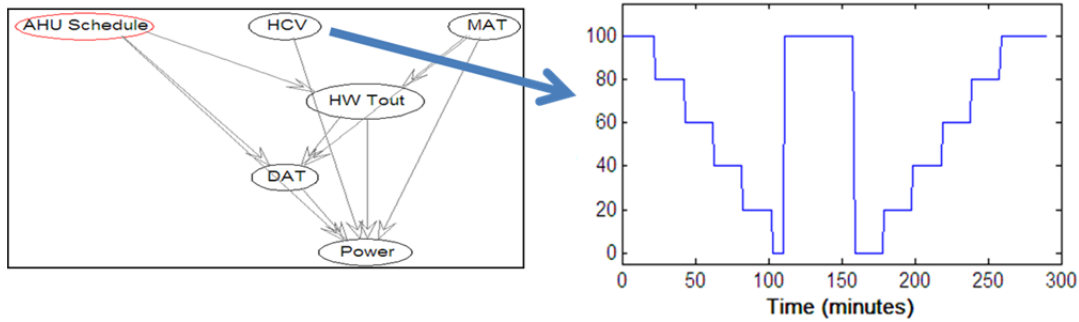


Figure 2.12 Illustration of a functional test to generate good quality data for graphical model learning

Fault Propagation with Graphical models

To improve the scalability of our method, we propose decomposing the HVAC system into smaller components. This decomposition allows one to build smaller models that communicate with each other, rather than one large model, which may be difficult to learn. For example, an HVAC system can be decomposed into *Economizer* and *Heat Exchanger* as shown in figure 13. The models of these subsystems can be learnt independently. The communication between them is via a set of common variables that appear in both the models. The question that arises is how do we assess the impact of a fault occurred in an upstream component (Economizer) on some downstream component (Heat Exchanger). For example, a damper stuck open in winter can cause excessive heat transfer in heat exchanger. To analyze such propagation of faults UTRC team developed capability of fault propagation between different subsystems. Figure 2.13 illustrates the idea behind the proposed fault propagation scheme. As

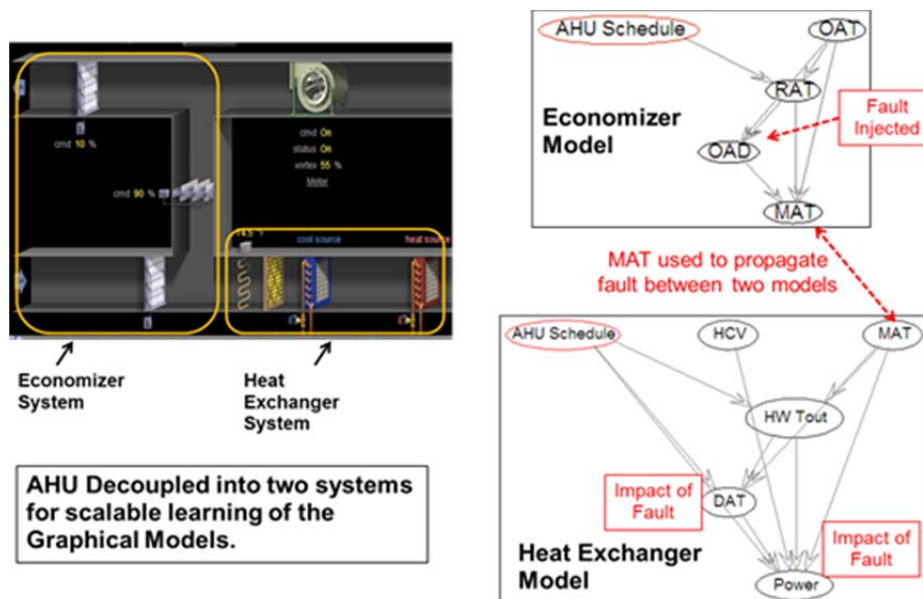


Figure 2.13 Fault propagation capability for operation based models data

shown in Figure 2.13, a fault in the economizer damper is first used to estimate the MAT. The estimated MAT value is propagated to the Heat Exchanger model, where it is used to estimate the power consumption and DAT (discharge air temperature) at the heat exchanger under fault condition (OAD stuck).

Demonstration and Results

We have completed and demonstrated the prototype of the automated process for estimating energy impact of any damper and valve faults in air-handling system. Figure 2.14, shows the steps involved in the fault impact assessment prototype. The fault impact process involves three sub-processes (1) interfacing with middleware – partially completed, (2) automated fault impact model generation, and (3) output visualization of fault impact. The current implementation is in MATLAB and we are in the process of developing interfaces with middleware.

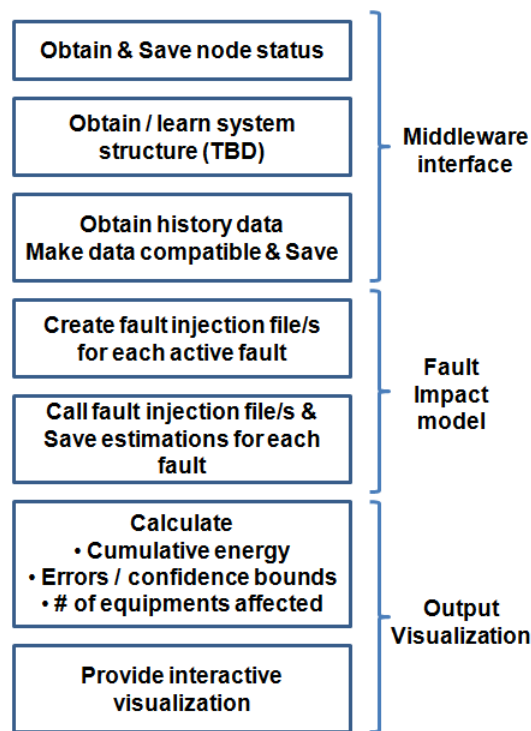


Figure 2.14 Fault impact analysis process

Figure 2.15 demonstrates the accuracy of our fault impact assessment method on the building 101 simulation data. The top of Figure 15 shows Graphical Models for the Economizer (left) and the AHU Heat Exchanger (right). To quantify the energy impact for a stuck damper fault (damper stuck at 20% opening), we take the following steps. Using the measured values of outside air temp (OAT), outside air humidity (OAH), return air temp (RAT) and the fault value (20%) of the outside air damper (OAD), we estimate the MAT using the graphical model for Economizer. The MAT value is propagated to the heat

exchanger model, where we compute other intermediate variables such as heating coil valve (HCV) position, hot water outlet temperature (HW_Tout), discharge air temp (DAT) etc. before computing the thermal power under the fault conditions. For the validation purposes, we compared the excess energy consumption due to a stuck damper estimated using the proposed method with that obtained from the TRNSYS model for building 101. The baseline (no-fault) energy consumption is also included as a reference. Clearly, the proposed fault assessment method does a reasonably good job of estimating the energy consumption under fault conditions, when compared with the TRNSYS model. Note that these graphical models can be obtained using limited operational data (model training) and don't require detailed physical knowledge about the equipments or buildings.

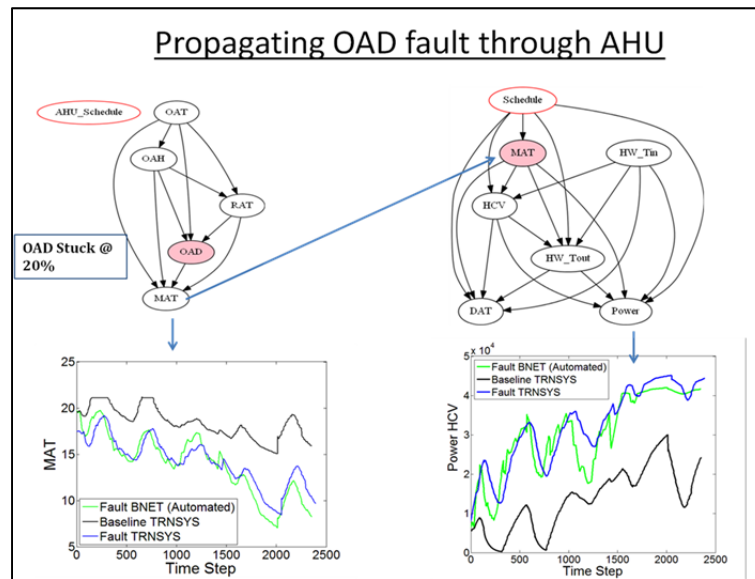


Figure 2.15 Comparison of automated fault impact assessment process with the TRNSYS model, for fault energy impact analysis.

Concluding Remarks and Future Work

UTRC completed the development and prototyping of a scalable approach to quantify energy impact of faults during operational phase and to prioritize corrective actions. The current prototype can estimate energy impact of any damper and valve faults in air-handling system. The automated process invokes individual data driven equipment models based on where the fault is detected in air handling system. In addition, the process also propagates the effect of fault in the rest of the air-handling system (e.g. effect of damper stuck fault in economizer gets propagated to all AHUs and VAVs downstream). We have tested the prototype of the automated fault impact process by comparing the results with the TRNSYS model for building 101.

3. RTU Fault Diagnosis

3.1. Introduction

3.1.1. Background/Need

According to the U.S Department of Energy (DOE, 2010), space heating, ventilation and air conditioning (HVAC) account for 40% of residential primary energy use, and for 30% of primary energy use in commercial buildings. A study released by the Energy Information Administration (EIA, 2003) indicated that packaged air conditioners are widely used in 46% of all commercial buildings, serving over 60% of the commercial building floor space in the U.S. This study indicates that the annual cooling energy consumption related to the packaged air conditioner is about 160 trillion Btus.

A study conducted by Messenger (2008) indicates that unitary air conditioners typically do not achieve rated efficiency because of improper installation or lack of servicing in the field. This paper suggested that service and replacement programs could yield energy savings on the order of 30 to 50%. Another investigation (Katipamula, 2005) suggested that faults or non-optimal control could cause the malfunction of equipment or performance degradation from 15 to 30% in commercial buildings. Therefore, improvements in air conditioner and heat pump maintenance can lead to significant reductions in overall energy use and environmental impact.

Braun (2003) presents automated FDD systems in HVAC&R applications that have the potential to produce operating costs savings by lowering service and energy utility costs, and improve business productivity based on the reduction of equipment downtime. In order to be cost effective, automated FDD system for HVAC in commercial buildings should have low installation cost and low-cost reliable sensors. In order to accomplish this goal, automated FDD systems for HVAC&R applications could be integrated into individual equipment controllers to provide on-line monitoring, fault identification, and diagnostic outputs with sufficient information to choose an appropriate action.

3.1.2. Objectives

The primary goal of this research is to develop and demonstrate a complete automated fault detection and diagnostic implementation using virtual sensors for rooftop air conditioners (RTUs) with fixed speed compressors and a DX system with variable stage compressor. To achieve this goal:

1. Various virtual sensors are developed and evaluated
2. A complete diagnostic system is demonstrated for a RTU system
3. Performance indices are developed to assess whether RTU service should be performed.

As a first step, virtual sensors are improved and evaluated based on existing laboratory data and UTRC RTU test data. The virtual sensors included in the study are:

1. Refrigerant charge
2. Three different approaches for refrigerant mass flow rate
3. Compressor power
4. Condenser and evaporator air flow rate
5. Outdoor-air fraction provided by the economizer.

After the virtual sensors have been evaluated, impacts of individual faults on capacity and COP are evaluated using existing data for a number of different units. This information is useful in understanding the necessary sensitivity of virtual sensors to be used for fault detection and diagnostics.

Laboratory testing was performed on a 4-ton RTU using refrigerant R-410A. The tests were conducted under different normal and faulty conditions using the psychrometric chambers at Purdue University's Herrick Laboratories. Virtual sensors are developed and evaluated for the RTU system. Each of these virtual sensors is needed as part of an overall fault detection and diagnostics system. In addition, methods for on-line assessment of fault impacts are developed and evaluated. Finally, the developments are integrated into an overall diagnostic system and demonstrated within a laboratory setting.

3.1.3. Literature Review

3.1.3.1. Earlier FDD approaches for RTU

Over the past 20 years, various FDD approaches have been developed for RTU systems. This section provides a review of some representative publications. Based on the review of literature, most papers did not address a complete automated FDD system.

Rossi and Braun (1997) developed a statistical FDD method based on a steady-state model for a RTU system with fixed-speed compressor and fixed orifice expansion device (FXO). The FDD system used nine temperature and one relative humidity measurements for inputs, and estimated seven representative temperature outputs. Residuals were formed as the difference between the measured output states and those predicted by the steady state model. The calculated residual values were used with a Bayesian decision classifier to determine whether the operation was faulty or normal. Faults were detected when the probability of normal performance fell below a threshold. After a fault was detected, a fault diagnosis was performed using a statistical, rule-based classifier. The fault diagnostic classifier could identify the most likely cause of the faulty behavior using a rule-based pattern chart that related each fault to the direction of residual change corresponding to each type of the fault. The fault diagnostic classifier module was devised assuming individual features as a series of independent probabilistic occurrences, an standard Bayesian classifier assumption.

Chen and Braun (2001) developed a rule-based FDD method for a rooftop air conditioner with a thermal expansive valve (TXV). The FDD algorithm was a modified version of the approach developed by Rossi and Braun (1997) and was able to detect and diagnose seven faults within the system:

1. Evaporator air flow faults
2. Condenser air flow faults
3. Liquid line restrictions
4. Compressor valve leakage
5. Refrigerant leaks
6. Refrigerant overcharge
7. Non-condensable gas mixed with the refrigerant.

The approach for fault isolation used temperature residuals between measurements and normal operation predictions to compute "sensitivity ratios" that were sensitive to individual faults. The approach required six temperature sensors and one relative humidity sensor. Sequential rules were developed that compared the sensitivity of residuals organized within a fault characteristic chart was used for FDD. The advantage of this method was insensitivity to variations in operating conditions while maintaining sensitivity to specific faults.

Li and Braun (2007a) presented improvements to the original statistical ruled-based FDD algorithm for rooftop air conditioning units with fixed-speed compressors and FXOs. The performance of the original method that is based on a diagonal covariance matrix was evaluated and compared to Monte-

Carlo simulation (MCS) based on a non-diagonal covariance matrix. The study found that the original method was not sufficiently robust, whereas the MCS method was robust but not useful for online implementation due to a large computational requirement. This study also provided an improved classifier method that did not require a covariance matrix, but instead uses a normalized distance method. The method also takes advantage of statistical methods to minimize the false alarms rate. It was determined through experimental results that this FDD method was relatively insensitive to parameters over a wide range of operating conditions of the system. A steady-state detector was also developed based on moving-window variance and slope method to filter out transient data and large noise.

Li and Braun (2007b) developed a decoupling FDD methodology that utilizes features that uniquely depend on individual faults and therefore readily handles multiple faults for packaged air conditioning equipment. In order to realize a cost effective method, they also developed a number of virtual sensors that provide high value decoupled features using a combination of low cost measurements and models. The virtual sensors were developed for the compressor, expansion valve, condenser, evaporator, and refrigerant charge. The work described in this research is based on the use of this approach and includes the development of additional virtual sensors, improvements to existing sensors, and extensive validation.

The Outdoor Air/Economizer Diagnostician is a fault detection and diagnostic method for outdoor-air ventilation and economizer operation for commercial buildings. It is actually a module of the Whole-Building Diagnostician developed by Brambley et. al. (1998). The tool uses data available from building automation systems (BASs) and uses diagnostics based on engineering models of proper and improper air-handler performance. Rules are implemented as a decision tree and data collected from the BAS are used to navigate through the decisions sequentially until a diagnosis is reached. The tool provides diagnoses for ventilation faults as well as economizer operation problems. It was designed to work with common types of economizer and ventilation systems, including temperature or enthalpy controlled economizers and constant- or variable-volume systems. Additionally, the method is able to diagnosis faults in economizers using high-limit (change-over) or differential control.

Air handling performance assessment rules (APAR) is a fault detection tool that uses a set of expert rules to detect faults in air handling units (Schein 2003). The expert rules are derived from mass and energy balances for different modes of operation determined from control signals. A steady-state detector is used to filter out transient operation. Subsets of the rules corresponding to the mode of operation are evaluated to determine whether a fault is present. Application of APAR is computationally simple enough to be embedded in commercial control systems and relies only on commonly available sensor data and control signals. The fault detection method was originally developed for application to single duct variable-volume or constant volume air handling units. Packaged air conditioners were not specifically considered nor were tested. Nonetheless, many of the rules can be applied to these type systems without difficulty since these packaged systems are in themselves AHUs with an integrated cooling system. The rules are related only to temperature control and therefore fault detection was restricted to only components and control strategies directly related to temperature control. Economizer fault diagnosis was not designed.

An integrated method of AHU control and sequencing logic is described by Seem & House that uses sensors commonly found in AHUs (2009). This differs from the other two economizer FDD methods by imposing steady-state conditions using the sequencing logic with the controller. This eliminates the need for a steady-state detector and makes the tool slightly simpler. Model-based fault detection is performed by generating residuals values using the data collected from measurements and control signals. During faulty operation, one or more of the residuals is expected to have a value significantly different from normal behavior. This can be used to diagnose faults; however, this was not discussed.

3.1.3.2. Impact of refrigerant charge fault

Refrigerant leaks occur when a seal or joint within the refrigeration system is compromised and allows refrigerant to leak into the surrounding environment. There have been laboratory studies that have documented the impact of refrigerant charge on the performance of air conditioning equipment, including the research by Rice (1987), Breuker & Braun (1998a,1998b), and Goswami (2002). Based on research of more than 4,000 residential cooling systems in California, only 38% have correct refrigerant charge (Downey, 2002) and the data from Blasnik et al. (1996) have indicated that an undercharge of 15% is common.

Recently, Kim and Braun (2012a) found that a refrigerant charge reduction of 25% led to an average energy efficiency reduction of about 15% and capacity degradation of about 20%. These studies showed that improper refrigerant charge could significantly decrease energy efficiency and capacity. Additionally, the study found improper charging can lead to operating conditions that decrease equipment lifespan. Refrigerant charge leakage can contribute to global warming in the long term since refrigerants enter the atmosphere and contribute to the greenhouse effect. Other long-term impacts are caused by the extra carbon dioxide emissions produced by fossil fuel power plants due to lower equipment energy efficiency.

3.1.3.3. Impact of heat exchanger fouling fault

Heat exchanger fouling occurs as a result of dust or other debris covering a heat transfer surface. The fouling can reduce air flow as a result of increased pressure drop and also increase the thermal resistance due to an added insulating layer. Fouling can have a significant impact on system efficiency for air conditioners and heat pumps. In previous studies, there have been two methods for simulating heat exchanger fouling during experiments: 1) reduction of air flow and active surface area by placing an obstruction over a portion of the heat exchanger surface and 2) reduction of the fan speed associated with the heat exchanger.

Siegel and Nararoff (2003) evaluated the impact of evaporator fouling for air conditioner systems and found that energy efficiency was reduced by 7% with a 20% reduction in heat exchanger area. Ahn et al. (2006) noted that pressure drop of heat exchangers increases by between 10-30% due to the deposition of indoor pollutants that are larger than 1 μ m in size during exposures lasting over 7 years. They collected 30 evaporator samples from air conditioners from inns, restaurants, and offices in the field. A reduction of heat exchanger area by 45% led to a cooling capacity decrease of 15%. They also found that the fouling material became a bacteria cultivator.

3.1.3.4. Summary of field surveys for RTUs

Based on a survey and analysis of 215 rooftop units for 75 buildings in California (CEC, 2003), it was shown that 46% of the units were not properly charged, which resulted in reductions in capacity and energy efficiency. The average energy impact of refrigerant charge problems was found to be about 5%.

A study by ADM (2009) evaluated 109 units for 75 buildings in California. Table 3.1 provides summary data associated with the fault incidence analysis. This study found that 89 of the 109 units had fault conditions and 31 of these had two or more faults. The study also found that 45% of the units were not properly charged and 55% of the systems were operating with insufficient airflow rate. Table 3.2 summarizes field data performance addressing the energy impacts of faults. The average EER for the units increased from 6.6 before servicing to 7.0 after servicing, an average increase of 6.1%. The survey data indicates that faults or non-optimal control can cause the malfunction of equipment or performance degradation by 20% for system with one fault and by 50% for system with three different fault conditions.

Table 3.1 Summary of fault incidence analysis

Fault Type	Comp. Fault	Ref. rest	Cond. fouling	Evap. Fouling	Refrigerant charge			Airflow		Total
					High	Low	Non-cond.	High	Low	
Number	4	4	0	2	30	6	12	2	59	109

Table 3.2 Summary of fault impact analysis

Number of fault	Number of fault units	Baseline EER For standard cond.		Rated cooling capacity (tons)		Measured cooling capacity (tons)		Total measured input (kW)	
		Average	STD	Average	STD	Average	STD	Average	STD
None	20	8.2	2.48	3.4	0.63	2.58	0.88	3.66	1.03
One	58	6.4	2.15	3.8	0.77	2.16	0.69	4.14	1.07
Two	27	5.8	2.38	3.9	0.9	1.93	0.75	4.11	0.93
Three	4	4.3	3.2	4.1	0.63	1.81	1.29	4.74	1.89
Total	109	6.5	2.24	3.7	0.79	2.17	0.79	4.07	1.07

3.2. RTU Laboratory and Field Testing for Offline Analysis (UTRC)

Experimental data are needed for development of robust diagnostics methods as well as for its validation and demonstration. Experimental data were generated by UTRC in a well-controlled environment of lab tests and also in more realistic field conditions. The collected data were transferred to Purdue University for validation of diagnostic methods.

3.2.1. Laboratory Testing

The objectives for lab testing are: 1) reliable data generation for FDD model development and 2) validation of developed models. Advantages of the lab testing include 1) easy control of conditions and fault creation and 2) a great amount of high quality data in a short period.

A 7.5 ton Carrier RTU HC unit was down selected for the testing due to its high popularity in HVAC applications. Typical fault detection thresholds are about 10% performance for capacity degradation. The degradation may be caused by one or multiple faults at the system level (refrigerant charge, compressor power etc), component level (TXV, liquid line, condenser etc) and sensor level (TC drift, etc.). The scope of current testing in the lab was only focusing on refrigerant charge caused performance degradations.

As shown in Figure 3.1a, a 7.5-ton RTU HC unit 48HCDD08 was acquired from Carrier for our refrigerant charge diagnostics lab testing. The unit consists of two R410A circulation loops. Each loop has an evaporator, a Danfoss compressor, a condenser, a filter dryer and a TXV. As shown in Figure 3.1b, the two circuits are independent. However, their evaporators and condensers are stacked together in parallel. Indoor and outdoor air is blown through them. Two single speed outdoor fans are adopted for outdoor air circulation through L-shape RTPF condensers coils. An indoor air blower is used to provide indoor air recirculation.

Table 3.3 Testing Condition Matrix

Testing Matrix						
Charge, %	IA flow, cfm	OA TDB, °F	IA TDB, °F	IA TWB, °F	Circuit	Total Tests
140%/100%/ 85%/80%/75%/70%	2930/2250	85/95/105/115	80/75	67	2 and 1	102

The charge fault is our focus. The charge varies from 70% to 140% of the normal charge amount. Testing data accuracy and reliability are evaluated before charge fault diagnostics analysis. Figure 3.3 shows energy balances between air and refrigerant in evaporator and condenser, and along refrigerant loop. Over 90% data are within $\pm 5\%$ difference between air and refrigerant in the evaporator. All testing data are within $\pm 5\%$ difference in the condenser. It's within $\pm 1.5\%$ along the refrigerant loop. The energy balance check confirmed the accuracy and reliability of the testing data.

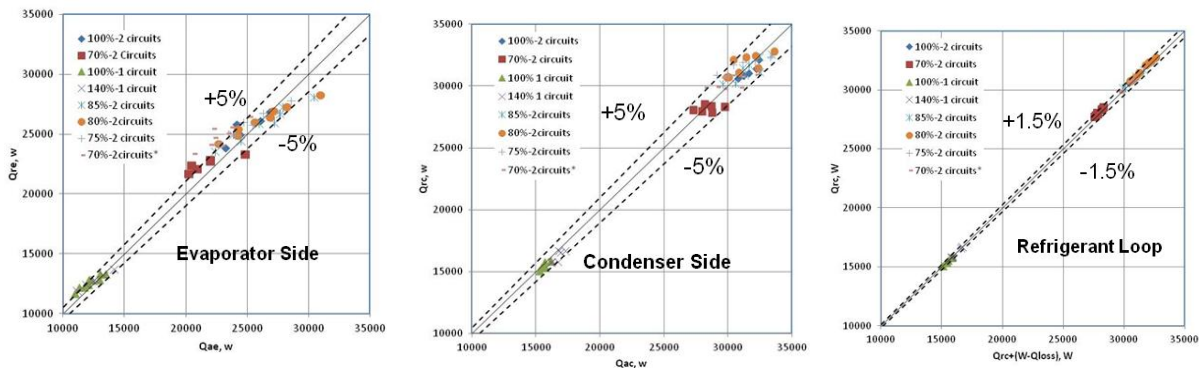
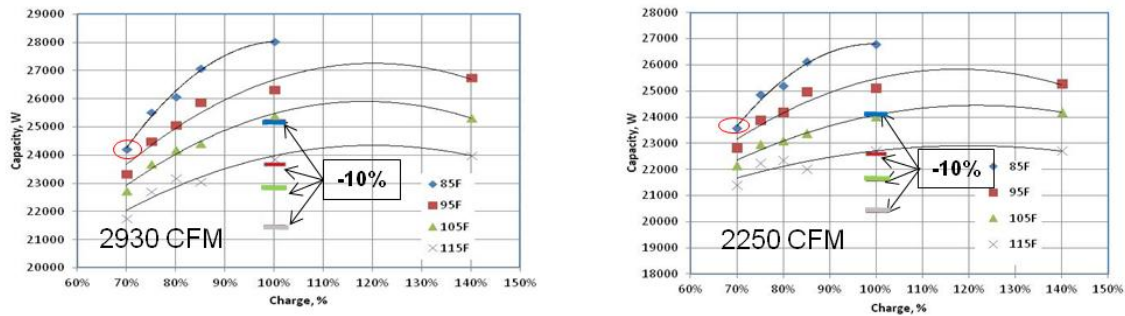
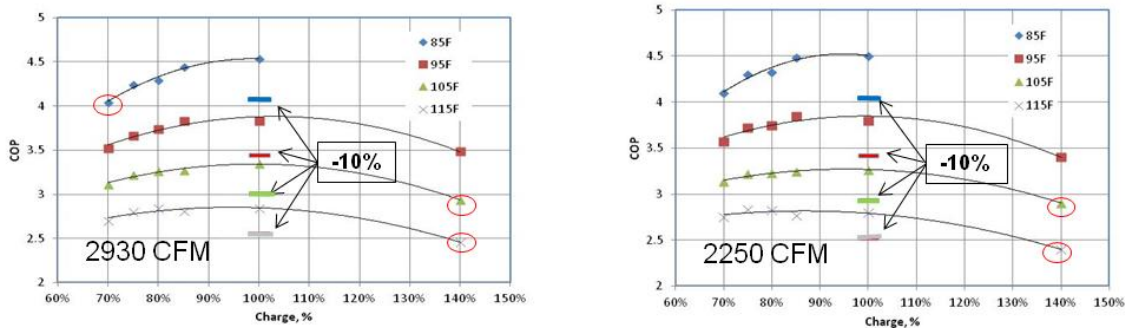


Figure 3.3 Energy Balances between Air and Refrigerants

Figure 3.4 shows system performance variations caused by refrigerant charge levels under different outdoor temperatures (85, 95, 105, 115F) and indoor air flow rates (2250 and 2930 CFM). The indoor condition is 80F (DB) and 67F (WB). As shown in Figure 3.4a, the system cooling capacity degrades when the refrigerant charge decreases. The lower the outdoor temperature, the more significant the degradation. At 85F outdoor temperature, the degradation is over the 10% threshold for both indoor air flow rates. The cooling capacity changes insignificantly when the system is overcharged (up to 40%). The overcharge amount of refrigerant most likely is accumulated in the condenser. However the compressor power is going up because the compressor discharge temperature is going up due to two phase condensation heat transfer area reduction in the condenser. This reflects in the system COP. As shown in Figure 3.4b, COP has the similar trend as the cooling capacity does when the system is undercharged. However, COP decreases when the system is overcharged and more significant at higher outdoor temperatures. The system COP degradation is over 10% threshold at 140% charge level for both air flow rates and outdoor temperatures at 105 and 115F. In addition, The COP degradation also is over 10% when the charge at 70%, 85F ODT and 2930 CFM indoor air flow rate.



a) Cooling Capacity Degradation



b) System COP Degradation

Figure 3.4 Impacts of Refrigerant Charge Levels on System Performance

Figures 3.5 shows the virtual flow rate sensors accuracy in comparison with the measured data. Two virtual flow sensors are calculated through the compressor map and compressor energy balance. The flow rate differences between two virtual sensors are within $\pm 5\%$. The measured flow rates are also within $\pm 5\%$ at over 85% charge level in comparison with the virtual sensors. The deviations are over 5% once two phase flow occurs at the condenser outlet under 80% charge level. Overall the virtual flow meters are practical approaches for charge fault diagnostics with a reasonable accuracy.

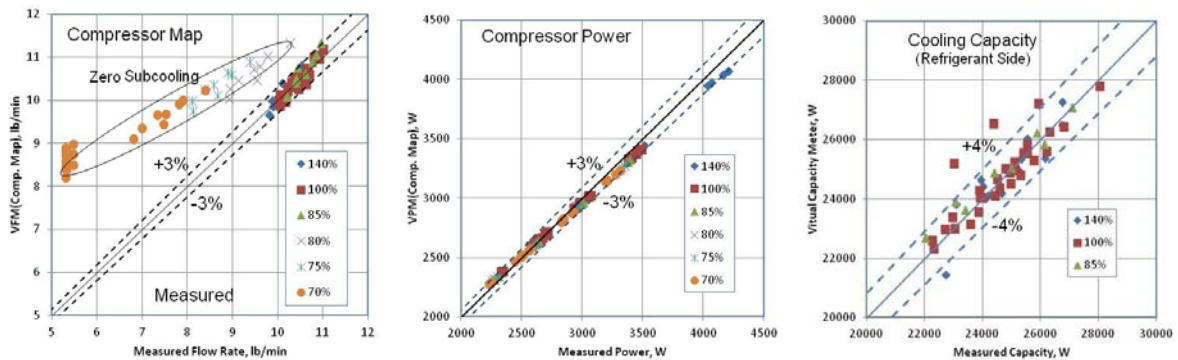


Figure 3.5 Virtual Flow Sensors Accuracy Comparison

A total of 102 test runs were done covering 6 charge levels, 4 outdoor air temperatures, 2 indoor air temperatures and 2 indoor air flow rates. Quality of testing data is verified through three energy balances between air and refrigerant ($\pm 5\%$) and along the refrigerant loop ($\pm 1.5\%$). Two charge faults (more than 10% performance degradation) are found at 70% and 140% charge level. Virtual flow meter, compressor power meter and capacity meter have $\pm 3\%$, $\pm 3\%$ and $\pm 4\%$ accuracy.

The detailed experimental data containing the values in Table 3.4 was transferred to Purdue University for further analysis and validation of fault diagnostics methods.

Table 3.4 Laboratory Measurements

Label	#	Meaning	Units [SI]	Units [IP]
SysID	1	System identifier		
Fault	2	Faults Type		
T_RA	3	Return Air Dry Bulb	[°C]	[°F]
WB_RA	4	Return Air Wet Bulb	[°C]	[°F]
DP_SA	5	Supply Air drybulb	[°C]	[°F]
WB_SA	6	Supply Air Wet Bulb	[°C]	[°F]
T_amb	7	Ambient Drybulb	[°C]	[°F]
T_air_ce	8	Condenser exit air temperature	[°C]	[°F]
P_suc	9	Suction Pressure (absolute)	[bar]	[psia]
T_suc	10	Suction Temperature	[°C]	[°F]
P_dischg	11	Discharge pressure	[bar]	[psia]
T_dischg	12	Discharge temperature	[°C]	[°F]
P_cond	13	Condenser exit pressure	[bar]	[psia]
T_cond	14	Condenser exit temperature	[°C]	[°F]
P_LL	15	Liquid Line pressure (absolute)	[bar]	[psia]
T_LL	16	Liquid Line Temperature	[°C]	[°F]
P_evap	17	Evaporator inlet Pressure (absolute)	[bar]	[psia]
T_evap	18	Evaporator inlet Temperature	[°C]	[°F]
Power	19	Total power to system	[W]	[W]
Power_id	20	Indoor fan power	[W]	[W]
Power_od	21	Outdoor fan power	[W]	[W]
Q_ref	22	Refrigerant side cooling	[kW]	[ton]
Q_air	23	Air side cooling	[kW]	[ton]
SH	24	Superheat	[°C]	[°F]
SC	25	Subcooling	[°C]	[°F]
m_ref	26	Refrigerant mass flow rate	[kg/min]	[lbm/min]
Chrg	27	Refrigerant charge	[kg]	[lbm]
Chrg%	28	Charge as %nominal	[%]	[%]
V_i	29	Indoor coil airflow rate	[m ³ /s]	[CFM]
V_i_%	30	Airflow as percent of nominal	[%]	[%]
V_o	31	Outdoor coil airflow rate	[m ³ /s]	[CFM]
V_o_%	32	Outdoor coil blockage	[%]	[%]

3.2.2. Field Testing

Quality field-operation data is required to demonstrate and validate performance of fault detection and diagnosis (FDD) methods on a building system. However, such data availability is very limited. Therefore it was decided to conduct tests on a roof-top unit (RTU) on UTRC campus for the purposes of setting up and demonstrating FDD methods.

The selected RTU is named AC24F (Carrier unit: 50PG-C12-D-60-S4). It has 2 refrigerant circuits with a nominal cooling capacity of 10 tons. The RTU has no heating function, has an interlocked modulating outside-air and return-air dampers with a damper position feedback signal, the RTU is located in IECC climate zone 5. Figure 3.6 are photos of the RTU, the exhaust damper is a barometric damper.

Field testing was performed in cooling season of 2012. Tests were run when weather permitted and AC24F was available. Investigated faults included: abnormal charge levels, reduced condenser air flow rate, and stuck dampers.

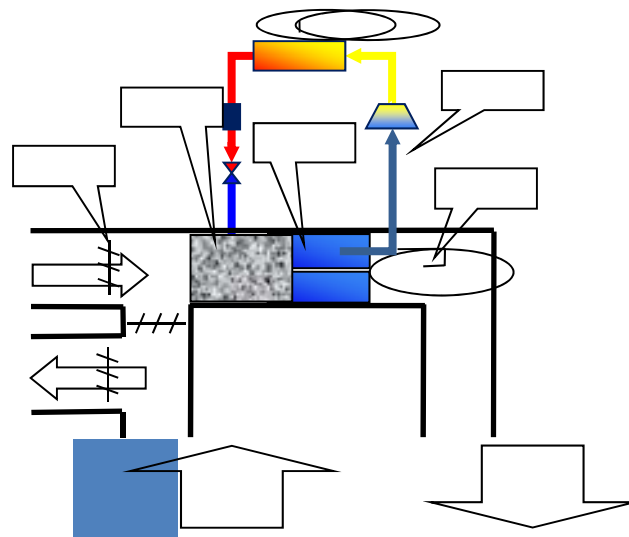
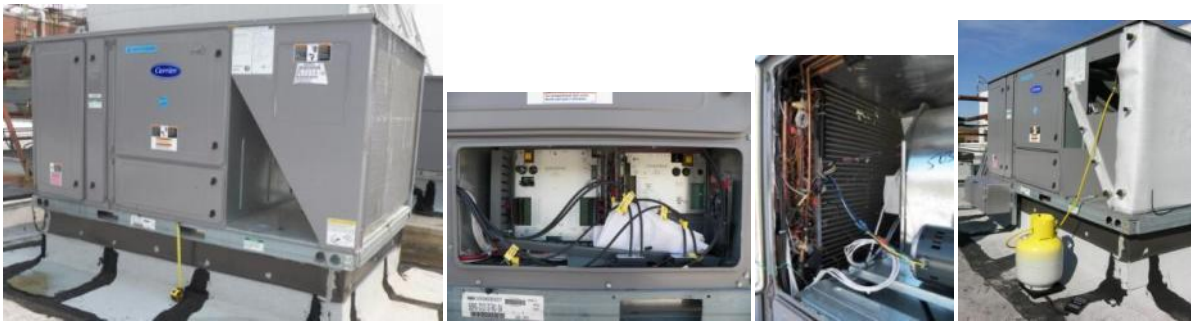


Figure 3.6 The selected RTU (AC24F) on UTRC campus

Table 3.5 lists the conditions tested in 2012. Note that the RTU under normal conditions (i.e. fault-free) was also tested for comparison purposes; and into the 1st circuit in all the tests of 2012. The RTU ran in each combination of the conditions for at least 1 hour. Data sampling rate was 1 minute.

Table 3.5 Tested conditions in 2012

Refrigerant charge levels	70%, 80%, 90%, 100%, and 120% of normal charge
Condenser air flow rate reduction	0%, 30%, 43%, and 56% of normal flow
Outside-air damper opening	0%, 25%, 50%, 75%, and 100%

In order to acquire complete performance data of AC24F and monitor its operation closely, additional sensors were installed. Additional sensors are categorized as: a) temperature and pressure sensors on refrigerant circuits; b) dry-bulb temperature, relative humidity, flow rate and differential pressure sensors on air side; c) power sensors for compressors and fans. Table 3.6 lists additional sensors installed. Key temperature and pressure sensors were calibrated to make sure manufacturer-specified accuracy is achieved.

Table 3.6 Additional sensors

Measured parameter	Model	Spec.	Output	Qty.
Temperature (refrigeration side)				
Tll - Liquid line	Omega SA1-TH-44006-80-T		Thermistor	2
Tdis- Discharge temp.	Omega SA1-TH-44006-80-T		Thermistor	2
Tx - Expansion valve inlet	Omega SA1-TH-44006-80-T		Thermistor	2
Tevap - Evaporator temp.	Omega SA1-TH-44006-80-T		Thermistor	2
Tsuc - suction superheat	Omega SA1-TH-44006-80-T		Thermistor	2
Temperature (air side)				
Taoc - Condenser outlet	Omega ON-906-44006		Thermistor	2
Taoe - Evaporator outlet	Vaisala HMT330 1A0A001BCAF200A41AABAA1		4-20 mA	2
MAT - Mixed air temp.	Vaisala HMT330 3E0A001BCAC200A01AABAA1		4-20 mA	1
RAT - Return air temp.	Vaisala HMD60Y		4-20 mA	1
RH				
OARH - Outdoor RH	Vaisala HMD60UO	±2% RH	4-20 mA	1
MARH - Mixed air RH	Vaisala HMT330 3E0A001BCAC200A01AABAA1	±2% RH	4-20 mA	1
RARH - Return air RH	Vaisala HMD60Y	±2% RH	4-20 mA	1
SARH - Evaporator outlet RH	Vaisala HMT330 1A0A001BCAF200A41AABAA1	±2% RH	4-20 mA	2
SARH - Supply air RH	Vaisala HMD60U	±2% RH	4-20 mA	1
Pressure (refrigerant side)				
Condenser pressure	Setra 1000psi		4-20 mA	4
Pressure (air side)				
ΔPevap - Evaporator	Setra	5" W.C.	4-20 mA	1
ΔPcond - Condenser	Setra	5" W.C.	4-20 mA	2
Flow Meters				
Ebtron air flow	Ebtron		4-20 mA	1
Watt Meters				
compressors	Ohio semitronics GW5-015EG	8 kW, 9.6A, 3ø, 460VAC	4-20 mA	2
2 condenser fans	Ohio semitronics GW5-108EG	1 kW, 2 FLA, 1ø, 460VAC	4-20 mA	1
1 evaporator fan	Ohio semitronics - GW5-006EG	4 kW, 4.8 FLA, 3ø, 460VAC	4-20 mA	1

An air balancing test was conducted on the unit by a NEBB/TABB certified contractor. The objective of the test is to obtain the ground-truth data of the air side. The contractor provided a test report, which presents comprehensive information on the air side in terms of flow rate, speed and pressure. Figure 3.7 illustrates static pressure profile of the RTU when the outside-air damper is at its minimum position (20% opening). Table 3.7 lists average of multiple-points air speed measurements across inlet surface of evaporators.

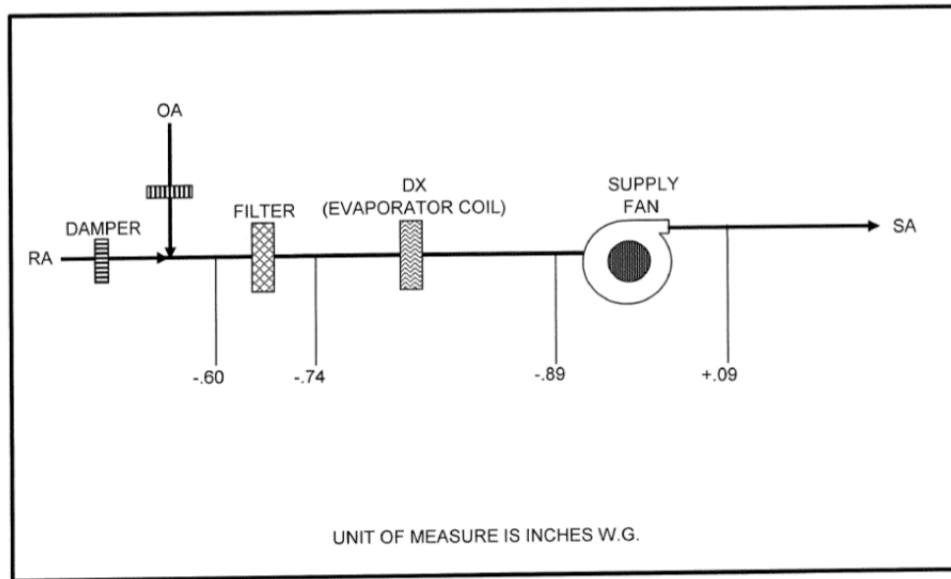


Figure 3.7 Static profile from air balancing report

Table 3.7 Air speed data from air balancing report

AC-24F (EVAPORATOR COIL)

** AIR INLET REPORT **

ROOM NO.	DESIGNATION	NO.	0%	20%	40%	50%	60%	80%	100%
			ACTUAL VEL						
	UPPER COIL	1	561	560	551	555	539	549	555
	LOWER COIL	2	574	575	571	573	559	569	581

NOTE: THE EVAPORATOR COIL WAS NOT FULLY ACCESSIBLE.
 THESE READINGS ARE APPROX VELOCITIES ACROSS PARTS OF THE COIL.

In addition to air balancing test, 3 more tests were conducted to find air-side performance that is important for FDD. The first test is to find the effect of damper position on supply air flow. AC24F has a fixed-speed centrifugal supply fan, but a change of damper position could change the upstream flow resistance, such that supply air flow might be different. Figure 3.8 is a photo of AC24F’s outside-air and return-air dampers. During the test outside-air damper position was fixed at 6 openings: 0%, 20%, 40%, 60%, 80% and 100%, and supply air speed was measured by an Ebtron® flow station. It turned out that the air speed was not very sensitive to damper position. So the supply-air volumetric flow rate was considered constant. Figure 3.9 is a snapshot of Building Energy Management System showing supply air speed vs. outside-air damper position.

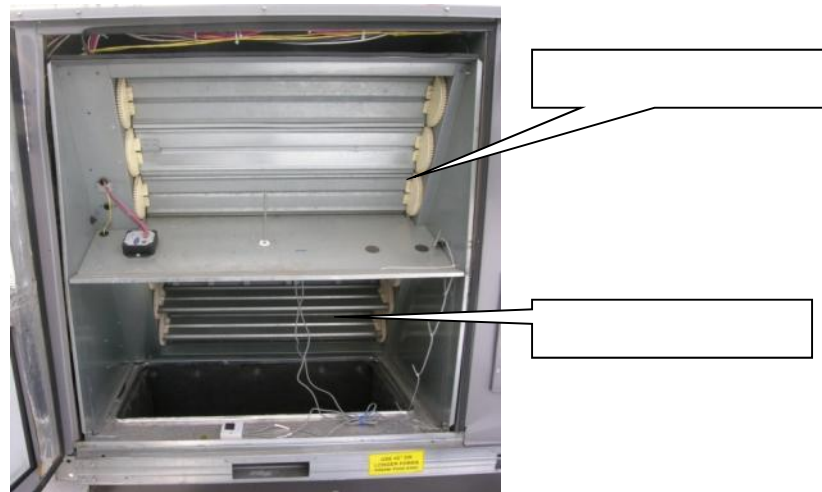


Figure 3.8 Dampers of AC24F

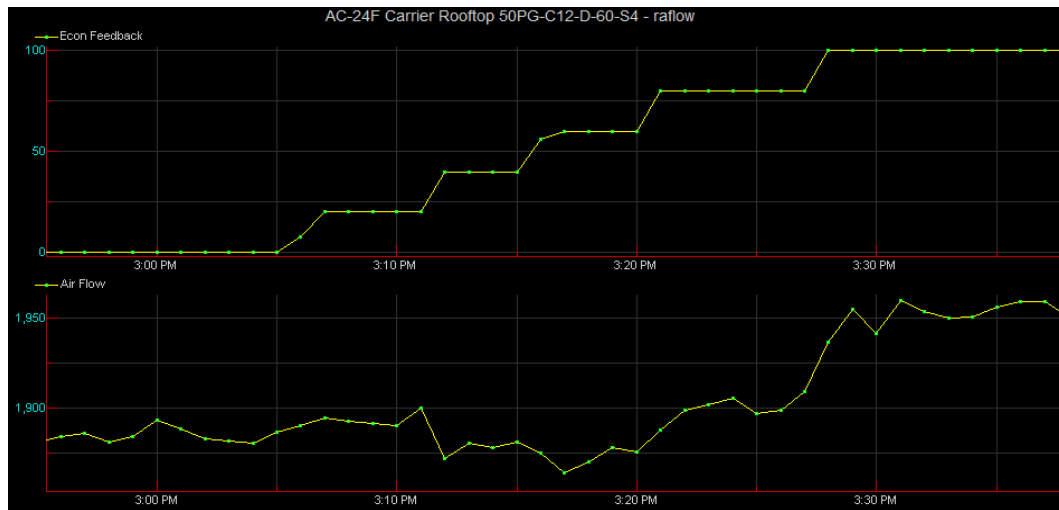


Figure 3.9 Supply-air speed vs. outside-air damper position

The second test was to determine a correlation between outside-air flow rate and outside-air damper position. The correlation was used for verification of FDD methods. Since the outside-air path is ductless, it is difficult to accurately measure outside-air flow rate directly. The adopted method was to measure return air flow instead, so that difference between supply-air and return-air flow rate will be outside-air flow rate. A Shortridge AirData multimeter was used to measure air speed across the return-air duct. The return-air flow rate was calculated with average speed and return duct cross section area. The supply-air flow was from an Ebtron flow station. Figure 3.10 shows measured return-air flow rate vs. outside-air damper opening. The supply-air flow rate was assumed to be constant, and the outside-air flow rate in the figure was calculated. A sigmoid-type empirical model was built upon the data, which has the following format:

$$OA \text{ flow} = SA \text{ flow} \times \left(k_1 - \frac{1}{k_2 + e^{-k_3(OAD - k_4)}} \right) \quad (3-1)$$

where OA-outside-air, SA-supply-air, OAD-outside-air damper opening, and k's are coefficients identified from a nonlinear regression. The relative error of the model is <3%.

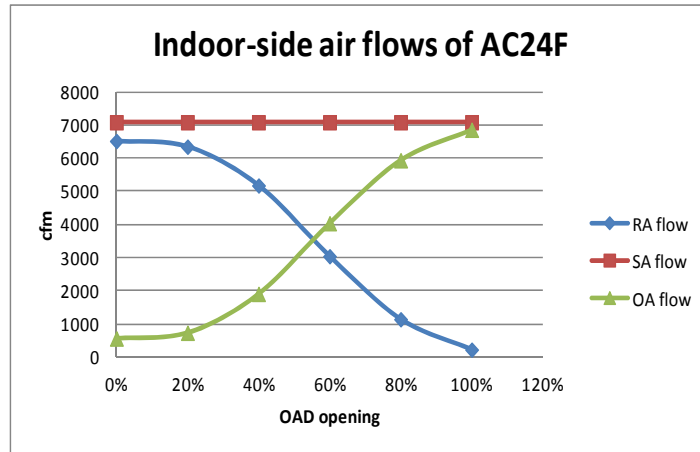


Figure 3.10 Air flows vs. outside-air damper opening

The third test was to evaluate how accurate measurements of mixed-air temperature are. In AC24F outside air and return air are mixed before entering air filter. There is one temperature sensor installed on the unit to measure mixed-air temperature. It is well known that actual air mixing in a RTU or AHU is far from uniform. This test revealed air-mixing condition on AC24F. In order to measure air temperatures at different locations across an evaporator inlet, an air sampling tree was built as shown in Figure 3.11.

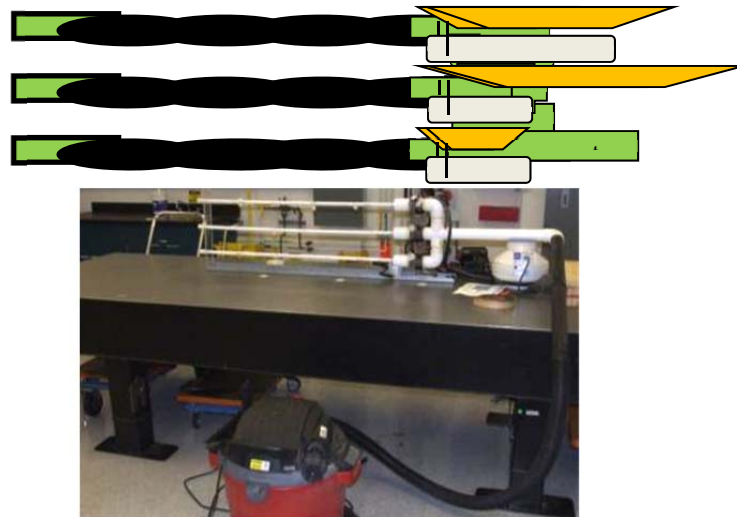


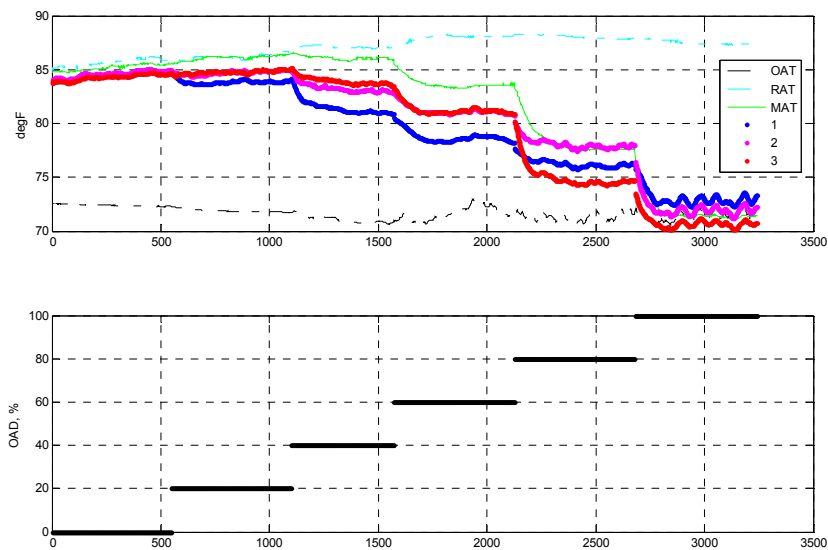
Figure 3.11 A custom-built air sampling tree

The tree has 3 branches, each of which has 4 holes. A vacuum sucks air out of 3 branches, and air temperature of sucked air through each branch is measured individually. By covering some holes on a branch, air temperature of an interested location can be measured. HOBO® data loggers and temperatures sensors were employed, which were calibrated before use. Figure 3.12 shows the air sampling tree was placed in the upper filter compartment in order to collect data of evaporator inlet air temperature on the second circuit.

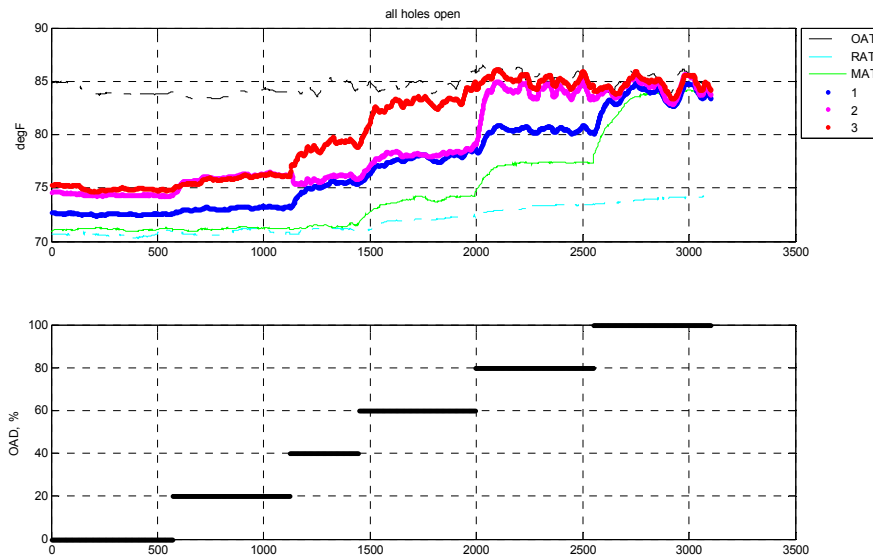


Figure 3.12 Air sampling tree on AC24F

Figure 3.13 shows temperature measurements, when all the holes on 3 branches were left open and outside-air damper was in different openings. Legends correspond to the branch numbers in Figure 3.6. The green curve was measured mixing-air temperature by the installed temperature sensor. It is clear that air temperature at inlet of an evaporator is highly non-uniform. Based on this test, it was decided to use a calculated mixing-air temperature based on enthalpy and mass balance, rather than the measured one, in analysis and FDD method verification.



(a) at inlet of the first-circuit evaporator



(b) at inlet of the second-circuit evaporator

Figure 3.13 Mixing-air temperature

Three typical faults were injected into AC24F: abnormal refrigerant charge, condenser air flow reduction and stuck outside-air damper.

The normal charge (R410a) of each circuit on AC24F is 13.7 lbs. Charge was added or removed from a circuit to simulate undercharge and overcharge. Refrigerant in AC24F was first reclaimed, and circuits were vacuumed first; then each circuit was charged to its normal level; when needed, charge amount was adjusted accurately using a refrigerant scale. Figure 3.14 shows refrigerant charge operations on AC24F.

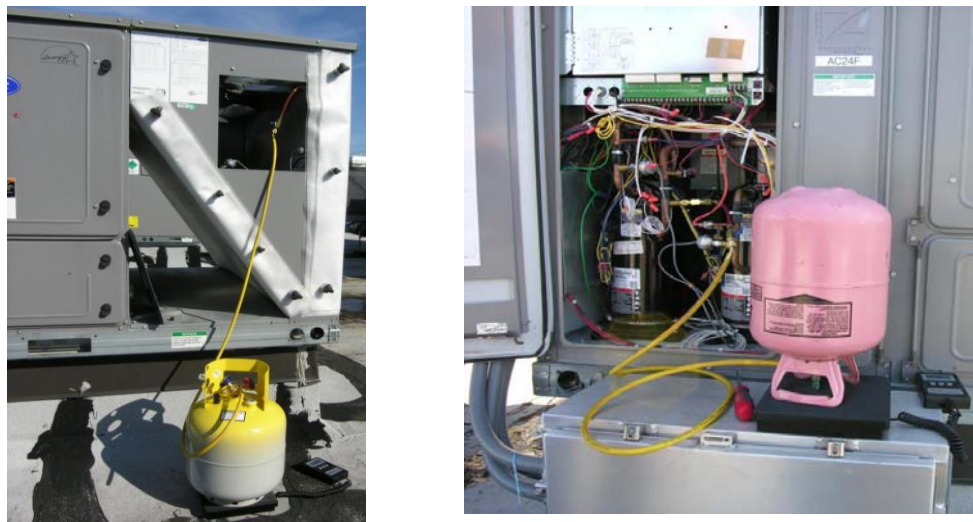


Figure 3.14 Charge adjustment

Condenser air flow was reduced by covering condenser inlet surface with multiple layers of plastic mesh to increase flow resistance. A trial-and-error process was taken to figure out the type and layers of mesh to reduce air flow by certain percentage. Air speed at 12 spots across a condenser inlet surface was measured with a Shortridge AirData multimeter, and an average speed was calculated for air reduction. Figure 3.15 shows air speed measurement at inlet of the first-circuit condenser.



Figure 3.15 Measurements of speed of air entering the first-circuit condenser

AC24F has an outside-air damper interlocked with a return-air damper, i.e. position of outside-air damper is always complementary with that of return-air damper. The RTU comes with a sensor measuring position of outside-air damper, and the measurement is available in the Building Energy Management system. A stuck damper was introduced by fixing its position during a test.

Faults listed in Table 3.1 were introduced in the following order: firstly, refrigerant charge was adjusted to a specified level; secondly, condenser air inlet surface was covered by layers of mesh to reduced air flow to a required level; thirdly, outside-air damper was held at a specified opening. The RTU was run in mechanical cooling for each combination of the three faults for at least one hour.

The experimental data with variable charge, condenser flow and damper position were generated for the state-of-the-art RTU in field conditions. Table 3.8 contains operating ranges for the conducted tests for 70%, 80%, 90%, 85%, 100% and 120% charge level; Condensed flow restriction for 0%, 30%, 43%, 56% and damper position 0, 25%, 50%, 75%, 100%. All the tests have been done except the case of charge=120% and condenser air reduction = 56%, because of cold ambient conditions in October of 2012.

Table 3.8 operating ranges

Test #	Start Time	Charge	Condenser flow	Damper Position
1	June	70%	0%	0, 25%, 50%, 75%, 100%
2	June	70%	0%	0, 25%, 50%, 75%, 100%
3	July	70%	30%	0, 25%, 50%, 75%, 100%
4	July	70%	30%	0, 25%, 50%, 75%, 100%
5	July	70%	43%	0, 25%, 50%, 75%, 100%
6	July	70%	56%	0, 25%, 50%, 75%, 100%
7-10	July	80%	0%, 30%, 43%, 56%	0, 25%, 50%, 75%, 100%
11-14	August	90%	0%, 30%, 43%, 56%	0, 25%, 50%, 75%, 100%
15-18	September	100%	0%, 30%, 43%, 56%	0, 25%, 50%, 75%, 100%
19-22	October	120%	0%, 30%, 43%, 56%	0, 25%, 50%, 75%, 100%

The difference between RTU air side and refrigerant side energy balance was analyzed to evaluate accuracy of the test data. The plot below is for Test 15 (100% charge, 56% condenser flow reduction). The discrepancy between air side and refrigerant side energy is less than 20% except for the transition period during the change of damper position – Figure 3.16.

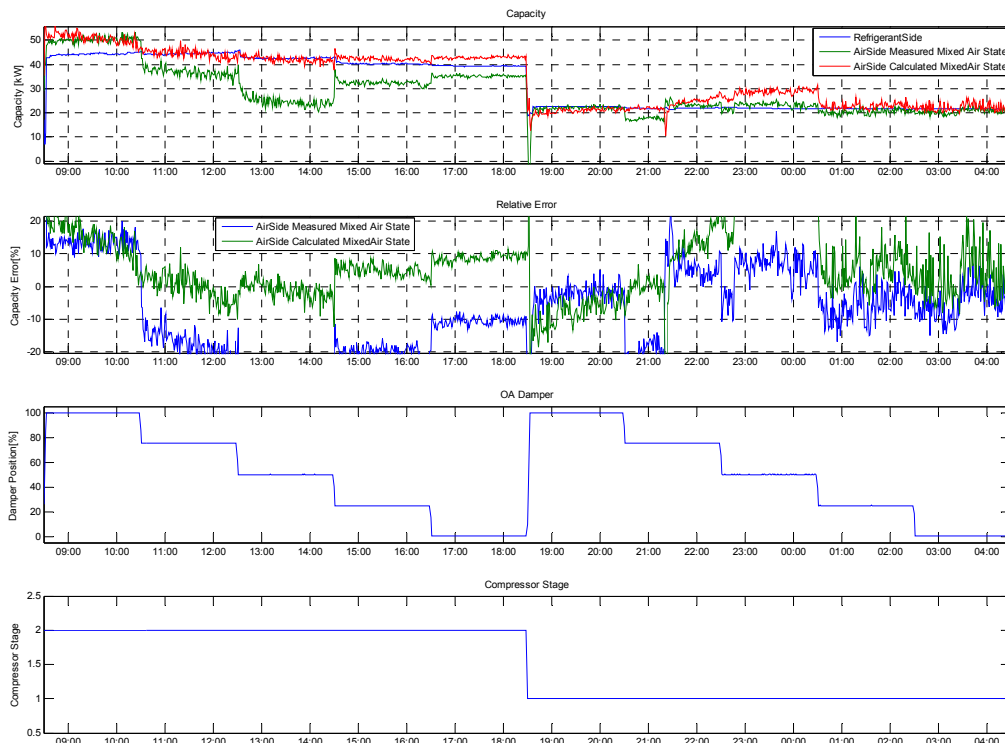


Figure 3.16 Comparison of air side and refrigerant side energy

The average condenser air side thermal capacity for each test is calculated for each test. The thermal capacity decreases proportional to condenser air flow reduction – Figure 3.17.

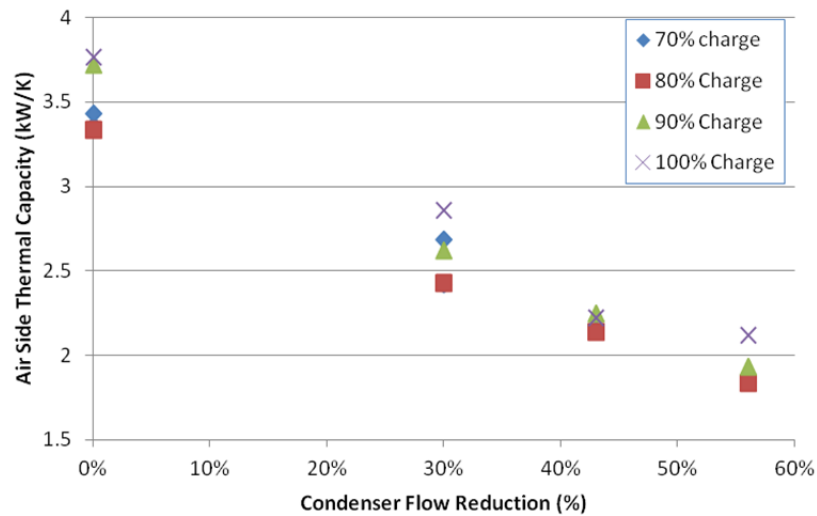


Figure 3.17 Air side thermal capacity vs. condenser flow reduction

All the sensors are connected to the Building Energy Management system. The sampling rate was set to one minute for all the tests. Data was collected and saved on a data server.

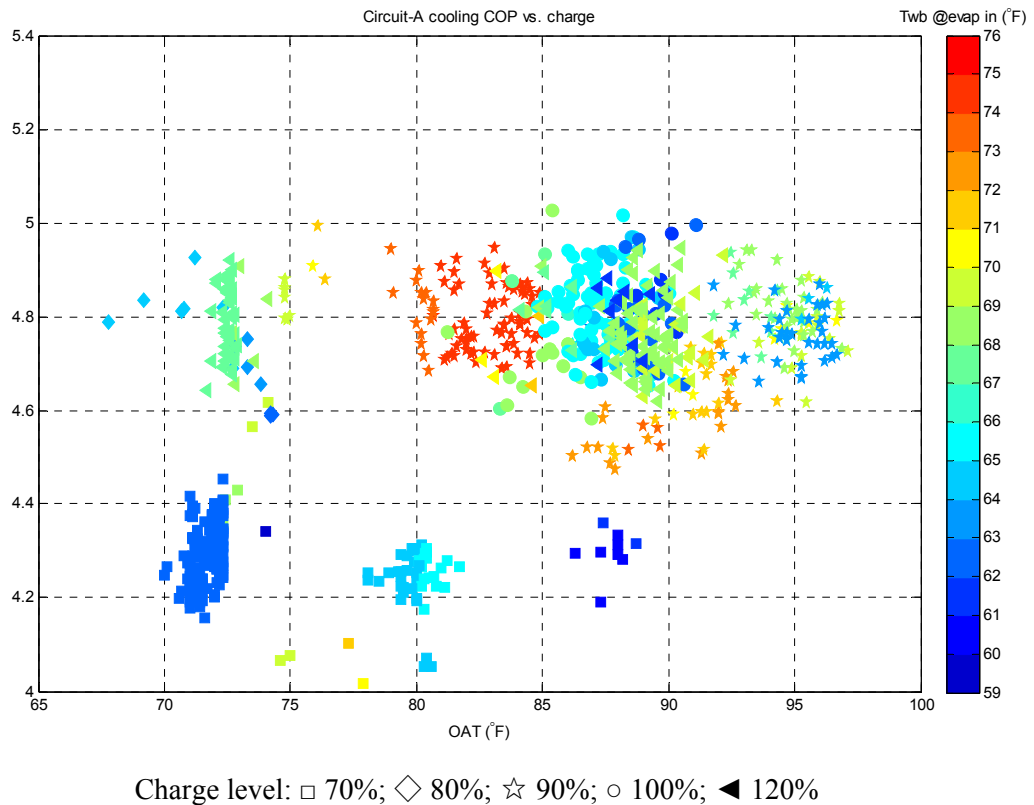
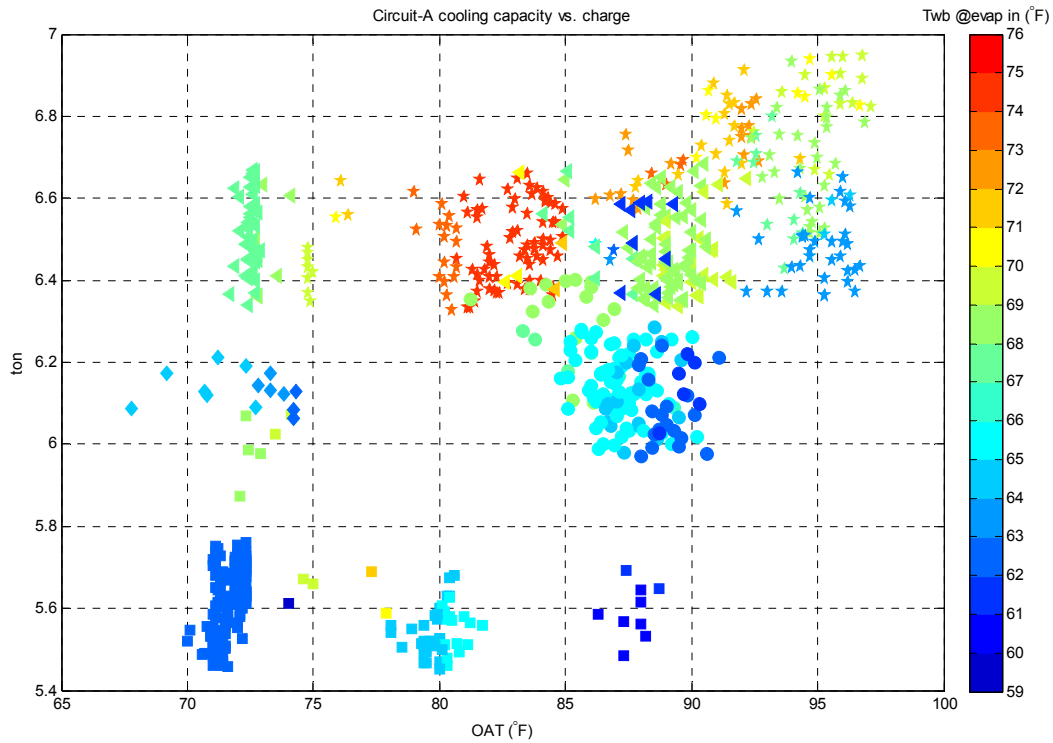


Figure 3.18 Subset of data from tests of cooling season of 2012

Figure 3.18 shows a subset of data from tests of cooling season of 2012. Each dot in the plot represents COP of the first circuit vs. outside-air dry-bulb temperature (OAT). In calculation of COP, electrical power includes compressor power of the circuit, 50% of indoor fan, and 50% of outdoor fans' power. Color of dot represents wet-bulb air temperature at inlet of evaporator. Shape of dot denotes refrigerant charge level. It is clear in the figure that COP at 70% charge is lower than that of other levels except a few outliers. Actually average degradation of 70% charge from 100% charge is 10.8%.



Charge level: □ 70%; ◇ 80%; ☆ 90%; ○ 100%; ◀ 120%

Figure 3.19 Cooling capacity of the same set of data

Figure 3.19 shows cooling capacity of the same set of data. The same trend is shown in the plot, which reveals 70% charge is a turning point of the RTU performance. In terms of cooling capacity, average degradation of 70% charge from 100% charge is 8.7%.

The detailed experimental data containing the values from Table 3.9 was transferred to Purdue University for further analysis and validation of fault diagnostics methods.

Table 3.9 Data set

Field Measurements		
Label	Meaning	Unit
Fault	Faults Type	
T_RA	Return Air Dry Bulb	[°F]
T_SA	Dry-bulb temperature of air leaving circuit-A evaporator	[°F]
T_amb	Ambient Drybulb	[°F]
RH_RA	Return-air relative humidity	[%]
RH_SA	Relative humidity of air leaving circuit-A evaporator	[%]
RH_amb	Ambient relative humidity	[%]
P_suc	Suction Pressure	[psig]
T_suc	Suction Temperature	[°F]
P_dis	Discharge pressure	[psig]
T_dis	Discharge temperature	[°F]
P_cond	Condenser exit pressure	[psig]
T_cond	Condenser exit temperature	[°F]
P_LL	Liquid Line pressure	[psig]
T_LL	Liquid Line Temperature	[°F]
T_evap	Evaporator inlet Temperature	[°F]
Power_comp	Compressor power of circuit A	[W]
Power_id	Indoor fan power (fan shared by 2 circuits)	[W]
Power_od	Outdoor fan power (fans shared by 2 circuits)	[W]
Chrg%	Charge as %nominal	[%]
V_i	Indoor total airflow rate (split between 2 circuits)	[CFM]
V_o_%	Outdoor coil air flow reduction in circuit A	[%]
OAD	Outside-air damper opening	[%]
T_air_ce	Condenser exit air temperature	[°F]
dp_evap	Evaporator air-side pressure drop	[in of water]
Tzone	Zone temperature	[°F]
T_exvi	EXV inlet temperature of circuit A	[°F]

3.3. RTU FDD Assessments using Offline Data

3.3.1. Impact of Faults on Performance and Costs Using Offline Data

This section provides details of the impact of individual faults on cooling and heating capacity and energy efficiency for a number of air-conditioning systems tested in the laboratory under a wide range of operating conditions. Improper operation can cause significant reduction in both cooling and heating capacity. This capacity degradation impacts runtime of the equipment and can lead to shorter equipment

life. It can also lead to loss of comfort if the capacity degradation is significant enough. Reductions in energy efficiency due to improper operation lead to greater overall electrical energy usage and operating costs. Information about the reduction in capacity and efficiency could be used within an on-line tool to assess the economics associated with servicing a unit.

Impact of refrigerant charge on performance and cost

To evaluate the impacts of faults on performance, the equipment capacity was determined. A capacity ratio was defined as the ratio of the capacity at the indicated fault level to the capacity at the rated condition under nominal operation. To provide a partial evaluation of the economic impact of faults in cooling equipment, annual cost of electricity was estimated for some case studies based on the tested units. The annual cost is the cost per year of operating the system. Costs were estimated using SEER, nominal capacity, estimated runtime, and average electric utility rates. The annual cost ratio is defined as the ratio of the annual energy costs at the indicated charge to the annual cost at the nominal charge.

Existing laboratory data from Kim and Braun (2012a) for several air conditioner systems (A1, A2, A3, and A4) and a heat pump system (A5) were used to evaluate the impact of refrigerant charge. Table 3.10 shows specification data for each system. The test conditions for cooling and heating mode are given in Table 3.11.

Table 3.10 System Specifications

System	Capacity [tons]	Compressor		Refrigerant	Expansion device	Accumulator
A1	3	Fixed-speed	Scroll	R22	EEV	Yes
A2	3		Reciprocating		FXO	Yes / No
A3	3		Reciprocating		FXO	Yes / No
A4	3		Rotary-Tandem		FXO	Yes
A5	3		Scroll	R410A	TXV	Yes

Table 3.11 Test Conditions

	Mode	Refrigerant Charge	Indoor temperature		Outdoor temperature	Indoor Air flow rate
		Nominal (%)	Dry (°C)	Wet (°C)	Dry (°C)	(%)
A1	Cooling	80 ~ 100	27	19	35	100
A2		60 ~ 110				
		75 ~ 100				
A3		60 ~ 100				
		75 ~ 100				
A4	60 ~ 100					
A5	Cooling	40 ~ 130	20	-	7	
	Heating					

The system A1 used an electronic expansion valve (EEV) as the expansion device and was tested with refrigerant charge levels between approximately 80-100%. The systems A2 and A3 had two configurations; with and without accumulators. Systems A2 and A3 were tested with refrigerant charge levels between 75-100% without an accumulator and between 60-100% with an accumulator. The system A4 included two tandem type compressors and was tested with refrigerant charge levels that ranged from 70 to 120% under rated test conditions. The heat pump A5 used a thermal expansion valve (TXV) as the

expansion device was tested with refrigerant charge levels between 40 to 130% of normal charge for cooling and heating mode.

Figure 3.20 shows the effects of refrigerant charge on cooling capacity for systems A1-A5. The capacity of system A1, was reduced by 5% with a 25% decrease of the refrigerant charge. The mass flow rate control provided by an EEV allows the system to compensate for variations in charge level while maintaining a specified superheat condition at the evaporator outlet.

Systems A2 and A3 have two cases: with and without an accumulator. A charge level reduction of 20% reduced cooling capacity by approximately 20% for both cases. The capacity decrease was more significant than for system A1 because a FXO was used as an expansion device. There was also a reduction in refrigerant mass flow rate with reduction in charge. When the refrigerant charge exceeded 100%, the capacity started to decrease for the system without an accumulator. This was caused by the decrease in condensing efficiency that resulted from the surplus refrigerant that accumulated in the condenser.

System A4 showed a rapid reduction in both cooling capacity when the charge level was decreased below 70% of the normal charge level. The step change that occurred at 90% was caused by the staging of the compressors. Only one compressor was operated instead of two compressors between 90 and 100% of refrigerant charge level. For system A5, the capacity significantly decreased when the refrigerant was charged less than 70%. Although the system uses a TXV to control superheat, it becomes fully open at low charge levels and acts like a FXO. Based on these results, it can be concluded that refrigerant charge levels below about 80 % of nominal charge can cause significant reductions in capacity.

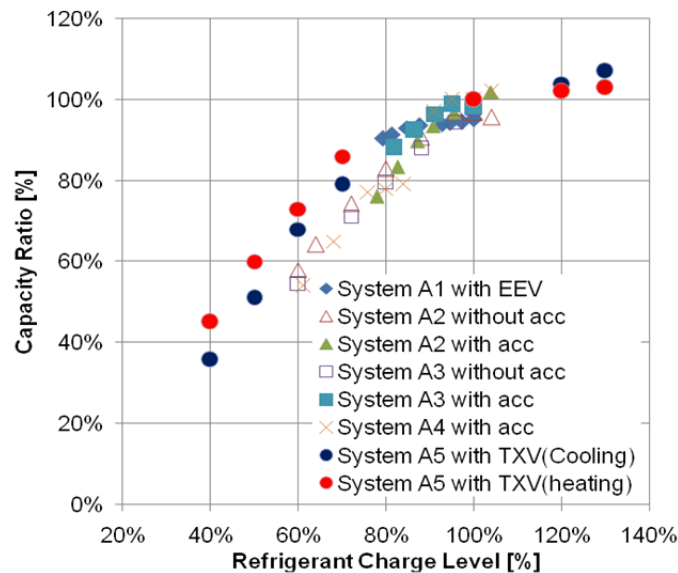


Figure 3.20 Capacity ratio for existing test data based on the refrigerant charge

The efficiency of air conditioners is rated using SEER which is defined by the Air Conditioning, Heating, and Refrigeration Institute in its standard ARI 210. Figure 3.21 shows the annual cost ratio of electricity that was calculated using laboratory test data. Low refrigerant charge can cause significantly higher operating costs.

In the case of system A2 without an accumulator, a 35% decrease of the refrigerant charge increased annual energy cost by about 30% (\$105 per ton of rated capacity). Using system A3 with an accumulator, the electricity consumption was increased by 20% when a 33% reduction of the nominal charge is used. For typical electricity rates of 0.12\$/kWh, this increase in electricity would result in an annual energy cost penalty of about 15% (\$52 per ton) for this unit. In case of system A4 with the tandem compressor, 65% of normal refrigerant charge led to an increase in the annual operating cost by about \$140/ton. For the system A5 with TXV as expansion device, a reduction of charge level by 60% increased an estimated annual cost penalty of \$232/ton.

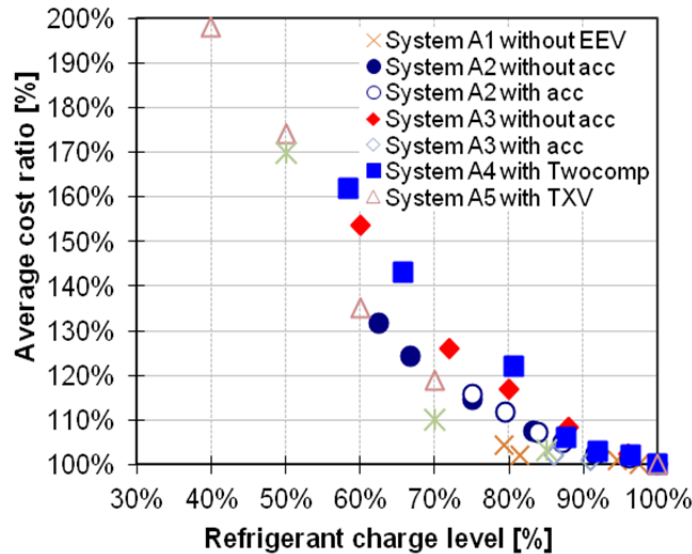


Figure 3.21 Annual cost ratios for all test data as a function of refrigerant charge

Impact of heat exchanger fouling on performance and cost

Heat exchanger fouling can have two effects on performance: 1) thermal resistance of the heat exchanger increases due to deposits collecting on the surfaces because the conductivity of the deposit is lower than that of the metal of the heat exchanger, 2) air flow rate is reduced due to higher pressure drop resulting from the deposits. The reduction of air flow rate can significantly impact the performance of the air conditioner system. Previous work (Li et.al, 2007) has demonstrated that the effect of reduced air flow is more significant than that associated with increased thermal resistance.

Laboratory test data were used to evaluate the impact of heat exchanger fouling on air-conditioner performance. Table 3.12 provides system specifications for the systems studied, including three RTUs and three residential split air-conditioners. R-410A and R-407C were used as refrigerants with both FXO and TXV as expansion devices in the systems.

Table 3.12 System Specifications

	System	Capacity [tons]	Compressor	Refrigerant	Expansion device	Assembly type
B1	RTU1	5	Scroll	R410A	TXV	Rooftop
B2	RTU2	5	Scroll	R407C	FXO	Rooftop
B3	RTU3	3	Scroll	R410A	FXO	Rooftop
B4	Split1	2.5	Reciprocating	R410A	TXV	Split
B5	Split2	3	Reciprocating	R410A	FXO	Split
B6	Split3	3	Reciprocating	R410A	TXV	Split

The test conditions used to assess heat exchanger fouling impact are listed in Table 3.13. Rated ambient and indoor conditions were maintained. Condenser fouling was simulated by reducing the condenser air flow rate in the all systems except B4. Fouling was simulated by blocking a portion of the condenser area in system B4. The condenser air flow rates for systems B1-B3 and B5-B6 were varied between 30-100% of the nominal air flow rate. The blocked heat exchanger area for system B4 ranged from 0-50%. To simulate evaporator fouling, the supply fan speed was reduced. Evaporator air flow rates were considered from 5% to 115% of nominal.

Table 3.13 Test Conditions

	System	Indoor temperature		Outdoor temperature		Evaporator air flow rate	Condenser air flow rate
		Dry (°C)	Wet (°C)	Dry (°C)	Wet (°C)	[%]	[%]
B1	RTU1	27	19	35	24	5 ~ 115	-
B2	RTU2					35 ~ 115	55 ~ 105
B3	RTU3					40 ~ 100	70 ~ 100
B4	Split1					70 ~ 100	50 ~ 100 (Blocking)
B5	Split2					55 ~ 115	30 ~ 100
B6	Split3					40 ~ 100	30 ~ 100

Figure 3.22 shows the impact of evaporator fouling on refrigeration capacity. Fouling was simulated using reduction of air flow rate that would occur due to increase pressure drop without the effect of an increase of thermal resistance due to deposits. On average, the capacity was reduced by 10% when a 40% reduction of evaporator air flow rate was provided. Capacity impacts are relatively small over this range. However, the impact of evaporator fouling on capacity increases dramatically below about 40% of normal air flow rate. The reduction of evaporator air flow rate by 50% decreased capacity by 17%. The results show that a 20% increase of evaporator air flow has an insignificant effect on capacity.

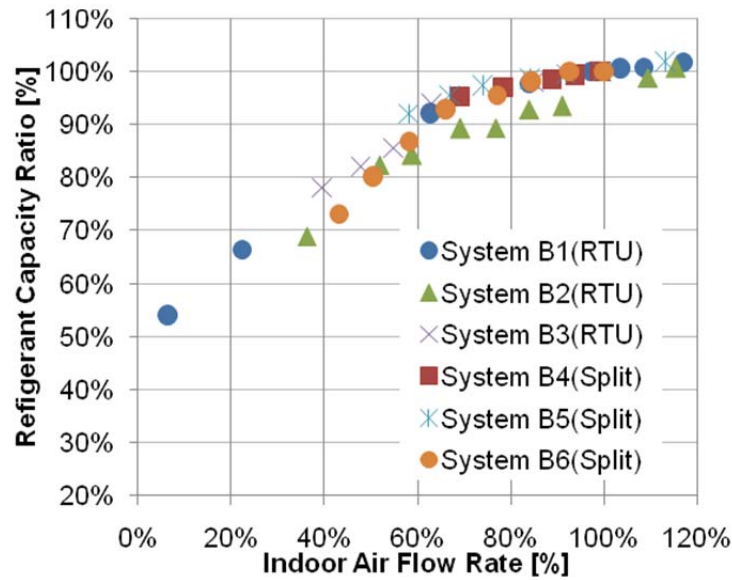


Figure 3.22 Capacity ratio for RTU and split air conditioners based on indoor air flow rate

The impact of condenser fouling on capacity is shown in Figure 3.23. On average, a 50 % reduction of condenser air flow rate decreases the cooling capacity by 9 %. Covering 50% of the heat exchanger area reduced cooling capacity by 22% in system B4. The condenser fouling simulated by 70% reduction of the air flow has about the same impact on capacity as 50% area blocking.

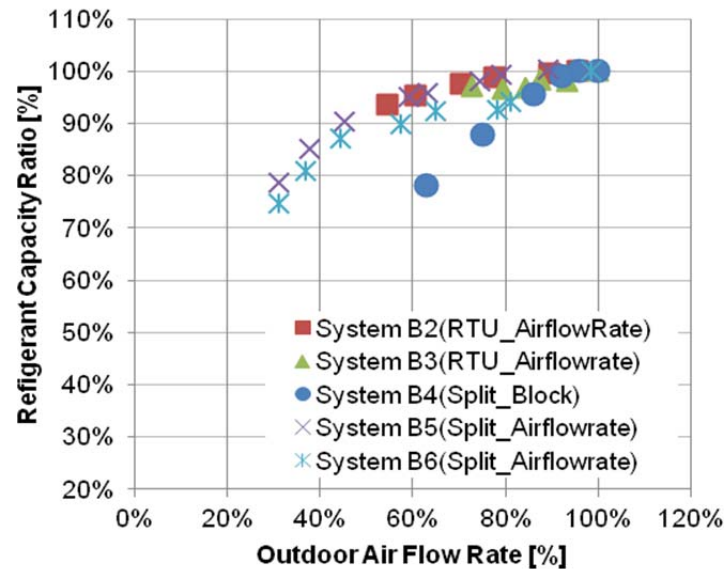


Figure 3.23 Capacity ratio for RTU and split air conditioners based on outdoor air flow rate

Figure 3.24 shows results for economic impact of evaporator fouling that were determined using laboratory test data. A 40% reduction of evaporator air flow rate led to an annual energy cost increase of

about 12%. The annual operating cost would increase by about \$25 per ton, on average, at 40% of the normal evaporator air flow rate.

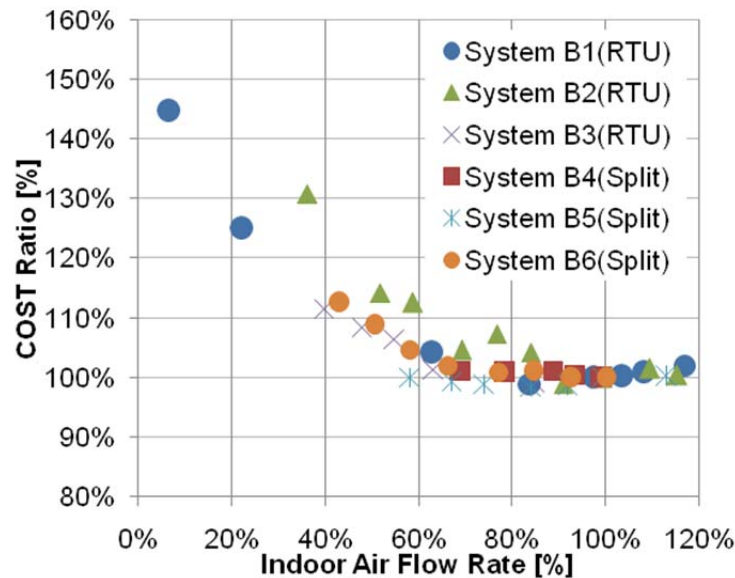


Figure 3.24 Cost ratio for RTU and Split air conditioner based on indoor air flow rate

Figure 3.25 shows impact of condenser fouling on energy costs. The results imply that extreme condenser fouling can cause significant increases in the operating costs. Electricity consumption was increased by 40% when a 40% reduction of the condenser air flow rate was imposed. In the case of heat exchanger blocking, a 35% decrease of area caused an increase in the annual operating cost by about \$70/ton.

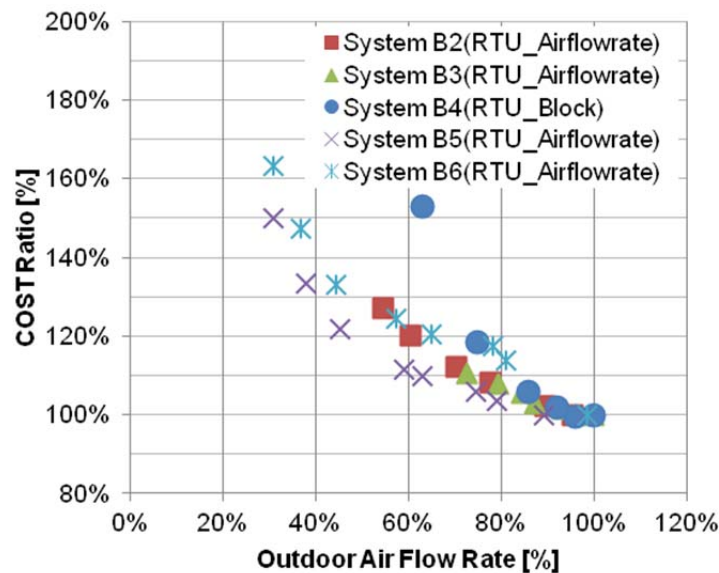


Figure 3.25 Cost ratio for RTU and Split air conditioner based on outdoor air flow rate

3.3.2. Development and Assessment of Virtual Sensors Based on Existing Laboratory Data

Virtual Refrigerant Charge (VRC) sensor

Li and Braun (2009) developed a VRC sensor model 1 used to correlate the refrigerant charge level to superheat and subcooling. Deviations from nominal charge can be obtained by using four measurements and four parameters, shown in equation (3- 2),

$$\frac{(m_{total} - m_{total,rated})}{m_{total,rated}} = \frac{1}{K_{ch}} \left\{ (T_{sc} - T_{sc,rated}) - K_{sh/sc} (T_{sh} - T_{sh,rated}) \right\} \quad (3- 2)$$

where m_{total} is the actual total charge, m_{rated} is the nominal total refrigerant charge, $K_{sh/sc}$ and K_{ch} are two constant parameters of a given system, and $T_{sc,rated}$ and $T_{sh,rated}$ are liquid line subcooling and suction line superheat at rated conditions with the nominal charge, respectively. The sensor was designed to minimize influence of other faults and operating conditions on its output.

As presented by Li and Braun (2009a), $K_{sh/sc}$ and K_{ch} can be estimated using the following equations

$$K_{ch} = \frac{m_{total,rated}}{K_{sc}} = \frac{T_{sc,rated}}{(1 - \alpha_o) \cdot X_{hs,rated}} \quad (3- 3)$$

$$K_{sh/sc} = \frac{K_{sh}}{K_{sc}} = \frac{(T_{sc} - T_{sc,rated})}{(T_{sh} - T_{sh,rated})} \quad (3- 4)$$

where $X_{hs,rated}$ is the ratio of high-side charge to the total refrigerant charge at the rated condition and α_o is the ratio of refrigerant charge necessary to have saturated liquid at the exit of the condenser to the rated refrigerant charge.

Based on data available from Harms (2002), a reasonable estimate value for $X_{hs,rated}$ was found to be 0.73 and a value of 0.75 was determined for α_o as default parameters. A reasonable estimate for $K_{sh/sc}$ for systems using a TXV or FXO as the expansion device is 1/2.5 based on previous test results from Li and Braun (2009).

Alternatively, $K_{sc/sh}$ and K_{ch} for the VRC sensor can be tuned to improve accuracy if data are available over a range of refrigerant charge levels and operating conditions. It is necessary to have variations in charge level to adequately determine parameters, but the data could also include variations in outdoor air flow rate, indoor air flow rate, ambient temperature, and indoor dry-bulb temperature. The parameter tuning method minimizes the errors between predicted and known refrigerant charge using linear regression.

Under extreme conditions such as low indoor air flow rate and low ambient temperature, the laboratory test results had zero subcooling and superheat. In these cases, the model 1 approach, which uses subcooling and superheat measurements as inputs, cannot accurately predict the charge level. Therefore, two other approaches (model 2 and 3) were developed to provide improved performance in these situations. Only model 2 results are presented in this report. Model 3 is a modification of the model equation (3- 2) that includes a correlation for refrigerant charge in terms of discharge superheat of the compressor and inlet quality of evaporator, shown in equation (3- 5).

$$\frac{(m_{total} - m_{total,rated})}{m_{total,rated}} = \frac{1}{K_{ch}} \left[(T_{sc} - T_{sc,rated}) - K_{sc/sh} (T_{sh} - T_{sh,rated}) + K_{sc/x} (x_{evap,in} - x_{evap,in,rated}) + K_{sc/dsh} (T_{dsh} - T_{dsh,rated}) \right] \quad (3- 5)$$

where $K_{sc/dsh}$ and K_x are a constant characteristics of a given system, and $T_{dsh, rated}$ is discharge superheat of the compressor and $x_{evap, in, rated}$ is evaporator inlet quality at rated conditions with the nominal charge.

To analyze the VRC sensor with models 1 and 3, existing laboratory data were used from Kim and Braun (2012b). The data were obtained for two systems from a manufacturer and laboratory testing data for two more systems. The specifications for the four systems are shown in Table 3.14. Table 3.15 shows the range of refrigerant charge and other conditions considered for each unit.

Table 3.14 System descriptions for air conditioner

System	Capacity (kW)	Refrigerant	Compressor	Accumulator	Expansion device	Type
C-1	14.5	R-22	Tandem	Yes	EEV	Air Split
C-2	15.2	R-22	Rotary	Yes	FXO	
				No		
C-3	10.5	R-22	Scroll	Yes	TXV	
C-4	10.5	R-410A	Scroll	Yes		

Table 3.15 Test conditions for air conditioners

System	Indoor Temp.		Outdoor Temp.	Indoor Air Flow rate	Refrigerant Charge Level
	Dry	Wet	Dry		
	(F)	(F)	(F)	[%]	(%)
C-1	80	67	95	100	80 ~ 100
C-2					60 ~ 110
C-3			67 / 95 / 105	50 / 100	70 ~ 130
C-4			43 / 95 / 115	100	40 ~ 130

Figure 3.26 presents performance of the VRC sensor model 1 based on default parameters. The overall RMS error of VRC sensor model 1 was about 12%. As the refrigerant charge level decreased, there were bigger differences between predicted and actual charge amounts. The errors were also large at low ambient temperature. For example, the VRC sensor predicted 60% of nominal charge when the system was charged at 40% of nominal charge; a 20% deviation.

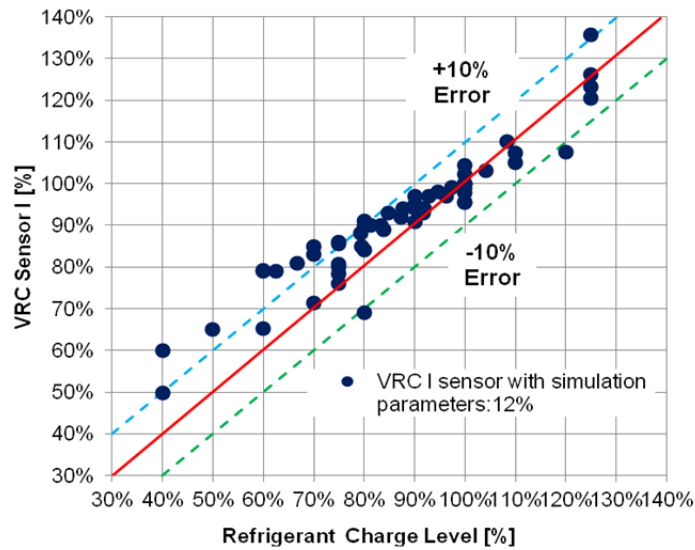


Figure 3.26 Performance of VRC sensor model 1 based on default parameters

When the model 1 using tuned parameters were applied, the VRC sensor showed better performance, as shown in Figure 3.27. The performance of model 1 is very good over a wide range of refrigerant charge levels and operating conditions. However, for extreme test conditions such as low outdoor temperatures, the VRC sensor model I with tuned parameters needed to be improved to predict all charge amounts within 10%.

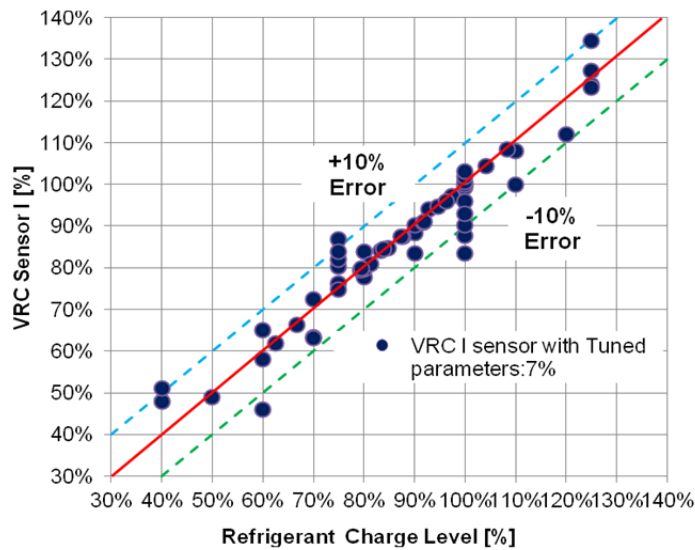


Figure 3.27 Performance of VRC sensor model 1 based on tuned parameters

Figure 3.28 shows performance of VRC sensor model 3 based on tuned parameters. The model 3 showed better performance than when model 1 with the tuned parameters was applied at low charge

levels. Overall, both the model 1 and 3 with tuned parameters showed good performance in terms of predicting charge levels for systems. However, when test conditions are at low outdoor temperature with low refrigerant charge, the VRC model 3 can lead to improvements in cases where the model 1 parameters do not work well.

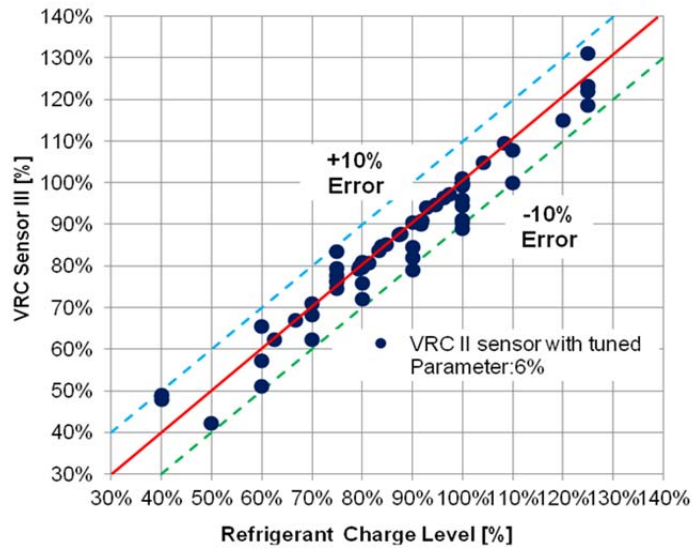


Figure 3.28 Performance of VRC sensor model 3 based on tuned parameters

3.3.2.2. Virtual Compressor Power (VCP) sensor

Laboratory test data (Payne, 2008) was used to develop and evaluate a virtual compressor power (VCP) sensor, virtual refrigerant mass flow rate (VRMF), and virtual air flow (VAF) sensors.

Table 3.16 gives specifications for equipment where data were obtained through laboratory testing. The systems used a TXV as an expansion device and R-410A as a refrigerant. Table 3.17 presents the range of operating test conditions with variations in both indoor and ambient temperature. The system was tested with different condenser and evaporator airflow rates, which could represent faults associated with a dirty air filter or coil fouling. Different refrigerant charge levels to simulate improper charge service and refrigerant leakage were also tested. Simulated compressor valve leakage faults, where a portion of the discharge flow from the compressor was bypassed to the compressor suction, were tested. Thus, this data set could be used to represent faulty compressor behavior. The system also included fault testing for a liquid line restriction (additional pressure drop increase through liquid line) and the presence of non-condensable gas (injection of nitrogen gas into the system). In general, only normal operating (i.e., no-fault) data were used to learn parameters of the VCP, VRMF, and VAF sensors. However all of the data were used for assessing the performance.

Table 3.16 System descriptions for system A-5

System		Size (kW)	Refrigerant	Expansion Device	Accumulator	System Type
C-5	(Payne, 2008)	8.8	R-410A	TXV	Yes	Air Split Type

Table 3.17 Test conditions for laboratory test data for system A-5

System	Indoor Temperature		Ambient temperature	Percentage of refrigerant mass flow rate	Indoor airflow rate	Outdoor coil block	Refrigerant charge
	Dry	Wet					
	(C)	(C)	(C)	[%]	[%]	[%]	[%]
C-5	27/21	19/15/Dry	28/ 35/ 39	60~100	70~100	0 ~ 50	70~130

The map-based method uses curves to fit the compressor motor power input to match the published performance data. Compressor map models are developed under the normal operating conditions of compressor. According to ANSI/ARI Standard 540-1999, a compressor power map can be represented as a 10-coefficient polynomial equation in the form of

$$\dot{W} = c_1 + c_2 T_e + c_3 T_c + c_4 T_e^2 + c_5 T_c^2 + c_6 T_e \cdot T_c + c_7 T_e^3 + c_8 T_e \cdot T_c^2 + c_9 T_e^2 \cdot T_c + c_{10} T_c^3 \quad (3-6)$$

where c_i are empirical coefficients, T_e is evaporating saturation temperature, T_c is condensing temperature.

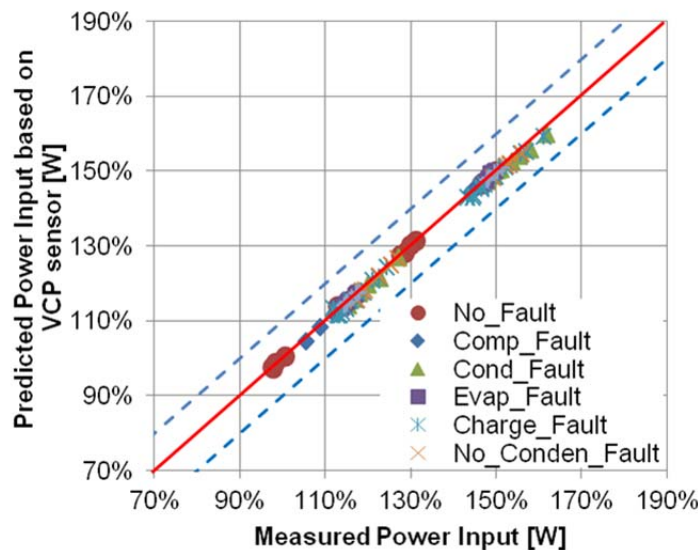


Figure 3.29 Performance of VCP sensors for system C-5 under no fault and multi fault condition

Figure 3.29 shows the VCP sensor for system C-5 can predict the performance within 5%. The terms “Normal”, “Comp Fault”, “Cond Fault”, “Evap Fault”, “Liquid Fault”, “Charge Fault”, and “NonCond Fault” stand for no fault, compressor leakage fault, condenser fouling fault, evaporator fouling fault, liquid-line restriction fault, refrigerant leakage fault, and non-condensable gas fault, respectively. Although the compressor map model was developed based on a specified amount of superheat, the VCP

sensor predicts compressor power consumption with reasonable accuracy under multi-fault conditions. This indicates the VCP sensor is independent of the various faulty conditions tested.

3.3.2.3. Virtual refrigerant mass flow rate (VRMF) sensor I based on compressor map

Refrigerant mass flow rate is an important measurement for monitoring equipment performance and enabling fault detection and diagnostics. However, a traditional mass flow meter is expensive to purchase and install. Three different VRMF sensors were developed and evaluated in this study that use mathematical models to estimate flow rate using low cost measurements. The three approaches use: 1) compressor map for refrigerant mass flow rate that uses inlet pressure and temperature and outlet pressure as inputs, 2) energy-balance method that employs the VCP sensor, 3) semi-empirical correlations for thermostatic expansion valves (TXV) that are based on an orifice equation (3-7).

A compressor map is used to estimate refrigerant mass flow rate using input measurements of inlet and outlet pressure. Based on ARI Standard 540, the VRMF Sensor I was determined using equation.

$$\dot{m}_{map} = \rho_{suc} \cdot (a_0 + a_1 T_c + a_2 T_c + a_3 T_e^2 + a_4 T_e^2 + a_5 T_c \cdot T_c + a_6 T_e^3 + a_7 T_e^3 + a_8 T_e^2 \cdot T_c + a_9 T_c^2 \cdot T_e) \quad (3-7)$$

where m_{map} is the estimated refrigerant mass flow rate, the a's are empirical coefficients, T_e is evaporating saturation temperature, T_c is condensing saturation temperature, and ρ_{suc} is the density at the suction (inlet) of the compressor.

Figure 3.30 shows the performance of VRMF sensor I for system C-5 under no fault and various faulty conditions. The root mean square (RMS) error is generally less than 2% for normal operation and with a variety of faults except for compressor valve leakage. RMS errors were shown for each fault type in Figure 3.30. For the range of compressor leakage conditions considered, the RMS error for the VRMF sensor I was 19%. In general, the error increases with the severity of the compressor leakage fault. As a result, differences between refrigerant flows determined using VRMF sensor I and other VRMF sensors can be used to diagnose a fault associated with the compressor not delivering the proper refrigerant flow.

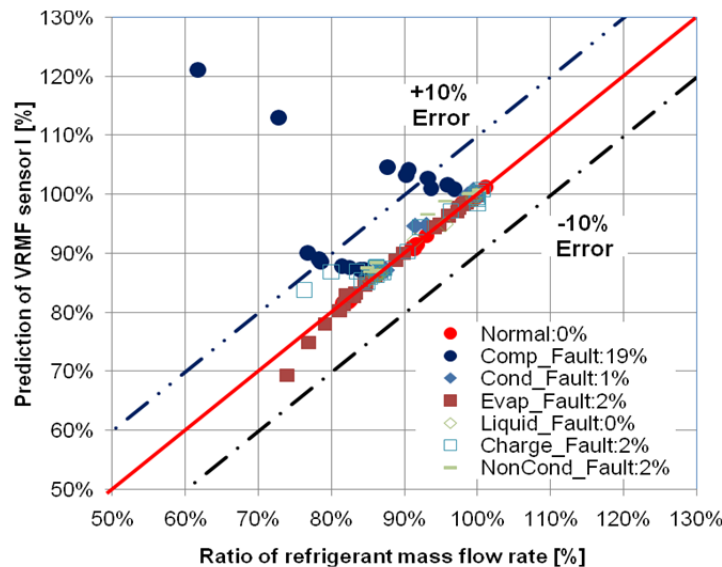


Figure 3.30 Performance of VRMF 1 based on compressor map

3.3.2.4. Virtual refrigerant mass flow rate (VRMF) sensor II based on energy balance

In order to diagnose compressor flow problems, it is necessary to have an alternative VRMF sensor. One alternative approach is VRMF sensor II developed based on a compressor energy balance using compressor power and compressor heat loss as shown in equation (3- 8). Compared to the map-based method, the energy balance model is much simpler and can be used for both fixed-speed and variable-speed compressors. To provide more accurate mass flow rates predictions under various faulty conditions, an empirical model for α_{loss} was developed in equation (3- 9). The model was trained using regression applied to normal test data.

$$\dot{m}_{energy} = \frac{\dot{W} \cdot (1 - \alpha_{loss})}{h_{dis}(T_{dis}, P_{dis}) - h_{suc}(T_{suc}, P_{suc})} \quad (3- 8)$$

$$\alpha_{loss, pred} = c_0 + c_1 P_{dis} + c_2 P_{suc} + c_3 T_{dis} + c_4 T_{suc} \quad (3- 9)$$

The parameter α_{loss} is compressor heat loss ratio, \dot{W} is compressor power consumption, and $h_{dis}(T_{dis}, P_{dis})$ and $h_{suc}(T_{suc}, P_{suc})$ are the discharge line and suction line refrigerant enthalpy. The compressor power consumption, discharge pressure (P_{dis}) and suction pressure (P_{suc}) can be estimated using other virtual sensors. The c 's are empirical coefficients, T_{dis} is compressor discharge temperature, and T_{suc} is suction temperature.

Figure 3.31 shows the performance of VRMF sensor II for system C-5. The mass flow rate prediction was determined using heat loss estimates and predictions from the VCP sensor. The heat loss model was determined using data for normal operation where the heat loss was determined from an energy balance on the compressor with the flow measured. The RMS error for the VRMF sensor was less than 3% for all of the data, including both normal and faulty conditions. The VRMF sensor II is relatively independent of compressor faults compared to the VRMF sensor I.

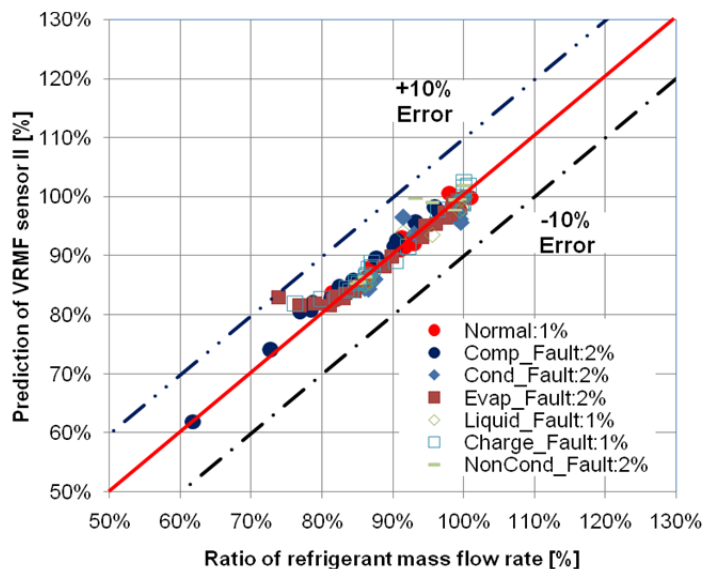


Figure 3.31 Performance of VRMF sensor II based on an energy balance

3.3.2.5. Virtual refrigerant mass flow rate (VRMF) sensor III based on TXV model

Expansion devices are used to reduce the pressure of the refrigerant and to regulate the refrigerant mass flow rate in response to changing loads. The TXV adopts a mechanical control method to obtain relatively constant superheat at the evaporator outlet. The valve opening for a TXV is determined by a force balance on a diaphragm, as depicted in Figure 3. 32. The bulb and suction line pressure act on opposite sides of the diaphragm and coupled with the spring force, control the effective orifice area.

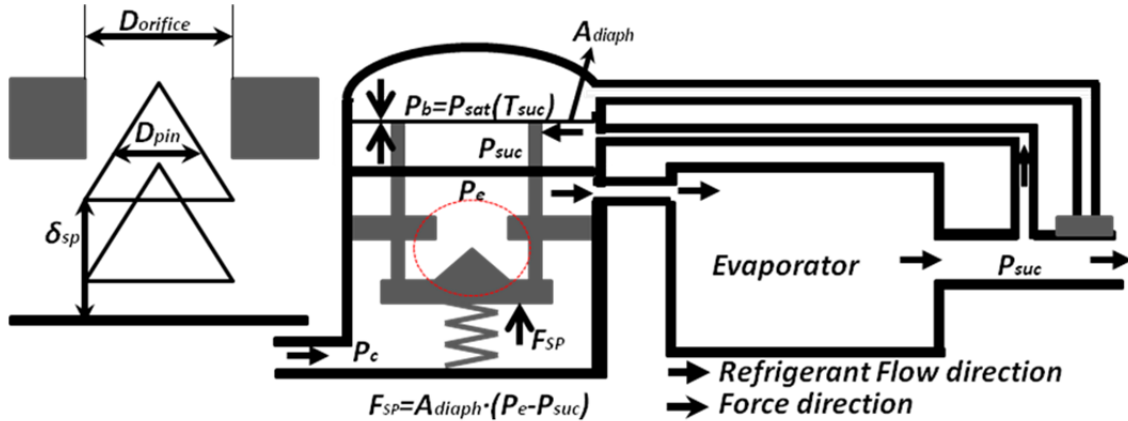


Figure 3. 32 Diagram of TXV

The VRMF sensor III for TXV was developed based on a semi-empirical model using the difference between suction and evaporating pressure as shown in equation (3- 10).

$$\dot{m}_{TXV} = (a_3(P_e - P_{suc})^2 + a_4(P_e - P_{suc}) + a_5) \cdot C_1 \cdot \sqrt{(2 \cdot \rho_f [P_c - P_e \cdot K])} \quad (3- 10)$$

$$K = C_2 \cdot \left(\frac{SC + 2}{T_{cri}} \right)^{C_3} + C_4 \left(\frac{P_{cri} - P_e}{P_{cri}} \right) + C_5 \quad (3- 11)$$

The C's are empirical coefficients, $(P_c - P_e)$ is the difference between the valve inlet pressure and the evaporating pressure, ρ_f is the density of the refrigerant at the valve inlet, SC is the subcooling of the refrigerant at the valve inlet, T_{cri} and P_{cri} are the critical temperature and pressure. $(P_b - P_{suc})$ is the pressure difference between bulb and suction line, and A_{diaph} is the area of diaphragm. $F_{sp,cl}$, A_{diaph} and k_{sp} are constants based on the valve design and initial setting.

The empirical coefficients C_1 , C_2 , C_3 , C_4 and C_5 within orifice equations (3- 10 and 3- 11) were estimated by minimizing mass flow rate prediction errors using fully open TXV test data and non-linear regression. Fully open TXV test data were collected from the conditions where superheat of the compressor inlet was higher than the rated superheat. The empirical coefficients a_3 , a_4 , and a_5 within the TXV model equation (3- 10) were estimated based on the available normal test data with superheat under control using linear regression. The data includes variations in ambient temperature, and indoor dry bulb temperature with positive subcooling entering the valve. Since equation

(3- 11) uses subcooling as an input, zero subcooling data were disregarded for training and testing. The parameter estimation methods minimized the errors between predicted and known mass flow rates. The resulting model with empirical coefficients determined from normal data was applied to predict refrigerant mass flow rate for all of the available data including various fault conditions.

Figure 3.33 shows refrigerant mass flow rate estimated from the VRMF sensor III for the TXV installed in system C-5 with six different kinds of faults individually implemented. The overall RMS errors were about 1% for no fault conditions and 3% of actual mass flow rate for all fault conditions. The performance of the VRMF sensor is very good over a wide range of refrigerant mass flow rates and operating conditions regardless of the fault. There were some significant errors of about 10% for low refrigerant charge levels when the entering subcooling was almost zero. With zero subcooling and two-phase conditions entering the TXV, the VRMF sensor III may not be reliable.



Figure 3.33 Performance of VRMF sensors III based on TXV model under no fault and fault conditions

3.3.2.6. Application of VRMF sensors for fault detection and diagnosis

Differences between the three VRMF sensors can be used within a diagnostic system to isolate compressor faults since the accuracy of the energy balance model and expansion device models are independent of compressor flow faults.

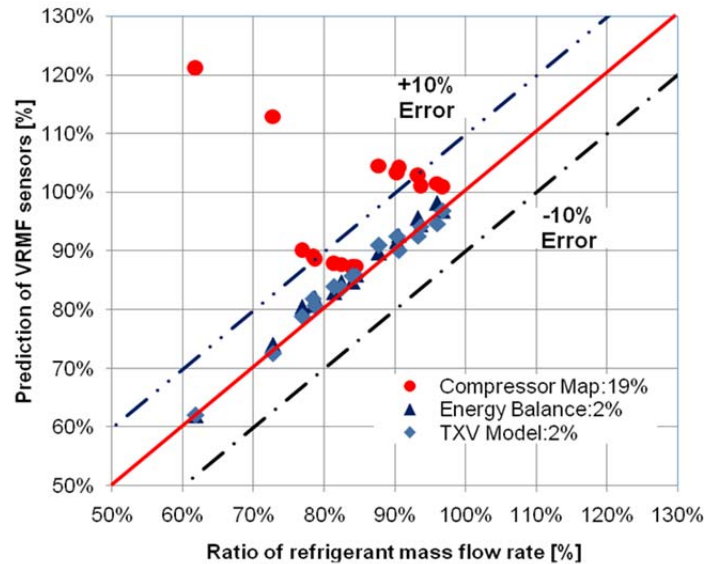


Figure 3.34 Comparison of VRMF sensor outputs for system C-5 with compressor flow fault

Figure 3.34 shows comparisons of the three VRMF sensors with mass flow measurements for system C-5. With a simulated compressor valve leakage fault, the refrigerant mass flow rate is reduced compared to normal operation. As a result, the compressor map over-predicts refrigerant mass flow rate whereas the other VRMF sensors provide accurate flow estimates. The RMS errors for compressor energy balance model and TXV models were about 2 %, whereas the RMS error for compressor model was 19 %. Thus, a compressor flow fault could be isolated through comparison of the VRMF sensors for this case.

3.3.2.7. Virtual Air Flow rate (VAF) sensor for condenser

To diagnosis condenser fouling conditions, a virtual sensor for condenser air flow rate is employed. Air flow measurements are generally very expensive and unreliable for field applications. Air flow rates can be estimated using energy balances on the condenser as expressed in equation (3-12).

$$\dot{V}_{predicted} = \frac{\dot{m}_{ref} (h_{dis}(P_{dis}, T_{dis}) - h_{liquid,in}(P_{li,in}, T_{li,in}))}{(T_{a,oc} - T_{a,ic})} \frac{v_{cond,a}}{C_{p,air,cond}} \quad (3-12)$$

where $\dot{V}_{predicted}$ is condenser air volume flow rate, $v_{cond,a}$ is condenser air specific volume, $C_{p,air,cond}$ is air specific heat, $T_{a,oc}$ is condenser outlet air temperature, $T_{a,ic}$ is condenser inlet air temperature, \dot{m}_{ref} is refrigerant mass flow rate provided from VRMF sensor, h_{dis} is discharge line refrigerant enthalpy, P_{dis} is discharge line pressure, T_{dis} is discharge line temperature, $h_{li,in}$ is liquid-line refrigerant enthalpy, $P_{li,in}$ and $T_{li,in}$ is liquid-line pressure and temperature.

Predicted air flow rate can be compared to a target air flow rate to detect fouling. The target flow can be obtained from a manufacturer’s catalog or from a normal value when the FDD scheme is implemented assuming that there is no fouling. The energy balance model has the limitation of not being valid when subcooling at the outlet of the condenser is zero. However, zero subcooling is typically associated with low refrigerant charge, which can be diagnosed using the VRC sensor.

Figure 3.35 shows the condenser air flow rate estimated from the VAF sensor for system C-5 with normal and faulty conditions. Overall, the VF sensor predicted the target condenser air flow rate, 1300 [CFM] within 3% except under condenser fouling fault conditions. As the severity of the condenser fouling increases, the estimated air flow rate is decreased. Condenser air flow rate reduction is an independent feature for condenser fouling. It also is a good feature for diagnosing condenser fan problems.

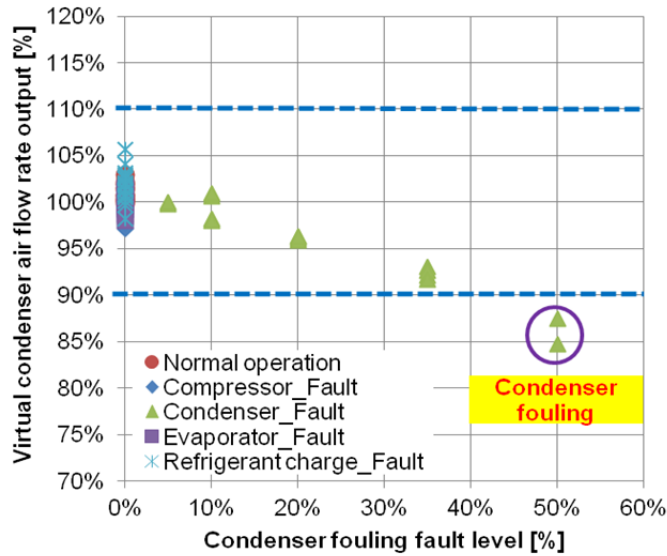


Figure 3.35 Predicted condenser air flow from an energy balance versus expected value for system C-5

3.3.2.8. Virtual Air Flow rate (VAF) sensor for evaporator

Evaporator air flow is estimated from an energy balance using Equation (3-13),

$$\dot{V}_{predicted, evap} = \frac{\dot{m}_{ref} (h_{evap, out}(P_{evap, out}, T_{evap, out}) - h_{evap, in}(P_{evap, in}, T_{evap, in})) \cdot v_{evap, a}}{(h_{a, ie} - h_{a, oe})} \quad (3-13)$$

where $\dot{V}_{predicted, evap}$ is evaporator air volume flow rate, $v_{evap, a}$ is evaporator air specific volume, $h_{a, ie}$ is evaporator inlet air enthalpy, $h_{a, oe}$ is evaporator outlet air enthalpy, \dot{m}_{ref} is refrigerant mass flow rate provided from a VRMF sensor, $h_{evap, out}$ and $h_{evap, in}$ are evaporator refrigerant outlet and inlet enthalpy, $P_{evap, o}$ and $T_{evap, o}$ are evaporator refrigerant outlet pressure and temperature, and $P_{evap, i}$ and $T_{evap, i}$ are evaporator refrigerant inlet pressure and temperature.

The indoor unit typically has more than one speed setting, but the air flow is constant for a given setting. Therefore, the virtual sensor can be used to estimate the air flow rate for each fan setting and compared with a target air flow rate. Figure 3.36 shows the accuracy of the air flow prediction from an energy balance for system C-5 with normal and faulty operation. The overall RMS error is about 3%. As the fault level of evaporator fouling increased, there was bigger difference between the estimated and normal air flow rate of 1000 CFM.

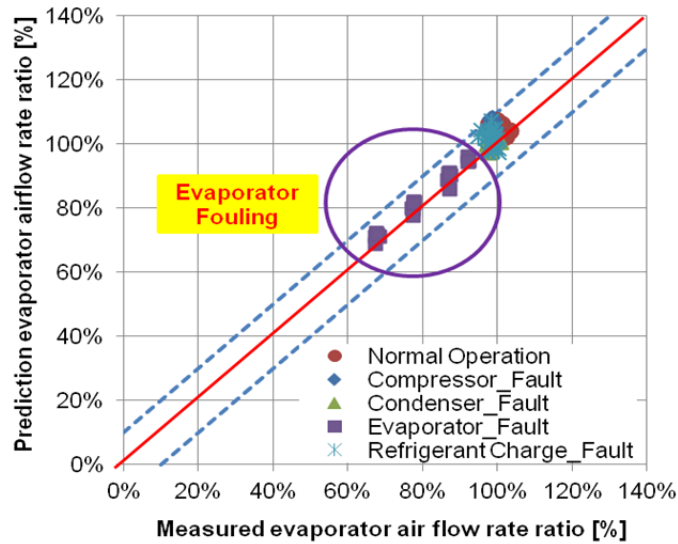


Figure 3.36 Predicted evaporator air flow from an energy balance versus expected value for system C-5

3.3.3. Assessments of Virtual Sensors using UTRC RTU Data

3.3.3.1. Evaluation of virtual sensors based on laboratory test data

Laboratory test data provided by UTRC was used to evaluate the performance of virtual sensors. Table 3.18 gives specifications for the 7.5 ton RTU system where data were obtained through laboratory testing. The system employed a TXV as the expansion device and R-410a as the refrigerant. The ranges of test conditions are given in Table 3.19. Refrigerant charge levels were varied between approximately 70 and 140% of nominal charge levels. The tests were performed at different operating conditions. The ambient temperatures ranged between about 83 and 113 °F. The indoor dry/wet bulb temperatures were considered from 70 to 80 °F and from 60 to 66 °F, respectively. The damper position was kept at 100% for all tests.

Table 3.18 Specification of system

Nominal Capacity	Refrigerant	Expansion Type	indoor coil airflow rate	Outdoor coil airflow rate	Total Power of system	Indoor fan Power	Outdoor fan Power
[tons]	-	-	[CFM]	[CFM]	[W]	[W]	[W]
7.5	R410A	TXV	2885	5750	6800	1350	497

Table 3.19 Testing conditions

Return air		Supply air		Ambient	Indoor	Outdoor		System
Dry temp.	Wet temp.	Dry temp.	Wet temp.	Dry temp.	Airflow rate of nominal	Airflow rate of nominal	Damper Opening	Refrigerant charge level
[°F]	[°F]	[°F]	[°F]	[°F]	[%]	[%]	[%]	[%]
71 ~ 81	60 ~ 66	50 ~ 67	46 ~ 65	83 ~ 113	60, 78	100	100	70, 75, 80, 85, 100, 140

VRC sensor models 1 and 3 were evaluated in terms of RMS deviation between predicted and actual charge levels relative to nominal charges. VRC model 1 was evaluated based on the use of default and tuned parameters and model 3 was evaluated based on tuned parameters only. Figure 3.37 shows the performance of VRC sensor model 1 using default parameters. The VRC sensor using default parameters can provide accurate estimates of refrigerant charge level, since the difference between actual and prediction charge levels is less than 10%. The accuracy of the refrigerant charge predictions is good using default parameters, however the use of the default parameters led to some significant errors greater than 10% when the system was significantly overcharged.

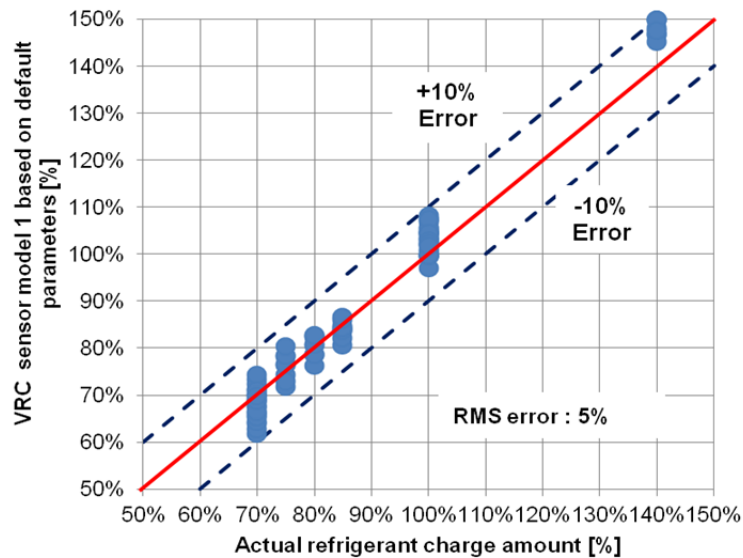


Figure 3.37 Performance of VRC sensor model 1 based on default parameters for UTRC laboratory data

To increase the accuracy of the VRC sensor, the parameters were tuned for each specific system based on measurements obtained at different refrigerant charge levels. When tuned parameters were applied to the models 1 and 3, the VRC sensors showed better performance than when the default parameters were used. Figure 3.38 and Figure 3.39 show the performance of VRC sensor models 1 and 3 with tuned parameters. The parameters for the VRC sensors were tuned by using 10 data points under four different refrigerant levels. The RMS errors were reduced to 4% for model 1 and 2% for model 3. The results verified that tuned parameters significantly improve the accuracy of the VRC sensor. Compared to model 1, model 3 led to some improvements in cases where model 1 shows some deviation at low refrigerant charge level.

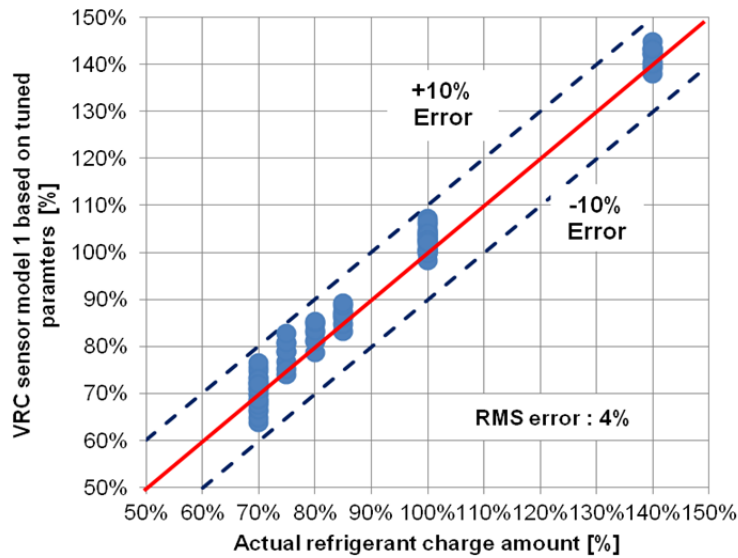


Figure 3.38 Performance of VRC sensor model 1 based on tuned parameters for UTRC laboratory data

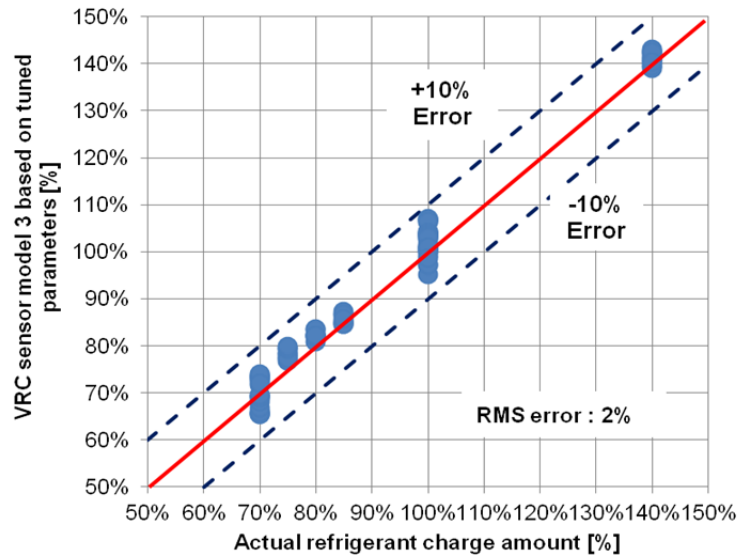


Figure 3.39 Performance of VRC sensor model 3 based on tuned parameters for UTRC laboratory data

Figure 3.40 shows performance of the VCP sensor for input power under no fault and refrigerant fault conditions. The parameters for the VCP sensor were trained using normal operation data points only. The RMS error of the estimated input power consumption was less than 5% over a wide range of conditions. Overall, the VCP Sensor is able to make accurate estimations of input power for the laboratory test data provided by UTRC.

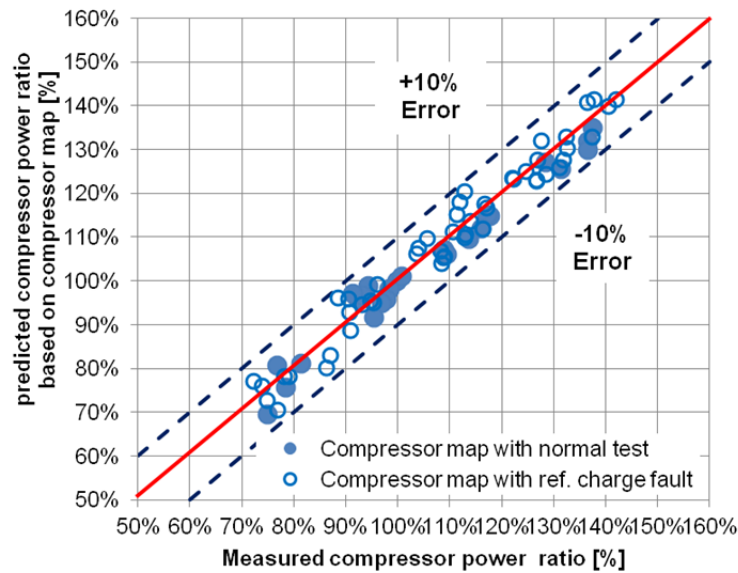


Figure 3.40 Performance of VCP sensor for UTRC laboratory data

Figure 3.41 shows performance of the VRMF sensor I based on the compressor map. The mass flow rate estimates were compared to measurements from laboratory test data. The accuracy of VRMF sensor I is within 10% of the actual measured value. The errors are somewhat higher (9%) at high refrigerant charge level, but the sensor outputs are still reasonable for this fault.

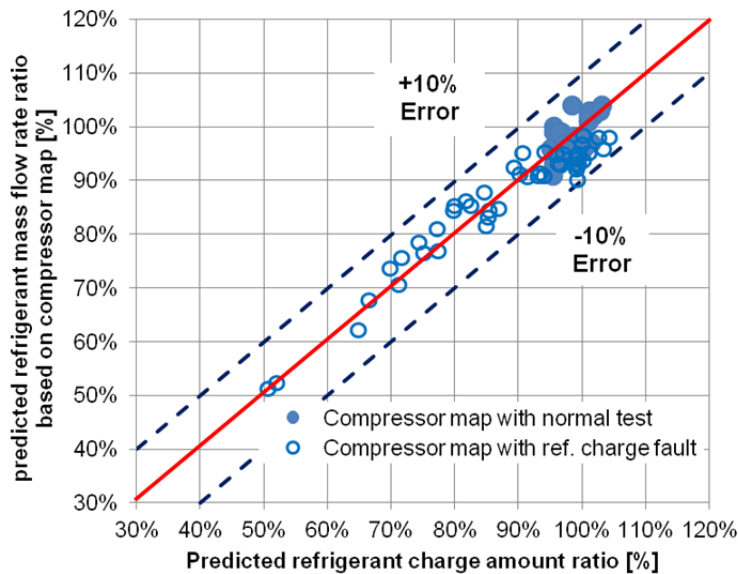


Figure 3.41 Performance of VRMF sensor I based on compressor map for UTRC laboratory data

Figure 3.42 shows the performance of VRMF sensor II based on the compressor energy balance. The RMS error for the VRMF sensor II is less than 10% and works well regardless of the fault conditions applied. However, there were some significant errors (10%) at high refrigerant charge level. The incorrect compressor suction enthalpy due to a two-phase refrigerant inlet state led to the inaccurate

estimations. Additional work is necessary to accurately determine heat loss for overcharged condition using VRMF sensor II.

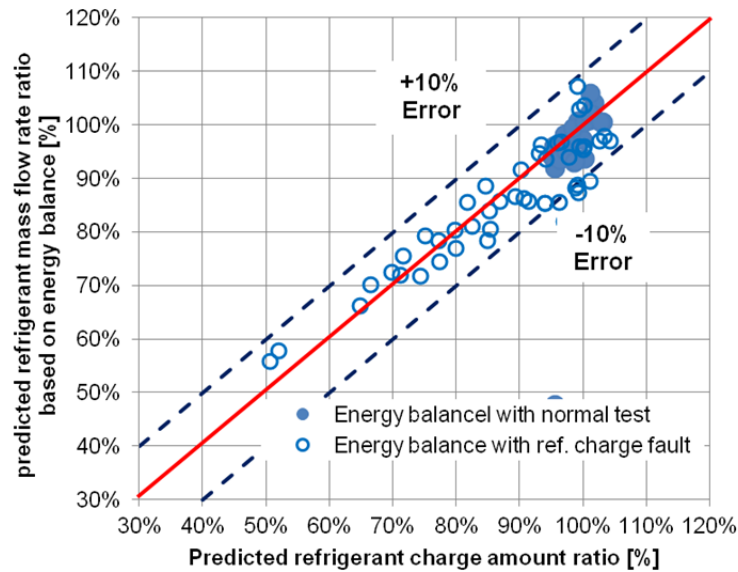


Figure 3.42 Performance of VRMF sensor II based on energy balance for UTRC laboratory data

The empirical coefficients of the orifice equation for VRMF sensor III were determined using non-linear regression applied to fully open TXV data. Equation 3-11 uses subcooling as an input so data with zero subcooling were not used to tune the parameters. Once the empirical coefficients of the orifice equation were obtained, the TXV model was fit to normal operating (i.e., no-fault) data using linear regression. Figure 3.43 shows performance of VRMF sensor III. VRMF sensor III provides results that generally fall within 10% of the actual mass flow rate over a wide range of operating conditions. Larger errors were produced under low refrigerant charge levels because the subcooling at the condenser outlet was below 2 °F.

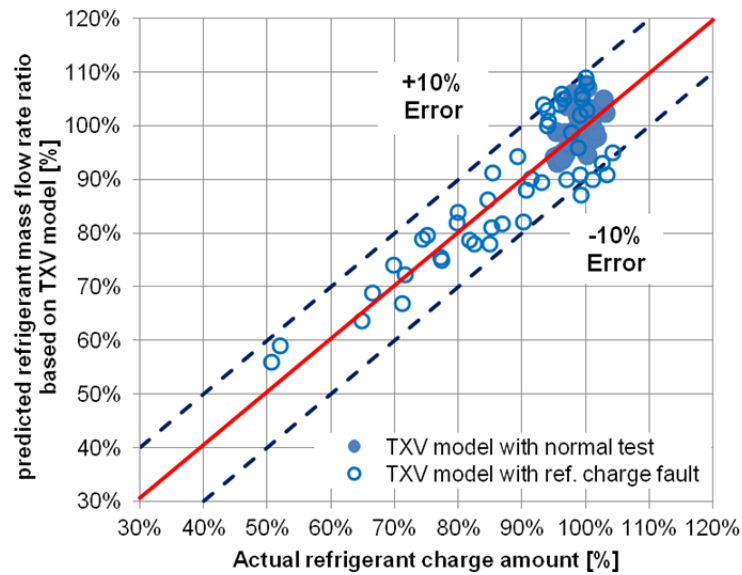


Figure 3.43 Performance of VRMF sensor III based on TXV model for UTRC laboratory data

3.3.3.2. Evaluation of virtual sensors based on field test data

Field test data collected by UTRC were used to evaluate the performance of virtual sensors. The specifications of the RTU system and the testing conditions are given in Table 3.20 and Table 3.21. The installed system had a cooling capacity of 10 tons using R410A as a refrigerant. A TXV was used as an expansion device in the system. The refrigerant charge was varied from 70 to 140% of normal charge. Condenser fouling was simulated by blocking a portion of the condenser heat exchange area. The effects of reduced air flow rate were considered from about 45 to 100% of the normal value. During the field test period, the outdoor-air temperature was as high as 97 °F during the daytime and dropped as low as 61 °F. The indoor dry-/wet-bulb temperatures were as high as 86/75 °F and dropped as low as 68/38 °F. The outdoor-air damper openings were varied between 0-100% during each normal and faulty test condition.

Table 3.20 System specification for RTU system

Nominal Capacity	Refrigerant	Expansion Type	indoor coil airflow rate	Outdoor coil airflow rate	Total Power of system	Indoor fan Power	Outdoor fan Power
[tons]	-	-	[CFM]	[CFM]	[W]	[W]	[W]
10	R410A	TXV	3400	8300	9750	2760	800

Table 3.21 testing condition for RTU system

Return air		Supply air		Ambient	Indoor	Outdoor		System
Dry temp.	Wet temp.	Dry temp.	Wet temp.	Dry temp.	Airflow rate of nominal	Airflow rate of nominal	Damper opening	Refrigerant charge level
[°F]	[°F]	[°F]	[°F]	[°F]	[%]	[%]	[%]	[%]
68 ~ 86	38 ~ 75	46 ~ 66	82 ~ 97	61 ~ 97	100	45, 57, 70, 100	0, 25, 50, 75, 100	70, 75, 80, 85, 100,

The charging method specified by the manufacturer and the VRC sensor were evaluated using the RTU field test data. The approach used to verify refrigerant charge in the field for this system required the use of pressure measurement at the service valve. Compressor discharge pressure and liquid line temperature are used to indicate the charge level. The technicians evaluated whether to add or remove refrigerant based on a difference between the measurement and a target value based on the charging chart supplied by the manufacturer.

Figure 3.44 and Figure 3.45 show the manufacturers' charging method for the RTU system monitored by UTRC under the various operating conditions. The manufacturers' approach uses discharge pressure and outdoor coil temperature for finding the nominal charging amount. The solid line indicates the target pressure and temperature combination. The points that are above the line indicate that more refrigerant needs to be charged into the system and those below the line indicate that refrigerant needs to be removed.

Figure 3.44 shows the charging results under no heat exchanger blocking. It showed 70-80% as undercharged, 90-100% as nominal, and 120% as overcharged. Overall, the manufacturers' charging method can provide accurate estimates when no heat exchanger blocking is present.

Figure 3.45 shows the charging results when heat exchanger blockage is present. While it showed 70% as undercharged, 80-90% was detected as nominal charge and 100-120% was detected as overcharged. This suggests that when there is condenser fouling the charging method can indicate normal charge even when the unit is undercharged by as much as 20%. In addition, the manufacturers' charge verification utilizes pressure gauges or transducers installed at the service valve. The installation of these gauges or transducers can lead to refrigerant leakage. Because of these limitations, the current protocols for checking refrigerant charge may be doing more harm than good in many situations.

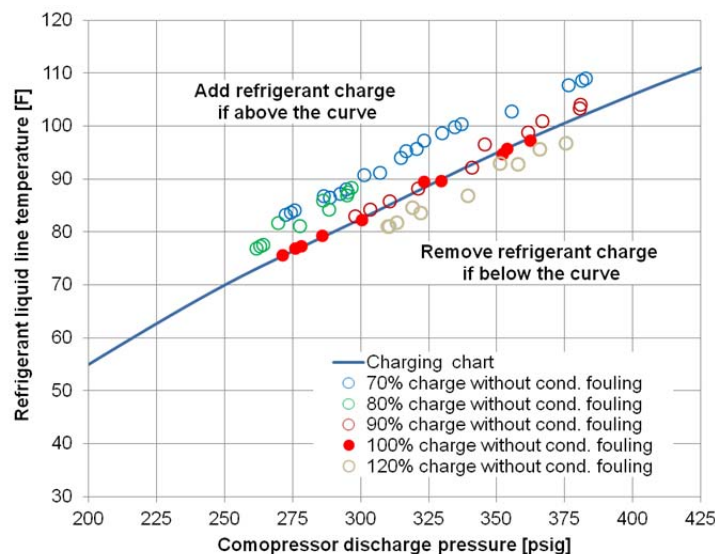


Figure 3.44 Charging results based on manufacturers' charging method under no heat exchanger blocking

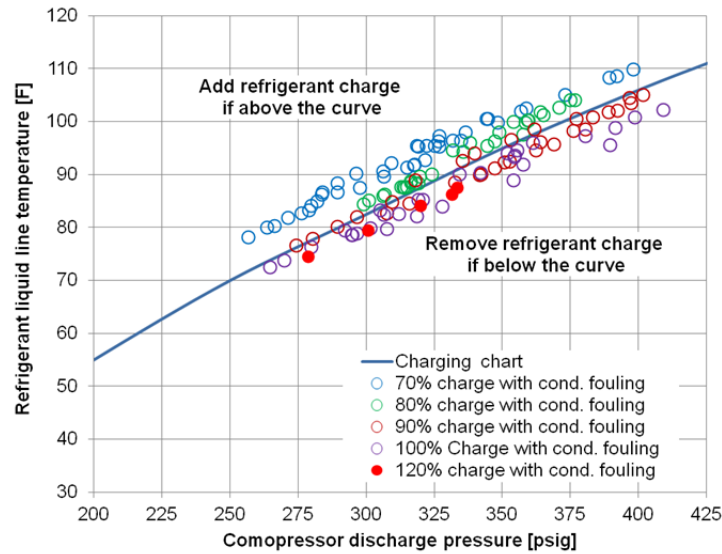


Figure 3.45 Charging results based on manufacturers' charging method under heat exchanger blocking

Figure 3.46 and Figure 3.47 show the accuracy of VRC sensor models 1 and 3 based on tuned parameters using all test data points. The performance was evaluated in terms of RMS deviation from the actual charge levels presented on a percentage basis. Figure 3.46 shows performance based on tuned parameters. Overall, the RMS errors of the VRC sensor algorithm for model 1 were 4% under no fouling conditions. In many cases, the accuracy of the refrigerant charge predictions is good. Although the VRC sensor can predict the charge amount within 10%, the errors were still large at high charge levels when the superheat exiting the compressor was nearly zero under low ambient temperature conditions.

Figure 3.47 shows performance of VRC sensor 1 under fouling conditions. In this case, the RMS errors of model 1 were 9%. When model 1 was applied, there were some points with significant refrigerant charge estimate errors compared to no fouling conditions. In particular, the VRC sensor 1 overestimates charge amount at high condenser fouling levels and conditions having almost zero subcooling.

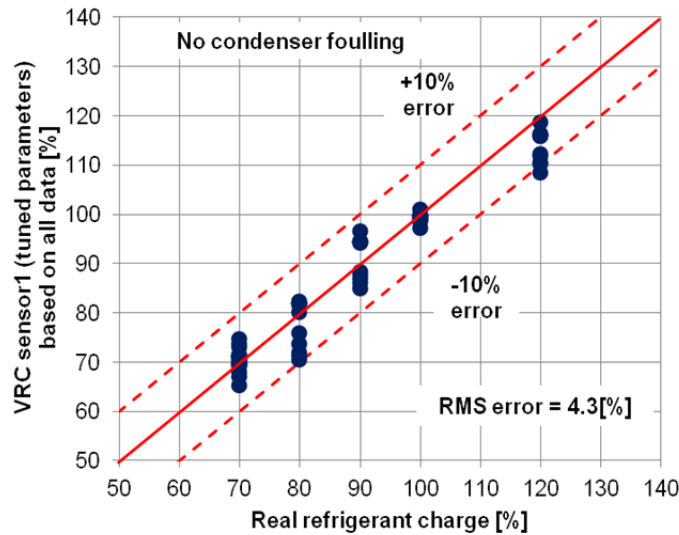


Figure 3.46 Performance of VRC sensor model I based on tuned parameters under no condenser fouling

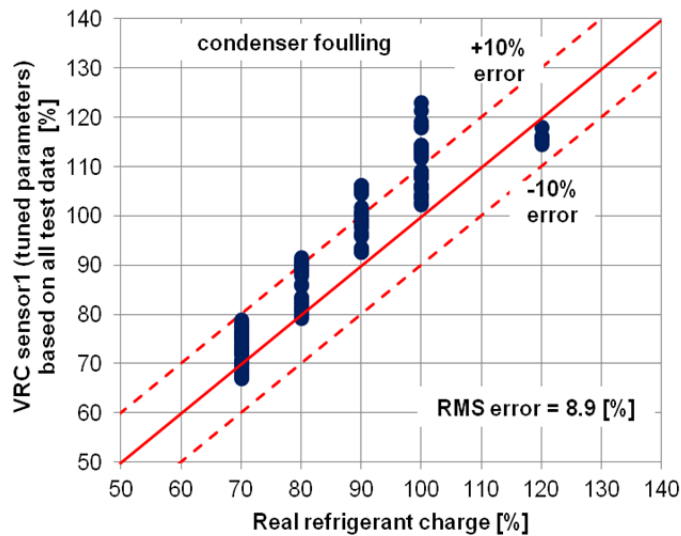


Figure 3.47 Performance of VRC sensor model I based on tuned parameters under condenser fouling

Figure 3.48 and Figure 3.49 show the results of VRC sensor model 3. Figure 3.48 shows the results under no heat exchanger blocking. The model 3 based on tuned parameters showed RMS errors of 4%. Accurate charge evaluations are possible for refrigerant charges less than 100%. All results had less than 10% error except when refrigerant was charged at 120% of the nominal charge. Overall, model 3 did not improve the performance of the VRC sensor compared to the model 1 under no fouling condition.

Figure 3.49 shows the results under heat exchanger blocking. The VRC model 3 is better than model 1 for characterizing refrigerant charge levels with condenser fouling conditions present. Some data points between 80 and 90% refrigerant charge levels were slightly over 10%. These points are

associated with large condenser blocking of approximately 50%. The cases where the VRC sensor had difficulty were when the system operated with zero subcooling at over 50% reduction of condenser air flow rate. In this case, the VAF sensor for condenser would be helpful predicting the condenser fouling fault.

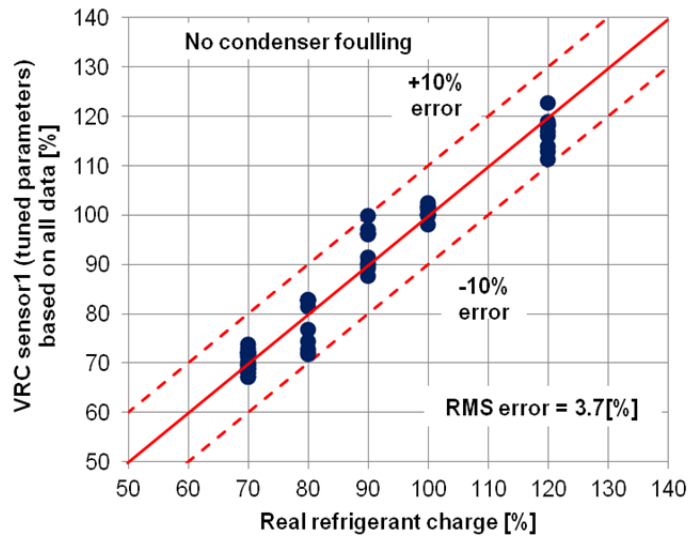


Figure 3.48 Performance of VRC sensor model III based on tuned parameters under no condenser fouling

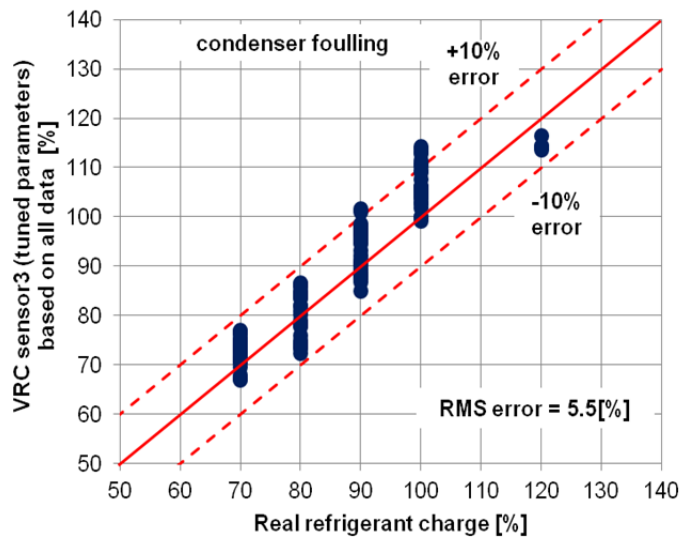


Figure 3.49 Performance of VRC sensor model III based on tuned parameters under condenser fouling

Figure 3.50 shows the performance of the VCP sensor. The VCP sensor can predict power consumption with RMS errors of $\pm 5\%$. The VCP sensor also works well under multi-fault conditions such as condenser fouling and refrigerant charge.

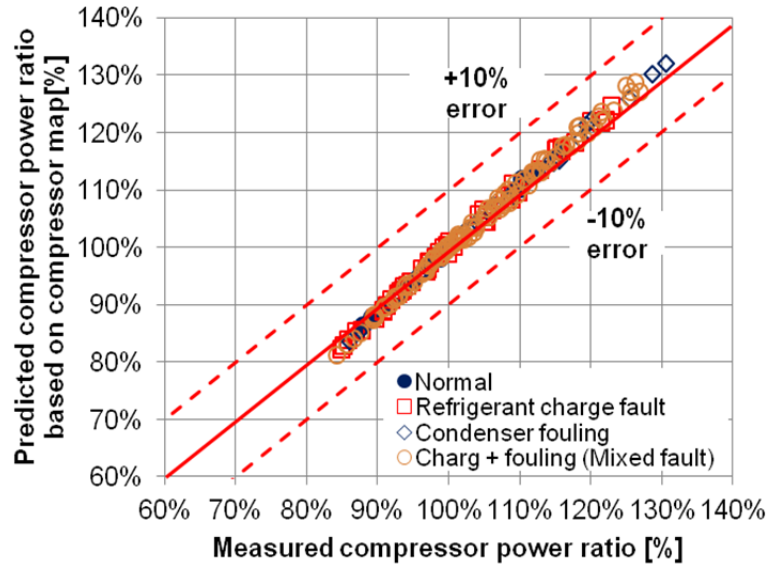


Figure 3.50 Performance of VCP sensors under normal and faulty conditions

Figure 3.51 shows comparisons of VRMF sensor I predictions (based on a compressor map) and sensor II outputs using an energy balance under no fault and various fault conditions. A refrigerant mass flow meter data was not installed in this system to confirm the accuracy of the prediction. Because the results shown in VCP sensor based on compressor map are consistent with the power measurement, we relied on the compressor map predictions. The RMS errors between VRMF model I and II were less than 10% for condenser fouling and refrigerant charge. However, the RMS error was about 9% when multiple faults were tested. The larger errors occurred when the superheat at the compressor inlet was below 1.5 °F. The system was overcharged and serious condenser fouling was applied in these situations.

Figure 3.52 shows comparisons of VRMF sensor I predictions based on a compressor map and VRMF sensor III outputs using the TXV model both with and without faults. The RMS errors between model I and III were less than 10%. Except for several multiple simultaneous fault conditions, the VRMF works well regardless of the fault implemented. Some of the larger errors may be associated with two-phase refrigerant conditions at the TXV inlet with near-zero subcooling under low refrigerant charge and condenser fouling conditions.

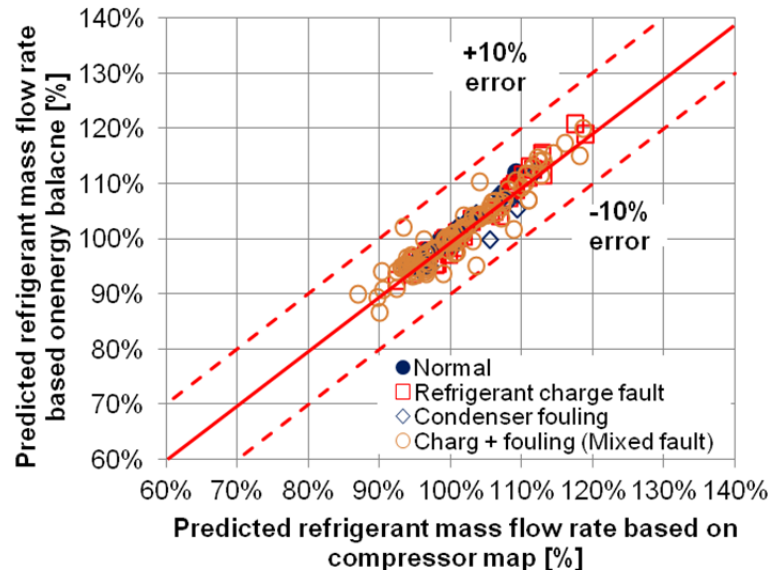


Figure 3.51 Performance of VRMF sensors based on model I and II under normal and faulty conditions

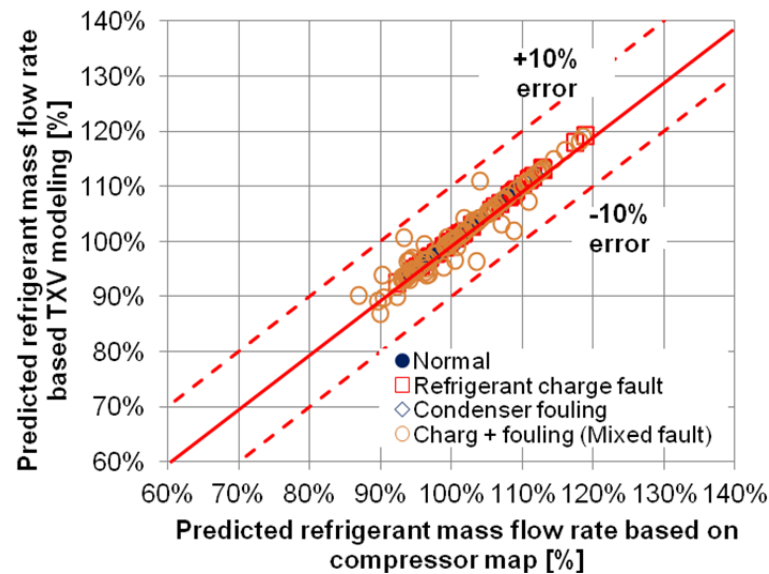


Figure 3.52 Performance of VRMF sensors based on models II and III under normal and faulty conditions

A virtual air flow rate (VAF) sensor for the condenser based on an energy balance was evaluated based on the RTU field test data provided by UTRC. Figure 3.53 and Figure 3.54 show the results after applying the VAF sensor. This sensor was able to detect condenser blockage. Figure 3.53 shows the results of VAF sensor under nominal refrigerant charge. As the heat exchanger blocking level increased,

the estimated air flow rate was decreased. When the blocking level was over 40%, air flow rate decreased to 65% of the nominal air flow rate. Air flow rate reduction is an independent feature for condenser fouling. Figure 3.54 shows similar results but with a larger spread of predictions when the system was undercharged.

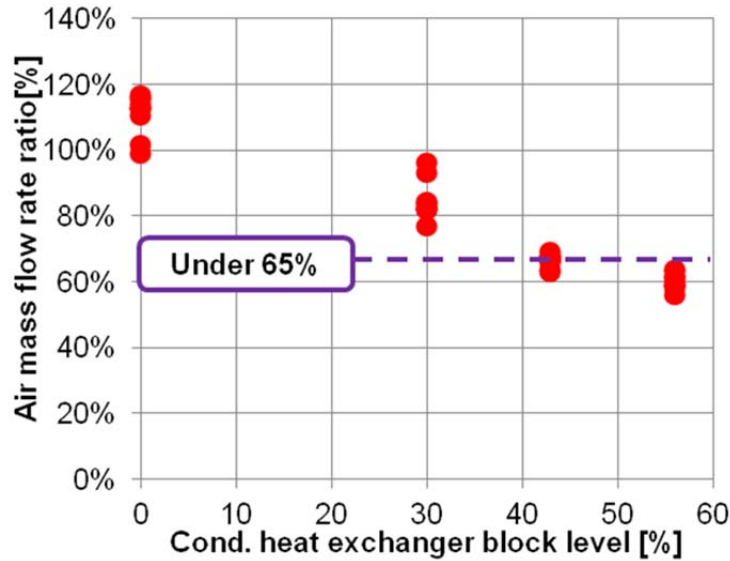


Figure 3.53 Performance of VAF sensors for condenser under normal refrigerant charge level

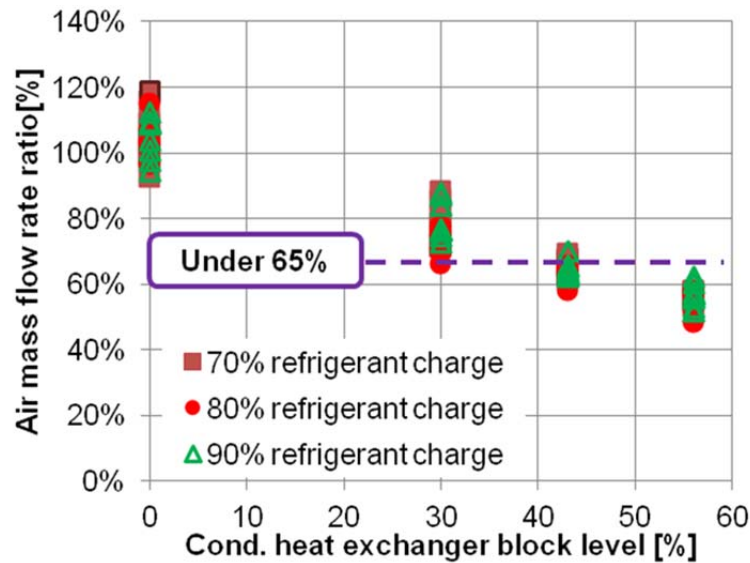


Figure 3.54 Performance of VAF sensors for condenser under different refrigerant charge levels

3.4. Embedded AFDD (Automated Fault Detection and Diagnosis) for RTU

3.4.1. System descriptions and test conditions for refrigerant charge, heat exchanger fouling, economizer, and supply fan faults

A 4-ton RTU system was installed in the psychrometric chambers in Herrick Laboratories. Table 3.22 provides an overview of the RTU system that was tested. To obtain data containing faults, laboratory tests were performed with the RTU system with faults injected. The ranges of test conditions are given in Table 3.23. Refrigerant charge levels were varied between 50% and 100% of nominal charge levels with outdoor temperatures between about 65 °F and 115 °F. Data for relatively low outdoor temperatures were used to validate the algorithms for conditions that would occur during off-season when regular maintenance procedures are often performed. Condenser fouling was simulated by blocking different amounts of the air inlet area. The blocked heat exchanger area ranged from 0% to 70%. The simulated method for evaporator fouling was to reduce indoor fan speed.

A mass flow meter, thermocouples, and pressure sensors were installed in accordance with the refrigerant circuit schematic presented in the Figure 3.55. Since an extra liquid line was added in order to install refrigerant mass flow meter, tests were performed to determine the nominal charging amount. The refrigerant charge levels were determined using the subcooling obtained from the technical data provided from the manufacturer.

Table 3.22 System specification

Type	Size (Tons)	Refrigerant	Compressor	Expansion Device	Accumulator
RTU	10	R-410A	Fixed-speed comp.	TXV	No

Table 3.23 Test conditions

Air indoor Temp.		Air outdoor Temp.	Outdoor H/X block area ratio	Indoor fan speed	Refrigerant charge rate
F	F	F	[%]	Hz	%
80	67	65, 95, 115	0, 15, 20, 45, 60, 70	60, 30, 15	50, 65, 75, 85, 100

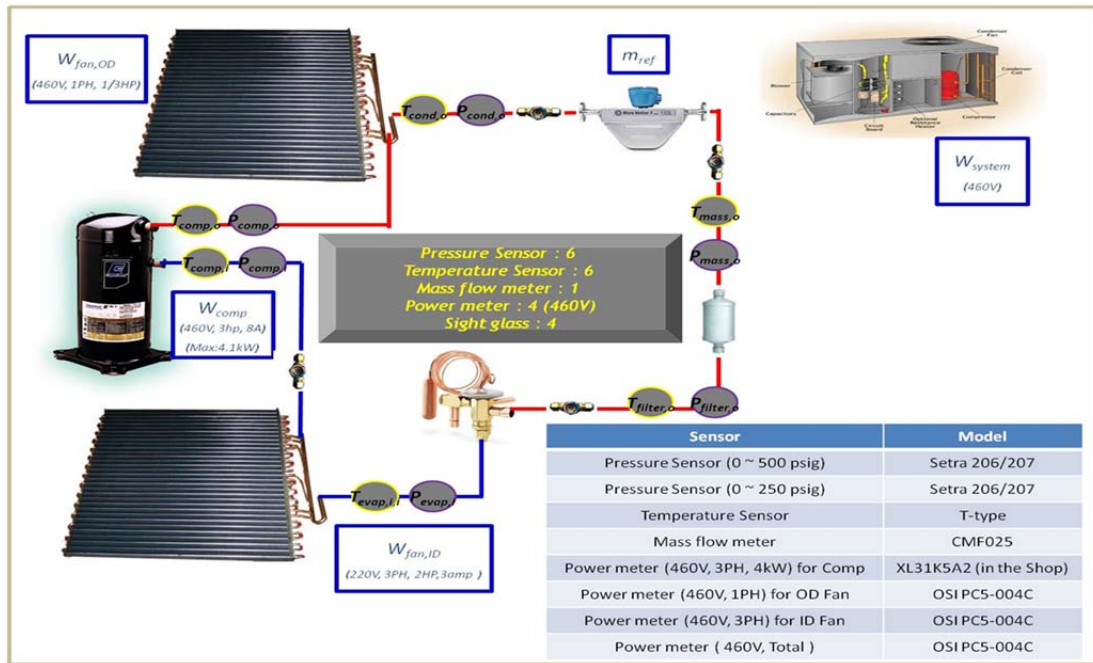


Figure 3.55 Schematic of RTU system

3.4.2. Virtual sensor (refrigerant charge, refrigerant mass flow rate, and air flow rate) assessments for RTU

Laboratory tests were performed on the RTU system to develop an initial FDD demonstration for refrigerant and air-side faults, including faulty economizer operation, heat exchanger fouling, and faulty refrigerant charge. Data collected from these test have been used to build models and virtual sensors that will increase the sensitivity, robustness, and fault diagnostic capability of the tools.

A number of virtual sensors (VRC, VRMF, and VAF sensors) were developed using the RTU test data. The accuracy of the virtual sensors was evaluated for all of test data in terms of the RMS deviation from the actual measurements presented on a percentage basis.

Figure 3.56 shows the performance of the VRC sensor based on model 1 with tuned parameters. The regression techniques for tuning the parameters were applied to data points collected at the rated test condition over a range of refrigerant charge levels. Overall, the RMS errors of the VRC sensor for model 1 were 7%. However, there were some points where refrigerant charge estimates deviated from the actual charge when under evaporator fouling faults.

Figure 3.57 shows performance of the VRC sensor based on model 3 with tuned parameters. The RMS errors were reduced to 4% using this model. The results verified that accuracy is improved using model 3 under normal and faulty conditions. Overall, the VRC sensor provided charge predictions that were within 10% of the actual charge and were typically within 5%. Based on the data analyzed in this study, it appears that undercharging a unit by 10% would result in less than a 5% impact on efficiency and overcharging by 10% would have a minimal impact. Therefore a VRC accuracy of 5 to 10% is acceptable.

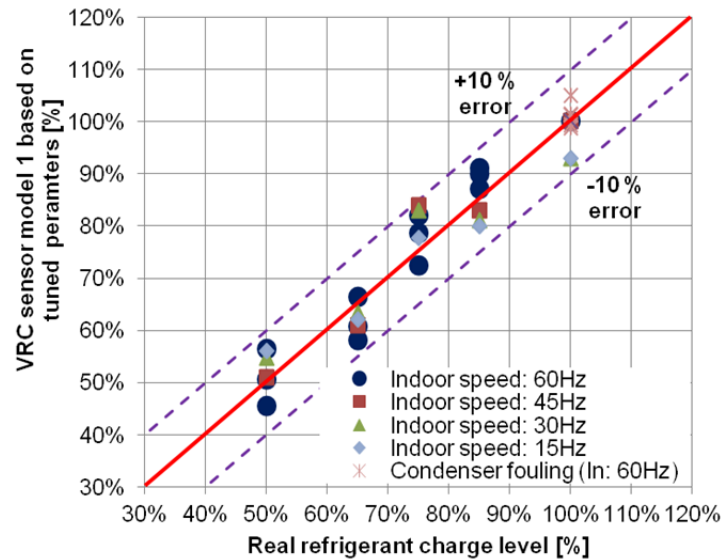


Figure 3.56 Performance of VRC sensor model 1 based on tuned parameters for RTU system.

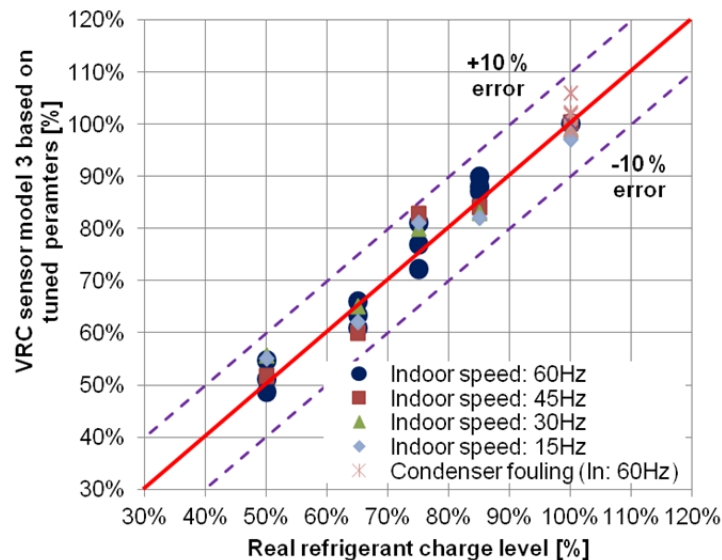


Figure 3.57 Performance of VRC sensor model 3 based on tuned parameters for RTU system.

Figure 3.58 shows condenser air flow rate estimated from the VAF sensor for the RTU unit with normal and faulty conditions. Predicted air flow rate based on the VAF sensor can be compared to a target air flow rate to detect fouling. The target flow can be obtained from a manufacturer’s catalog or from a normal value when the FDD scheme is implemented assuming that there is no fouling. Overall, the VAF sensor predicted the target condenser air flow rate within 10 % except under condenser fouling fault conditions. As the severity of the condenser fouling increases, the estimated air flow rate is

decreased. Condenser air flow rate reduction is an independent feature for diagnosing condenser fouling or fan problems.

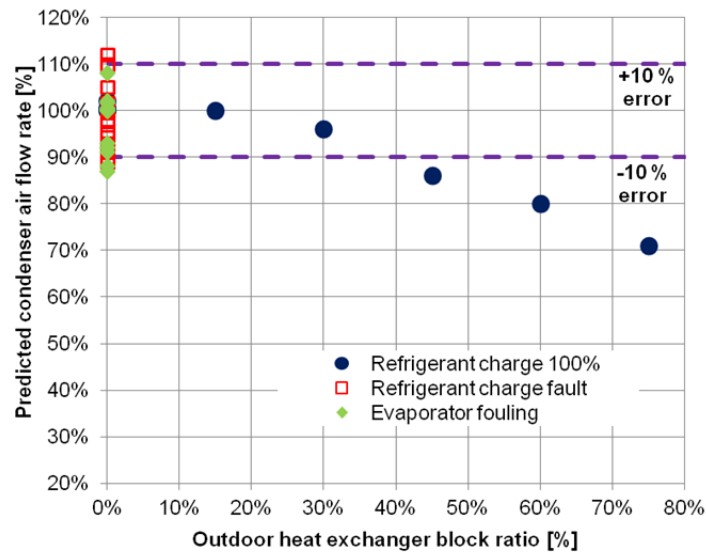


Figure 3.58 Predicted condenser air flow from an energy balance versus expected value.

Figure 3.59 shows the accuracy of the air flow prediction from an energy balance with normal and faulty refrigerant charge. The indoor unit typically has more than one speed setting, but the air flow is constant for a given setting. Therefore, the VAF sensor can be used to estimate the air flow rate for each fan setting and compared with a target air flow rate. The VAF sensor for the evaporator predicted the target air flow rate based on the fan setting within 10%. The VAF sensor based on an energy balance model has the limitation of not being valid when subcooling at the outlet of the condenser is zero. However, zero subcooling is typically associated with low refrigerant charge, which can be diagnosed using the VRC sensor.

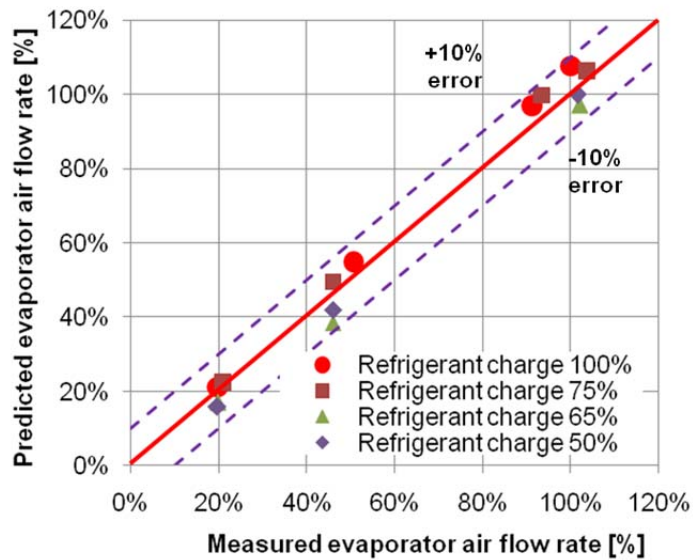


Figure 3.59 Predicted evaporator air flow from an energy balance versus expected value based on fan setting.

The virtual compressor power (VCP) sensor is used to estimate compressor input power using input measurements of inlet and outlet pressure. The VCP sensor was trained based on normal and faulty operation data. Figure 3.60 shows performance of the VCP sensor under normal and faulty conditions. The RMS error of estimated input power consumption was less than 5% over a wide range of conditions. Overall, the VCP sensor provides accurate estimates for both no fault and faulty conditions.

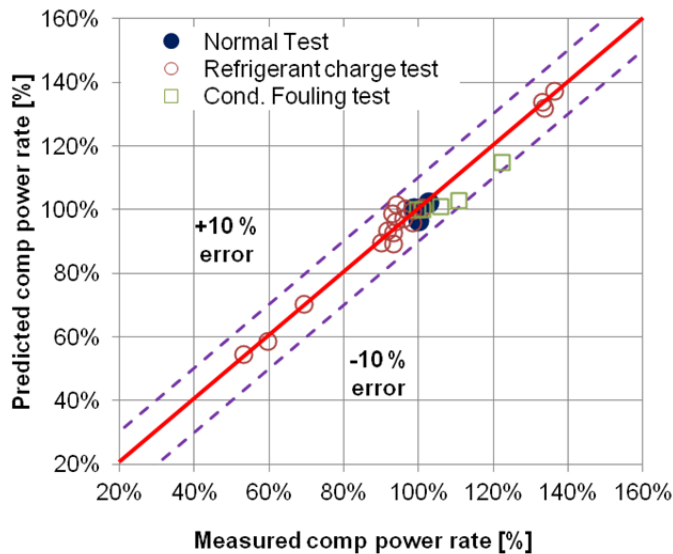


Figure 3.60 Performance of VCP sensor under no fault and fault conditions

Figure 3.61 shows comparisons of the three VRMF sensors with mass flow measurements. The performance of the VRMF sensors is very good over a wide range of mass flow rates and test conditions both with and without faults. The three VRMF sensors work well in estimating the refrigerant mass flow rate with less than a 10% RMS error. There were some significant errors of over 10% for low refrigerant charge levels with zero subcooling (TXV model) and high refrigerant charge levels with zero superheat (energy balance model).

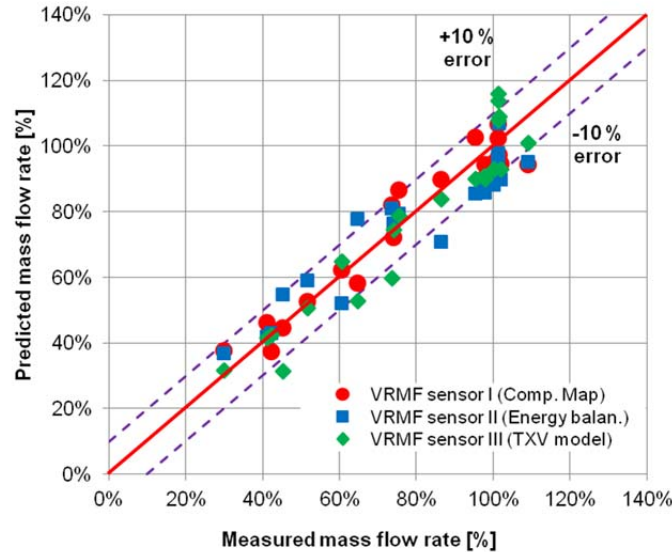


Figure 3.61 Comparison of three VRMF sensor outputs for RTU unit

3.4.3. Structure for a Diagnostic Decision System based on Virtual Sensors

The primary objective of this section is to present a structure for a diagnostic decision support system for RTU air conditioners. The proposed FDD system is based on the use of virtual sensors as depicted in the block diagram of Figure 3.62. The FDD method is broken down into four steps: preprocessor, fault detection, fault diagnosis, and decision.

In the preprocessor block, transient input and output measurements are filtered out using a steady state detector. Once measurements are collected, a fault detection step is used to determine if a fault has occurred. The FDD detection uses three types of virtual sensors; sensor level, component level, and system level. The outputs of the virtual sensors are processed by a fault classifier which compares outputs from the virtual sensors to expected values associated with normal behavior to evaluate whether a fault is present. The fault diagnosis block determines the cause of the fault from a list of possibilities. Once the existence of fault has been detected and identified, a decision block recommends the proper maintenance needed based upon economic considerations.

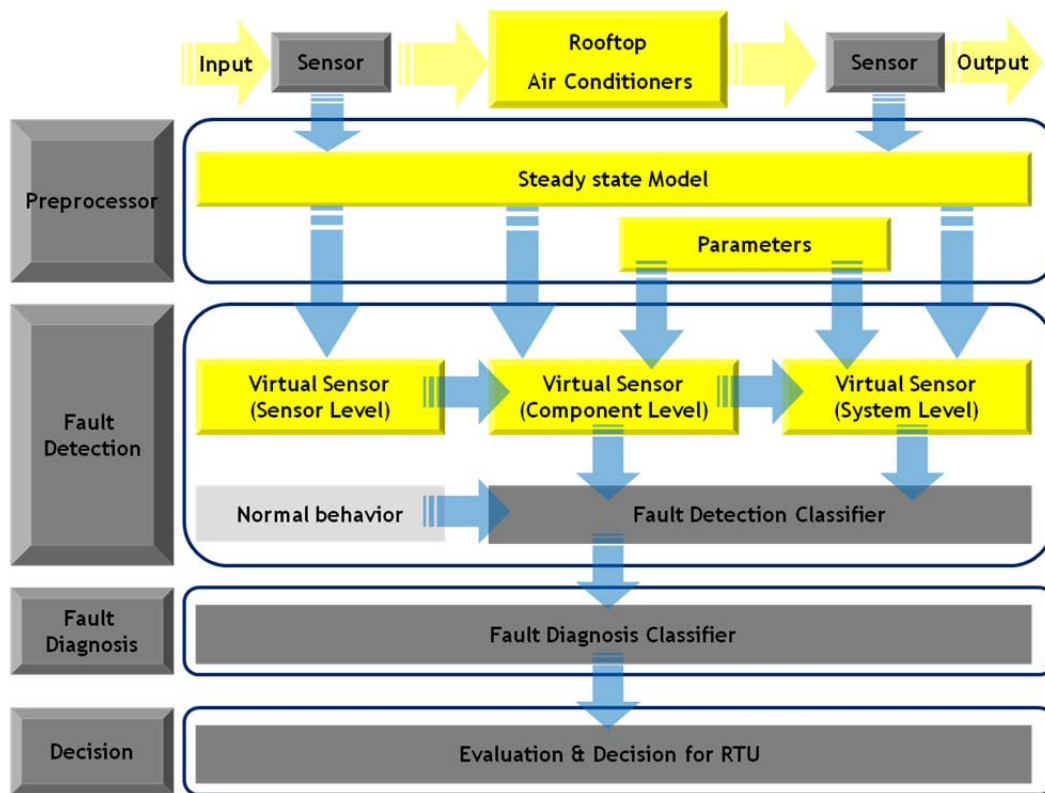


Figure 3.62 FDD block diagram for RTUs

The virtual sensors can be divided into three classes: sensor-level, component-level, and system-level as depicted in Figure 3.63. The sensor level provides virtual sensors that replace real measurements (e.g., refrigerant pressure) using lower cost measurements (refrigerant saturation temperature) and correlations that do not depend on component performance (e.g., refrigerant property correlations). The component level sensors utilize component models (e.g., compressor maps) and low cost measurements to determine quantities (e.g., refrigerant mass flow rate) that can be used for fault detection and diagnosis and as inputs to evaluate fault impacts. In order to be useful for isolating fault sources, these component level virtual sensors should provide outputs that are only influenced by individual faults within that component (e.g., compressor mass flow and valve leakage). System level virtual sensors provide outputs for quantities that could not be determined solely using component level information, including overall refrigerant charge, cooling or heating capacity, and COP.

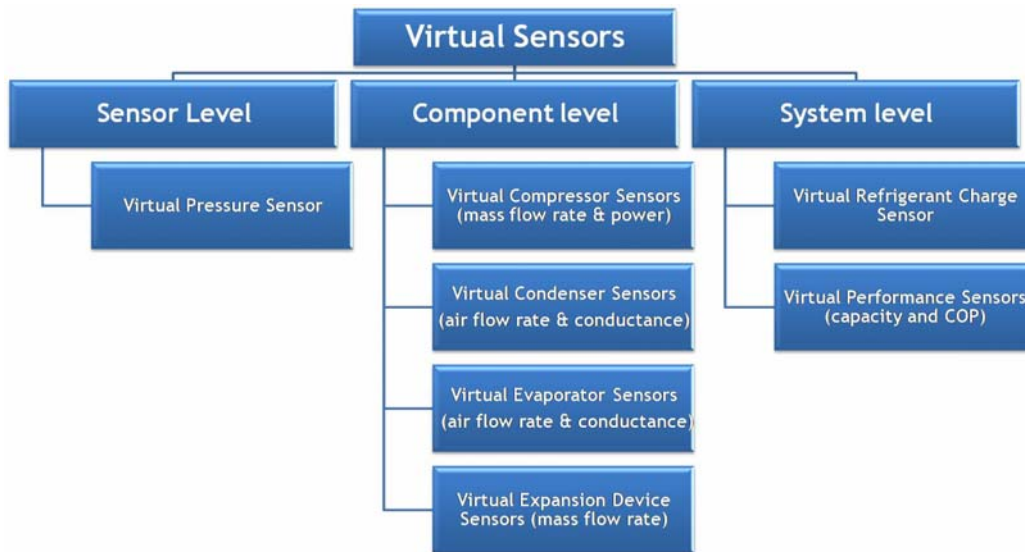


Figure 3.63 Virtual sensor classifications for air conditioner

Widespread application of virtual sensors in air conditioning equipment would require an integrated, on-line performance monitoring and diagnostic system. To achieve an integrated system, the virtual sensors should have linkages with shared outputs and inputs, and provide real-time information about capacity, power consumption, and energy efficiency for assessing economic impact. Figure 3.64 shows an example of inter-relationships between real and virtual sensors within an integrated FDD system for air conditioning equipment. Sensor-level virtual pressure sensors estimate condensing and evaporating pressures using saturation temperature measurements and property relations. A component level virtual sensor for refrigerant flow rate uses the outputs of the virtual pressure sensors and a component model. The output of the derived virtual refrigerant flow sensor is used for input to a system level sensor (virtual performance sensor) to calculate COP or EER.

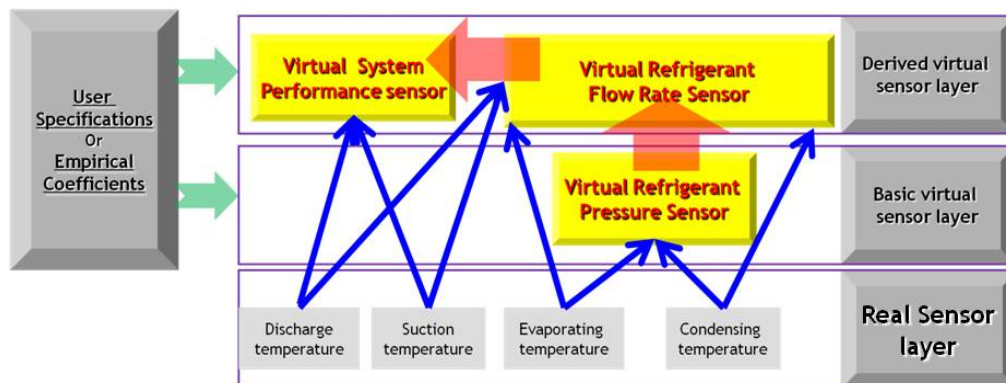


Figure 3.64 Example of virtual sensor interactions for air conditioning equipment

3.4.3.1. Steady state detector for preprocessor

A steady-state detector is used to filter out transient data, since the virtual sensors are based on steady-state operating conditions. A combined slope and variance steady-state detection algorithm (Li and Braun, 2003) is used. This algorithm uses a fixed-length sliding window of recent measurements to compute the slope (k) of the best-fit line shown in Equation 3-14 and standard deviation about the mean shown in equation (3- 15). If both the slope and standard deviation for the sliding window are smaller than corresponding thresholds, the system is assumed to be in a quasi-steady condition. The sliding window is specified by the number (n) of data points ($y_m, y_{m+1} \dots y_{m+n-1}$) and sampling time (τ).

A small threshold leads to more stable states, but less input data for FDD. On the other hand, large thresholds increase the uncertainty of the FDD outputs. Therefore, it is necessary to find thresholds that minimize the uncertainty of the FDD system while maximizing the use of input data.

$$y_i = a + k(i - m)\tau, \quad i = m, m + 1, \dots, m + n - 1 \quad (3- 14)$$

$$S = \sqrt{\frac{1}{n} \sum_{i=m}^{m+n-1} (y_i - \frac{1}{n} \sum_{i=m}^{m+n-1} y_i)^2} \quad (3- 15)$$

3.4.3.2. Fault detection

Faults can be detected by comparing fault-free expected values to current values based on measurements, and analyzing their residuals. Virtual sensors provide estimates of current features that can be compared to expected values for fault-free operation. A classifier is used to determine whether the deviation between current and expected values are statistically significant. In fault detection, estimated variables representing current operation are classified as normal or faulty. The residuals between outputs from virtual sensors and expected values for normal operation are used by a fault detection classification. The fault detection classifier estimates the overlap between probability distribution of residuals for current and normal operation. The probability for abnormal operation is lower than for normal operation based on statistical analysis. In this section, a statistical rule-based (SRB) fault detection classifier proposed by Rossi and Braun (1997), and a normalized distance fault detection classifier presented by Li and Braun (2007b) are reviewed.

There are several possible statistical classifier designs for fault detection. A parametric design was chosen over a non-parametric design because it is assumed that measurement noise is caused by independent random processes that are normally distributed. A Bayes decision classifier is the best choice among the parametric classifiers. Equation (3- 16) shows the algorithm of the Bayes decision classifier, given by Fukunaga (1990).

$$(Y - M_N)^T \Sigma_N^{-1} (Y - M_N) - (Y - M_C)^T \Sigma_C^{-1} (Y - M_C) > 0 \quad (3- 16)$$

where Y is a vector of current residuals, M_N is the mean vector matrix describing the distribution of residuals without faults (normal operation), Σ_N is the covariance matrix describing the uncertainty of residuals without faults, M_C is the mean vector matrix describing the distribution of current residuals, and Σ_C is the covariance matrix describing the uncertainty of current residuals.

The average covariance matrix is determined as the weighted average of Σ_N and Σ_C according to equation (3- 16).

$$\Sigma = S\Sigma_N + (1-S)\Sigma_C \quad (3-17)$$

Equation (3-18) can be rewritten using equation (3-16) and (3-17) as

$$V = (S\Sigma_N + (1-S)\Sigma_C)^{-1} (M_C - M_N) \quad (3-18)$$

The classification error (ε) in the Bayes classifier can be calculated using residuals with normal and fault distributions for fault detection. Equation (3-16) can be rewritten as equation (3-19) using equation (3-20) from Fukunaga (1990). A fault is indicated whenever the classification error is below a threshold, which is determined based on fault-free conditions.

$$\varepsilon = P_1 \cdot \text{erfc} \left(\frac{-V^T M_N - v_o}{\sqrt{2\sigma_N^2}} \right) + P_2 \cdot \text{erfc} \left(\frac{-V^T M_C - v_o}{\sqrt{2\sigma_C^2}} \right) \quad (3-19)$$

$$v_o = P \left(\frac{(S\sigma_N^2 V^T M_C + (1-S)\sigma_C^2 V^T M_N)^{-1}}{\sigma_N^2 + (1-S)\sigma_C^2} \right) \quad (3-20)$$

where standard deviations of normal and fault conditions are $\sigma_N^2 = V^T M_N V$, and $\sigma_C^2 = V^T M_C V$.

3.4.3.3. Fault diagnosis and decision

Most of the earlier work involving FDD for air conditioning equipment has involved the use of residuals between measurements and expected values from models for state variables. Once a fault is detected, then a fault diagnostic classifier is employed to find the best match between the changes in residuals and a set of rules associated with different types of rules. One difficulty in applying this approach with a fault diagnosis classifier is in handling multiple faults that occur simultaneously because the state variables can depend on more than one fault along with the operating conditions as illustrated in Figure 3.65. An FDD method should be able to decouple these effects in order to handle multiple simultaneous faults.

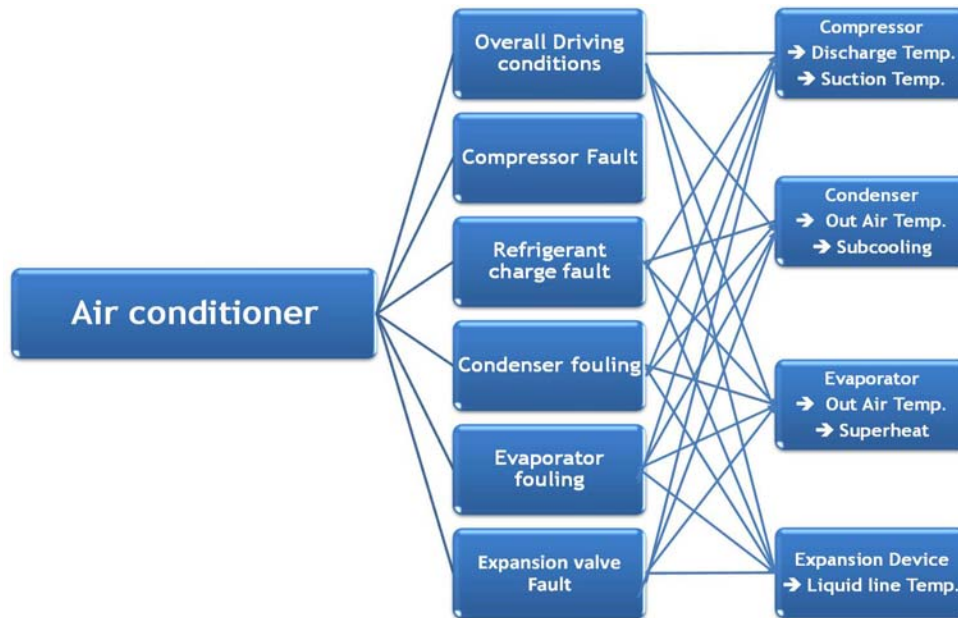


Figure 3.65 Overall fault interactions for air conditioning equipment

Li et al. (2007b) presented a decoupling FDD approach that relies on the use of virtual sensors that are uniquely dependent on individual faults and decoupled from the effects of other faults. Virtual sensors are used in place of real sensors in most cases because the measurements required for the decoupling features would be prohibitively expensive (e.g., refrigerant mass flow flow). With the decoupling approach, it is not necessary to have a separate diagnostic classifier. Fault diagnoses result directly from identifying when decoupled features deviate significantly from expected values as determined with the fault detection classifier.

Once faults are detected and the causes of the faults are identified, proper action should follow to fix the problems, adapt the control, or flag them for continued monitoring. An assessment of the severity of the fault is essential to this decision process and virtual sensors for system performance can be used as inputs to this analysis. Future work will address the fault impact evaluation and decision step.

3.4.3.4. Fault detection and diagnosis analysis

As an example, fault detection and diagnosis based on the Bayes classifier were applied to the residuals of refrigerant mass flow rate obtained with the three VRMF sensors. A fault detection classifier is applied to each combination of residuals to identify the existence of a fault. There are two possible fault diagnoses for this example: low compressor flow due to a leaky valve or other internal fault and a faulty expansion device. If a fault is detected based on statistical evaluation of the residuals, then the fault diagnosis is accomplished by identifying the specific virtual measurement that is responsible

Data for system C-5 were used to evaluate the different fault detection classification methods and demonstrate the application of virtual sensors for fault diagnosis. For the classifier approach, the minimum classification error based on analysis of normal data was found to be $9.3E-03$. Faults were identified if the deviation was lower than the minimum threshold value. Table 3.24 shows the results of the analysis of the normal data used to determine the fault detection thresholds for the two approaches. If

thresholds were set too close to normal conditions, the FDD system would be too sensitive leading to false alarms. If thresholds were set too far from normal conditions, on the other hand, the FDD system might miss faults that potentially reduce system performance. Therefore, it is very important to define reasonable thresholds for appropriate fault detection.

Table 3.24 Calculation for threshold for Bayes classifier

Test Condition for system III			1) Compressor Map / 2) Energy balance	2) Energy balance / 3) Expansion device	1) Compressor Map / 3) Expansion device	
#	ID Temp.		OD Temp.[C]	Classification Error (ϵ)	Classification Error (ϵ)	Classification Error (ϵ)
	DB [C]	WB [C]				
1	20	15	29	7.84E-02*	9.30E-03*	1.26E-02*
2	27	19		2.07E-02	3.41E-02	1.49E-02
3	20	15	35	6.06E-02	4.92E-02	2.99E-02
4	27	19		7.79E-02	5.02E-02	3.51E-02
5	20	15	40	2.91E-02	3.13E-02	1.55E-02
6	27	19		4.68E-02	3.13E-02	1.85E-02

Table 3.25 shows outputs from the Bayes fault detection classifier for a compressor valve leakage fault. The classification errors for residuals involving the compressor map were less than the threshold and indicating faults for most of the faulty cases. However, residuals for the energy balance and expansion valve sensors were greater than the thresholds with no fault indications. Based on the results, low compressor flow could be diagnosed as a fault. Although there were four points that were missed, they were all at low fault levels having relatively low impacts.

Table 3.25 FDD response to compressor valve leakage based on Bayes classifier

Test	Fault Level [%]	1) Compressor Map / 2) Energy balance		1) Compressor Map / 3) Expansion device		2) Energy Balance / 3) Expansion device	
		Classification Error (ϵ)	Diagnosis	Classification Error (ϵ)	Diagnosis	Classification Error (ϵ)	Diagnosis
3	2.50	1.31E-02	No Fault	4.67E-02	No Fault	3.13E-02	No Fault
	5.00	2.04E-04	Fault	1.02E-02	No Fault	3.44E-02	No Fault
	9.30	0.00E+00	Fault	1.63E-05	Fault	3.51E-02	No Fault
	11.40	0.00E+00	Fault	5.64E-08	Fault	3.49E-02	No Fault
4	4.00	6.80E-05	Fault	1.51E-04	Fault	2.61E-02	No Fault
	6.70	0.00E+00	Fault	3.25E-08	Fault	2.91E-02	No Fault
	9.50	0.00E+00	Fault	0.00E+00	Fault	3.21E-02	No Fault
	27.20	0.00E+00	Fault	0.00E+00	Fault	3.50E-02	No Fault
	38.20	0.00E+00	Fault	0.00E+00	Fault	2.91E-02	No Fault

Table 3.26 shows outputs from the Bayes classifier under low refrigerant charge, condenser fouling, and liquid line restriction faults. All values were higher than the threshold, and thus no refrigerant flow faults were detected. The results suggest that this method correctly decouples refrigerant flow faults from other faults in the system.

Table 3.26 FDD responses to 1) low refrigerant charge, 2) condenser fouling, and 3) liquid line restriction faults based on Bayes classifier

Test	Fault Level	1) Compressor Map / 2) Energy balance	1) Compressor Map / 3) Expansion device	2) Energy Balance / 3) Expansion device
------	-------------	--	--	--

	[%]	Classification Error (ϵ)	Diagnosis	Classification Error (ϵ)	Diagnosis	Classification Error (ϵ)	Diagnosis
5	Refrigerant Charge fault						
	-10.00	8.50E-02	No Fault	3.04E-02	No Fault	2.61E-02	No Fault
	-20.00	1.48E-02	No Fault	3.08E-02	No Fault	1.22E-02	No Fault
	-30.00	5.69E-03	No Fault	4.42E-02	No Fault	1.45E-02	No Fault
	Condenser fouling fault						
	5.00	5.95E-02	No Fault	3.85E-02	No Fault	3.46E-02	No Fault
	10.00	6.17E-02	No Fault	5.02E-02	No Fault	3.47E-02	No Fault
	20.00	1.48E-02	No Fault	5.08E-02	No Fault	2.90E-02	No Fault
	35.00	8.01E-03	No Fault	4.61E-02	No Fault	3.00E-02	No Fault
	50.00	4.34E-02	No Fault	5.05E-02	No Fault	2.86E-02	No Fault
	Liquid line restriction fault						
	5.30	5.73E-02	No Fault	5.19E-02	No Fault	3.30E-02	No Fault
	10.40	7.55E-02	No Fault	4.92E-02	No Fault	3.19E-02	No Fault
	20.20	7.44E-02	No Fault	4.77E-02	No Fault	3.50E-02	No Fault

3.4.4. Economizer Fault Detection and Diagnosis

3.4.4.1. Air-Side Economizer Control Strategies

To reduce energy consumption during mild outdoor conditions, economizer control strategies are implemented. The economizer control mode is enabled based on outdoor-air dry-bulb temperature (dry-bulb economizer) or a comparison between outdoor-air enthalpy and return-air enthalpy (enthalpy economizer). Most commonly, dry-bulb measurement of outdoor-air temperature is used to enable economizer control because required sensors for enthalpy controller are often not present or unreliable. Return-air relative humidity (RH) measurements are uncommon in packaged air conditioners. Concern for RH sensor maintenance and accuracy has discouraged adoption of enthalpy economizers as well (Taylor 2010). Figure 3.66 and Figure 3.67 show detailed schematics of the economizer used in the packaged air-conditioner along with the direction of the air flows when the outdoor-air damper is open and closed.

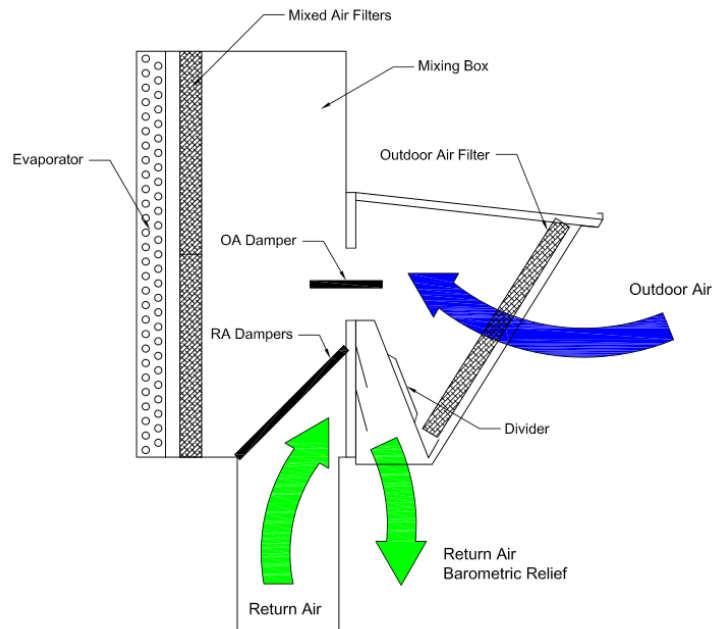


Figure 3.66 Packaged air-conditioner ventilation configuration when supplying 100% outdoor-air.

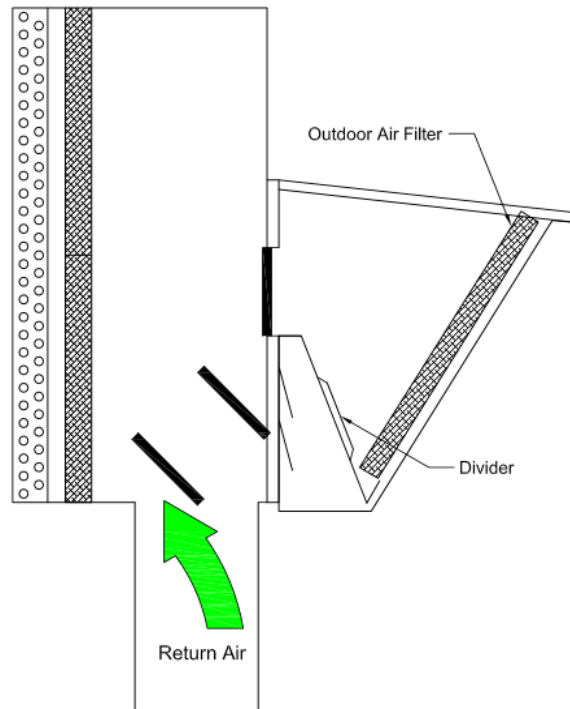


Figure 3.67 Packaged air-conditioner ventilation configuration when outdoor-air damper is fully closed

Dry-bulb economizers are enabled when the outdoor-air temperature falls below an activation or change-over temperature. The best change-over temperature is very dependent on the humidity of the climate where the economizer is installed. In humid climates with large latent loads, the change-over temperature should be significantly lower than the return-air temperature (ASHRAE 2011). In dry climates, the change-over temperature may be closer to the return-air temperature.

By decreasing the mixed-air temperature using cooler outdoor-air, the coil load can be decreased or eliminated during mild or cold weather. Figure 3.68 shows a typical control sequence for a dry-bulb economizer with increasing outdoor-air temperature.

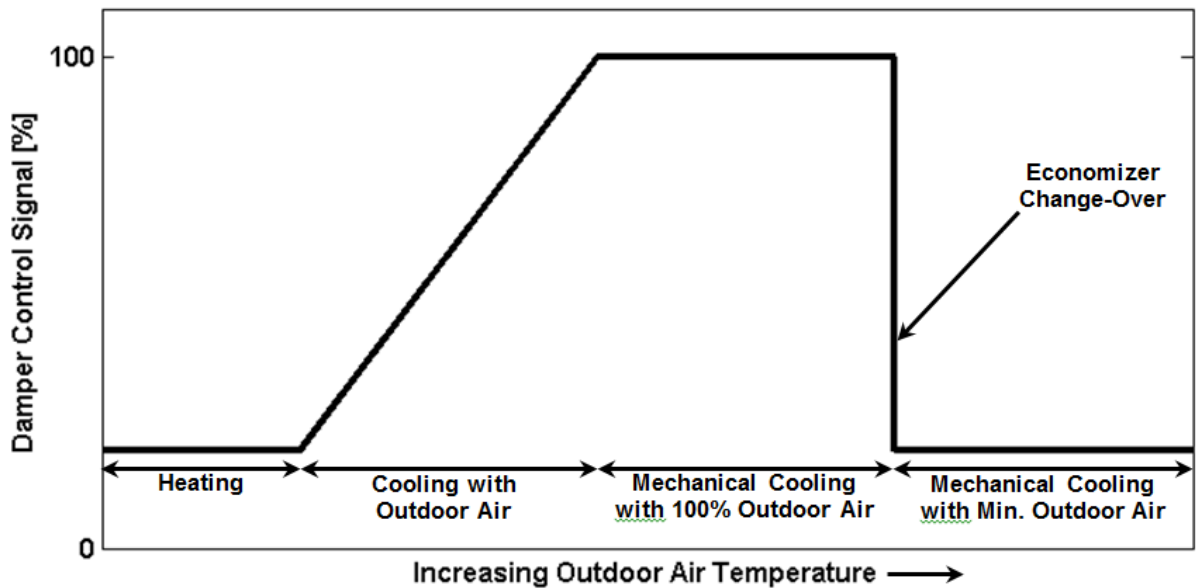


Figure 3.68 Economizer control sequence for dry-bulb economizers with increasing outdoor-air temperature

The economizer cooling sequence can be broken down into four modes or states.

Table 3.27 summarizes the position of the outdoor-air damper, compressor status, and heating coil status for each state. With a call for heating, the economizer controls the outdoor-air damper to the minimum position to minimize the amount of cold outdoor-air mixed with the return-air. Free cooling mode exists when the outdoor-air is sufficiently cool to provide the necessary cooling for the load. During this state, the compressor in the packaged air-conditioner is off and all cooling is essentially free.

Table 3.27 Economizer cooling states along with damper position, compressor status, and heating coil status for each state

State	Damper Position	Compressor	Heating Coil
1 – Heating	Minimum Outdoor-Air	Off	On
2 – Free Cooling	Controlled to maintain mixed-air set point	Off	Off
3 – Mechanical Cooling with 100% Outdoor-air	100%	On	Off
4 – Mechanical Cooling with Minimum Outdoor-air	Minimum Outdoor-air	On	Off

When the outdoor-air is sufficiently cool to provide cooling, but not enough to meet the cooling load in the space, the economizer enters State 3. During this state, the economizer controls the outdoor-air damper to the maximum position and the compressor is turned on to meet the remaining portion of the load. During this mode, cooling energy is reduced by minimizing the amount of warm return-air cooled.

During times when the outdoor-air is warmer than the change-over set point, the outdoor-air damper is controlled to the minimum outdoor-air position and the compressor is used to control the supply-air temperature. During this mode, the quantity of outdoor-air is reduced to the minimum allowed by ventilation standards.

3.4.4.2. Outdoor-Air Economizer Faults

Faults in outdoor-air economizers (OAE) generally consist of outdoor-air damper position faults, temperature sensor faults, and controller faults. Each of these faults can lead to poor performance of the OAE and may increase energy consumption over time. Typically, economizer performance is not closely monitored and careful maintenance practices are not followed. In one study, it was found that as many as 50% of all economizers installed in packaged air-conditioners will experience a fault over a fifteen year lifespan (CASE 2011).

The most import faults in terms of the effect on energy consumption in packaged air-conditioners are damper position faults. This is because of the significant increase in cooling or heating energy required when the damper is stuck open, closed, or at some intermediate position. When the damper becomes stuck due to blockage, actuator failure, or control signal disconnect, the amount of outdoor-air entering the air-conditioner is no longer controlled.

Figure 3.69 shows the effects of a stuck outdoor-air damper during a simulated summer day. The outdoor-air damper was simulated as being stuck at the 70% open position, which causes a greater amount of outdoor-air to be brought into the building than is required. Because a greater fraction of outdoor-air is brought into the air-conditioner, a large difference between faulty and normal mixed-air temperatures exists. The normal mixed-air temperature was simulated by controlling the damper to the minimum position, which was set to 15%. The difference between the faulty and normal mixed-air temperatures translates to greater cooling energy required to maintain the space temperature.

In the same way, a stuck damper can cause larger heating energy in the winter when it is stuck in an open position. The stuck damper causes colder outdoor-air to mix with the return-air, which lowers the mixed air temperature. Because the mixed-air temperature is lower, more heating energy must be used to maintain the supply-air temperature set point.

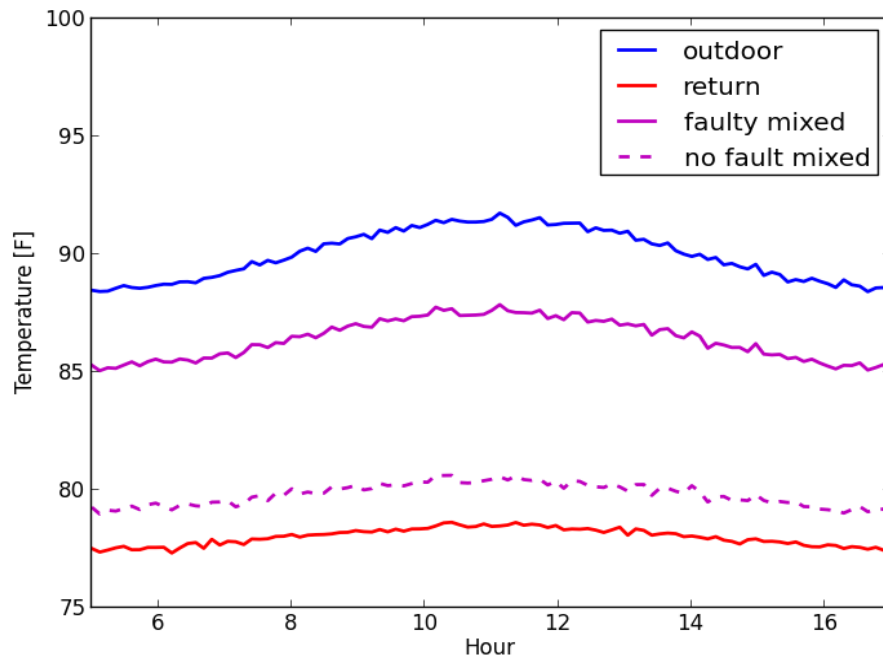


Figure 3.69 Simulated effects of a stuck open outdoor-air damper in the summer during a day.

Stuck damper faults can also increase cooling energy consumption when the damper is stuck in a closed position. In this scenario, the outdoor-air conditions could be advantageous for economizer cooling but with no possibility for operation in this mode.

Temperature sensor faults are also important in the operation of the OAE. When the outdoor-air temperature sensor is biased, it could in some cases lead to missed free cooling opportunities. This would occur if the outdoor-air temperature measurements were too high. Alternatively, if the outdoor-air temperature measurements were too low, the outdoor-air damper may be opened prematurely.

Likewise, other temperature sensor faults can lead to incorrect operating modes and damper positions. When a mixed air temperature is measured incorrectly, the damper may be controlled to allow too much or too little outdoor-air as compared with proper operation. In differential temperature controllers that monitor a difference between outdoor- and return-air conditions, errors in either sensor can lead to incorrect operation of the economizer.

3.4.4.3. Sensor Requirements

For effective dry-bulb economizer diagnostics, at least four temperature sensors are required:

- outdoor-air temperature entering air-conditioner
- return-air temperature
- mixed-air temperature in mixing box
- supply-air temperature after supply-fan.

Due to the compactness of the packaged air-conditioner, a single-point temperature sensor may provide a very inaccurate measurement air conditions across a duct. This is especially true in the case of the mixed-air temperature measurement where a very non-uniform temperature and flow pattern exists in the mixing box. Additionally, in order to gain some redundancy, the ability to compare the outdoor-air

temperature measurement to a more robust measurement from other packaged air-conditioners or via weather station data obtained online is useful for diagnostics.

The economizer damper control signal sent to the outdoor-air damper actuator is useful for effective diagnostics as a means of estimating outdoor-air fraction. The ability to override the outdoor-air damper control signal is also advantageous to perform active diagnostics.

3.4.4.4. Economizer Sensor-Correction and Estimation Models

3.4.4.4.1. OAE Performance Testing

In order to characterize the performance of the OAE, extensive testing was performed of the RTU installed at the Herrick Laboratories. These tests included running the packaged air-conditioner in economizer or fan-only mode in order to characterize how the system responds under different outdoor-air temperatures and damper positions. Outdoor-air temperature and mixed-air temperature corrections were designed using this data. Additionally, an outdoor-air fraction model was created based on outdoor-air damper position.

Table 3.28 shows the tests performed to characterize economizer performance under varying conditions. A set of psychrometric rooms were used to control the outdoor and indoor conditions. A return-air duct was connected from the indoor room to the return-air inlet of the air-conditioner installed in the outdoor room. The OAE hood was installed within the air-conditioner, which enabled it to bring in outdoor room air when the damper was controlled open. The supply-air duct was connected from the outlet of the air-conditioner to a nozzle box flow meter station. A booster fan was installed downstream of the nozzle box to maintain differential pressure between the rooms. The tests were recorded once steady-state conditions were reached and conditions were maintained for the duration of each test. During economizer testing, the compressor was disabled in order to maintain purely free-cooling mode operation.

Table 3.29 lists the air-side measurements recorded for the OAE tests.

Table 3.28 Outdoor-air economizer performance test conditions for outdoor-air temperature, indoor-air temperature, outdoor-air damper position, and supply fan speed.

Outdoor Air Temperature °C (°F)	Indoor Air Temperature °C (°F)	Outdoor-Air Damper Position (%)	Supply-Fan Speed
7.22 (45)	25.56 (78)	0, 25, 50, 75, 100	auto
12.78 (55)	25.56 (78)	0, 10, 20, 30, 40, 50, 60, 70, 80, 90, 100	auto
18.33 (65)	25.56 (78)	0, 10, 20, 30, 40, 50, 60, 70, 80, 90, 100	auto
21.11 (70)	25.56 (78)	0, 20, 40, 60, 80, 100	auto
23.89 (75)	25.56 (78)	0, 50, 100	auto
29.44 (85)	25.56 (78)	0, 20, 40, 60, 80, 100	auto
35.00 (95)	25.56 (78)	0, 10, 20, 30, 40, 50, 60, 70, 80, 90, 100	auto

Table 3.29 Outdoor-air economizer test measurements.

Measurement	Type	Configuration
Outdoor-Air Temperature, T_{oa}	T-type thermocouples	9-point measurement grid, equally-spaced inside OAE hood after outdoor-air filter
Return-Air Temperature, T_{ra}	T-type thermocouples	9-point measurement grid, equally-spaced inside return-air duct before entering mixing box
Mixed-Air Temperature, T_{ma}	T-type thermocouples	16-point measurement grid, equally-spaced after air filter in mixing box.
Supply Fan Inlet Temperature, $T_{sf,in}$	T-type thermocouples	6 thermocouples mounted near centrifugal supply fan inlet
Supply-Air Temperature, T_{sa}	T-type thermocouples	9-point measurement grid, equally-spaced inside supply-air duct after leaving air-conditioner
Outdoor-air Dew Point, $T_{dp,oa}$	Dew point hygrometer	4-point measurement grid, equally-spaced inside OAE hood after outdoor-air filter
Return-air Dew Point, $T_{dp,ra}$	Dew point hygrometer	Single-point dew point monitor located in return-air duct
Supply-air Dew Point, $T_{dp,sa}$	Dew point hygrometer	4-point measurement grid, equally-spaced inside supply-air duct at supply-fan exit
Return-Air Flow Rate,	Hot-wire anemometer	Anemometer mounted in return-air duct before entering mixing box
Supply-Air Flow Rate,	ASME nozzle box flow station	Nozzle box located downstream of air-conditioner supply
Supply-Fan Power,	Power meter	Power meter measuring supply-fan power consumption

3.4.4.4.2. Single-Point Outdoor-Air Temperature Correction Model

When performance testing the packaged air-conditioner in psychrometric rooms, the behavior of the outdoor-air temperature measurement was unexpected. When the outdoor-air damper position was changed, the outdoor-air temperature also showed some change. Because a nine-point, thermocouple grid was installed upstream of the outdoor-air damper at the outdoor-air filter, it was believed that this measurement should be independent of the damper's position since it was upstream. On closer inspection, it was realized that return-air that was exhausted through the barometric relief vents on the air-conditioner was recirculated back into the outdoor-air intake hood. This behavior is illustrated in Figure 3.70.

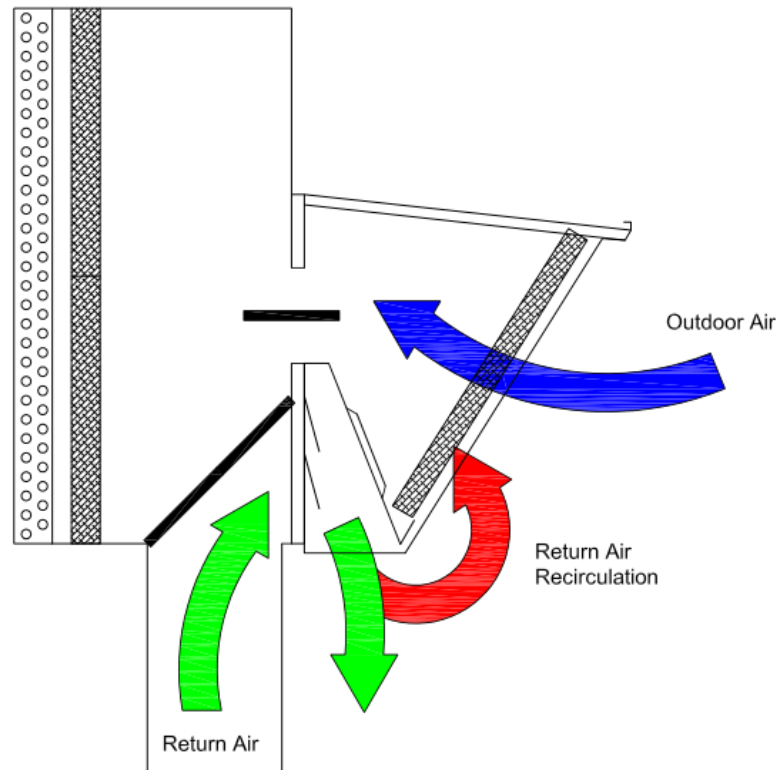


Figure 3.70 Return-air recirculation present in the packaged air-conditioner economizer hood.

In order to confirm that return-air was recirculated into the outdoor-air inlet stream, observation of individual thermocouples in the measurement grid was used as evidence. The psychrometric room where the air-conditioner was installed was held at a constant temperature near 12.5 °C (55 °F) and the return-air temperature was held at a constant 25.8 °C (78 °F) during one test. As the damper was opened during this test, the average outdoor-air temperature increased. More specifically, the thermocouples near the bottom of the filter, near the barometric relief exhaust outlet, became warmer by as much as 6 °C as the damper opened. This behavior is shown in Figure 3.71.

In order to isolate that the warm temperatures were caused by recirculation air, the barometric relief vents were forced closed with aluminum tape. This ensured that no return-air could mix with the outdoor-air in the economizer hood. The results, shown in Figure 3.72 indicate that warmer temperatures were caused by the exhaust air reentering the air-conditioner, since a uniform temperature was observed when the exhaust vents were forced closed.

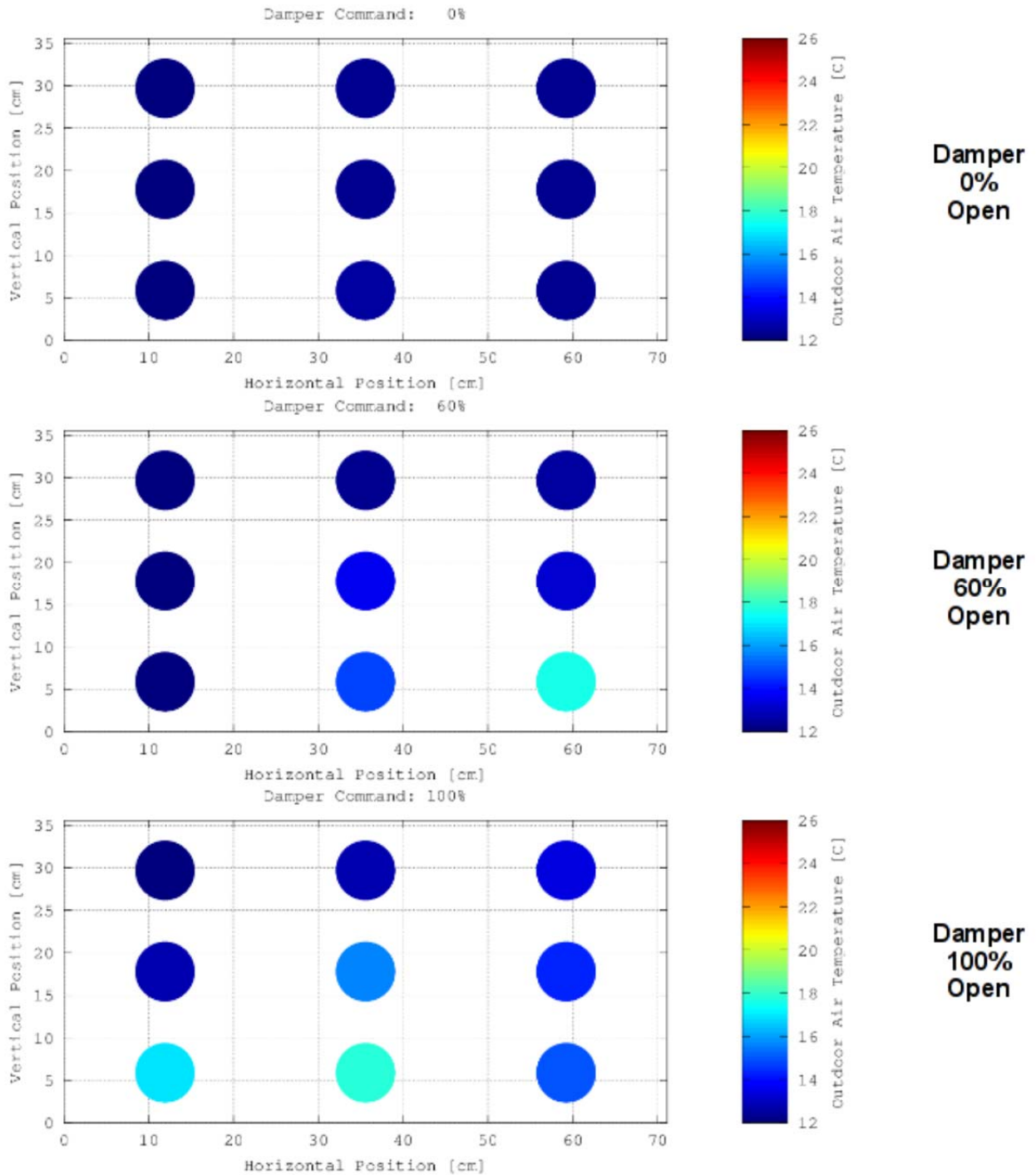


Figure 3.71 Outdoor-air temperature grid for three different damper positions. Temperature measurements at the bottom of the grid are warmer than the rest of the thermocouples due to return-air recirculation.

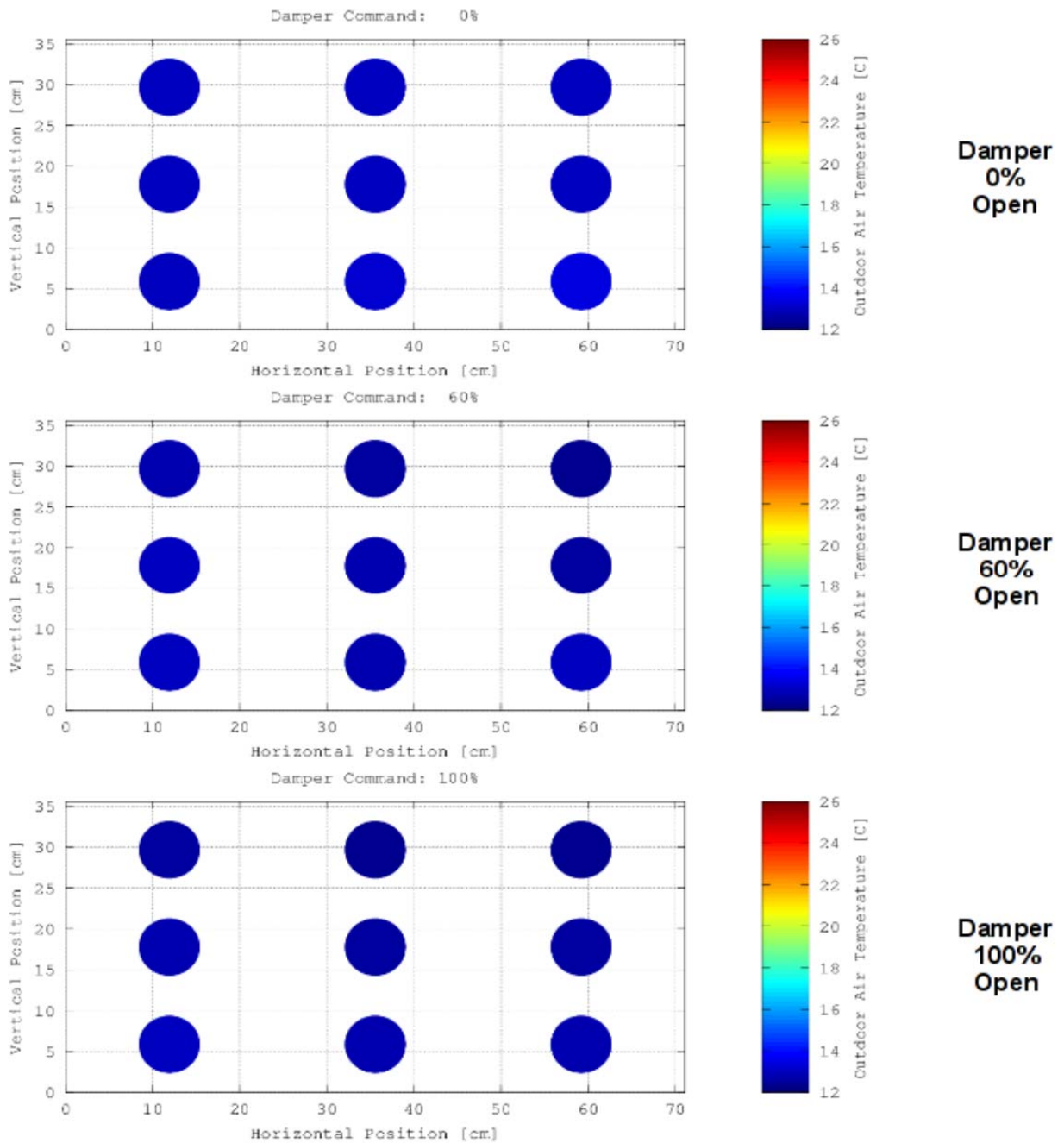


Figure 3.72 Outdoor-air temperature grid for three different damper positions when barometric relief vents were forced closed.

It is important to note that this is a problem in the design of the economizer hood and that the OAE FDD is not a solution for this. Because return-air recirculates into the packaged air-conditioner, the effectiveness of the economizer is decreased since it is unable to provide 100% outdoor-air. The air-

conditioner still benefits from the economizer since the recirculation air comprises only a fraction of what enters.

When the return-air is recirculated into air-conditioner, the temperature distribution in the economizer hood is non-uniform. Because of this non-uniformity, the outdoor-air measurement becomes inaccurate when a single-point measurement is used. Depending on the placement of the thermocouple, the inaccuracy can become significant. Additionally, estimating outdoor-air fraction using temperature measurements requires accurate measurements. At the same time, in order to keep costs low, a single-point temperature measurement is attractive to manufacturers.

To balance cost and outdoor-air temperature sensor accuracy, a correction model was made that allows use of a single-point sensor. Since an accurate temperature of the outdoor-air entering the economizer hood was required for training, the mean value of the nine-point thermocouple grid was used. In order to account for return-air that may be recirculated into the hood, a return-air measurement and the outdoor-air damper control signal were used to build a model. The functional form of the corrected, single-point outdoor-air temperature, $T_{oa,corr}$, is shown in equation (3- 21).

$$T_{oa,corr} = c_0 + c_1 T_{oa,meas} + c_2 T_{ra,meas} + c_3 OAD_{cmd} \quad (3- 21)$$

where $T_{oa,meas}$ is the single-point outdoor-air temperature measurement, $T_{ra,meas}$ is the single-point return-air temperature measurement, OAD_{cmd} is the outdoor-air damper control signal, and

$$c_0 = -4.833412 \text{ } ^\circ\text{C}$$

$$c_1 = 1.000976 \text{ [-]}$$

$$c_2 = 0.187833 \text{ [-]}$$

$$c_3 = -0.144251 \text{ } ^\circ\text{C}$$

The model regression was performed using the thermocouple at the center of the measurement grid as the single-point sensor. This thermocouple was chosen because its placement gave the best estimate of the average outdoor air temperature before correction. A comparison between the corrected outdoor-air temperature as a function of the actual outdoor-air temperature is plotted in Figure 3.73. The correction model showed good accuracy with a maximum error of $\pm 1.0 \text{ } ^\circ\text{C}$.

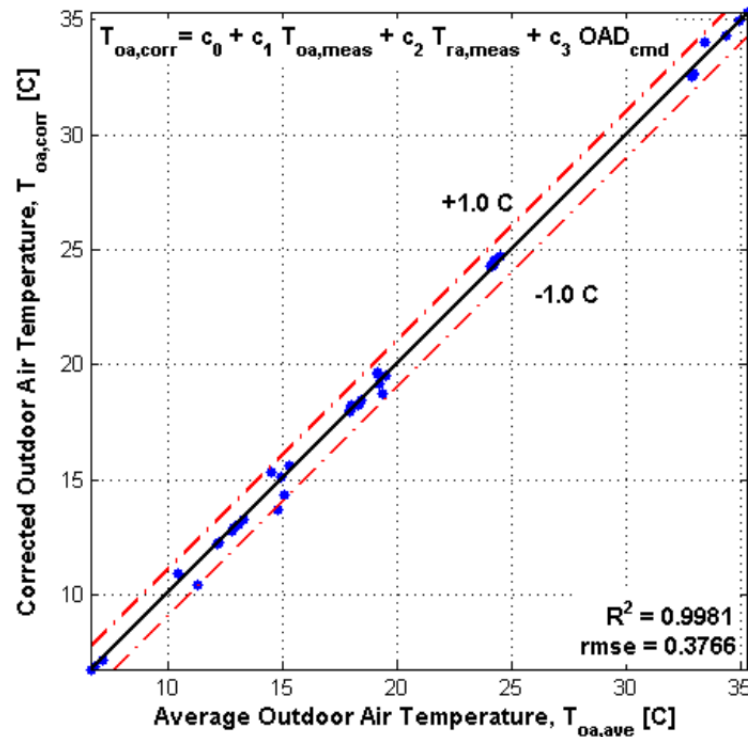


Figure 3.73 Corrected single-point outdoor-air temperature model fit.

3.4.4.4.3. Single-Point Outdoor-Air Temperature Correction Model

Mixed-air temperature is an important measurement for estimating outdoor-air fraction, $OAF_{est,ma}$, based on an energy balance on the mixing box (Friedman 2001):

$$OAF_{est,ma} = \frac{T_{ma} - T_{ra}}{T_{oa} - T_{ra}} \quad (3-22)$$

Since the return-air stream is generally well-mixed at its measurement location a single-point temperature measurement is sufficient. Outdoor-air temperature can be reliably estimated using the correction-model previously mentioned. However, a robust mixed air-temperature measurement is needed to realize accurate outdoor-air fraction estimates.

The small size of the mixing chamber in an RTU can lead to very non-uniform conditions and make it very difficult to measure mixed-air temperature accurately. In Figure 3.74, the mixed-air temperature measured at sixteen locations before entering the evaporator is shown. The damper was held at 60% open during the test. The color scale in the figure ranges from the outdoor-air temperature (blue) to the return-air temperature (red). Clearly, a large non-uniform temperature distribution exists within the mixing box.

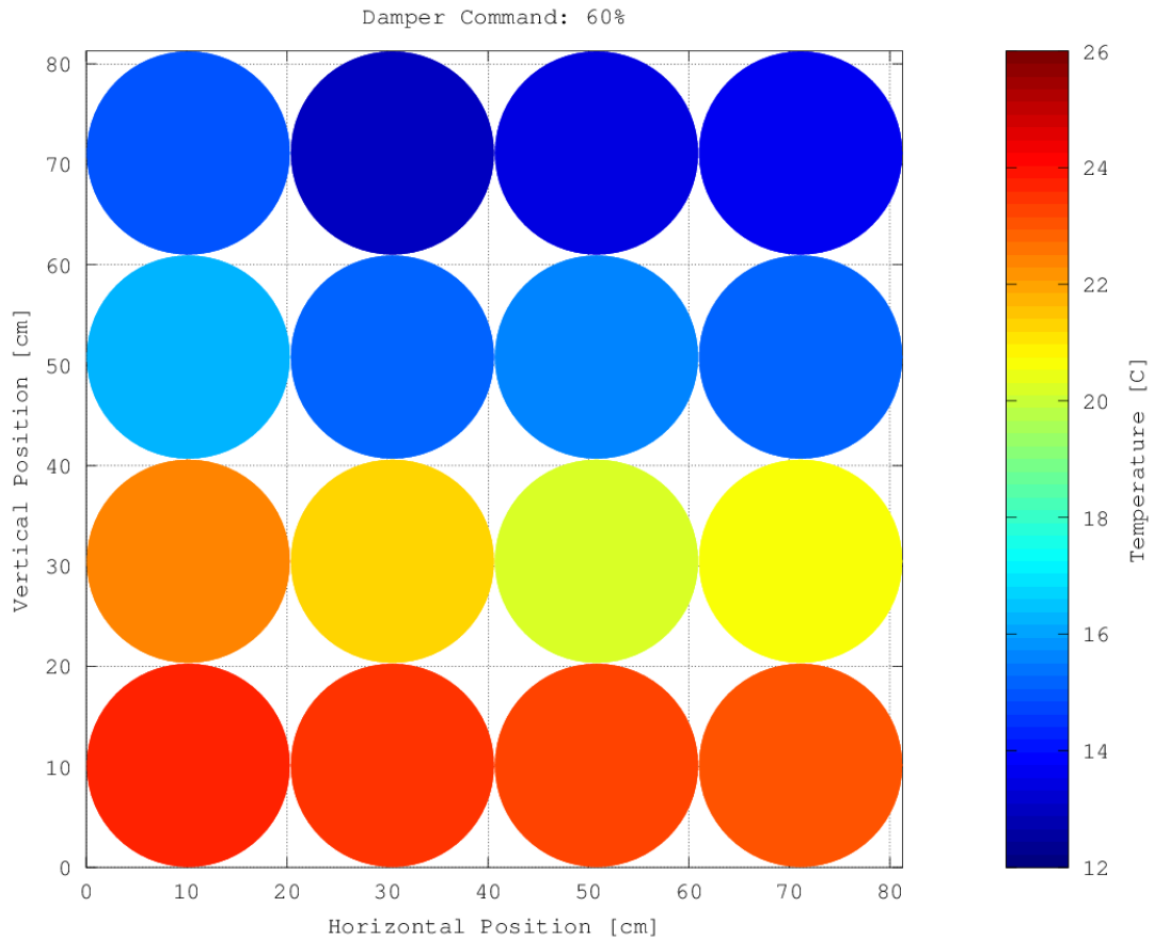


Figure 3.74 Non-uniform mixed-air temperature distribution at the evaporator inlet position with the outdoor-air damper 60% open. The color scale ranges from outdoor-air temperature (blue) to return-air temperature (red)

There are two possible solutions to overcome this problem. The first is to use a measurement grid inside the mixing box to calculate an average temperature, which could be used as an estimate. However, this solution increases the instrumentation cost of FDD. Additionally, a simple average assumes that the mass flow rate of air at each measurement location is the same. Due to the small geometry of the mixing box, and the locations and directions of the entering outdoor-air and return-air streams, this is a poor assumption.

A better solution is to perform a correction to a single-point mixed-air temperature sensor. This keeps the mixed-air temperature measurement costs low and accounts for non-uniform temperature and flow across the evaporator. In order to build a correction model, a robust measurement of the mixed-air temperature is required for a range of outdoor-air temperatures and damper positions. Unlike the outdoor-air temperature, a simple average is not sufficient because of non-uniform velocities so another measurement must be used. For this purpose, the supply-air temperature is used when the compressor is off to train the mixed air correction factor.

When the compressor is off, the refrigerant circuit provides no cooling effect in the evaporator. Therefore, the supply-air and mixed-air temperatures should be nearly equal. The only difference between these temperatures is the temperature rise caused by the supply fan. Therefore, by characterizing the supply fan temperature rise, the supply-air temperature can be used to build the mixed-air temperature correction model. An added advantage of using this measurement is that the air-stream is well-mixed since it passes through the supply fan.

The supply fan temperature rise, ΔT_{sf} , can be calculated using an energy balance between the inlet and

outlet of the fan, given by equation

$$\Delta T_{sf} = \frac{\dot{W}_{sf}}{\dot{m}_{sa} c_p} \quad (3-23).$$

$$\Delta T_{sf} = \frac{\dot{W}_{sf}}{\dot{m}_{sa} c_p} \quad (3-23)$$

where \dot{W}_{sf} is the supply fan power transferred to the airstream, \dot{m}_{sa} is the mass flow rate of air, and c_p is the specific heat of air. In order to account for the dependence of supply fan speed on the supply fan power, the following form was used to predict the supply fan temperature rise,

$$\Delta T_{sf, pred} = c_0 + c_1 \left(\frac{\dot{W}_{sf}}{\dot{m}_{sa} c_p} \right) + c_2 \left(\frac{\dot{W}_{sf}}{\dot{m}_{sa} c_p} \right)^2 \quad (3-24)$$

where \dot{W}_{sf} was measured using a power meter, \dot{m}_{sa} was measured using a nozzle box and c_i are regression coefficients. The regression was performed on test data whose outdoor-air and return-air temperatures were the same. This ensured that the non-uniform temperature distribution would have no impact on the average mixed-air temperature measurement. The coefficients determined using the test data were

$$\begin{aligned} c_0 &= 0.306040 \text{ }^\circ\text{C} \\ c_1 &= 0.306040 \text{ }^\circ\text{C} \cdot \text{kg} / \text{kJ} \\ c_2 &= 0.306040 \text{ }^\circ\text{C} \cdot \text{kg}^2 / \text{kJ}^2 \end{aligned}$$

The results of the supply fan temperature predicted by the model are plotted against the actual measured values in Figure 3.75. The model showed good behavior with a maximum prediction error of less than ± 0.05 $^\circ\text{C}$.

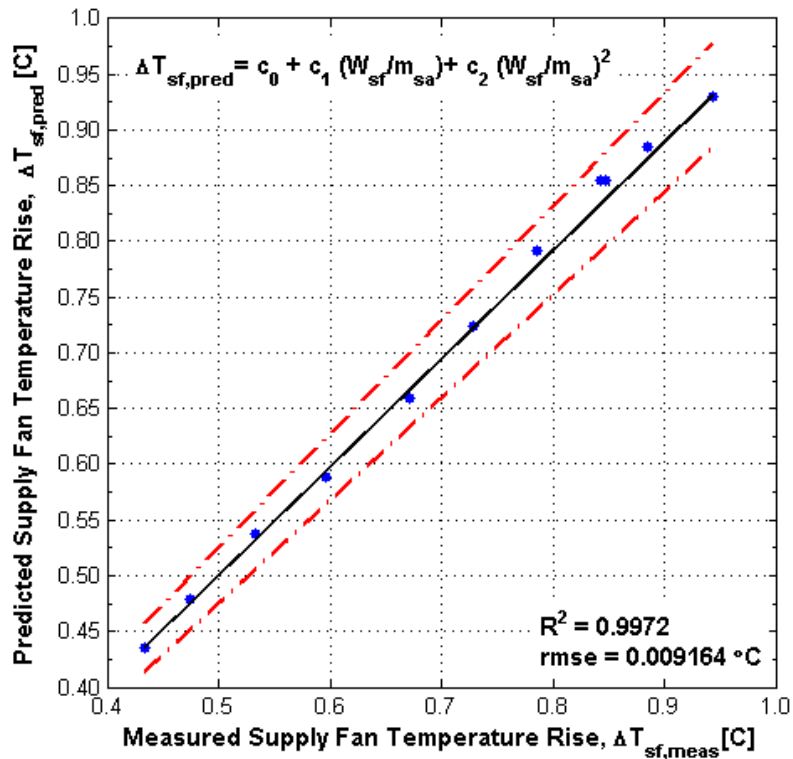


Figure 3.75 Predicted supply fan temperature rise model results

Using the predicted supply fan temperature rise, a more robust mixed-air temperature estimate was used, given by equation (3- 25).

$$T_{ma,rob} = T_{sa,meas} - \Delta T_{sf,pred} \quad (3- 25)$$

To correct the mixed-air temperature, a simple model was formed to account for the outdoor-air damper influence and the difference between outdoor- and return-air temperatures. Equation (3- 26) gives the form of the corrected single-point mixed-air temperature, $T_{ma,corr}$, regression equation,

$$T_{ma,corr} = c_0 + c_1 T_{ma,meas} + c_2 (T_{oa,corr} - T_{ra,meas}) OAD_{cmd} \quad (3- 26)$$

where $T_{ma,meas}$ is the uncorrected, single-point mixed-air temperature measurement and c_i are regression coefficients. Using data collected from the OAE tests, the mixed-air temperature correction model was fitted. The resulting regression coefficients are shown below.

$$c_0 = 10.398035 \text{ } ^\circ\text{C}$$

$$c_1 = 0.589726 \text{ [-]}$$

$$c_2 = 0.252398 \text{ [-]}$$

The results of the mixed-air temperature correction model are plotted against the robust mixed-air temperature measurement in Figure 3.76. The data plotted included the range of temperatures and damper

positions detailed in the OAE testing section. Also plotted are the uncorrected single-point mixed-air temperature measurements in order to show the improvement made by the model.

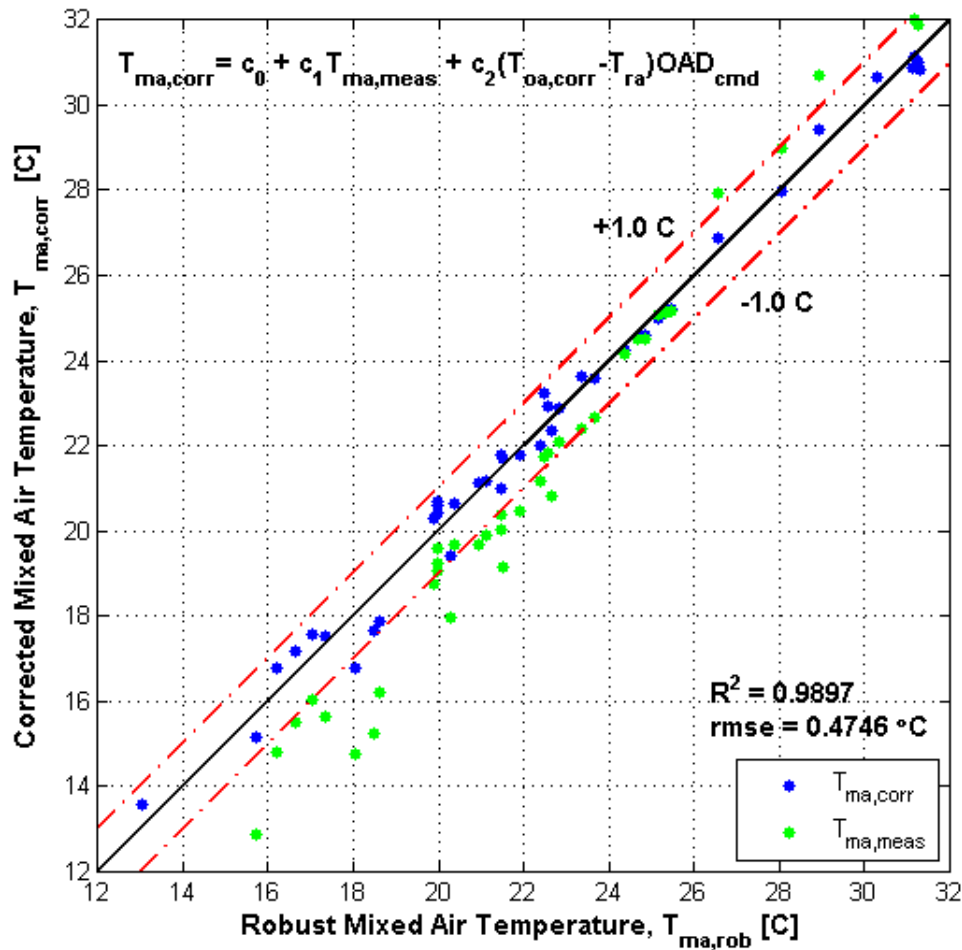


Figure 3.76 Corrected single-point mixed-air temperature model fit.

3.4.4.4. Outdoor-Air Fraction Estimation Model

Outdoor-air fraction is a critical metric for OAE fault detection because it is an indicator of damper position and temperature sensor faults. Outdoor-air fraction (OAF) is defined as the amount of outdoor-air brought into the building as a fraction of the total supply-air used to maintain the space temperature, given by equation (3-27),

$$OAF = \frac{\dot{m}_{oa}}{\dot{m}_{sa}} \quad (3-27)$$

where \dot{m}_{oa} is the outdoor-air mass flow and \dot{m}_{sa} is the supply-air mass flow rate. Since a mass air-flow rate is never measured in packaged-air conditioners, an alternative estimate must be used. Typically, the estimation proposed by Friedman and Piette (2001) is used as the estimate, given in equation

(3- 22). This estimate is acceptable when an accurate mixed-air temperature measurement is present. If this is not the case, an alternative OAF estimation that relies on supply-air temperature must be used, given by equation (3- 28).

$$OAF_{est,sa} = \frac{T_{sa} - \Delta T_{sf} - T_{ra}}{T_{oa} - T_{ra}} \quad (3- 28)$$

This estimation is only valid when the compressor is off, since $T_{sa} \approx T_{ma}$ in this case. OAF estimates that use outdoor-air and return-air temperatures are not valid when these two temperatures are equal or almost equal. For this reason, these estimations are only performed when the difference between outdoor- and return-air temperatures is greater than 2 °C.

While estimations using temperature sensors are indicators of current operating conditions, it is also desirable to have another estimate for the expected outdoor-air fraction when the air-conditioner operates normally. This was accomplished with the packaged air-conditioner, by using the OAE test data to characterize the OAF behavior under different outdoor-air damper positions and temperatures. This behavior is shown under different temperature conditions in Figure 3.77. From the response, it should be noted that significant leakage exists when the damper is all the way closed and open. Some of the leakage when the damper opens is actually due to return-air recirculation.

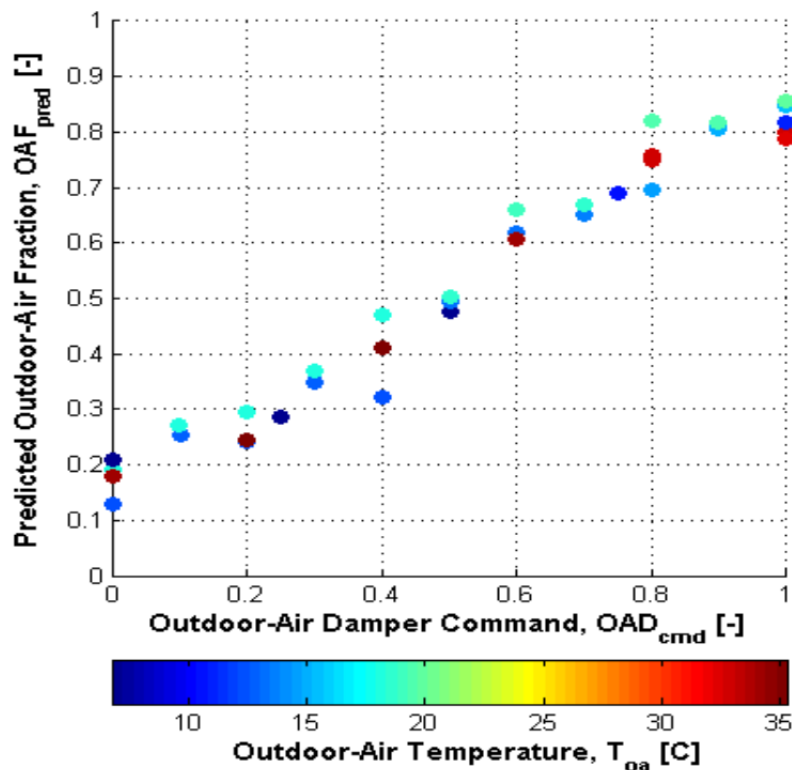


Figure 3.77 OAF response to different outdoor-air damper positions under different outdoor-air temperatures.

Because of the leakage and return-air recirculation present, the OAF response to changing damper position is not linear. To form an accurate model, the following function form using damper position was used

$$OAF_{pred} = c_0 + c_1 OAD_{cmd} + c_2 OAD_{cmd}^2 + c_3 OAD_{cmd}^3 \quad (3-29)$$

where

$$c_0 = 0.189948 \text{ [-]}$$

$$c_1 = 0.124964 \text{ [-]}$$

$$c_2 = 1.537778 \text{ [-]}$$

$$c_3 = -1.026001 \text{ [-]}$$

The resulting model is shown in Figure 3.78 against the outdoor-air fraction estimate using equation (3-22).

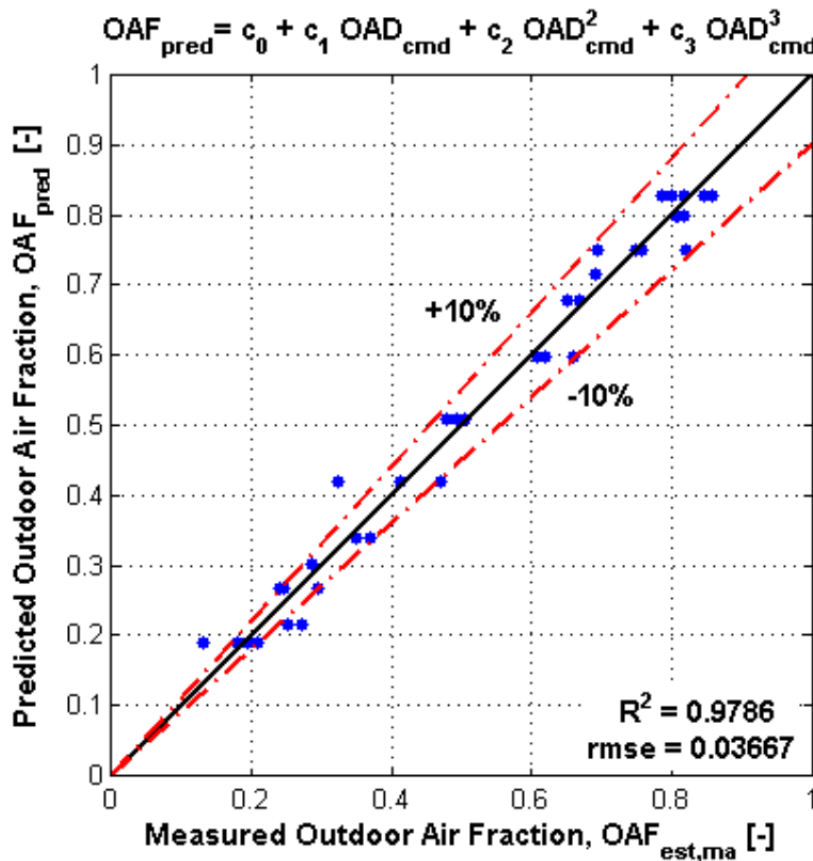


Figure 3.78 Outdoor-air fraction model fit.

3.4.4.5. Economizer Fault Detection and Diagnostics

Economizer fault detection and diagnostics has been separated into two separate procedures. Fault detection is performed on-line throughout the operation of the packaged air-conditioner monitoring performance. Fault diagnostics is only employed when a fault is detected. Unlike the fault detection operation, fault diagnosis takes active control of the outdoor-air damper in order to determine a diagnosis of the fault. The operational flow of the FDD algorithm is shown in Figure 3.79.

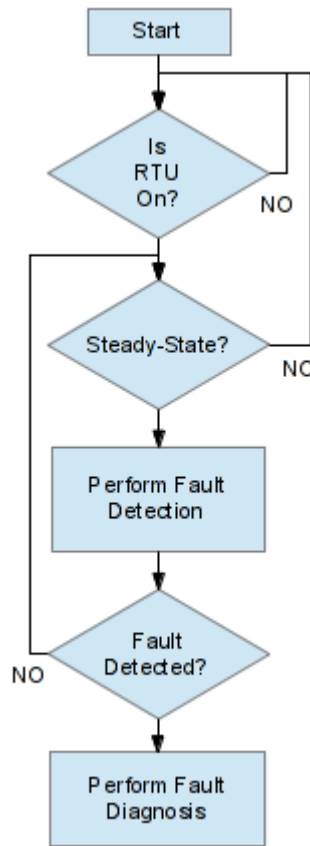


Figure 3.79 FDD Overall Flow Chart

3.4.4.5.1. Outdoor-Air Fraction Based Economizer Fault Detection

Typically, economizer fault detection and diagnostics tools rely on a small set of rules that are used to indicate problems within the economizer (Schein 2003) (Seem 2009). These rules often compare an estimate of outdoor-air fraction to an expected value when the damper is in a known position. Most commonly, these rules are applied when the outdoor-air damper is at the minimum position acceptable to meet the ventilation requirement or at the 100% open position. Additionally, many of the FDD tools are designed for built-up systems so additional rules that monitor the hot and cold water valves are used.

While these tools have been shown to be effective at detecting economizer faults, a more simple approach can be implemented for packaged-air conditioners (Hjortland 2012). Because characterizing the

performance of a packaged-air conditioner is much easier and cost-effective than a built-up system, rules can be made to monitor operation at all times instead of at a discrete set of damper positions. For instance, the outdoor-air fraction model can be used to monitor current damper position and temperature sensors when the compressor is running or during free-cooling. When current performance measured using temperature sensors deviates from the expected performance, a fault is detected.

A list of metrics that could be used to monitor the system's performance and detect deviations from normal behavior was made. The first metric, M_1 , is used to monitor the components of the mixing box and it is defined as the residual between the expected outdoor-air fraction and the estimated outdoor-air fraction given by equation (3- 30),

$$M_1 = OAF_{pred} - OAF_{est,ma} \quad (3- 30)$$

where OAF_{pred} is given by equation (3- 29) and $OAF_{est,ma}$ is given by equation (3- 22). Because the outdoor-air fraction is controlled by the outdoor-air damper in the mixing box, this metric is decoupled from the refrigerant circuit. The outdoor-air fraction is estimated using the outdoor-, return- and mixed-air temperatures and without the supply-air temperature, thus any cooling taking place in the evaporator has no effect. Therefore, this metric is suitable whenever the air-conditioner is in operation; when the supply-air fan is on.

The second performance metric aims to detect controller faults. This is accomplished by comparing the outdoor-air damper position controlled by the economizer controller to the damper position calculated using economizer control strategy logic within the FDD software. This comparison is useful to detect if the economizer is locked out or disabled for some reason. This metric would also detect if the economizer is economizing when it shouldn't be or not economizing when it should be possibly to do poor set points.

In order to detect faults, a method to distinguish between normal behavior and faulty behavior is needed. Hypothesis testing is used to accomplish this. More specifically, a t-test is used to determine if the means of the current performance metrics differs from the metrics calculated using normal test data.

A hypothesis test is used to either reject or confirm a null hypothesis. In this case, the null hypothesis is the current data sample has the same mean as the normal data. Essentially, the test measures whether the average value differs from the expected value. The indicator used to test the hypothesis is called the p-value, which is the probability of obtaining a hypothesis test at least as extreme as the one that is actually observed. If the p-value is smaller than a threshold, e.g. 1%, 5%, etc., then the hypothesis is rejected. When the hypothesis is rejected, a fault is declared.

Hypothesis testing may be more easily understood using a diagram. Shown in Figure 3.80 is a histogram of M_1 studentized (studentizing is simply dividing the sample by its standard deviation) along with the expected distribution of the metric based on normal data. 100 points of steady-state data when the damper was at 60% with an outdoor-air temperature of 12.78 °C were used to evaluate the current performance. The normal operational data showed a similar distribution to the data that was collected during training. Because of this, the p-value was near one and no difference in the mean of the current operation of the economizer could be detected. If this was collected in actual operation, no faults would be detected.

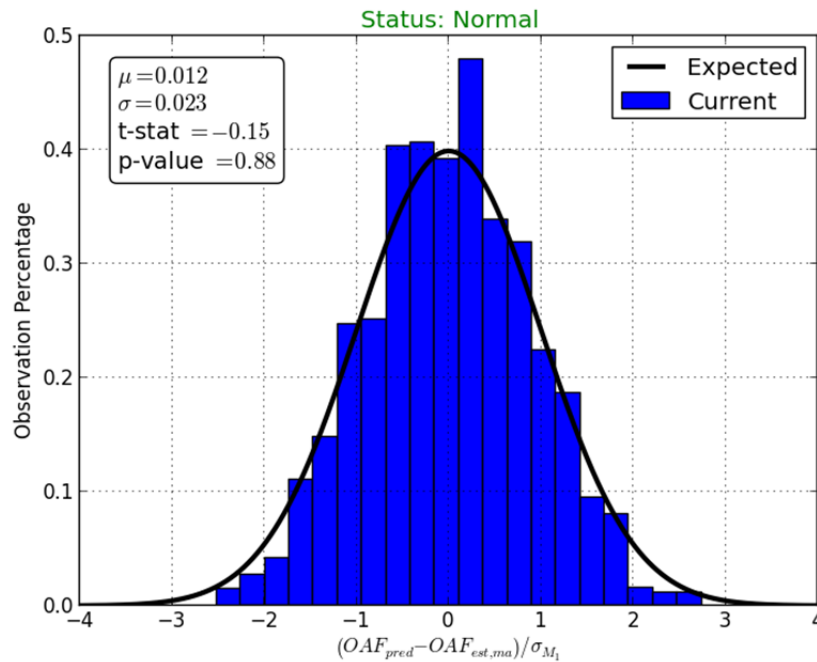


Figure 3.80 Histogram of fault-free economizer operation when outdoor-air damper is at 60% and outdoor-air temperature at 12.78 °C. Note that the M1 matches closely with the expected behavior, which makes the p-value close to 1.

Figure 3.81 shows the behavior of the outdoor-air fraction performance metric when there is a damper fault present. In this situation, the damper was held at the 40% open position with an outdoor-air temperature 12.78 °C. The damper was simulated to be controlled at 60% open, thus creating a fault. A clear deviation in performance between normal and actual operation exists, which indicates the presence of a fault. This is reinforced by the near zero p-value of the t-test, which leads to the rejection of normal operation.

Another example of an economizer fault that is determined using the outdoor-air fraction metric is an outdoor temperature sensor fault. In this case, test data were used where the outdoor-air damper was 100% open with an 18.33 °C outdoor-air condition. A -2.0 °C sensor bias was added to the outdoor temperature data and then was processed using the fault detection algorithm. The resulting M_1 histogram is shown in Figure 3.82.

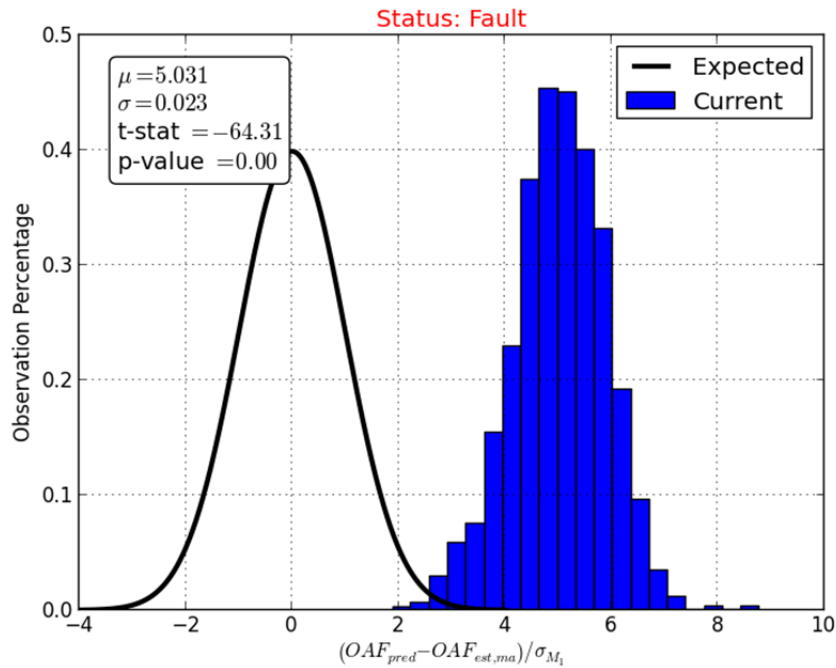


Figure 3.81 Histogram of the outdoor-air fraction metric, M1, with a 20% difference between the controlled and actual damper position at an outdoor-air temperature of 12.78 °C. A clear deviation exists between the current and normal operation, signifying an economizer fault.

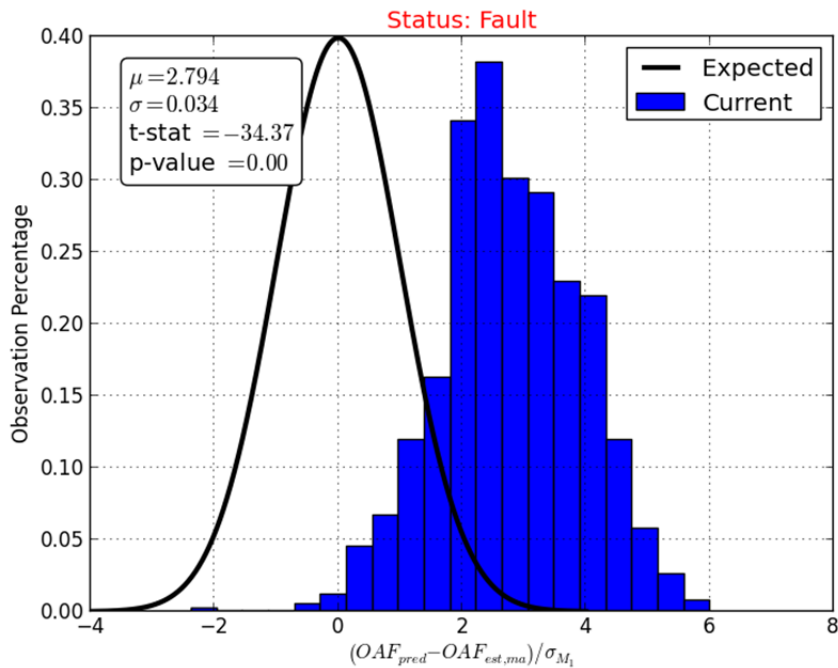


Figure 3.82 Histogram of the outdoor-air fraction metric, M1, when a -2.0 °C sensor bias is applied to the outdoor-air temperature sensor.

In order to use this method to detect OAE faults, a threshold must be chosen that maintains good fault detection sensitivity while reducing false alarm rates. The p-value is important in determining whether to reject the null hypothesis, so a p-value threshold is needed. As stated earlier, the p-value is the probability that the current sample is equivalent to the normal data that was determined using test data. For fault detection, the p-value chosen that provided good fault detection effectiveness was 0.01. This value yielded good results when using the test data for both stuck damper faults as well as temperature sensor bias faults.

Table 3.30 details the results of applying the fault detection algorithm to the OAE test data collected under various steady-state normal and faulty conditions. For stuck damper faults, the fault condition is defined as the deviation between the actual damper position and the expected position if it were working properly. For temperature sensor faults, the fault condition is defined as a difference between the “sensed” temperature and the actual temperature. The fault detection algorithm performed well when using a p-value threshold of 0.01. No false-alarms were produced for the normal data processed at different outdoor-air temperature and damper positions. The method was also able to detect damper faults that deviated by 20% of the expected position. Faults were declared for all temperature sensor faults that deviated from the actual measurement by 2 °C except for one case.

Table 3.30 Fault detection results for normal data and various types of faults.

Fault Condition	Outdoor-Air Temperature (°C)	Expected Damper Position (%)	t-test p-value [-]	Status
Normal	12.78	20	0.7364	Normal
Normal	12.78	50	0.9837	Normal
Normal	12.78	100	0.8139	Normal
Normal	18.33	80	0.6793	Normal
Normal	35	0	0.7996	Normal
Normal	35	20	0.4728	Normal
-10% Damper Position Fault	12.78	100	0.0733	Normal
-20% Damper Position Fault	12.78	70	0.0025	Fault
-30% Damper Position Fault	12.78	100	0.0014	Fault
-10% Damper Position Fault	18.33	90	0.0292	Normal
-20% Damper Position Fault	18.33	60	0.0056	Fault
+30% Damper Position Fault	18.33	70	0.0051	Fault
+20% Damper Position Fault	35	20	0.0001	Fault
+30% Damper Position Fault	35	10	0.0005	Fault
+1.0 °C Outdoor-Air Sensor Fault	12.78	100	0.7695	Normal
+2.0 °C Outdoor-Air Sensor Fault	12.78	100	0.0095	Fault
+3.0 °C Outdoor-Air Sensor Fault	12.78	90	0.0023	Fault
+1.0 °C Outdoor-Air Sensor Fault	18.33	100	0.2832	Normal
+2.0 °C Outdoor-Air Sensor Fault	18.33	80	7.1E-5	Fault
+3.0 °C Outdoor-Air Sensor Fault	18.33	100	0.0010	Fault
+1.0 °C Mixed-Air Sensor Fault	12.78	100	0.6454	Normal
+2.0 °C Mixed-Air Sensor Fault	12.78	80	0.0034	Fault
+3.0 °C Mixed-Air Sensor Fault	12.78	100	0.0036	Fault
+1.0 °C Return-Air Sensor Fault	29.44	20	0.6321	Normal
+2.0 °C Return-Air Sensor Fault	29.44	20	0.2531	Normal
+3.0 °C Return-Air Sensor Fault	29.44	0	0.0091	Fault

3.4.4.5.2. Active Economizer Diagnostics using a Bayesian Classifier

In order to diagnose OAE faults, one method is to take active control of the outdoor-air damper in order produce system redundancy. This system redundancy is desirable because it narrows down the possible sources of the fault by comparing equivalent measurements. A simplified approach to active OAE diagnostics is shown in Figure 3.83 (Fernandez 2009). Typically, the damper is controlled all the way closed and then all the way open. At these positions, steady-state data is collected with the cooling system off. Ultimately, the mixed-air temperature is compared with the return- and outdoor-air temperatures at each location and a diagnosis is determined using a set of logical expectations.

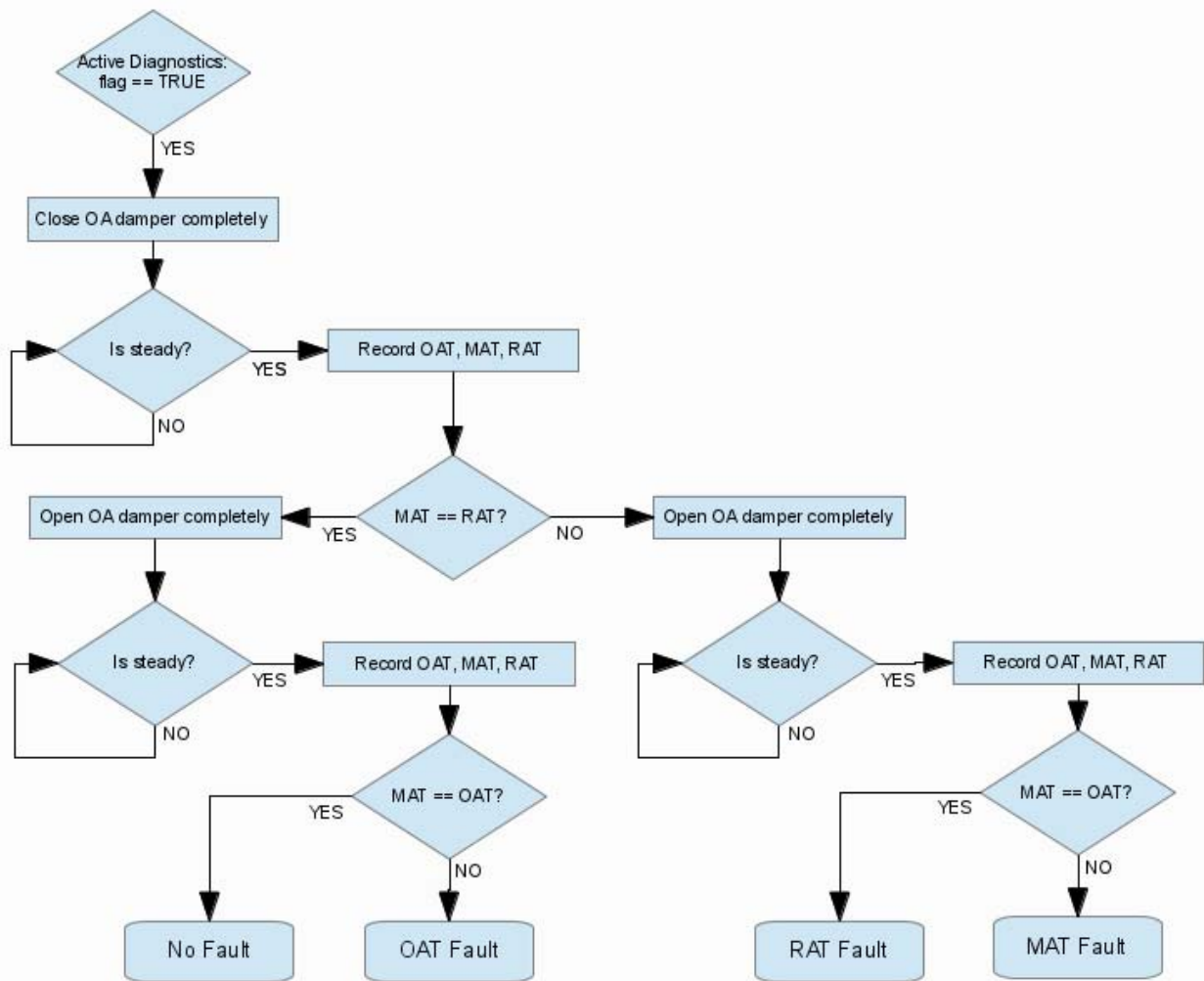


Figure 3.83 OAE active diagnostics using only dry-bulb temperature sensors and control of the outdoor-air damper position (Fernandez 2009).

While this type of method is able to correctly identify different faults in air-conditioning systems, there is a lack of rigor. There is no sense of a statistical confidence associated with the diagnoses. In order to evaluate a level of confidence associated with a diagnosis, a Bayesian classifier has been used along with the active diagnostics approach. A Bayesian classifier is a simple probabilistic classifier applying Bayes' theorem:

$$P(A|B) = \frac{P(B|A)P(A)}{P(B)} \quad (3-31)$$

Bayes' theorem gives the relationship between the probabilities of A and B (denoted by $P(A)$ and $P(B)$) and the conditional probabilities of A given B , $P(A|B)$, and B given A , $P(B|A)$. Because a probability is essentially a measure of confidence and a conditional probability is a measure of confidence while knowing some evidence, Bayes' theorem links the confidence of a proposition before and after accounting for evidence.

It is assumed when applying a Bayesian classifier that each feature of a class is independent of the features of other classes. In the case of economizer diagnostics, a feature could be any measurement of performance that is altered when a fault is present and a class is a specific type of fault. Essentially, the Bayesian classifier is a set of rules for determining a class by minimizing the probability of making a wrong decision. Active diagnostics is used with the outdoor damper controlled all the way closed and all the way open to collect steady-state data. Once the data has been collected, the current operation is classified according to type of fault.

In order to classify the faults, a set of residuals is used to characterize the current operation of the air-conditioner. Approximately half the residuals are calculated when the outdoor-air damper is closed; the other half when the damper is open.

When the damper is closed, the mixed-air temperature should equal the return-air temperature, yielding the first residual:

$$r_1 = |T_{ra} - T_{ma,corr}|_{closed} \quad (3-32)$$

Since the compressor is off when active diagnostics is performed, the mixed-air temperature should also equal the supply-air temperature when the damper is closed:

$$r_2 = |T_{sa} - T_{ma,corr}|_{closed} \quad (3-33)$$

The third residual compares the measured outdoor-air temperature to a robust outdoor-temperature measurement $T_{oa,rob}$.

$$r_3 = |T_{oa,corr} - T_{oa,rob}|_{closed} \quad (3-34)$$

The robust outdoor-air measurement could be obtained in a few different ways. One method could be to obtain a local air temperature measurement from a meteorological website. Another method could be to use other rooftop unit outdoor-air temperature measurements if there are more units available at the location.

The difference between the predicted and estimated outdoor-air fractions using mixed-air temperature is determined when the damper is closed and defines the fourth residual:

$$r_4 = \left| OAF_{pred} - OAF_{est,ma} \right|_{closed} \quad (3-35)$$

The last residual calculated with the outdoor-air damper closed is the similar to the fourth; however it uses the supply-air temperature to estimate the outdoor-air fraction:

$$r_5 = \left| OAF_{pred} - OAF_{est,sa} \right|_{closed} \quad (3-36)$$

After collecting steady-state data with the damper closed, the damper opens to the maximum position. At this position, the mixed air-temperature should equal the outdoor-air temperature:

$$r_6 = \left| T_{oa} - T_{ma,corr} \right|_{open} \quad (3-37)$$

The remaining residuals are identical to the residuals r_2 , r_4 , and r_5 except they are calculated when the outdoor-air damper is all the way open.

$$r_7 = \left| T_{sa} - T_{ma,corr} \right|_{open} \quad (3-38)$$

$$r_8 = \left| OAF_{pred} - OAF_{est,ma} \right|_{open} \quad (3-39)$$

$$r_9 = \left| OAF_{pred} - OAF_{est,sa} \right|_{open} \quad (3-40)$$

When these residuals are calculated, they can be used to classify the current operation. When the system is operating normally, all of these residuals should be near zero. For a fault, some of these residuals will change and will deviate from the normal value. In fact, each different fault will have a different set of residual responses. Table 3.31 shows a list of possible economizer faults along with a designated classification.

Table 3.31 Types of economizer faults with Bayesian classifier class

Type of Fault	Class
No Fault – Normal	0
Outdoor-Air Damper Fault	1
Return-Air Temperature Fault	2
Mixed-Air Temperature Fault	3
Outdoor-Air Temperature Fault	4
Supply-Air Temperature Fault	5

This is explained most easily with an example. When the damper becomes stuck, the fault detection algorithm will declare a fault is present and activate the fault diagnosis algorithm. Diagnosis will be performed at the next available time, most likely when the building becomes unoccupied. The diagnostics algorithm will attempt to control the damper to the all the way open and closed positions and collect steady-state data. The response of the set of residuals is shown in Table 3.32. When the damper is stuck, the mixed- and supply-air temperature should remain equal. This is why, along with residual r_3 , these residuals do not deviate from the normal behavior even with a fault present.

Table 3.32 Residual response to stuck damper fault.

R	r_1	r_2	r_3	r_4	r_5	r_6	r_7	r_8	r_9
Response	↑			↑	↑	↑		↑	↑

In a similar manner, the other types of faults display a set of residual responses, R . These are tabulated in Table 3.33. The most important characteristic of these different residual responses is that they are unique. Each different type of fault has a different residual response, which makes classification possible.

Table 3.33 Summary of economizer residual responses.

Class	R								
	r_1	r_2	r_3	r_4	r_5	r_6	r_7	r_8	r_9
0									
1	↑			↑	↑	↑		↑	↑
2	↑			↑	↑			↑	↑
3	↑	↑		↑		↑	↑	↑	
4			↑	↑	↑	↑		↑	↑
5		↑			↑		↑		↑

The Bayesian classifier must be trained before it can be used to diagnose faulty economizer operation. Training consists of building arrays of the residual responses and fault classifications that correspond to one another. In order to do this, the OAE performance test data was used to train normal operation and faulty operation. For normal operation, the fault diagnosis residuals were calculated under different outdoor-air temperatures with the damper controlled to 0% and 100%. This data is representative of how the economizer would react if fault diagnosis were being performed when there was not an actual fault present.

The damper faults were trained using the same data set, however instead of using only 0% and 100% damper positions, intermediate positions were also provided. In order to simulate a stuck damper at the 0% position, the residuals that are normally calculated when the damper is all the way open were calculated using with the closed position data. The opposite was done to simulate a stuck damper at 100%. Temperature sensor faults were trained by applying increasing bias to each measurement in the range of ± 1 -5. Table 3.34 details the types of data that were used to train each fault class.

Table 3.34 Bayesian classifier training data.

Class	Outdoor-Air Temperature (°C)	Outdoor-Air Damper Position (%)	Temperature Sensor Bias (°C)
0	12.78, 18.33, 29.44, 35.00	0, 100	None
1	12.78, 18.33, 29.44, 35.00	0, 20, 40, 60, 80, 100	None
2	12.78, 18.33, 29.44, 35.00	0, 100	$T_{ra} \pm 1, 2, 3, 4, 5$
3	12.78, 18.33, 29.44, 35.00	0, 100	$T_{ma} \pm 1, 2, 3, 4, 5$
4	12.78, 18.33, 29.44, 35.00	0, 100	$T_{oa} \pm 1, 2, 3, 4, 5$
5	12.78, 18.33, 29.44, 35.00	0, 100	$T_{sa} \pm 1, 2, 3, 4, 5$

The results of testing the algorithms against normal data are shown in Table 3.35 along with the probability of each test belonging to each fault class C_i . This probability, $P(C_i|R')$, is known as the posterior probability estimate. The situation where fault diagnostics is applied to an economizer that is operating normally could occur if the fault detection algorithm declares a false alarm. Classifying normal operation has the benefit of reducing the number of false alarms that are reported to the building manager. The results of applying the fault diagnostics algorithm to normal data showed no misclassification and showed high levels of statistical confidence.

Table 3.35 Results of applying the fault diagnostics approach to normal operation data.

T_{oa} (°C)	P(0 R')	P(1 R')	P(2 R')	P(3 R')	P(4 R')	P(5 R')	Fault Class
7.22	1.0000	0.0000	0.0000	0.0000	0.0000	0.0000	0
12.78	1.0000	0.0000	0.0000	0.0000	0.0000	0.0000	0
18.33	0.9999	0.0000	0.0000	0.0000	0.0000	0.0000	0
21.11	0.9523	0.0476	0.0000	0.0000	0.0000	0.0000	0
29.44	0.9988	0.0002	0.0009	0.0000	0.0000	0.0000	0
35.00	1.0000	0.0000	0.0000	0.0000	0.0000	0.0000	0

Damper faults were processed by applying the algorithm to data that simulated the outdoor-air damper being stuck at different positions. The results of these tests are shown in Table 3.36. The approach successfully classified the damper faults with high classification probability estimates.

Table 3.36 Results of applying the fault diagnostics approach to stuck damper fault data.

T_{oa} (°C)	P(0 R')	P(1 R')	P(2 R')	P(3 R')	P(4 R')	P(5 R')	Fault Class
0	0.0782	0.9218	0.0000	0.0000	0.0000	0.0000	1
10	0.0000	1.0000	0.0000	0.0000	0.0000	0.0000	1
30	0.0000	1.0000	0.0000	0.0000	0.0000	0.0000	1
50	0.0000	1.0000	0.0000	0.0000	0.0000	0.0000	1
70	0.0000	0.9999	0.0001	0.0000	0.0000	0.0000	1
90	0.0000	0.9706	0.0294	0.0000	0.0000	0.0000	1
100	0.0915	0.9085	0.0000	0.0000	0.0000	0.0000	1

3.4.5. Impact of faults on system performance for AFDD demonstration RTU

The impact of individual faults on capacity and energy efficiency were evaluated for a range of operating conditions for the RTU unit tested at the Herrick Laboratories. To evaluate the impacts of faults on performance, capacity and COP ratio were determined. Figure 3.84 shows the impact of improper refrigerant charge on capacity and energy efficiency. When the refrigerant was charged less than 70%, capacity was significantly decreased. This is because the TXV becomes fully open at low charge levels and then the system acts like a system having an FXO as an expansion device. The COP ratio has the same trend as the capacity. The extreme undercharge of refrigerant by 50% reduced cooling capacity and energy efficiency by 60%.

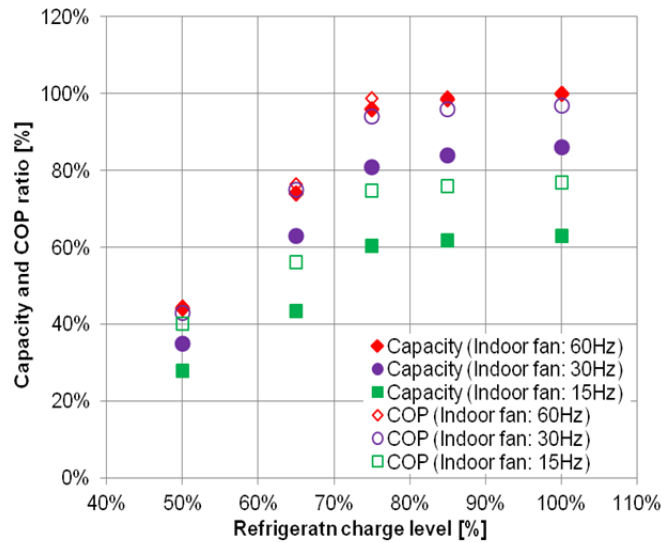


Figure 3.84 Capacity and COP ratio based on different refrigerant charge levels.

Figure 3.85 presents the impact of heat exchanger fouling on performance. Evaporator fouling was simulated using reduction of air flow rate. The results show the impact of evaporator fouling on capacity and COP increases dramatically below about 50% of normal air flow rate. The results also show that capacity is more strongly influenced by evaporator fouling than efficiency. The condenser fouling test was simulated by blocking the area of the heat exchanger. For condenser fouling, the result shows that efficiency is more strongly influenced than capacity.

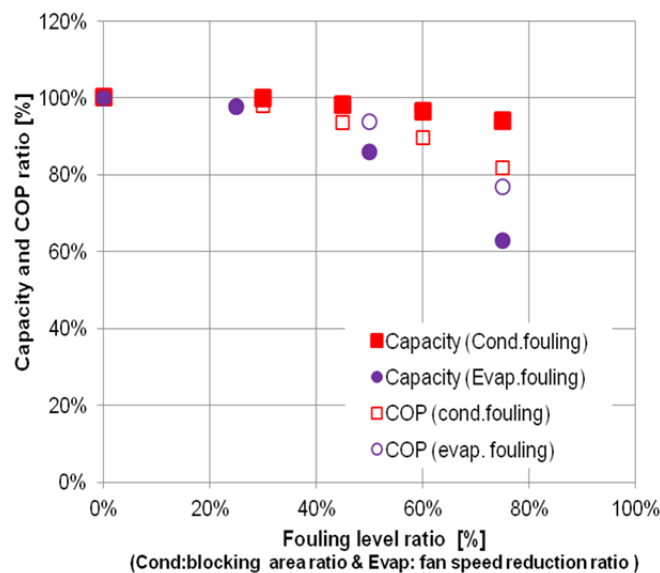


Figure 3.85 Capacity and COP ratio based on the different fouling level.

3.4.6. Develop user interface for initial diagnostic demonstration

3.4.6.1. Initial diagnostic demonstration

Initial video demonstrations have been developed for RTU diagnostics. The refrigerant charge and condenser air flow display interface shows the virtual gauge readings to users, as depicted in Figure 3.86. The capacity and COP impacts are also displayed within the interface. The VRC and VAF sensors only require six temperature inputs: evaporating, condensing suction line, liquid line, condenser air inlet and condenser air outlet temperature. The data acquisition device provides input channels for the six temperature sensors (e.g., thermocouples) and provides calibrated measurements as inputs to the steady-state detector and virtual sensor algorithms.

For demonstration, 75% refrigerant was charged in the RTU system using a scale to simulate the undercharged condition. The outdoor heat exchanger had no blockage, as shown in the left side of Figure 3.88. Figure 3.86 shows the gauge readings displayed within the user interface correctly indicate a 75% refrigerant charge level and 100% condenser air flow rate (0% condenser fouling). The capacity and COP ratio indicate 95% and 96% of normal performance for the current operation. The results demonstrate that the impact of refrigerant charge on performance is relatively small for 75 % of the rated charge at this operating condition. However, there was a dramatic reduction in both cooling capacity and energy efficiency when charge was decreased below 70% refrigerant charge, shown in Figure 3.84.

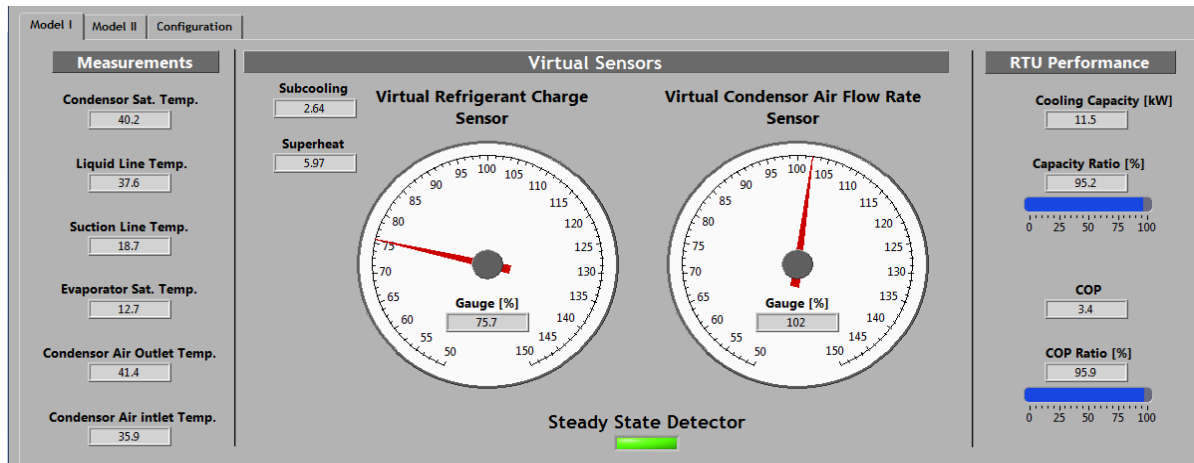


Figure 3.86 75% refrigerant charge level & 0% condenser fouling level demonstration

The system was recharged to 100% of the nominal charge level by weighing the change in mass of a refrigerant canister. For this situation, Figure 3.87 shows that the VRC and VAF sensor gauges indicated 100%, respectively. Both capacity and COP ratio were increased to 98 % of the expected values.

Condenser fouling was simulated by blocking the bottom part of the heat exchanger with paper strips. Figure 3.88 shows an example of simulated condenser fouling with a fault level of 50% (shown on the right side). The fault level is defined as the percentage of blocked heat exchanger face area. For 70% blockage, Figure 3.89 shows that the VAF sensor indicated a condenser air flow rate that was 63% of the normal value. A condenser fouling fault could be detected by comparing this estimated air flow rate with

a target value. As the severity of the condenser fouling increases, the estimated air flow rate decreases relative to the target value. The VRC sensor made accurate prediction of refrigerant charge amount even when the outdoor heat exchanger was blocked.

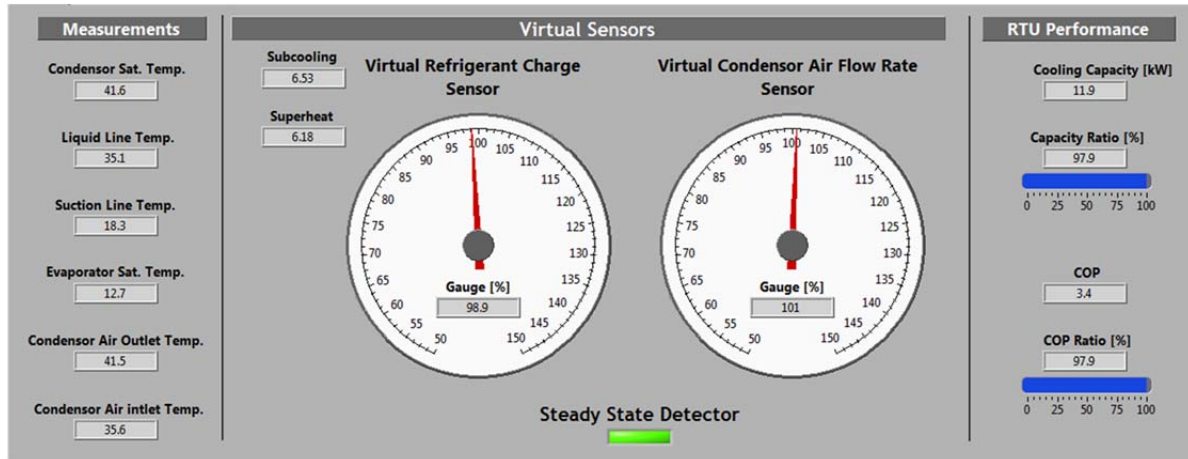


Figure 3.87 100% refrigerant charge level & 0% condenser fouling level demonstration



Figure 3.88 Condenser status of RTU system (left side: normal & right side: 50% blocking)

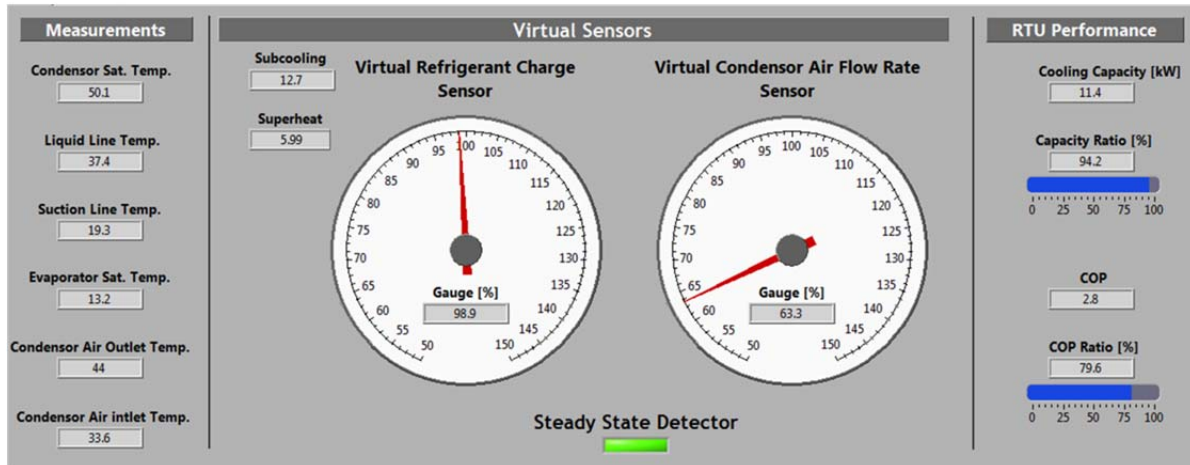


Figure 3.89 100% refrigerant charge level & 70% condenser fouling level demonstration

3.4.6.2. Development of complete AFDD RTU implementation and demonstration

This section presents the interface for a complete implementation and demonstration of an AFDD system applied to RTUs. The implementation incorporates integrated virtual sensors to provide the diagnostic outputs and the performance impact of the fault(s). The AFDD RTU demonstration system provides the following diagnostic outputs: 1) loss of compressor performance, 2) low or high refrigerant charge, 3) fouled condenser or evaporator filter, 4) faulty expansion device or liquid-line restriction, and 5) economizer faults.

Once faults are detected and the causes of the faults are identified, proper action should follow to fix the problems, adapt the control, or flag them for continued monitoring. An assessment of the severity of a fault is essential to the decision process and virtual sensors can be used as inputs to this analysis. If thresholds were set too close to normal conditions, the AFDD system would be too sensitive leading to false alarms. If thresholds were set too far from normal conditions, the AFDD system might miss faults that significantly reduce system performance. Therefore, it is very important to define reasonable thresholds for appropriate fault detection.

Health and economic status reports for equipment can be generated using fault impact indices, such as system cooling capacity and efficiency (COP). In particular, the fault impact indices can be used to assess the economics associated with servicing a unit if faults existed.

Figure 3.90 shows the diagnostic demonstration interface based on using UTRC field data for no fault conditions. The user interface for the AFDD system incorporates 1) the status of compressors and fans, 2) integrated virtual sensors, 3) performance indices, and 4) information about FDD status. The status of fans and compressors are displayed on the left side. If steady-state conditions are detected, shown on the middle of the left side, the virtual sensors will indicate their detected values. Virtual sensors were implemented for the compressor, TXV, condenser and evaporator fan/motor combinations, heat exchangers, refrigerant charge, and economizer. On the right side, the system performance is also displayed to show the capacity and COP ratios. The capacity and COP ratios are 91% and 94% of the

normal condition for this example. Based on the readings, the diagnostic outputs indicated the status of RTU system is acceptable and any service is unnecessary at the bottom of right side.

Figure 3.91 shows a screen that is displayed by clicking the VRC sensor button. The current and recent trending of refrigerant charge levels are shown. In addition, probability distributions are shown that correspond to the current estimations from the VRC sensor and expected values for a normal condition. The mean and standard deviation for the current distribution is also presented. The difference between current and expected values is used as a residual input to a Bayesian classifier in order to evaluate whether a refrigerant fault is present. For the no fault test data, there is a significant overlap between the current and expected probability distributions indicating normal operation.

Figure 3.92 shows the diagnostic demonstration displayed on the user interface using UTRC 70% refrigerant charge field test data. The demonstration AFDD system recommends that service is needed for this refrigerant undercharge fault (bottom right side of display). For this case, the capacity and COP ratio were reduced to 82% and 86% due to the low charge. Figure 3.93 shows detailed refrigerant charge information obtained by clicking the VRC sensor button. The probability graph shows much larger differences between the current estimated refrigerant charge and expected values. The trending graph provides more evidence for the existence of this fault.

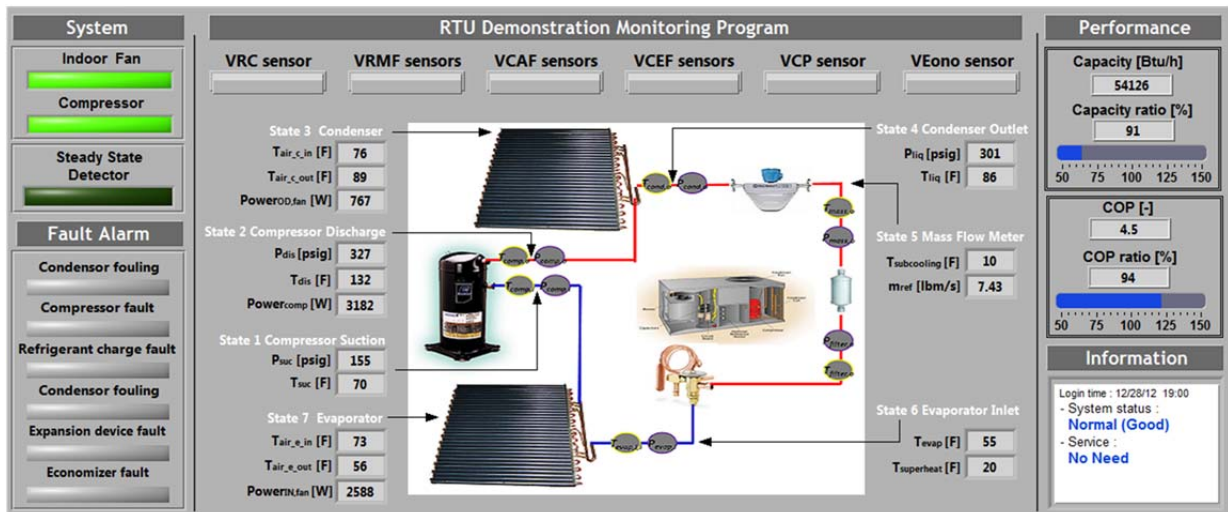


Figure 3.90 Implementation and demonstration of an automated FDD system for RTU under normal condition

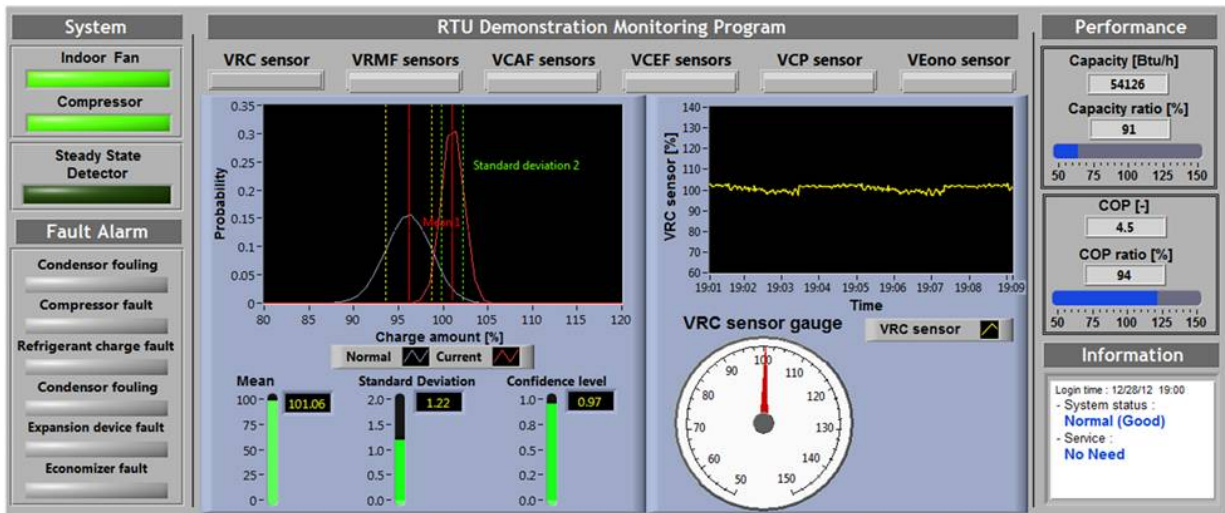


Figure 3.91 Implementation and demonstration of VRC sensor under normal condition

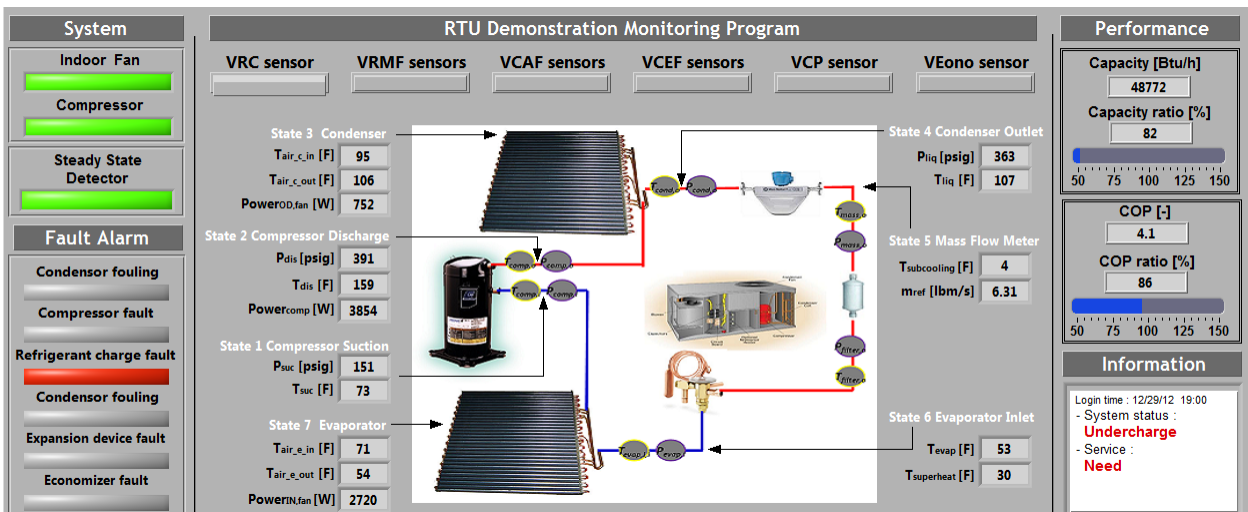


Figure 3.92 Implementation and demonstration of an automated FDD system for RTU under normal condition

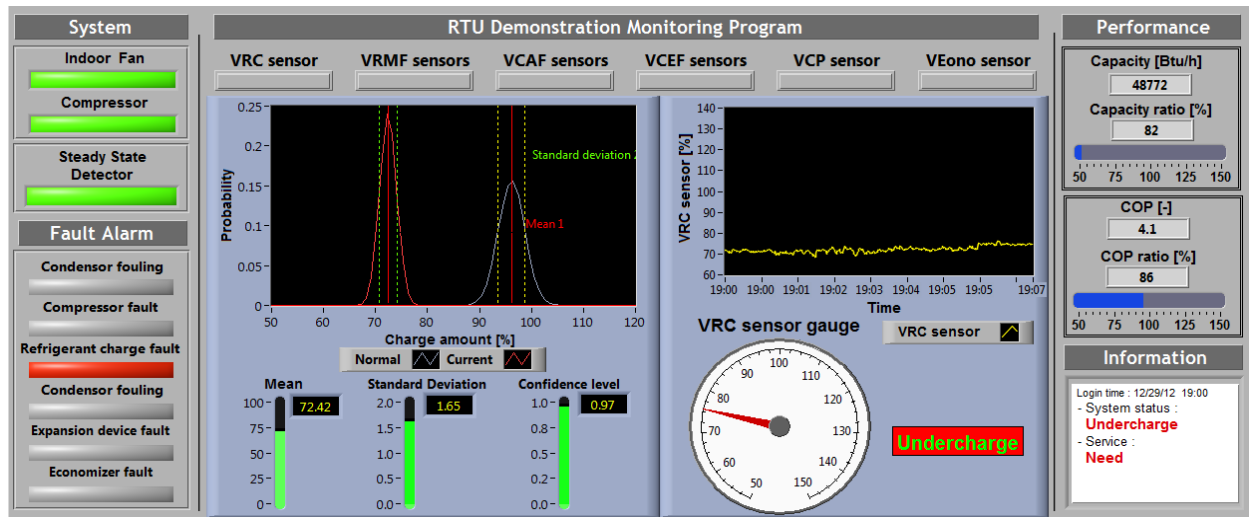


Figure 3.93 Implementation and demonstration of VRC sensor under normal condition

3.5. AFDD for Building 101 DX systems

3.5.1. System descriptions of Building 101 DX/AHU systems

AFDD was applied to data obtained for the condensing units associated with the DX cooling systems at Building 101. Table 3.37 shows the system specification for DX systems 2 and 3 at Building 101. The systems have two circuits with two semi-hermetic compressors and two TXVs as expansion device. Each of the two compressors is connected to a separate condenser.

Table 3.37 System specification of DX system 2 & 3

Nominal Capacity	Refrigerant	Expansion Type	Compressor Type	Outdoor coil airflow rate	Total Power of system	Outdoor fan Power
[Mbtu]	-	-	-	[CFM]	[kW]	[kW]
738	R22	TXV	Semi- Hermetic (3 stage)	36800	64.1	6.0 (1.5 kW /ea)

3.5.2. Virtual sensors developments/assessments for Building 101 DX systems

3.5.2.1. Virtual sensors developments for Building 101 DX system 2 and 3

Data for the building 101 DX systems were obtained from continuous monitoring and virtual sensors were developed. First, a VRC sensor was developed for DX system using data filtered using a steady-state detector. Measured data for condensing DX System 3A and 3B in building 101 were used to evaluate robustness of the VRC sensor. Figure 3.94 and Figure 3.95 show the sample outputs of the VRC sensor based on use of default parameters. Due to the limitation of changing refrigerant for a public system, it was not possible to apply the algorithm with tuned parameters. The outdoor temperature during this period ranged between 86 and 93 °F. Under this range of outdoor temperatures, the VRC sensor gave charge level predictions that varied by less than 10%. The DX unit #3B shows relatively larger deviations and it is due to the fact that fans and compressor are loading and unloading. These results are typical of the variation encountered during the test period (May).

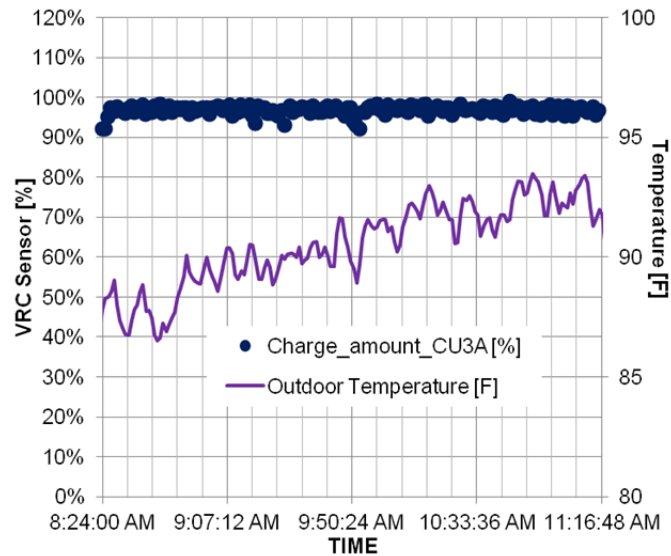


Figure 3.94 VRC sensor outputs based on default parameters for condensing unit #3A

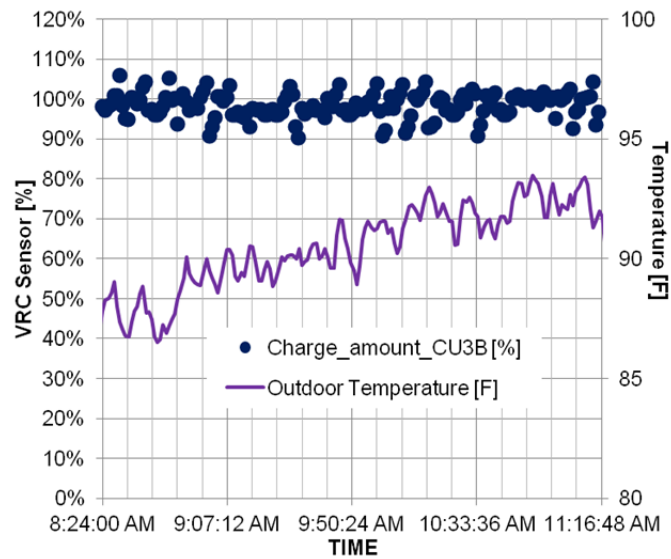


Figure 3.95 VRC sensor outputs based on default parameters for condensing unit #3A

Figure 3.96 shows outputs from a VRMF sensor developed for building 101 DX system 2A. The results are presented as the ratio of estimated flow rate to the mass flow rate for 3 stages operating at the measured operating conditions. The mass flow rate prediction was determined using heat loss estimates and predictions of other virtual sensors. The predicted refrigerant mass flow rates could not be compared with the actual measurements due to an absence of refrigerant mass flow meter data. The refrigerant mass flow meter was estimated to be 100% when three compressors were used and 60% when two compressors were used. Although it is not possible to validate the predictions, the results clearly show the overall

dependence on compressor staging. These estimations will be used as inputs for other fault detection (e.g., condenser fouling).

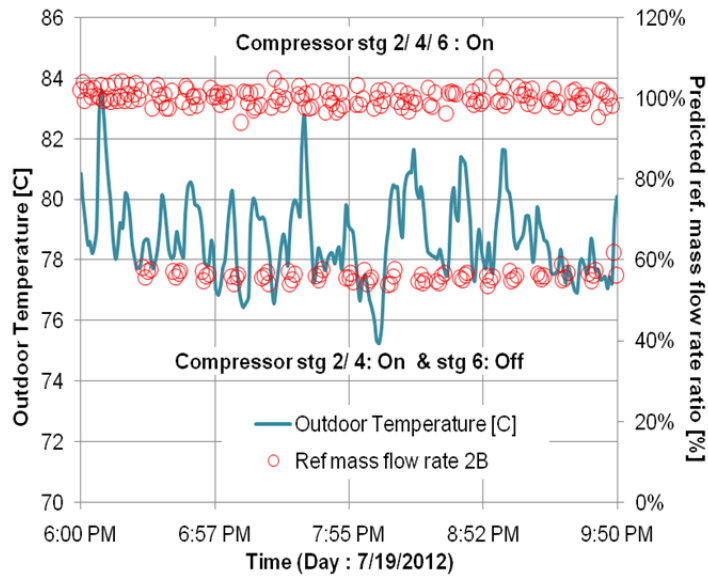


Figure 3.96 VRMF sensor outputs based on energy balance for DX unit 2A

Figure 3.97 shows outputs from a condenser VAF sensor for DX system 2 referenced to the flow for a single fan operating. Again, there were no direct measurements to validate the VAF sensor outputs, but the results show the dependence on fan staging. These outputs are useful as inputs for fault detection (e.g., condenser fouling).

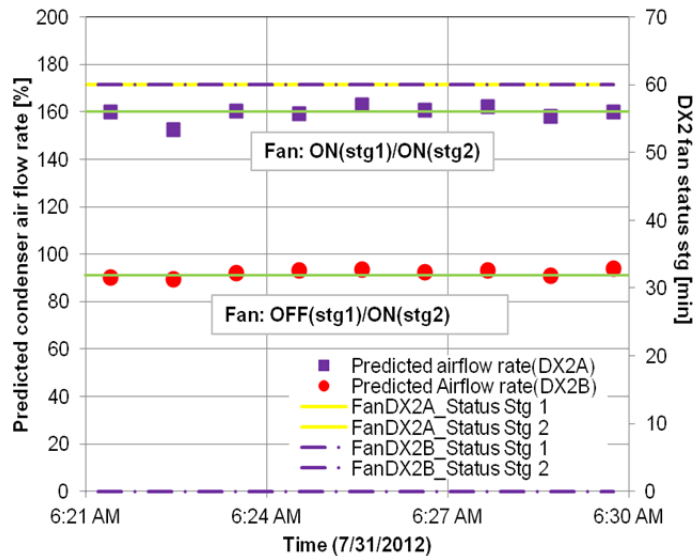


Figure 3.97 Performance of VAF sensors based on energy balance for DX unit 2A & 2B.

3.5.2.2. Virtual sensors assessment for Building 101 DX system 3 during summer season

Although refrigerant flow measurements were not available, compressor maps were obtained from the compressor manufacturer in order to assess the VRMF based on an energy balance. In order to assess the accuracy of the maps, predicted power from the compressor map was compared to power measurements and the results were within 10% regardless of number of compressor stages operating, as shown in Figure 3.98 and Figure 3.99 shows comparisons of the map-based flow estimates and outputs from the virtual refrigerant mass flow (VRMF) sensor for building 101 DX system 3. For these plots, the compressor power and mass flow rate are referenced to rated values for the compressor. The data were obtained from summer months and filtered for steady-state operation.

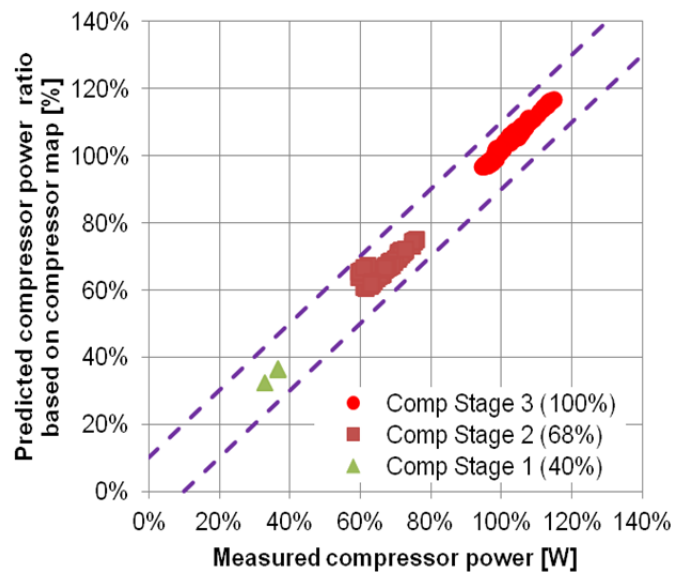


Figure 3.98 Accuracy of predicted power based on compressor map for DX unit 3 circuit 1

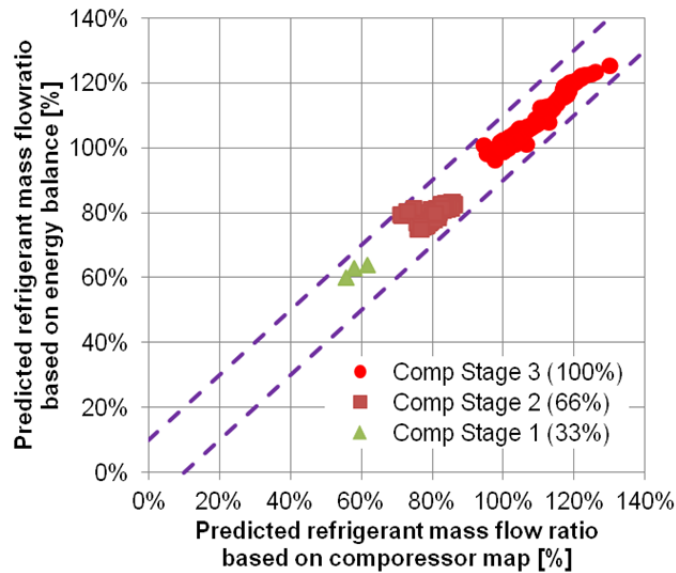


Figure 3.99 Evaluation of VRMF sensor based on energy balance in relation to compressor map for DX unit 3 circuit 1

The VRC sensor was also applied to steady-state summer data to evaluate consistency in predicting normal charge levels over a wide range of operating conditions. Figure 3.100 and Figure 3.101 show outputs from the VRC sensor based on default parameters for DX unit 3 for operating conditions during the summer where steady-state conditions were detected. The outdoor temperature during this period was between 70 and 100 °F. Under this range of outdoor temperatures, the VRC sensor gave charge level predictions that varied by less than 7% regardless of the time and cloud cover conditions. Since the charge level was help constant then these represent reasonable charge predictions. Future work will involve adjustments of charge level and a wider range of operating conditions.

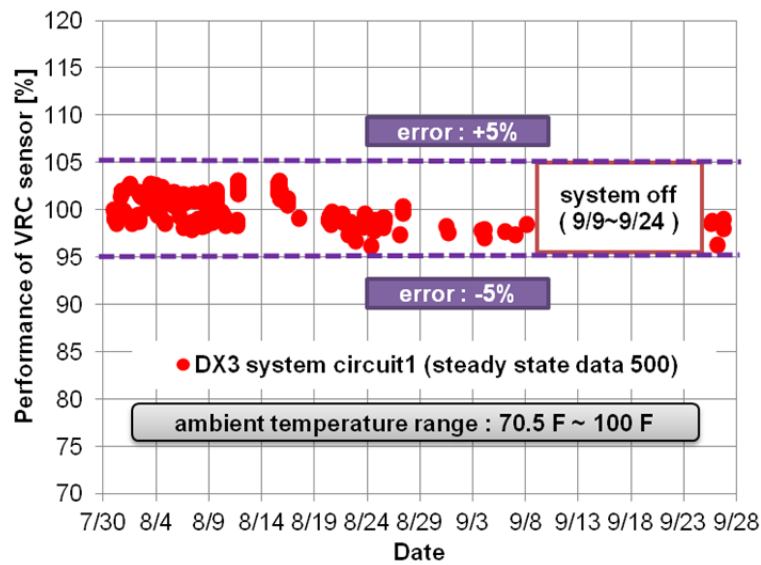


Figure 3.100 VRC sensor outputs based on default parameters for DX unit 3 circuit 1.

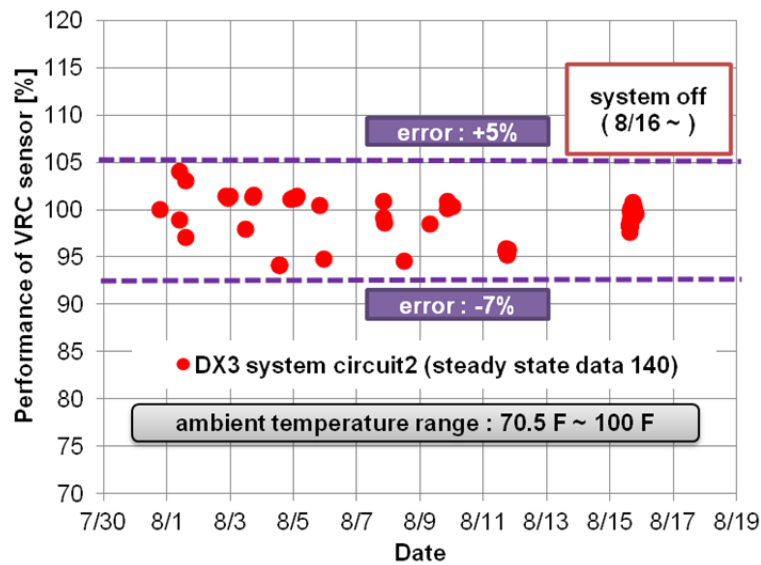


Figure 3.101 VRC sensor outputs based on default parameters for DX unit 3 circuit 2.

3.5.3. Initial demonstration of virtual sensor for Building 101 DX systems

Figure 3.102 shows the performance of VRC, VRMF, and VAF sensor for DX system 1. The steady detector using superheat filtered out the transient data which shows large deviation of predictions. When the steady detector indicates steady status, three virtual sensors consistently present 100% estimation.

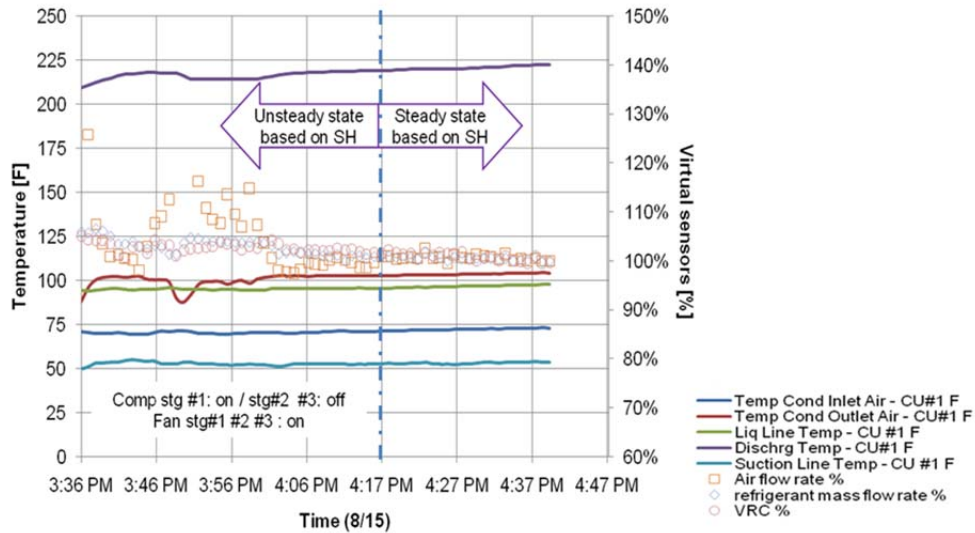


Figure 3.102 Performance of VRC, VRMF, and VAF sensor for DX unit 1.

User interface for diagnostic demonstration of Building 101 DX system have been developed, show in Figure 3.103. User interface includes 1) the status of compressors and fans, 2) three virtual sensors for DX systems, and 3) performance indices for a DX system at building 101 that show an output of the impact of the fault(s) on overall performance (capacity and COP). Figure 3.103 shows the example of demonstration under 100% refrigerant charge level, 100% refrigerant mass flow rate and 0% condenser fouling.

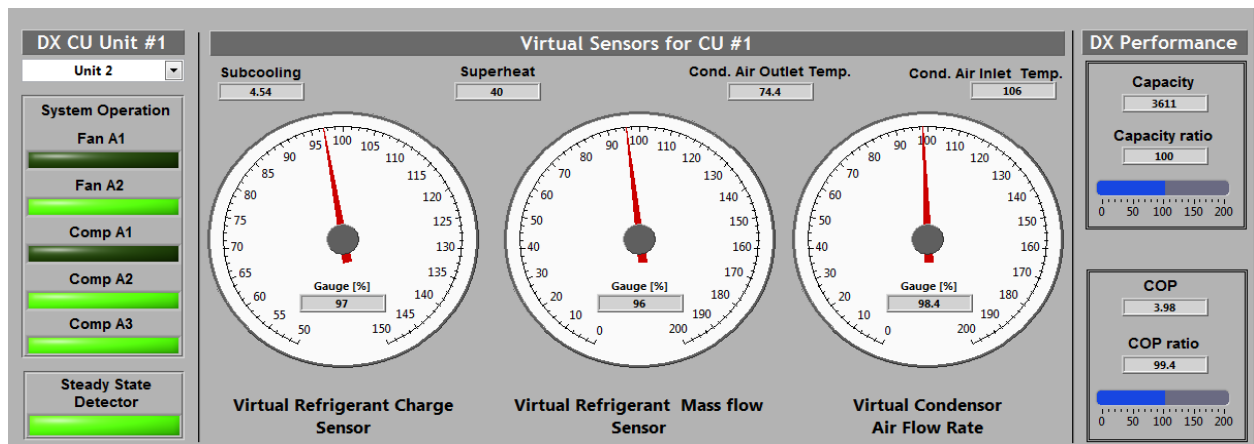


Figure 3.103 Example of demonstration for DX2A unit

3.6. Conclusions

About 60% of the total cooling requirements in the U.S. are met using a large number of relatively small packaged air conditioners (AC). Furthermore, several studies have demonstrated that this type of equipment tends not to be well maintained and generally operates much less efficiently than originally intended as a result of faults. Automated fault detection and diagnostics (FDD) has the potential for improving energy efficiency for packaged AC along with reducing service costs and comfort complaints.

The impact of individual faults on capacity and energy efficiency was evaluated for air conditioners over a wide range of operating conditions. Based on the results of this study, refrigerant undercharging in the range of 25% can lead to an average reduction of 20% in cooling capacity. Furthermore, an undercharge of about 25% would cause an average penalty in a cost penalty of \$60 per year per ton of rated capacity for typical electricity rates. For evaporator fouling, a reduction of air flow rate by 50% decreased average capacity by 14%, whereas annual cost increases by \$24 per ton. For condenser fouling, a reduction of air flow rate by 50% decreased average capacity by 9%, whereas annual cost increased by \$80 per ton.

Recent FDD research on packaged AC at Purdue has focused on the use of virtual sensors as a means of realizing a robust and low-cost approach to monitoring, detecting, and diagnosing faults. A virtual sensor estimates a quantity that would be expensive and/or difficult to measure directly. Various virtual sensors have been developed for vapor compression equipment. Virtual sensors can be embedded in a permanently installed control or monitoring system and used for early detection and diagnosis of faults. Existing data and laboratory tests were used to develop a FDD demonstration for refrigerant and air-side faults, including faulty economizer operation, heat exchanger fouling, and faulty refrigerant charge. A number of virtual sensors have been developed using RTU test data to enable a demonstration of diagnostics systems for RTUs. The RTU virtual sensors were shown to provide predictions that are within 10% of direct measurements. Some initial video demonstrations have been developed for RTU diagnostics.

In addition, a complete implementation for an FDD system has been developed and connected to data obtained from an RTU monitored in the field. The user interface incorporates integrated virtual sensors to provide diagnostic outputs and performance impacts of the fault(s). The diagnostic outputs include: 1) loss of compressor performance, 2) low or high refrigerant charge, 3) fouled condenser or evaporator filter, 4) faulty expansion device or liquid-line restriction, and 5) economizer faults. Health and economic status reports for equipment are generated using fault impact indices that measure degradation in system cooling capacity and efficiency (COP). More detailed fault information is provided that includes the probabilities for the existence of different faults and trending of fault indices. This data is thought to be useful in building confidence in the FDD system outputs by users.

VRC, VRMF, and VAF sensors for three DX systems at Building 101 have been developed and demonstrated using data from Building 101. Although it was not possible to fully validate these sensors, the outputs did demonstrate the proper dependence on compressor and fan staging and did not deviate from normal behavior during the course of the evaluation.

3.7. Future Studies

More extensive testing of the 4-ton RTU system at the Herrick Laboratories will be performed to provide a complete evaluation of the demonstration FDD system under a wide range of fault and operating conditions. A more complete video demonstration will be developed that illustrates all of the important features of the FDD system that includes performance impacts and service recommendations. The testing will include multiple-simultaneous fault implementation.

4. AHU-VAV Fault Diagnosis

4.1 Introduction

With the advent of more advanced building control systems, and the continuous reduction of sensor costs, there is a burgeoning opportunity to implement systems for early and effective detection and diagnosis of faults. Presently, faults in AHUs are most commonly identified through occupant complaints. As a result, only faults resulting in system not adequately conditioning the space will be detected. This leads to many energy-wasting faults persisting in an AHU-VAV system perpetually or for extended periods of time. AFDD for HVAC applications has been an active area of research for more than two decades, but yet there remains a lack of reliable, affordable, and scalable solutions for AHUs.

During BP2, the Drexel team worked to complete three deliverables in the effort to advance AFDD for AHUs toward widespread commercialization. Briefly, these three areas can be summarized as follows:

1. Completion of the Dynamic Fault Simulation Testbed for AHU-VAV systems;
2. Development and demonstration of the Pattern Matching Principle Component Analysis (PMPCA) fault detection method;
3. Investigation of fault incidence and associated energy impacts via engagement with local industry and experimental data.

The first deliverable, the fault simulation testbed, allows for the simulation of 51 discrete faults during any seasonal operating condition specified by the user. Additionally, the severities of these 51 faults can be adjusted as desired by the user, resulting in many more faults than could be tested experimentally. This testbed can now be used for comparison and analysis of AFDD strategies for this EEB HUB project. This allows researchers to identify the most effective AFDD methods as well as individual strengths and weaknesses of the methods. Additionally, this testbed is being shared with other researchers as part of a “beta test”, in which it can help progress the research in this field beyond solely the scope of the HUB.

For the second task, Drexel’s team was able to successfully demonstrate the efficacy of a novel fault detection method. This data-driven method that was shown to detect approximately 90% of the AHU faults studied, with an overall false-alarm rate of less than 1%. It is a purely machine-learning method requiring only fault-free training data, and with no requirement for customization for different AHU applications. These factors, combined with the high detection and low false-alarm rates, sets this AFDD technique apart from other methods recently proposed in the literature.

The third item, an investigation of the energy implications of AHU faults, combines analysis of experimental data with interviews conducted with local industry stakeholders. The primary intent of the interviews was to gain further insight into fault occurrence probabilities, as they are observed in the field. This type of information is essential for prioritizing the efforts of AHU diagnostic research, and also allows for increased accuracy when estimating the energy impacts and economic benefits of AFDD for AHUs. Beyond this primary goal of informing our fault incidence estimates, the interview process also provided feedback from industry regarding their needs and desires for effective AFDD. It is believed that this interaction will aid in the alignment of the research with industry needs, resulting in a method that can be readily commercialized.

The work performed by the Drexel team during BP2 is summarized in the following document. Below, a brief overview of the existing state of the industry and current research is provided for

background. This is followed by individual sections detailing the each of the three objectives described above. Each of these sections provides an overview of the goals and the methodology employed to achieve these goals, followed by a discussion of the results obtained and any relevant conclusions.

4.2. Background and Brief Review of Relevant Literature

Over the past couple of decades, significant research efforts have been undertaken to address the need for reliable AFDD for building HVAC systems. The research can be grouped into three broad categories of approaches: (1) physical modeling methods, (2) rule-based methods, and (3) data-driven methods (a good overview is provided by Katipamula et al., 2005a and 2005b). Additionally, a number of approaches have utilized hybrids of these method categories.

While a number of the different methods have made important progress, the lack of widespread industry adoption of AFDD for AHUs is indicative of certain drawbacks or limitations found in each of the existing methods. These limitations are often related to the time and costs required to customize or tune a system so that it can operate effectively in each building in which it will be employed.

This review includes a review of AHU AFDD methods and the literature related to the energy impacts of faults.

AFDD for AHU-VAV: Pattern Matching PCA Method

For the sake of brevity, this section includes a discussion of only the most recent advances in AFDD, with a focus on the most promising approaches for commercialization. It is organized with brief discussions of current trends and recent advances spanning the following topics:

- General AFDD techniques across various fields
- AFDD techniques for non-AHU HVAC applications
- AFDD methods for AHU applications
- PCA for non-AHU HVAC applications
- PCA for AHU AFDD applications

4.2.1.1. General AFDD Overview

Of the three general categories of AFDD methods, *model-based methods* are one of the most common approaches. Model-based methods, as the name implies, require some model of the system in question for analysis. This method has proven to be effective for self-contained factory-built HVAC systems, but it is often inefficient for built-up systems due to the impracticality of creating a new model for every building.

A derivative of the model-based system is a *rule-based method* founded in a priori knowledge of the dynamics of the system. These types of systems are typically derived from expert knowledge, in a troubleshooting method similar to how a technician would analyze the data, using a series of if-then type statements. Recently, these rule-based type systems have been combined with active diagnostic methods that alter a system's performance to gather more information, with relatively good success.

The third category of methods pertains to data driven models. These methods are typically divided into two different categories, black-box models and grey-box models. The difference between these two types of models is defined by if the model parameters utilized define a physical function of the system or not. Black-box type models include methods like multiple linear regression, artificial neural networks,

and fuzzy logic. In a grey-box model, the parameters are determined based upon system variables, and may require a priori knowledge to be incorporated.

The method presented in this paper is a data-driven method, which utilizes a principal component analysis (PCA) based detection method in the algorithm. PCA and Partial Least Squares (PLS) methods are among the most basic, and common statistical methods used for fault detection.

However, complex industrial processes operating under multiple operating conditions often invalidate the underlying assumptions of PCA and PLS techniques. Some assumptions inherent in when using PCA include linearity, and that the operating data follow a unimodal Gaussian distribution. To address this shortcoming in other industries with similar issues, clustering techniques have been suggested like Gaussian Mixture Models (GMM) (Yu and Quin, 2008), PCA-based GMM (Yu, 2011), and Hidden Markov Models (Lee et al., 2010).

Clustering is more effective in processes with fewer operational conditions than HVAC processes. The difficulty often encountered when using the classifier-type methods for HVAC applications results from the vast number of unique operating conditions experienced during building operation. During the learning process of these clustering methods, it is difficult to adequately define all of the states or operating conditions that the system will experience. The data is typically clustered into too few states for adequate fault detection.

Additionally, the use of these types of methods for fault diagnosis typically requires faulty training data that is not usually available for individual systems. The method presented in this paper attempts to overcome the non-Gaussian and non-linear operation of AHUs through the use of a pattern matching method. This method carefully selects the data used to train each PCA model in a manner that approximates a linear and Gaussian process.

4.2.1.2. AFDD for HVAC Applications

The HVAC field, as a whole, has experienced significant advances in AFDD over the past couple of decades. However effective fault detection for AHU-VAV systems still lags behind the progress made on other components of HVAC systems. Primary systems, like boilers and chillers, as well as packaged units, have the advantage of being able to be tested by the manufacturer in order to set tolerances and thresholds for fault detection and diagnosis.

In a recent analysis of data-driven AFDD methods for a primary system, Reddy (2007) analyzed four proposed chiller AFDD methods: model-free fault detection with a diagnosis table, a multiple linear regression model with diagnosis table, Principle Component Analysis (PCA) model with diagnosis table, and a linear discriminate and classification approach. The second method was identified the most promising chiller AFDD tool based upon a sensitivity analysis of false alarm rates.

Li and Braun (2007a, 2007b, 2009) investigated the effects of multiple simultaneous faults for air-conditioners and heat pumps. They found that decoupling the effects of the faults was the key for accurate diagnosis. This same strategy of decoupling was employed by Han (2011), using a support vector machine (SVM) approach.

Ma and Wang (2011) proposed a fault detection method based upon tracking various performance indices. Upon these indices flagging a fault, the diagnostic and control strategies are implemented using a rule-based method. It is unclear whether the thresholds utilized will be effective across multiple chillers, or whether the thresholds will have to be customized for each chiller model or each chiller application.

Zhao et al. (2013) proposed a chiller fault detection strategy that attempts to simulate the diagnostic process that an expert would utilize to diagnose faults. This method appears to be more robust than a simple rule-based method due to the incorporation of Bayesian belief network theory.

4.2.1.3. Literature: AFDD for AHU-VAV Systems

The AFDD techniques utilized for AHU-VAV systems are often similar to the approaches utilized for other HVAC components, but often add another level of complexity to address the various operational modes and custom installations.

House et al. (1999) demonstrated the application of several classification techniques for AFDD of seven different faults in an AHU. ANN classifiers, nearest neighbor classifiers, nearest prototype classifiers, a rule-based classifier, and a Bayes classifier were compared for both fault detection and fault diagnosis. The Bayes classifier appeared to be a good choice for fault detection. For fault diagnosis, there were not significant differences in the performance of six classifiers. In addition, all of the classification methods studied as well as neural networks method required both fault-free and faulty data for the development of models.

Wang and Jiang (2004) utilized CMAC neural networks to perform AFDD on the heating and cooling valves. Schein et al. (2006) demonstrated the utility of a rule-based AFDD method for AHUs, using the NIST-developed APAR (AHU performance assessment rules) method. This method first identifies the mode of system operation, then applies a set of rules accordingly. This method was found to be able to effectively detect a variety of faults. A potential drawback with this method may be some difficulty with setting the thresholds that trigger a fault for a variety of different AHU implementations.

Seem and House (2007) indicated that some of the problems with extending AFDD techniques from the simulations and laboratory tests include unstable control, a lack of standard control sequences, and data handling challenges. To combat these challenges, they recommended a novel method for integrated control and fault detection for AHUs. This method is based on finite state machine sequencing logic, combined with the measurement of residuals. The residuals are calculated after control logic imposes steady-state conditions on the system.

Tan and Dexter (2006) use a priori knowledge of variable interactions to infer air flow rates for which sensors are notoriously unreliable. Song et al. (2008) demonstrated an FDD tool for whole building HVAC AFDD, using a primarily rule-based method. This method relies on thresholds that must be calibrated for individual buildings. Yang et al. (2008) demonstrated a rule-based method for detecting faults in AHU sensors. Some of these rules require user-defined thresholds, but many of them are simply based upon relative sensor measurements that would not be found under normal operation of the system.

Fan et al. (2010) investigated AHU-VAV sensor faults, utilizing back propagation neural network models for fault detection and a combination of wavelet analysis with Elman neural network (a type of feed-forward neural network) for fault diagnosis. The BPNN model requires training with normal operating condition data, and the Elman model compares cluster centers with known fault cluster centers, so it requires faulty data for accurate fault diagnosis.

Wu and Sun (2011a and 2011b) proposed a method solely for fault detection, based upon unit energy consumption and a spatial-temporal partition strategy. This method requires offline training of normal and faulty behaviors to set the thresholds for fault detection.

Yang et al. (2011) proposed an AFDD method that utilizes fractal correlation dimension (FCD). This method is employed to deal with the measurement and system noise encountered in the AHU application.

They performed an investigation into the input parameters for the FCD method, and demonstrated the increased accuracy of fault detection using the de-noised data. Due to the time requirements of the FCD method, a hybrid method was proposed in Yang et al. (2013) in which FCD was combined with a direct-residual type method.

Some new trends in AFDD specifically with regard to AHU-VAV systems are the addition of proactive diagnostics and fault correction algorithms. Pakanen and Sundquist (2003) described this technique as automation-assisted fault detection. They utilized a method of artificially perturbing the system during normal operation, comparing with a model to generate a residual which can then be compared against some threshold. As mentioned previously, the modeling effort may limit the commercial applicability of this specific technique, but the concept of using system perturbations to identify abnormal behavior was successfully demonstrated.

Brambley et al. (2011) proposed an “active” method much nearer to commercial viability. This method used a combination of training tests during commissioning to develop models of normal operation, passive diagnostics to detect the symptoms of faults, proactive diagnostics to diagnose the cause of the fault, as well as fault correction algorithms. The fault correction algorithms were extensions of previous work performed at PNNL (Fernandez et al., 2009a and 2009b). Laboratory testing found that this combination was able to detect, diagnose, and correct faults in most of the cases tested. This paper also includes a useful list of faults that is among the most comprehensive in the literature.

The detection methods used require a number of training algorithms to create thresholds for the passive fault detection process. These thresholds are generated by running the system through a variety of operating conditions, and tracking the interactions of different variables. The diagnostic methods used are rule-based methods requiring a priori knowledge of the physics of the system. The algorithms were able to correctly diagnose all of the faults tested in the study. There was no discussion of how varying weather conditions and building loads affect the training, or the results.

Najafi et al. (2012) proposed a machine learning approach that utilizes a Bayesian framework that results in a probabilistic output. This type of output has significant benefit, especially with regard to the decision-making process that follows the fault detection process. A potential difficulty with this method is the requirement to estimate prior probabilities of faults. Additionally, this method requires fault signatures, described as hypothetical fault behavioral patterns, and it is unclear if these are applicable across many different AHU applications.

Wang et al. (2011) investigated terminal unit faults utilizing autoregressive time-series models to predict the measured variables, and cumulative sum control charts to detect and a rule-based fault classifier to diagnose faults.

Wang et al. (2012a and 2012b) use a combination of model-based and rule-based techniques to perform AFDD for AHUs. The innovative part of this method is the genetic algorithm-based optimization method that reduces the residual between the actual and predicted values as the system operates. The drawback to this method is that, due to its continuously-adaptive nature, it is only effective for detecting abrupt faults and cannot detect degradation faults.

Zhu et al. (2012) demonstrated AHU sensor fault detection using a neural network technique preprocessed with wavelet transform and fractal methods. The wavelet and fractal methods analyze the original data and determine the complexity of the data, and the neural network is used for fault detection.

4.2.1.4. Principal Component Analysis Literature

In this paper, *principal component analysis (PCA)*, is used to transform a number of related process variables to a smaller set of uncorrelated variables. PCA serves as the most fundamental multivariate statistical process monitoring (MSPS) method, and is proven to be effective for reducing the dimensionality of a large feature space. Kourtí (2004) provided a good overview of the PCA method.

There are numerous variations or extensions of the PCA method that have been utilized for fault detection algorithms. Some examples of this include **multi-block PCA**, in which a large data matrix is divided into smaller blocks (Qin et al., 2001, Smilde et al., 2001, Du and Jin 2007a, 2007b, and 2007c), **dynamic PCA** in which a time-series relationship can be incorporated into the conventional PCA analysis (Ku et al., 1995), **kernel PCA** in which input vectors are mapped into a high-dimensional feature space via a kernel function (Yoo et al., 2006), provided a useful demonstration of this type of method, **recursive PCA**, in which the model is recursively updated based upon different criterion (Li et al., 2000), and **multi-scale PCA**, incorporating wavelet transforms (Bakshi, 1998 and Hwang and Han, 1999), among many others.

Ralston et al., 2004 proposed a technique that uses confidence limits on the residuals of each individual variable, rather than the overall residual. Sun et al. (2005) utilized a PCA-based method for boiler leak fault detection. This method uses an s-term sum method for data pre-processing and a moving cumulative alarm method to reduce the false alarms typically associated with the use of Hotelling's T^2 and SPE metrics for fault detection.

The increasing popularity of the use PCA methods for fault detection has resulted in many multiple applications being proposed for HVAC fault detection. This section provides a summary of the PCA-based methods recently proposed for HVAC components, excluding the AHU-VAV components. The following section will delve into the PCA-based methods proposed for AHU-VAV systems.

Wang and Chen (2004) demonstrated a PCA-based AFDD method for central chilling systems. This paper focused on the sensors, and utilized the unreconstructed variance method for creating the PCA models. Wang and Qin (2005) used both the T^2 and SPE thresholds for detecting VAV sensor faults, and isolated the fault using the contribution plot method. This method uses the VRE method for creating the PCA models.

Xu et al. (2008) developed an enhanced sensor AFDD strategy for centrifugal chillers using wavelet analysis method and PCA method. Processing measurements of sensors without pre-treatment may deteriorate the performance of sensor AFDD strategy using PCA because of the embodied noises and dynamics. Wavelet analysis can extract the approximations of sensor measurements by separating noise and dynamics.

Chen and Lan (2009) used a PCA-based method for fault detection of condenser fouling in an air-source heat pump. They were able to successfully demonstrate fault detection for a single, steady-state mode of operation. The variance of reconstruction error (VRE) method was used to create the PCA model, and the SPE threshold was used for fault detection. There was no discussion of overall detection rates or false alarm rates.

Chen and Lan (2010) used a PCA-based method for detecting sensor faults in building billing systems. They were able to successfully demonstrate fault detection using unreconstructed variance (UCV, similar to VRE) to create the PCA model and the SPE threshold was used for fault detection. Fault diagnosis was performed by reconstructing the data until it is not faulty, and isolating the fault "direction". Temperature sensor faults were diagnosed successfully, while flowrate sensor faults would require additional

diagnostic techniques. This testing was limited to steady-state operational conditions during the summer, and required only three days of training data. The fault detection limit for this process was reported as 1°C. There was no discussion of overall detection rates or false alarm rates.

Hu et al. (2012) utilized an adaptive PCA method for chiller FDD, in which the samples of the training data that exceed the SPE fault detection threshold are recursively removed. This paper stipulates that the rows of data, or samples, which are removed, are not healthy and contain useless or erroneous data. Wang et al. (2012) used PCA to reconstruct sensor faults and recalibrate sensors with bias.

PCA method has been widely used for AFDD in many fields, and there has recently been significant growth of interest in the use of PCA for AHU-VAV diagnostics. Some of the key difficulties with applying PCA methods in HVAC area lies in the fact that HVAC systems are highly nonlinear and greatly affected by outdoor and indoor conditions, such as weather conditions and internal load changes.

Wang and Xiao (2004) proposed a PCA-based scheme for AHU sensor fault diagnosis. In this scheme, faults are detected using the Q-statistic or squared prediction error (SPE). For the diagnostic stage, the faults are isolated through a combination of contribution plots and expert rules.

Qin and Wang (2005) proposed a hybrid method for AHU-VAV AFDD. This method utilizes different techniques for detecting different faults. Some faults are detected using a rule-based method, some by monitoring performance indices (based on system models), and others through the use of statistical process control models. These models utilize PCA, and are applied for the detection of terminal unit sensor flow biases. It utilizes a multi-block PCA method that separates the AHU from the terminal units, and also uses the PCA method to reconstruct and correct the sensor biases.

Wang and Fu (2006) presented an AFDD strategy for a typical AHU to detect degradation sensor faults. A condition-based adaptive scheme was used to update the PCA model to follow the normal shifts in the AHU process due to changing operating conditions, where the outdoor air temperature and humidity were selected to represent the changing operating conditions.

Du and Jin (2007a, 2007b, 2007c, 2009) used a PCA-based method to perform fault detection for AHU-VAV systems. All of the papers were very similar, and they utilized the same method for all cases, but used different variables to build the models to detect different faults, in a manner similar to the multi-block PCA method used by Qin et al. (2001). They reported successful results using PCA for fault detection, and by combining PCA with joint-angle-analysis (JAA) and expert rules for diagnosis. The use of JAA requires a fault signature library against which to compare the faults, and there is no discussion of whether this library can be generalized across different AHU-VAV systems. There was no indication given as to how they constructed the PCA models with regard to PC retention, and no overall detection or false-alarm rates were provided for any of the papers. All of their demonstrations were carried out using an AHU-VAV fault simulator. Also, a number of the sensors utilized in their analysis are not typically installed in AHU-VAV systems.

AHU Fault Energy Impact Literature

There is very limited information in the literature relating to the energy impacts of faults for HVAC and AHU-VAV systems. Energy impacts of faults are a function of multiple factors:

- The difference of energy consumed when comparing operation of the AHU-VAV system with the fault versus fault-free operation (can be positive or negative)
- The probability of the fault occurring
- The probability of the fault going undetected without an effective AFDD procedure in place

Lee and Yik (2010) investigated the energy implications of air-side faults in AHU-VAV systems. Ginestat et al. (2008) investigated the energy consumption impacts of AHU-VAV faults, but also incorporated an analysis of the impact of faults on indoor air quality (IAQ). Kwok et al. (2004) investigated failure rates of various HVAC components for the purpose of creating an optimal preventative maintenance model for office buildings. Qin and Wang (2005) performed a case-study in concert with designing an AFDD method, which resulted in some published data on fault occurrences for an AHU-VAV system.

Beyond these few papers, there is limited data on fault energy impacts on AHUs that is publicly available. A more detailed discussion of the findings mentioned here is included in Section 4.8, when the data from the literature are compared to the results obtained in this study.

4.3. Dynamic AHU-VAV Fault Simulation Testbed

Testbed Overview and Functionality

Despite the importance of the AHU-VAV systems and the AFDD strategy development, only limited experimental studies under restrictive scopes were available to evaluate AHU AFDD methods (Norford, et al, 2000, Carling 2002, and Castro et al, 2003). A dynamic AHU-VAV simulation model that is capable of producing fault free and faulty operation data for commonly used AHU configurations, and control and operation strategies is thus needed. Moreover, developed dynamic AHU simulation models need to be systematically validated with experimental data for both fault free and faulty operation before any credibility can be given to the prediction accuracy and usefulness.

In a recently completed ASHRAE project (Wen and Li, 2010), a virtual dynamic AHU-VAV testbed (referred to as the ASHRAE 1312 testbed hereafter) representing a small four-zone commercial building that is equipped with a single duct AHU-VAV system is developed. In this testbed, common AHU faults with various fault severities, are modeled. Both the fault free and fault system models are extensively validated using experimental data generated from a real small commercial building.

However, the ASHRAE 1312 testbed does not have fault models for the VAV terminal units. Therefore, in this project, the ASHRAE 1312 testbed is extended to include typical faults for a VAV terminal unit. Moreover, existing experimental data from a NIST project (NIST 6964, Castro et al. 2003) are used for the validation of the VAV terminal unit fault models. The ASHRAE 1312 user interface is also further developed to be more user-friendly and to include the VAV terminal unit faults selection.

In this section, the following perspectives are discussed:

1. Identifying common VAV terminal unit faults and their severities;
2. Extend an existing four zone AHU-VAV system model (Wen and Li 2010), so that it can produce faulty operational data from its VAV terminal units;
3. Identifying and collecting existing experimental data to validate the fault models developed for the VAV terminal unit model;

VAV Fault Model Development and Available Data

VAV terminal unit faults

Using a manner that is similar to that reported in the ASRHAE 1312 project (Wen and Li 2010), potential VAV terminal unit faults are identified. As listed in Table 4.1, the VAV terminal unit faults can be categorized as controlled device fault, controller fault, equipment fault and sensor fault. The controlled

device fault, like damper stuck, reheat valve stuck, is modeled by fixing the damper or valve position at certain stuck positions. In controller fault category, the controller unstable fault was modeled and simulated, by decreasing proportional band. The equipment fault, like reheat coil fouling, was modeled by changed the thermal and hydraulics properties.

Table 4.1 VAV terminal unit fault summary

NO.	Category	Device	Type of Fault	Simulation	
1	Sensor	Temperature sensor	Bias signal	Y	
2			Drift signal	Y	
3			Randomly varying	N	
4		CFM sensor	Bias signal	Y	
5			Drift signal	Y	
6			Randomly varying	N	
7	Controlled Device	VAV damper	Fully open	Y	
8			Stuck	Fully closed	Y
9				Partially open	N
10		Leaking	Y		
11		Valve of Reheating Coil	Stuck	Fully open	Y
12				Fully closed	Y
13				Partially open	N
14			Leakage	Y	
15			Flow block	N	
16		Valve Size	Improperly	N	
17	Controller	VAV Damper	No signal	N	
18			Unstable		Y
19			Software	Improper set point	N
20		Code error		N	
21		Reheating Coil	Unstable	Y	
22	Reverse Action	N			
23	Equipment	Reheating Coil	Fouling (fin and tube)	Y	
24			Reduced capacity	N	
25			Leakage	Y	

Fault modeling

The real physical mechanism of a fault was often very complicated and that the purpose of fault modeling was not to replicate all detailed physical phenomena but to replicate the most significant fault symptoms. And the objective of the validation process for faulty operation simulation model was to assure that the simulated operational data reproduce fault symptoms and fault severities. Most of the faults in this project are modeled similarly as in the ASHRAE 1312 which were by adding parameters or changing values of existing parameters.

Sensor fault

Two types of sensor faults, namely, discrete fault and drift fault were simulated in this project. Discrete faults were modeled by adding a user specified bias to the simulated sensor output, which was achieved by Eq.

$$Y_{output} = Y_{input} + Bi \quad (4-1)$$

where Y_{output} and Y_{input} were the output and input of a sensor model, Bi was an user specified bias which was kept as a constant.

Drift faults were modeled by linearly varying a bias, which resulted in a linearly varied simulated sensor bias as described in **Error! Reference source not found.**

$$Y_{output} = Y_{input} + S \times T \quad (4-2)$$

where T was the amount of time after a fault occurred, S was a user specified slope of drifting bias.

Controlled device fault

Controlled device category included three dampers (RA, EA, OA dampers) and two valves (heating and cooling valve). Two types of faults, namely, stuck fault and leaking fault were modeled. Damper or valve stuck faults were modeled by fixing the simulated controlled device position to be a user specified position. Leaking faults were modeled by adding a user specified flow rate when the controlled device was 100% closed

Controller fault

Only unstable control fault was simulated in this project, which was modeled by implementing a user specified proportional band for the PID controller.

Equipment fault

Two types of reheat coil fouling faults were simulated in this project, namely, air side fouling fault and water side fouling fault. In order to simulate the air side fouling faults the values of thermal conductivity of coil was decreased and the values of air flow resistance was increased. For the water side fouling faults the values of thermal conductivity of coil and water flow resistance were increased to imitate the fault symptom (House, Lee et al. 1999).

Available experimental data from NIST 6964

There are very limited experimental data available from the literature that focus on VAV terminal unit faults. The only experiment data that can be used to validate the VAV terminal unit fault models are from the NIST project (NISTIR 6964, Castro et al. 2003). The NIST 6964 experiment were performed at the Iowa Energy Center Energy Resource Station (ERS) in a similar manner as that reported in the ASHRAE 1312 experiments. More detailed information about the ERS test facility is provided in Section 4.6 and by Wen and Li, 2010. During the experiment, the VAV terminal unit faults were implemented in the A system of the test facility and the B system (which is completely identical to the A system with similar building loads) was served as the baseline fault free system. Three VAV faults were implemented artificially as described in the following section:

Hydronic Reheat Coil Valve Stuck Partially Open

By applying a control voltage from an independent source to the hydronic coil valve actuator in the West-A test room, the reheat coil valve was artificially stuck at certain positions.

Hydronic Reheat Valve Leakage

The fault was implemented by manually adjusting the reheat valve so that it did not close completely.

Failed Differential Pressure Sensor

The sensor was disconnected from the controller. This fault is not modeled in our testbed because this fault is often monitored by existing building control systems.

Model Validation

Validation process

For the two faults which have experiment data from the NIST 6964 project, the simulated results from newly developed fault model are compared with the experiment data to validate the simulated symptoms of those faults. For those faults without experiment data, the simulated fault results are compared with the simulated fault free results to analyze the fault symptoms.

VAV terminal unit reheat coil valve stuck open fault

Depending on the room condition, the reheat valve stuck open fault, generally yields more cooling load for the AHU to remove, especially in the summer. In this case, the discharge airflow rate increases to compensate the excess cooling load. Figure 4.1a shows the discharge airflow rate simulated from the testbed under fault-free and faulty conditions. The simulated discharge airflow rate when the fault exists is nearly two times of that under fault free conditions. The same fault symptom is reported in NISTIR 6964 (as shown in **Error! Reference source not found.**4.1b).

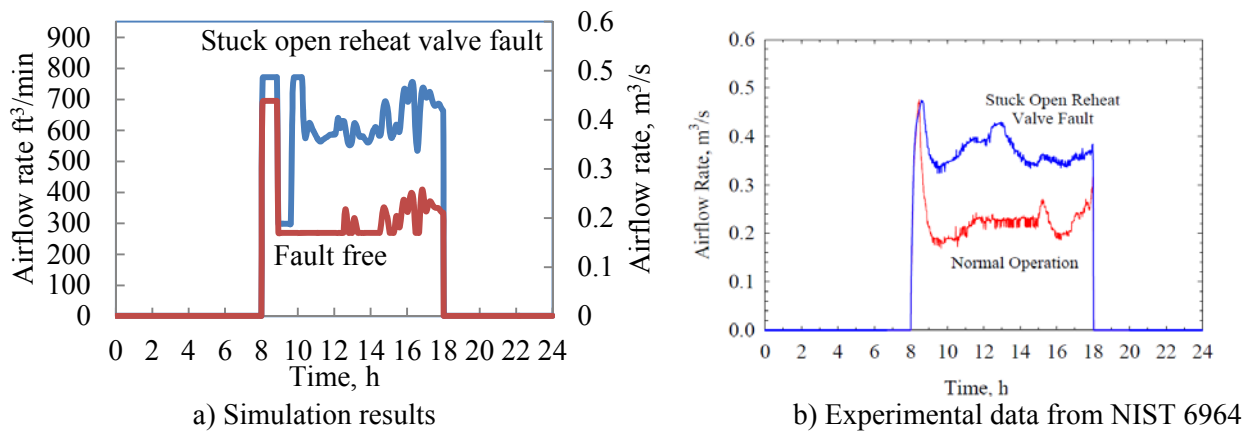


Figure 4.1 VAV terminal unit reheat coil stuck open valve fault

VAV terminal unit reheat coil valve leaking fault

Similar to that in the NIST 6964 project, a 10% leakage fault is simulated using the testbed. The fault causes an additional heat into the discharge air, which increases the discharge air temperature. Because discharge air temperature is not reported by the NIST project, this fault symptom is not compared with the experimental data here. In order to remove the same cooling load for the room, more discharge air is therefore needed. Figure 4.2 a and b demonstrate that the increased discharge air flow rate fault symptom is observed from both the testbed and the experimental data.

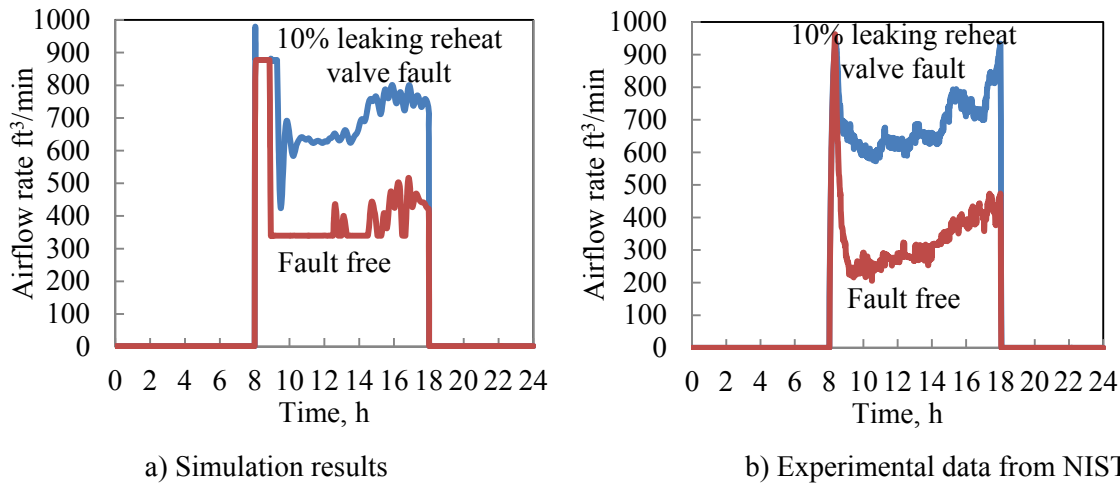


Figure 4.2 VAV terminal unit reheat coil valve 10% leaking fault

Other Modeled Faults

Other VAV terminal faults, such as VAV damper leaking, zone temperature sensor bias, zone airflow sensor bias, reheat coil fouling, VAV damper controller unstable, and reheat coil valve controller unstable faults, are also modeled in the testbed. Due to the lack of experiment data, the simulation results are only examined qualitatively. Both the fault free and faulty operation data are simulated using the testbed for each fault under the same weather condition (a summer weather condition). The fault symptoms are summarized by comparing the fault free and faulty operational data. This part of the results is summarized in Appendix 2.

4.4. Fault Detection Using the Pattern Matching PCA (PMPCA) Method

AHUs for “built up” or custom designed systems, pose a number of unique challenges to the typical fault detection paradigm. Model-based or heuristic methods are some of the most common techniques for performing AFDD, but these are not feasible for AHU applications. Since the design and implementation varies greatly from building to building, it is not cost-effective to create detailed models or perform extensive training.

Another complication when designing AFDD for AHUs results from the fact that building systems operate in nearly continuously transient states. During the course of the day, the system must compensate for the continuously varying weather and building loads. AFDD methods must be adaptable to function accurately regardless of the operational mode of the system. The non-linear manner in which the system moves through these different operational modes adds another layer of difficulty.

Additionally, the architecture of sensor networks in air handling units is not designed for diagnostic purposes. Constrained by cost, operational requirements, and practical considerations, many process variables that could facilitate AFDD are not typically measured. Figure 4.3 identifies a typical sensor system layout for an air handling unit.

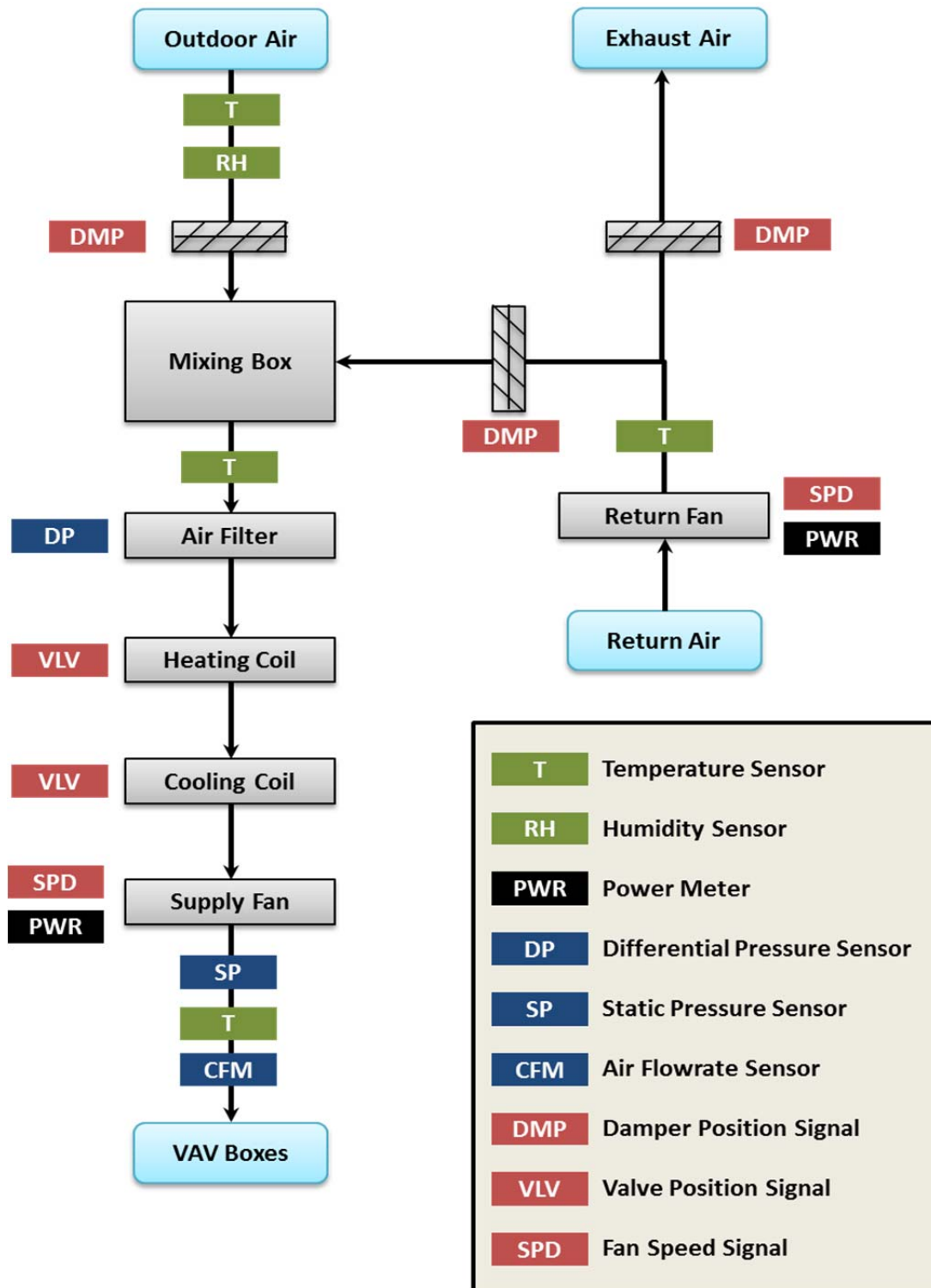


Figure 4.3 AHU schematic

The pattern matching PCA method proposed here overcomes the aforementioned difficulties by comparing current operational data with known fault-free data of the same operational conditions. By isolating only the most similar operating conditions for comparison, this method is able to overcome the non-linear and non-Gaussian constraints of AHU operational data.

The development and testing of an AFDD method for building HVAC systems should adhere to a minimum set of requirements, such that it will be practical for extension into industry. The objective is to create a practical AFDD protocol that:

- Can be implemented solely with historical fault-free data, and does not require data from faulty operation for training;
- Is efficient enough to be implemented for online monitoring;
- Is robust enough to handle all possible operating conditions;
- Can detect both degradation and abrupt type faults;
- Can detect both process faults as well as sensor faults;
- Has a very low false alarm rate, with a goal of less than 1%

The PMPCA method proposed meets all of these requirements, and overcomes many of the shortcomings of previously proposed methods that limit their ability for widespread commercial application. This section outlines the PMPCA method, starting by explaining the theory behind the pattern matching method and the PCA method for fault detection. The combination of pattern matching and PCA for AHU fault detection was first suggested by Li (2009), but the first large-scale demonstration of this method is presented herein. The use of this method for AHU fault detection required significant modification in order to consistently detect faults without false alarms, and the methods used for refinement are also outlined in this section.

Method Overview

The PMPCA method is comprised of two distinct phases: pattern matching to identify similar historical operating conditions that are known to be fault-free, and comparison of the online/test data with the historical training data using PCA-based fault detection techniques. The theory behind each of these methods is presented below, followed by an overview of the refinement process that was undertaken during BP2. The results of the method demonstration are presented in Section 6 of this paper.

4.4.1 PCA Overview

PCA is a statistical analysis method used for multivariate data when the correlation among the data is difficult to describe using math equations. This applies well to AHU-VAV systems with non-linear, hard to model, variable interactions. PCA rotates the coordinate axes and reduced the dimensionality of the variable subspace, transforming a group of correlated variables into a reduced set of variables that are uncorrelated or orthogonal to each other. For details on the theory and application of PCA methods, there are countless books and papers that have addressed this concept including Jackson (1991), Kourtis (2004), and Bishop (2008). The discussion provided here addresses only the specific ways in which the PCA method is applied for this method.

The PCA method maps the data into two subspaces, the principal component (PC) subspace and the residual subspace. The PC subspace captures the process systemic variations, while the residual subspace contains some of the noise from the system, and some error information. Both of these subspaces have applications for fault detection.

Prior to performing PCA decomposition, it is essential to pre-process the variables to make them non-dimensional. This requirement is primarily due to the fact that variables in the system have different units with different orders of magnitude. The preprocessing normalizes all of the variables to have zero mean and unit variance.

After normalization, the covariance matrix is calculated as

$$\Sigma = \frac{X^T X}{n - 1} \quad (4-3)$$

where X is the data matrix, and n is the number of process variables. An eigenvalue decomposition is then performed on the covariance matrix, and the eigenvalues and corresponding eigenvectors are obtained. The eigenvalues are non-negative real numbers with decreasing magnitude, i.e. $\lambda_1 > \lambda_2 > \dots > \lambda_n > 0$. The variance explained by each component in the PCA model is defined in Equation 4-4.

$$VE_k = \frac{\lambda_k}{\sum_{i=1}^n \lambda_i} \quad (4-4)$$

And the cumulative contribution to the overall variance is defined by Equation 4-5, below.

$$CV_k = \frac{\sum_{i=1}^k \lambda_i}{\sum_{i=1}^n \lambda_i} \quad (4-5)$$

The loading matrix corresponding to the first and largest eigenvalues describe the operating conditions of the system, while those associated with the smallest eigenvalues model the noise of the system and are not useful. The selection of the cut-point for when to stop including the decreasing PCs in the model is an important part of the use of the PCA method, and a variety of different techniques were investigated during the demonstration of this method. The details on this are presented below in Section 4.5.2.

Prior to presenting the details of the method, the concepts behind the pattern matching and fault detection are presented. This is followed by an overview of how the methods were refined, and the results of the demonstration.

4.4.2 Pattern Matching

A number of techniques have been developed for pattern matching in time-series data (Singhal and Seborg, 2002; Johannsmeyer et al., 2002), and the concepts behind these methods were utilized in the creation of the pattern matching method proposed here. The concept of pattern-matching is to select a “snapshot” of current data that is operating in steady-state, and find historical data that is sufficiently similar for comparison.

This is done using a moving window through the historical data. At different times during system operation, a window of time is selected and compared against all (or a subset of) historical data for similarity. Figure 4.4 provides a graphical representation of the various operating modes that a system moves between as a function of the outdoor air temperature. As the figure below indicates, outdoor air temperature is the primary driver of the different modes of operation, but the internal loads at any given time can vary greatly and also have a significant impact upon how the system is operating.

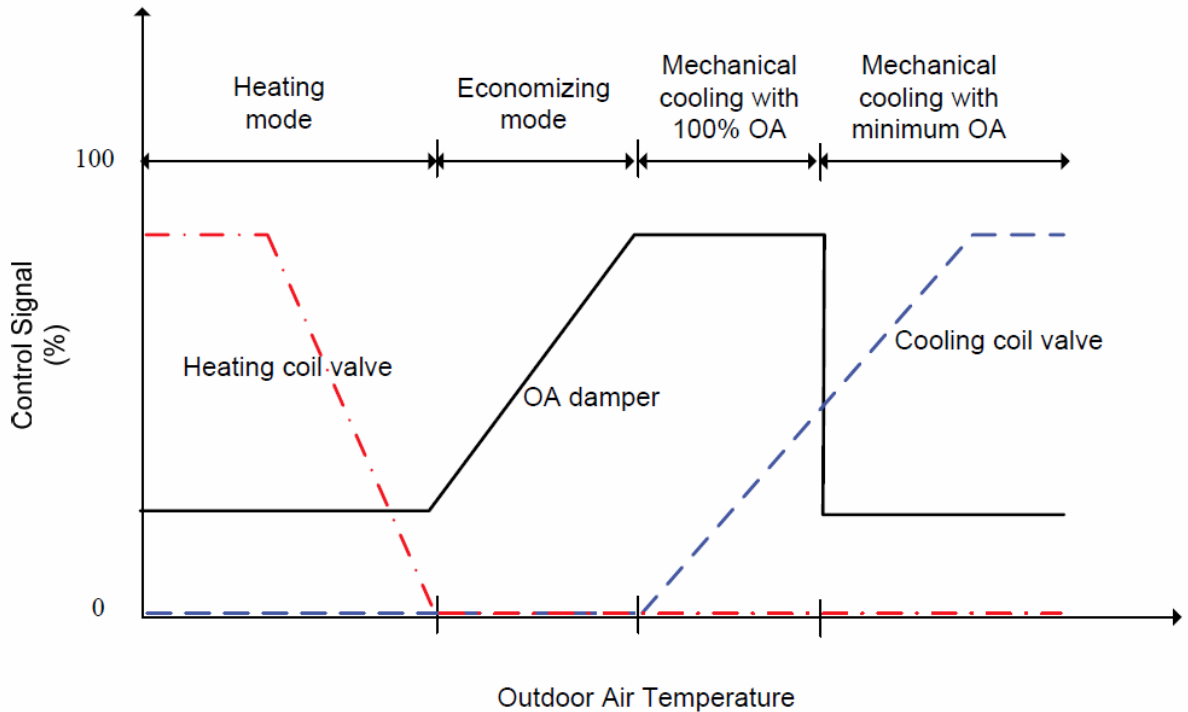


Figure 4.4 AHU operational modes

During the course of this demonstration, three different pattern matching metrics were tested: PCA similarity factor, modified PCA similarity factor, and distance similarity factor.

PCA Similarity Factor and Modified PCA Similarity Factor

The **PCA similarity factor** was first proposed by Krzanowski (1979). It creates a reduced PCA model and creates a PCA model for each data set. The PCA similarity factor compares the reduced subspaces of the PCA models, and is calculated from the angles between the principal components:

$$S_{PCA} = \frac{1}{k} \sum_{i=1}^k \sum_{j=1}^k \cos^2 \theta_{ij} \tag{4-6}$$

By reducing the dimensionality, it is possible to reduce the original principal component subspaces to smaller dimensions of the snapshot and historical data, designated as **L** and **M** respectively. Using this notation, the PCA similarity factor can easily be calculated as:

$$S_{PCA} = \frac{\text{trace}(L^T M M^T L)}{k} \tag{4-7}$$

Using the PCA similarity factor, all included components of the subspace are given equal weight. To improve upon this, the modified PCA similarity factor is weighted by the magnitude of the corresponding eigenvectors:

$$S_{PCA}^{\lambda} = \frac{\sum_{i=1}^k \sum_{j=1}^k (\lambda_i^l \lambda_j^m) \cos^2 \theta_{ij}}{\sum_{i=1}^k \lambda_i^l \lambda_i^m} \quad (4-8)$$

The comparison of how effective this improvement may be is included in the demonstration details provided in Section 6. Investigating the similarity of the PC subspace is only one part of the pattern matching test utilized. It is also important to identify the periods of time when the raw system data is most similar. To determine this, the distance similarity factor is also employed.

Distance Similarity Factor

The **distance similarity factor** is based upon the concept of using the Mahalanobis distance to measure the distance between the centers of the data sets. The center of the data is defined as the sample means of the historical and snapshot windows:

$$\bar{x}_S = \frac{1}{m_S} \sum_{i=1}^{m_S} x_i, \quad (4-9)$$

and the Mahalanobis distance is defined as:

$$\Phi = \sqrt{(x_H - \bar{x}_S)^T \Sigma_S^{*-1} (x_H - \bar{x}_S)} \quad (4-10)$$

where the matrix Σ^{-1} is the pseudo-inverse of the covariance matrix of the dataset. It is calculated using singular-value decomposition, incorporating only the number of eigenvectors used to explain the same data variance utilized for the PCA decomposition. The distance similarity factor is defined as the probability that the center of the historical dataset is at least a distance Φ from the snapshot dataset. By assuming a Gaussian probability distribution, this probability can be estimated by the complimentary error function, or:

$$S_{dist} = d \sqrt{\frac{2}{\pi}} \int_{\Phi}^{\infty} e^{-z^2/2} dz = 2 \times \left[1 - \frac{1}{\sqrt{2\pi}} \int_{-\infty}^{\Phi} e^{-z^2/2} dz \right] \quad (4-11)$$

As the program scans through the historical data, it calculates the PCA similarity factor, the modified PCA similarity factor, and the distance similarity factor for all historical windows compared to the snapshot window being tested. An overview of this process is included in Figure 4.5. Once these metrics have been computed for all historical windows, the most similar historical (known fault-free) windows are selected for comparison.

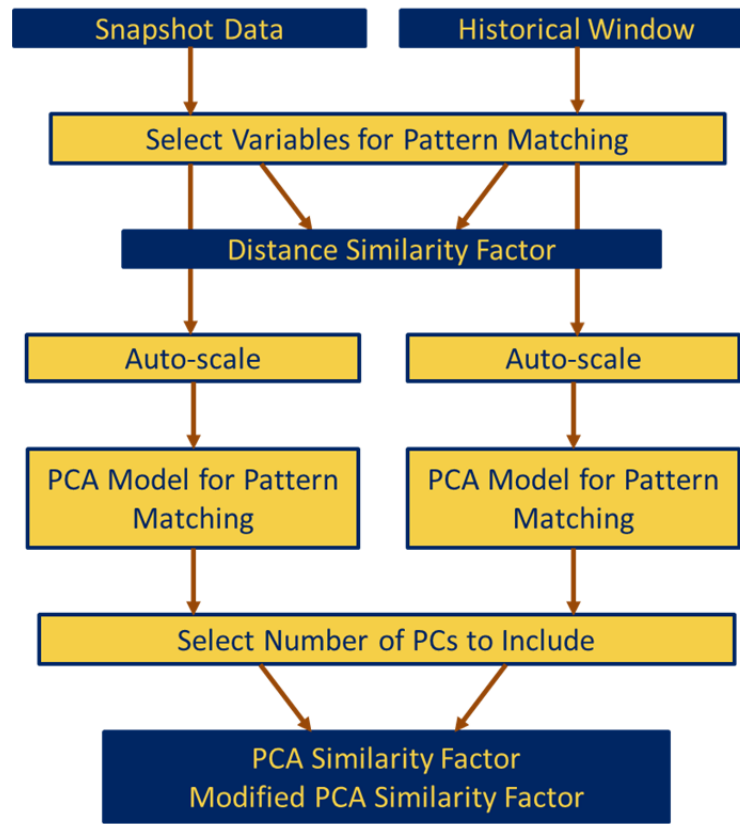


Figure 4.5 pattern matching algorithm schematic

To find the most similar historical windows, 5 different pattern matching metrics were used in total: the three described above (PCA similarity factor, modified PCA similarity factor, distance similarity factor) as well as two metrics that averaged the factors. One was the average of the PCA similarity factor and the distance similarity factor, and the other was the average of the modified PCA similarity factor and the distance similarity factor.

4.4.3 PCA Fault Detection

Once the historical data has been compiled, the next step is the PCA-based fault detection. As discussed above, the data is all normalized prior to analysis, then a PCA model is created based upon the historical data. From this PCA model, thresholds for faults are calculated in both the PC and residual subspaces. Once the fault thresholds have been calculated, the snapshot data undergoes the same scaling and PCA transformation as the historical data, and the results are compared with the thresholds. A fault is considered to have occurred when a certain percentage of the snapshot data points exceed the thresholds. Figure 4.6 provides a flowchart of the process for reference.

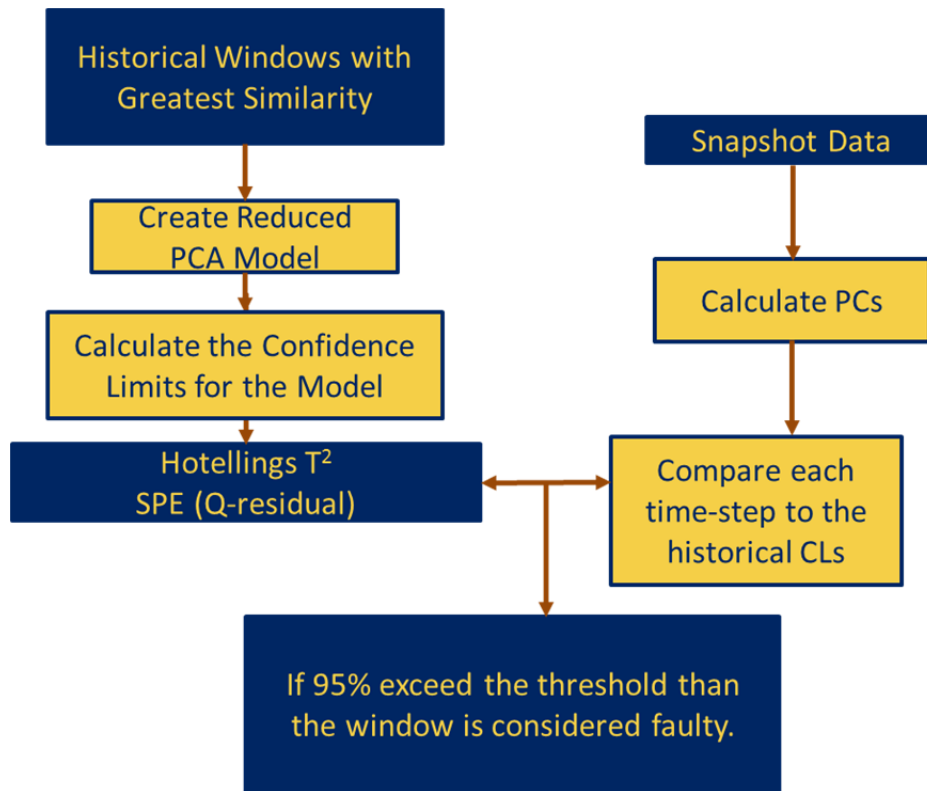


Figure 4.6 Fault Detection Algorithm Schematic

Hotelling's T^2

Once the reduced model was created using the historical data, the squared prediction error (SPE) and Hotelling's T^2 statistic for each time-step in the snapshot window data were calculated. The T^2 statistic can be calculated as

$$T^2 = x^T P \lambda^{-1} P^T x \leq T_\alpha^2 \quad (4-12)$$

where P is a matrix of the reduced space principal components, and x is the measurement matrix. The T^2 threshold assumes a Gaussian distribution, so the control limits at significance level α can be calculated as (Nomikos and MacGregor, 1995)

$$- \quad (4-13)$$

where n and s_{ref} are the number of observations and the estimated standard deviation of the t-score sample over the time interval. Note that the Gaussian assumption may not be valid for all AHU-VAV data, and the details of this investigation are included below. Since the size of the snapshot windows being used for the PCA analysis is relatively small, the threshold value is calculated using a larger window of multiple historical windows. This prevents the threshold from fluctuating too drastically from window to window.

Squared Prediction Error

The second metric used for fault detection is the SPE, or Q-statistic. The SPE is calculated from the residual subspace, and can be calculated using:

$$SPE = \|(I - PP^T)x\|^2 \leq \delta^2 \quad (4-14)$$

where x is a new sample vector, and δ^2 is the threshold for the SPE with a significance level α . The δ^2 value is calculated as (Nomikos and MacGregor, 1995)

$$\delta^2 = (s / 2m) \chi_{2m^2/s, \alpha}^2 \quad (4-15)$$

where the chi-squared variable is the critical value with $2m^2/s$ df at a significance level α , and m is the mean value of the Q-residuals from a larger window. Again, the threshold was calculated using the extended historical window. Additionally, two other methods were experimented with for setting the threshold – one built in method in the Matlab PCA Toolbox, and the other suggested in other literature.

For each time-step, the system was determined to be faulty if the 99% of the T^2 or SPE values exceeded the threshold within a given window. Since false alarms are known to plague PCA-based fault detection methods, this level was set very high. Different values for the alpha were tested during the demonstration and tuning of this method.

4.4.4 Method Development and Optimization for AHUs

The above methodology creates a framework upon which to base the AFDD algorithm, but this skeleton of a technique required significant experimentation for optimization. Optimization of this method is based upon maximizing the sensitivity of the algorithm to faults, under a strict constraint of minimal false alarms.

In practice, faults to AHU-VAV systems are not considered to be as critical as faults to primary systems like chillers and boilers, since space conditioning is often still possible under faulty operating conditions and the costs associated with AHU-VAV faults are perceived to be less costly. With increased investigation, the IAQ and cost impacts of hidden AHU faults are becoming better known, but for the purpose of this demonstration it was deemed essential to maintain an overall false alarm rate below 1%. This limit was determined through meetings with industry personnel who indicated a false alarm rate any greater would result in the AFDD system being ignored in practice.

Under this strict limitation, the sensitivity of the algorithm to fault detection was then maximized. This maximization was twofold: maximize the number of faults detected, and maximize the different conditions under which various faults can be detected. Due to the fact that AHU-VAV systems move through a multitude of different operating conditions based upon outdoor air conditions and interior building conditions, most faults are only detectable when they actually have a negative effect on the overall performance of the system.

In order to optimize the methodology a number of different variables were investigated. Due to the number of variables, and the time required to run each test, it was not possible to perform a parametric analysis of all possible combinations, but baseline values were selected based upon recommendations in existing literature and individual variables were varied one at a time, or in certain instances two or three at a time.

A brief overview of the variables/methodologies investigated is as follows:

1. **Data Scaling / Preprocessing** – The raw process data from the BMS arrives in many different units and magnitudes. In order to prepare this data for analysis, it must be scaled to even out the impact of the different variables. To do this, a few different methods were tested.
2. **Window Size** – The length of the window used for the snapshot window and the historical windows must be the same for the purpose of the pattern matching methods, however the optimal duration is unknown. Shorter windows capture a specific operating condition more effectively, but also result in less data being used in the analysis, so a balance must be struck.
3. **Number of Historical Windows Required** – Increasing the number of historical windows used to create the PCA model can result in a more robust model, but this can also result in the use of less similar windows in the model creation that could skew the model.
4. **Window Movement Rates** – The rate at which the snapshot windows need to be sampled, as well as the rate at which historical windows need to be sampled was experimented with. There is a trade-off between accuracy and speed that was investigated.
5. **Impact of Data Normality** – The use of PCA requires an underlying assumption that the data is Gaussian. This assumption is met to varying degrees by different training data and snapshot windows. The effect upon the results of the data normality was examined in this paper.
6. **Historical Data Requirements** – The quantity and quality of historical data plays a key role in the ability to perform accurate fault detection.
7. **Principal Component Retention** – PCA-based methods are widely applied across many different fields in the literature, and a number of different component retention methods have been proposed. A number of different methods have been investigated herein.

These different variables, and the way they impact the efficacy of the PMPCA algorithm were all explored, and the results of these analyses are included in Section 6, where the details of the refinement and demonstration are presented.

4.5. Pattern Matching PCA Demonstrations

The efficacy of the PMPCA method, detailed above, was demonstrated/tested during the course of the past year. The demonstrations during BP2 were all carried out using various sets of offline data, spanning different building types and all possible operating conditions. From the outset, the PMPCA method appeared promising by often accurately distinguishing faulty behavior from normal system operation. However, through the course of experimenting with various changes in the algorithm, the consistency of detection was significantly increased and, more importantly, the false-alarm rate was significantly decreased.

Demonstration Overview

The demonstrations conducted during BP2 consist of many different variations of the PMPCA algorithm tested across the following conditions:

- Small office building experimental data from winter, summer, and shoulder seasons: this dataset is from the ASHRAE 1312 project and the experiment is conducted at the Iowa Energy Center Energy Resource Station (ERS). More information is given in Sec. 4.6.2.1. The dataset is referred to as the ASHRAE 1312 ERS data.

- Medium-sized office building experimental data from winter months: this dataset is provided by the UTRC team (more description is provided in Sections 2.2 and 4.6.2.2) and is referred to as the UTRC data
- Small office building simulation data from the developed testbed

During all iterations of testing, detailed records were maintained. All tests were performed for all five different pattern-matching metrics, and the results were recorded in both the PC and residual subspaces (T^2 and X^2 thresholds, respectively). The records kept included the following items for all tests:

- Percentage of data points in each window that exceed the thresholds
- Percentage of windows deemed to be faulty
- Overall percentage of data points correctly identified (correctly found to be faulty or fault-free, or the inverse)
- Overall percentage of windows correctly identified as faulty or fault-free
- The individual breakdown of results by each fault and season for all of the various tests performed

Additionally, during the course of the study, a variety of different factors were hypothesized to be impacting the results. As the tests were conducted, some other metrics were tracked as well:

- The T^2 and X^2 threshold values for each window
- The mean and median T and Q values for each test window
- The mean, median, minimum, and maximum similarity factors for the historical data
- The number of historical windows that the test data was compared against for each window
- Various normality metrics
- The percentage difference of the means of the raw data between the snapshot and historical data for all of the variables measured
- Whether or not the window being tested was operating in steady-state conditions
- The overall slope of the snapshot window
- The standard deviations of the training and test window variables
- The raw data used to create the training and test models

For the purposes of space, information about all of this data for all of the different cases tested has not been included in this narrative. Included are the results that can provide insight on the method's efficacy and the tuning process of the method.

Base Case & Input Methodology

Above, the outputs and how they are tracked are discussed. This section discusses the inputs for the algorithm and how they were selected and then varied during the experiments. Due to the quantity of different inputs, and countless combinations of said inputs, it is not possible to conduct a parametric analysis of the inputs so a targeted approach was required. To this end, the first step was to select a "baseline" for the inputs used in the algorithm. This baseline was based upon values and results found in existing AFDD literature. These baseline values are as follows:

- Steady-state filter: off (data was tracked, but was not utilized for filtering at this stage)
- Percent of variance included in pattern-matching PCA models: 95%
- Window size for pattern-matching: 45 minutes
- Historical window scan rate: 5 minutes
- Number of historical windows used: 10
- Percent of variance included in fault-detection PCA models: 95%
- Alpha value for SPE threshold: 0.01
- Alpha value for T^2 threshold: 0.05
- Percentage of points in a window exceeding the threshold that constitutes a faulty window: 99%

These baseline values were used to test three different sets of data to demonstrate the PMPCA method, and then individual inputs were varied to test how the results responded to the various changes. Below is an overview of how the PMPCA baseline method worked for 3 different sets of data.

ERS Data

The first set of data tested was data acquired from the ERS test site during the ASHRAE 1312 project. This data was collected from a test-site that simulates a small office building. The office building layout is included in Figure 4.7 **Error! Reference source not found.** The building consists of two AHUs, each of which serves 4 different rooms. The design of the test facility was intended to have each AHU serving rooms with nearly identical loads. As can be observed, each AHU serves rooms facing east, west, south, and one interior room.

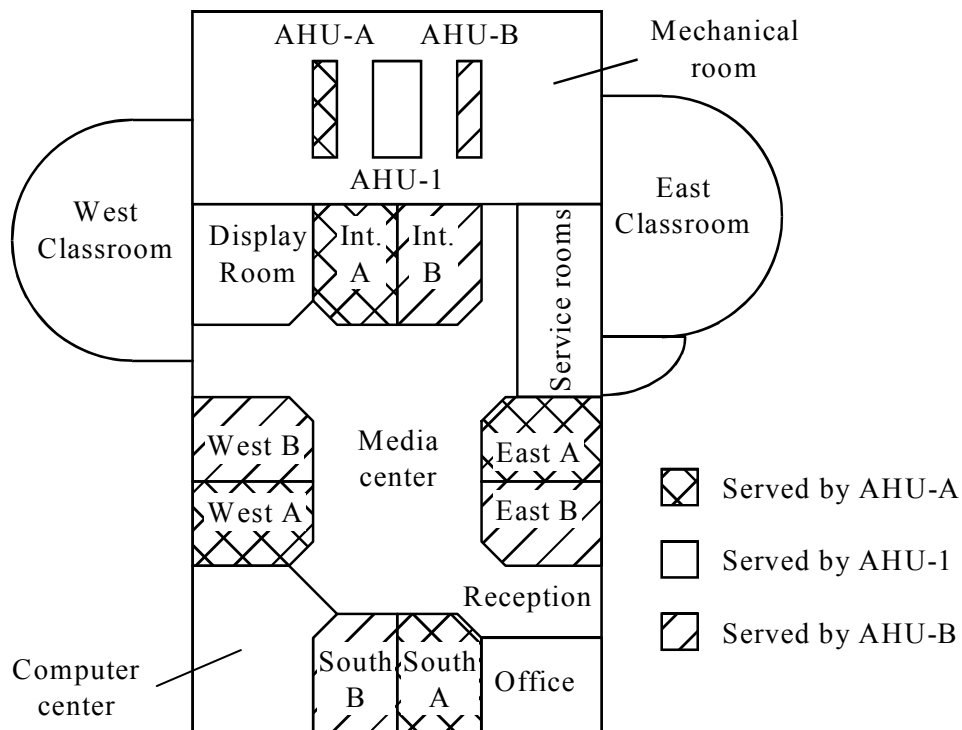


Figure 4.7 ERS experimental setup

While the two AHUs will not be exactly the same, the performance was found to be very similar under all different operating conditions. During the course of the study, AHU-B was continuously operated in a fault-free state, while AHU-A was artificially injected with various commonly-occurring faults.

For the purpose of this study, it was necessary to gather adequate fault-free data from the system, so AHU-B was used to train the model with fault-free data, and AHU-A was used for the test data. Although this is not ideal, it was hoped that they would operate similarly enough for effective testing of the AFDD method.

The ERS data was trained with 15 days of fault-free data from each season (summer, winter, and transition seasons) from AHU-B, and a variety of different faulty and fault-free states were tested using AHU-A. The results are reported for the combined pattern-matching metrics that utilize the combination of the PCA similarity factor and distance similarity factor (S_{tot}), and the combination of the modified

Table 4.2 Baseline results using ASHRAE 1312 ERS data (summer)

DATE	Description	Pct. Of Faulty Windows			
		X^2 Threshold		T^2 Threshold	
		S_{tot}	$S_{tot,mod}$	S_{tot}	$S_{tot,mod}$
	Total Fault-Free	36%	36%	1%	1%
	Total Faulty	69%	66%	33%	31%
19-Aug	Fault Free	9%	11%	0%	0%
25-Aug	Fault Free	61%	59%	2%	0%
4-Sep	Fault Free	37%	39%	0%	4%
20-Aug	EA Damper Stuck (Fully Open)	0%	2%	0%	0%
21-Aug	EA Damper Stuck (Fully Closed)	52%	17%	2%	4%
22-Aug	RF at Fixed Speed (30%)	98%	98%	61%	61%
23-Aug	RF complete failure	98%	98%	41%	26%
24-Aug	Cooling Coil Valve Control Unstable	30%	57%	13%	24%
26-Aug	OA Damper Stuck (Fully Closed)	100%	98%	37%	67%
27-Aug	Cooling Coil Valve Stuck (Fully Closed)	100%	98%	100%	98%
28-Aug	Heating Coil Valve Leaking (0.4GPM)	24%	7%	11%	0%
29-Aug	Heating Coil Valve Leaking (1.0GPM)	46%	35%	0%	0%
30-Aug	Heating Coil Valve Leaking (2.0GPM)	76%	61%	22%	17%
31-Aug	Cooling Coil Valve Stuck (15%)	85%	85%	80%	76%
2-Sep	Cooling Coil Valve Stuck (65%)	100%	100%	41%	46%
3-Sep	Cooling Coil Valve Reverse Action	100%	100%	89%	54%
6-Sep	OA Damper Leak (55%)	100%	100%	4%	22%
7-Sep	AHU Duct Leaking (after SF)	17%	33%	0%	0%
8-Sep	AHU Duct Leaking (before SF)	85%	76%	30%	0%

similarity factor and the distance similarity factor ($S_{\text{tot,mod}}$). Additionally, the results are reported for both the chi-squared threshold, corresponding to the Q-residual (or squared prediction).

As can be observed from Table 4.2, all of the pattern-matching metric and threshold combinations can generally distinguish between faulty operation and fault-free operation. The T^2 threshold has a false alarm rate of approximately 1%. The X^2 threshold has a much higher false alarm rate, but there is still a significant difference between the fault-free operation and faulty operation.

Looking at the faults that were not detected, many of these are expected to be difficult due to the limited impact on the performance of the system, or on the variables typically measured. For example, the duct leaking downstream of the supply fan is expected to be difficult to detect without incorporating information from the terminal units. Similarly, the faults surrounding the exhaust air damper are somewhat difficult to detect since it is the final exit point for air. For practical applications, it is much more important to be able to detect the EA damper being stuck fully closed than stuck fully open, as maintaining an open EA damper is often part of a recommended control strategy.

From this initial test, the potential for this method to be used for effective fault detection is clearly demonstrated, yet there remained some items that needed to be improved. The key areas for improvement were to increase the consistency of detection of leaking heating coil valves, improve detection related to the EA damper, and reduce the overall false alarm rate, especially the false alarm rate in the residual subspace. Note that the use of the S_{tot} pattern matching criterion is found to be slightly superior in this instance. Since the S_{tot} and $S_{\text{tot,mod}}$ both show potential, results from both pattern matching criteria are continued to be reported.

UTRC Data

The second set of data used for testing is referred to as the UTRC data, as that is the source of the data utilized. This data is from an AHU installed in a medium-sized office building. In this instance, there is a significant amount of normal, fault-free, operational data available but fewer dates where faults were artificially injected. The faults included in this study are less comprehensive than those injected in the ERS study, but they still provide a good test of how the algorithm detects abnormal AHU operation. A number of the faults are actually damper or valve sweeps, in which the damper or valve signal is overridden and the damper or valve is moved incrementally throughout the possible range of values from fully closed to fully open. Additionally, there is a day when stuck valve and damper faults were artificially introduced to the system (on February 14th). The results are included in

Table 4.3.

These results were obtained by randomly selecting 15 days from normal operation during December, January, and February as training data, then testing the days where known faults or abnormal behaviors were artificially injected into the system. As can be observed from

Table 4.3, the false alarm rate for this set of data is significantly higher than for the ERS data. Even with this higher false alarm rate, the overall difference between fault-free data and faulty data is significant so with some tuning of the method it was expected that an effective strategy could be created for this data as well.

Table 4.3 Baseline results using UTRC data

DATE	Description	Pct. Of Faulty Windows			
		X ²		T ² Threshold	
		S _{tot}	S _{tot,mod}	S _{tot}	S _{tot,mod}
	Total Fault-Free	41%	19%	33%	14%
	Total Faulty	64%	53%	61%	50%
02-12	Fault Free	45%	25%	39%	22%
12-16	Fault Free	41%	25%	36%	18%
02-03	Fault Free	7%	7%	0%	4%
01-23	Fault Free	55%	16%	60%	19%
01-06	Fault Free	56%	21%	29%	8%
12-06	Damper Sweeps	100%	100%	92%	100%
12-08	Damper Sweeps	71%	48%	69%	54%
12-09	Damper Sweeps	70%	54%	72%	53%
01-17	Damper Sweeps	71%	59%	76%	60%
01-26	Heating Coil Sweeps	40%	33%	37%	32%
01-30	Heating Coil Sweeps	32%	18%	34%	20%
02-14	OAD & HCV Faults	64%	57%	49%	28%

Simulation Data

The third set of data used to evaluate the baseline PMPCA method was simulation data from Drexel's AHU-VAV Dynamic Fault Simulation Testbed (see Section 4 for details). This testbed is based upon the same system utilized for the ERS experimental fault data. To maintain continuity with the previous tests, 15 days of fault-free data were utilized to train the algorithm, and the results from the faults obtained are detailed in Table 4.4, below.

Similar to the previous findings, the PMPCA method successfully identifies a difference between faulty behavior and fault-free behavior, and again is showing a high level of false alarms. This demonstrated a promising approach, given further tuning.

Method Refinement

Refining the method requires an optimization with multiple simultaneous goals/requirements. The target is to maximize the number or varieties of faults detected, and maximize the difference in the results between faulty operation and fault-free operation. Additionally, the false alarm rate must be reduced to a very low threshold, with an overall target of less than 1%.

Table 4.4 Baseline results using simulation data (summer)

DATE	Description	Pct. Of Faulty Windows			
		X ² Threshold		T ² Threshold	
		S _{tot}	S _{tot,mod}	S _{tot}	S _{tot,mod}
	Total Fault-Free	41%	21%	23%	22%
	Total Faulty	77%	74%	76%	75%
19-Aug	Fault Free	7%	8%	12%	9%
25-Aug	Fault Free	59%	21%	27%	35%
4-Sep	Fault Free	56%	33%	29%	21%
22-Aug	RF at Fixed Speed (30%)	100%	100%	98%	98%
23-Aug	RF complete failure	98%	100%	100%	100%
24-Aug	Cooling Coil Valve Control Unstable	0%	0%	2%	13%
26-Aug	OA Damper Stuck (Fully Closed)	62%	27%	36%	49%
27-Aug	Cooling Coil Valve Stuck (Fully Closed)	100%	98%	100%	100%
28-Aug	Heating Coil Valve Leaking (0.4GPM)	100%	100%	100%	100%
29-Aug	Heating Coil Valve Leaking (1.0GPM)	0%	0%	0%	2%
30-Aug	Heating Coil Valve Leaking (2.0GPM)	100%	100%	100%	100%
31-Aug	Cooling Coil Valve Stuck (15%)	100%	100%	100%	100%
2-Sep	Cooling Coil Valve Stuck (65%)	100%	100%	100%	100%
3-Sep	Cooling Coil Valve Reverse Action	100%	100%	100%	100%
5-Sep	Cooling Coil Valve Stuck (65%)	100%	100%	100%	100%
6-Sep	Cooling Coil Valve Reverse Action	100%	100%	100%	100%
7-Sep	OA Damper Leak (55%)	13%	13%	33%	31%
8-Sep	AHU Duct Leaking (after SF)	80%	69%	73%	38%

Fault Persistence

Without having to significantly alter the method, a simple technique can be employed to reduce the false alarm rates. This method deals with the addition of a *fault persistence* metric. The concept is to allow for some windows to be detected as faults prior to a fault being flagged. This allows for some outliers in the data, and for some brief periods of novel behavior prior to a fault alarm. By waiting for a fault to be persistently flagged, it is possible to minimize the false alarm rate.

For example, if a fault is flagged for the ERS data only when any 3 or more out of 25 windows are found to be faulty the false alarm rate goes to zero.

It is recommended that some type of fault persistence method be incorporated in the application of this method, but the initial effort is to minimize the false alarm rate without this additional layer. Without minimizing the false alarm rate prior to this layer, the PMPCA method would be effective but it would require some customization for each system to set the threshold for false alarms.

Historical Data Requirements

Some of the most important items for refinement pertain to the historical data required to train the PCA models. There are multiple aspects to analyzing the historical data necessary for accurate fault detection:

- Duration of historical windows
- Number of historical windows
- Historical data quality

By running multiple iterations of the PMPCA algorithm, while varying these inputs, significant insight was gained into the optimal inputs and data requirements for effective fault detection. For example, the window size was reduced from 45 minutes to 30 minutes, giving the results included in Table 4.5, below.

Table 4.5 Results with reduced window durations using UTRC data

DATE	Description	Pct. Of Faulty Windows			
		X ² Threshold		T ² Threshold	
		S _{tot}	S _{tot,mod}	S _{tot}	S _{tot,mod}
	Total Fault-Free	83%	71%	63%	56%
	Total Faulty	70%	60%	57%	45%
02-12	Fault Free	100%	100%	100%	100%
12-16	Fault Free	52%	27%	4%	2%
02-03	Fault Free	99%	95%	96%	77%
01-23	Fault Free	100%	98%	100%	86%
01-06	Fault Free	64%	34%	17%	15%
12-06	Damper Sweeps	96%	95%	89%	79%
12-08	Damper Sweeps	73%	52%	57%	44%
12-09	Damper Sweeps	77%	62%	62%	37%
01-17	Damper Sweeps	61%	59%	53%	34%
01-26	Heating Coil Sweeps	51%	39%	45%	37%
01-30	Heating Coil Sweeps	53%	47%	32%	26%
02-14	OAD & HCV Faults	81%	68%	61%	55%

As can be observed in the above table, the increased window duration was detrimental to the overall results, eliminating the ability to distinguish between faulty data and fault-free data due to the high false alarm rate. As a result, the following test increased the window duration to 60 minutes, and the results in Table 4.6 were obtained.

Increasing the window duration has effectively reduced the false alarm rates back to a level at which the difference between faulty and fault-free data can once again be distinguished. It is not at the target level, but modification of other variables was also explored to further understand the optimal inputs.

Table 4.6 Results with extended window durations using UTRC data

DATE	Description	Pct. Of Faulty Windows			
		X ² Threshold		T ² Threshold	
		S _{tot}	S _{tot,mod}	S _{tot}	S _{tot,mod}
	Total Fault-Free	24%	27%	10%	10%
	Total Faulty	55%	53%	46%	42%
Feb19	Fault Free	5%	12%	0%	0%
Feb24	Fault Free	38%	27%	9%	4%
Feb06	Fault Free	30%	36%	18%	16%
Feb13	Fault Free	25%	35%	12%	22%
Dec06	Damper Sweeps	66%	59%	70%	55%
Dec08	Damper Sweeps	58%	51%	39%	48%
Dec09	Damper Sweeps	67%	57%	37%	46%
Jan17	Damper Sweeps	56%	57%	52%	41%
Jan26	Heating Coil Sweeps	51%	41%	43%	32%
Jan30	Heating Coil Sweeps	34%	49%	34%	30%
Feb14	OAD & HCV Faults	54%	60%	44%	40%

When the same test was performed with the ERS data and simulation data, it was found that there was no significant difference in the use of different window lengths.

Table 4.7 Results of reduced number of historical windows using UTRC data

DATE	Description	Pct. Of Faulty Windows			
		X ² Threshold		T ² Threshold	
		S _{tot}	S _{tot,mod}	S _{tot}	S _{tot,mod}
	Total Fault-Free	52%	52%	14%	19%
	Total Faulty	66%	69%	42%	42%
Feb19	Fault Free	45%	60%	5%	16%
Feb24	Fault Free	48%	59%	2%	13%
Feb06	Fault Free	61%	48%	40%	38%
Feb13	Fault Free	52%	39%	11%	11%
Dec06	Damper Sweeps	74%	68%	38%	36%
Dec08	Damper Sweeps	67%	70%	46%	49%
Dec09	Damper Sweeps	75%	76%	45%	42%
Jan17	Damper Sweeps	71%	70%	49%	51%
Jan26	Heating Coil Sweeps	47%	58%	32%	34%
Jan30	Heating Coil Sweeps	47%	57%	28%	22%
Feb14	OAD & HCV Faults	81%	83%	56%	59%

Another variable impacting the quantity of historical data required is the number of historical windows used to create the PCA model for fault detection. Below, Table 4.7, is a sample of results from using only 5 historical windows (instead of 10).

The same reduction in windows was performed with the ERS data, and the results are provided below in Table 4.8. Overall, reduction of the window size by half resulted in slightly worse results, but it is clear that that algorithm is much more sensitive to window size modifications than to the number of historical windows used to create the PCA model for fault detection.

Note that overall the UTRC data has a higher false alarm rate than the ERS data. The difference between the two is primarily due to a high false alarm rate during start-up periods. This issue is addressed later during a discussion of the implications of isolating steady-state data.

Table 4.8 Results of reduced number of historical windows using ERS data

DATE	Description	Pct. Of Faulty Windows			
		X ² Threshold		T ² Threshold	
		S _{tot}	S _{tot,mod}	S _{tot}	S _{tot,mod}
	Total Fault-Free	51%	49%	9%	10%
	Total Faulty	77%	73%	41%	37%
19-Aug	Fault Free	20%	20%	4%	4%
25-Aug	Fault Free	72%	80%	15%	9%
4-Sep	Fault Free	63%	48%	7%	17%
20-Aug	EA Damper Stuck (Fully Open)	2%	9%	9%	0%
21-Aug	EA Damper Stuck (Fully Closed)	76%	46%	26%	20%
22-Aug	RF at Fixed Speed (30%)	100%	98%	70%	61%
23-Aug	RF complete failure	100%	100%	57%	43%
24-Aug	Cooling Coil Valve Control Unstable	37%	63%	20%	35%
26-Aug	OA Damper Stuck (Fully Closed)	100%	96%	61%	70%
27-Aug	Cooling Coil Valve Stuck (Fully Closed)	100%	86%	100%	86%
28-Aug	Heating Coil Valve Leaking (0.4GPM)	50%	35%	22%	9%
29-Aug	Heating Coil Valve Leaking (1.0GPM)	59%	48%	13%	11%
30-Aug	Heating Coil Valve Leaking (2.0GPM)	87%	67%	30%	28%
31-Aug	Cooling Coil Valve Stuck (15%)	89%	89%	74%	65%
2-Sep	Cooling Coil Valve Stuck (65%)	100%	100%	43%	57%
3-Sep	Cooling Coil Valve Reverse Action	100%	100%	74%	63%
6-Sep	OA Damper Leak (55%)	98%	96%	13%	20%
7-Sep	AHU Duct Leaking (after SF)	33%	37%	7%	15%
8-Sep	AHU Duct Leaking (before SF)	96%	96%	46%	7%

To see how the method responds to increasing the number of windows, tests were run using 15 windows of historical data. The results from this test are included in Table 4.9.

Table 4.9 Results of increased number of historical windows using ERS data

DATE	Description	Pct. Of Faulty Windows			
		X ² Threshold		T ² Threshold	
		S _{tot}	S _{tot,mod}	S _{tot}	S _{tot,mod}
	Total Fault-Free	28%	28%	1%	0%
	Total Faulty	68%	62%	34%	34%
19-Aug	Fault Free	0%	9%	0%	0%
25-Aug	Fault Free	57%	43%	2%	0%
4-Sep	Fault Free	26%	33%	0%	0%
20-Aug	EA Damper Stuck (Fully Open)	0%	0%	0%	0%
21-Aug	EA Damper Stuck (Fully Closed)	37%	24%	0%	4%
22-Aug	RF at Fixed Speed (30%)	98%	96%	67%	72%
23-Aug	RF complete failure	100%	100%	46%	24%
24-Aug	Cooling Coil Valve Control Unstable	26%	28%	17%	15%
26-Aug	OA Damper Stuck (Fully Closed)	93%	93%	43%	78%
27-Aug	Cooling Coil Valve Stuck (Fully Closed)	100%	93%	100%	100%
28-Aug	Heating Coil Valve Leaking (0.4GPM)	35%	9%	17%	2%
29-Aug	Heating Coil Valve Leaking (1.0GPM)	35%	30%	2%	2%
30-Aug	Heating Coil Valve Leaking (2.0GPM)	70%	57%	26%	17%
31-Aug	Cooling Coil Valve Stuck (15%)	85%	80%	78%	76%
2-Sep	Cooling Coil Valve Stuck (65%)	100%	100%	33%	50%
3-Sep	Cooling Coil Valve Reverse Action	100%	100%	98%	67%
6-Sep	OA Damper Leak (55%)	96%	93%	0%	30%
7-Sep	AHU Duct Leaking (after SF)	22%	30%	0%	0%
8-Sep	AHU Duct Leaking (before SF)	87%	65%	11%	0%

Using the increased number of historical windows has effectively reduced the false alarms for the T² threshold to an acceptable level. However, it does not differentiate between faulty and fault-free data as well as the baseline methodology. By increasing the quantity of historical data, the thresholds are increased but this reduces the ability to detect faults.

Component Retention for PCA Models

The number of principal components (PCs) retained, via determination of the “cut point”, is the most important step when building a PCA model. The number of PCs used to create the model has a direct impact on the method’s sensitivity to faults and/or the potential for oversensitivity resulting in false alarms. As a result of the import of this step, a number of different methods have been suggested in the literature, both as this process pertains to AFDD and also more generally.

Initial experimentation with this process for the PMPCA method has commenced, and some of the results have been included in this narrative. As mentioned previously, the individual eigenvalues correspond to a percent of the model variance they each explain. One of the first PCA retention tests was simply to reduce the percent of variance explained when creating the PCA models. An example of the results obtained using this technique is included in

Table 4.10.

Reduction of the percent variance threshold used to select the number of PCs to retain was very effective in decreasing the false alarm rate, especially for the chi-squared (Q-residual) threshold.

In addition to testing the PC retention method using the magnitudes of the eigenvalues, an additional methodology was tested. This method postulates that the principal components that should not be retained will decrease in a linear manner. In essence, this technique can automatically identify the “elbow” in the data as the break-point. This elbow technique has often been used when PCA is performed manually, so this method of testing the remaining eigenvalues for linearity is essentially a machine-learning method with the same concept. The results of this approach are detailed in Table 4.11.

Both the linear test and the reduced percentage of variance effectively reduce the false-alarm rate that is commonly known to plague PCA-based FDD approaches. Tests utilizing these methods are ongoing, and with some further analysis, the optimal PC retention approach will be determined.

Table 4.10 Results of reduced pc retention variance using ERS data

DATE	Description	Pct. Of Faulty Windows			
		X ² Threshold		T ² Threshold	
		S _{tot}	S _{tot,mod}	S _{tot}	S _{tot,mod}
	Total Fault-Free	4%	1%	1%	0%
	Total Faulty	35%	31%	15%	14%
2-May	Fault Free	8%	0%	0%	0%
3-May	Fault Free	7%	4%	2%	0%
4-May	Fault Free	1%	1%	1%	0%
5-May	Fault Free	1%	0%	0%	0%
6-May	Cooling Coil Stuck (Fully Closed)	99%	94%	96%	97%
7-May	OA Damper Stuck (Fully Closed)	100%	100%	100%	100%
8-May	OA Damper Stuck (40%)	100%	100%	99%	99%
9-May	EA Damper Stuck (Fully Open)	4%	1%	0%	0%
10-May	EA Damper Stuck (Fully Closed)	67%	27%	12%	0%
11-May	EA Damper Stuck (40%)	84%	65%	8%	0%
12-May	RF Complete Failure	89%	79%	3%	2%
13-May	MA Damper Unstable	2%	0%	1%	0%
14-May	MA Damper/ Cooling Coil Control Unstable	9%	6%	0%	0%
15-May	Cooling Coil Stuck (Fully Open)	100%	100%	60%	64%
16-May	Cooling Coil Stuck (50%)	100%	100%	12%	16%
17-May	Heat and Cool Sequence Unstable	6%	1%	0%	0%
18-May	RF Fixed Speed (20%)	98%	97%	29%	20%
19-May	RF Fixed Speed (80%)	96%	92%	31%	26%
20-May	EA Damper Stuck (Fully Open)	2%	0%	1%	0%
22-May	Air Filter Area Blocked 10%	0%	4%	0%	0%
23-May	Air Filter Area Blocked 25%	1%	1%	0%	0%
24-May	Air Filter Area Blocked 25%	16%	7%	2%	0%
25-May	Air Filter Area Blocked 25%	5%	1%	0%	0%
26-May	Air Filter Area Blocked 25%	1%	0%	0%	0%
27-May	EA Damper Fully Open	10%	8%	0%	0%
28-May	EA Damper Fully Open	3%	1%	0%	0%
29-May	OA Temperature Sensor Fault (+3 bias)	3%	0%	0%	0%
30-May	OA Temperature Sensor Fault (-3 bias)	17%	4%	10%	4%

Table 4.11 Results of linear test for pc retention using ERS data

DATE	Description	Pct. Of Faulty Windows			
		X ² Threshold		T ² Threshold	
		S _{tot}	S _{tot,mod}	S _{tot}	S _{tot,mod}
	Total Fault-Free	4%	1%	1%	0%
	Total Faulty	32%	28%	13%	12%
2-May	Fault Free	7%	0%	0%	0%
3-May	Fault Free	4%	2%	2%	0%
4-May	Fault Free	4%	0%	1%	0%
5-May	Fault Free	0%	0%	0%	0%
6-May	Cooling Coil Stuck (Fully Closed)	96%	93%	76%	89%
7-May	OA Damper Stuck (Fully Closed)	100%	100%	100%	100%
8-May	OA Damper Stuck (40%)	100%	100%	97%	95%
9-May	EA Damper Stuck (Fully Open)	4%	1%	0%	0%
10-May	EA Damper Stuck (Fully Closed)	59%	13%	7%	0%
11-May	EA Damper Stuck (40%)	80%	50%	1%	0%
12-May	RF Complete Failure	74%	76%	1%	1%
13-May	MA Damper Unstable	2%	0%	0%	0%
14-May	MA Damper/ Cooling Coil Control Unstable	4%	3%	0%	0%
15-May	Cooling Coil Stuck (Fully Open)	100%	100%	40%	50%
16-May	Cooling Coil Stuck (50%)	100%	100%	7%	10%
17-May	Heat and Cool Sequence Unstable	3%	0%	0%	0%
18-May	RF Fixed Speed (20%)	95%	91%	28%	13%
19-May	RF Fixed Speed (80%)	76%	77%	31%	25%
20-May	EA Damper Stuck (Fully Open)	3%	0%	3%	0%
22-May	Air Filter Area Blocked 10%	1%	2%	0%	0%
23-May	Air Filter Area Blocked 25%	1%	0%	0%	0%
24-May	Air Filter Area Blocked 25%	18%	7%	0%	0%
25-May	Air Filter Area Blocked 25%	3%	0%	0%	0%
26-May	Air Filter Area Blocked 25%	1%	0%	0%	0%
27-May	EA Damper Fully Open	12%	10%	0%	0%
28-May	EA Damper Fully Open	4%	0%	2%	0%
29-May	OA Temperature Sensor Fault (+3 bias)	0%	0%	0%	0%
30-May	OA Temperature Sensor Fault (-3 bias)	8%	1%	6%	2%

Discussion of Results

Overall, the method was successfully demonstrated for use in AHU-VAV fault detection. Although there is still further work and demonstration necessary, this method has the potential to be employed for commercial AFDD fault detection in the near-future. In the coming year, it will be demonstrated using an

online demonstration in Philadelphia, providing additional data and feedback for the method demonstration.

4.6. Recommendations for Continuing PMPCA Investigation

Testing with Additional Data (Online and Offline)

The upcoming BP 3 will provide the opportunity to test the PMPCA method in an online demonstration in conjunction with the Task 4 demonstration. This will provide the first in-situ use of this novel method. There is also expected to be an opportunity to test the data against additional offline data to gather additional results.

In preparation for the online testing, the final tuning of the PMPCA method must be completed at the start of BP3 to allow for enough time for it to be implemented as a part of the demonstration platform.

Final Tuning of the Method

The final tuning of the method is currently in progress, and is expected to be wrapped up during the first quarter of BP3.

Experimentation with Alternative Threshold Optimization Methods

One of the key advantages to the PCA-based FDD method is the automation of the threshold/confidence limits. Although this is automated, there are a few different techniques suggested in the literature for setting these limits. The various methods for creating the thresholds commonly produce similar results, however it will be beneficial to test the different methods to ensure the most accurate method is being used.

Impact of Steady-State Operation versus Non-Steady Operation

The general idea of the steady-state detector is to identify the times when the AHU-VAV system is operating in steady-state, so conditions can be analyzed while omitting the data that occurs during transient operating periods. The steady-state detector must balance the necessity of finding a steady-state that is reliable for fault detection and allowing for the variation found in practice so there are adequate samples to analyze. In an HVAC application, there are unavoidable fluctuations due to process and sensor noise, as well as variation in weather and various internal conditions.

A simple solution to this problem, proposed by Lee (2004), is employed here. The steps for this method require only the data from the cooling coil control signal, the mixing air temperature, the supply air duct static pressure, and the return air flow rate. The steps for the method are as follows:

The data is acquired from a 6 minute sliding window of the data. At each time step, the current values and the five prior values are analyzed. The maximum value, minimum value, and the mean of the values are calculated for each of the four data points.

The slope is calculated for each of the data points, as the difference between the maximum and minimum values, divided by the mean value.

The sum of these slopes is compared to the previously calculated steady-state threshold value.

Prior to filtering the steady-state data in practice, this threshold must first be calculated based upon known steady-state operating conditions in the presence of load changes. When the process is known to be operating in steady-state, the threshold value is calculated as 3 times the standard deviation of the sum of the slopes of the four variables.

This steady-state filtering procedure is being evaluated presently. The sum-of-slopes metrics are being actively monitored to better understand the effect of steady/unsteady operation on the results.

Component Retention for PCA Models

Going forward, it is recommended that continued testing with different PCA model creation (component retention) methods. This part of the process has been identified as a key factor in determining the accuracy and sensitivity of the PMPCA method, and thus garners some further analysis. There are a number of different approaches for component retention proposed for FDD-type applications across various fields of research. Some of the promising approaches are discussed briefly here.

Qin (2000) recommended the use of a variance reconstruction error (VRE) method. An advantage of this method is some improved robustness against some more common methods that use monotonically decreasing indices. As presented above, the most common PC retention criteria identify a “cut-point” at which there is a significant change in some quality of the PCs, after which the remaining PCs are discarded. Some potential shortcomings of monotonically decreasing PC retention criteria are instances where there is a rather constant decrement in the index being used or when there are multiple locations that satisfy the cut-point criterion.

Chen and Lan (2009) used the VRE method and SPE thresholds for fault detection of condenser fouling in an air-source heat pump. They were able to successfully demonstrate fault detection for a single, steady-state mode of operation.

4.7. Diagnostic Method Assessments and Comparison

Understanding the true strengths and weakness of the PMPCA method requires the context of other existing or proposed AFDD methodologies. In Section 4.2, multiple papers that propose different AFDD techniques are discussed, and many of these methods show promise for further analysis. The difficulty with finding benchmarks to compare with is primarily due to the limited testing of the methods that is typically reported. None of the papers identified above provided overall false alarm rates or overall fault detection rates, so there are no widely available benchmarks against which to compare. To properly evaluate FDD strategies, it is necessary to test them in conditions most similar to normal operation.

The overall fault detection rates for various faults and false alarm rates are one aspect. The second aspect of evaluating diagnostic methods pertains to the potential for commercialization of the method. To that end, a set of requirements were developed to help with the evaluation process:

- Minimizing the customization required for different systems is essential. All of the methods proposed require at least some minimal operator feedback, at least during the training phase, but industry feedback has shown that significant time or money will not typically be invested in the implementation of AFDD for AHU-VAV systems.
- The algorithm must be able to be trained using solely fault-free data from normal operation. Requiring any significant quantity of faulty data from implementation sites is not feasible for widespread commercial adoption. The acquisition of some limited abnormal data through a process of some brief system calibration may be possible, but this type of data would be limited in terms of the type of operational conditions it would be used for.
- The method must be efficient enough for online monitoring. Large commercial buildings operate with multiple AHUs, and the method must be continuously operating. The computational requirements must be small enough to meet this demand.

- It must be robust enough to maintain accuracy throughout all operating conditions. In some instances, this may include simply sensing that the strategy can't be effective for brief periods of unique or non-steady-state operation.
- The algorithm must be able to detect abrupt as well as slowly-occurring degradation faults.
- A successful detection scheme can detect both process faults as well as sensor faults.
- The false alarm rate must be minimized, with a goal of less than 1% of alarms being faulty. Higher false alarm rates will result in the alarms being ignored in practice.

Using these criteria, many of the methods proposed, while insightful, may not be ready for commercialization. Some recently proposed methods were tested using some of the same ERS data utilized in this study. Wall et al. (2011) proposed a Hidden Markov Model (HMM) based method for fault detection and this method was tested using the ERS summer data from ASHRAE 1312. This is the same data set used for the summer ERS tests included here.

Overall, the method proposed performed well when detecting faults, and showed the potential of this type of clustering method to work. The method performed similarly to the PMPCA method proposed here, effectively detecting the abnormalities in the data in a manner that corresponds to the severity of the fault. Two potential difficulties with this method are the potential difficulty calibrating a threshold for the log-likelihood at which point a fault should be flagged, and the potential for a very high false alarm rate that is often observed in clustering FDD algorithms.

4.8. Energy Implications of AHU-VAV Faults

A comprehensive understanding of the overall energy implications related to AHU-VAV faults is difficult to obtain given the information that is currently readily available. There are two key applications that can benefit from an increased understanding of the energy impact: fault remediation prioritization, and the design and valuation of AFDD tools.

For the first application, it is necessary to understand the energy impact of a fault over the course of a typical day, given the seasonal operating conditions. With an accurate estimate of this value, it is possible to effectively prioritize the repair work in the manner that is most economically and energetically efficient. Additionally, the probability that a fault will worsen, or make the system unable to effectively condition the space are also key factors in prioritizing faults for repair.

For the second application, it is necessary to estimate not only the energy impact, but also to estimate the fault occurrence probability and the probable duration that the fault will go undetected. Reliable estimates for these values are much more difficult to come by. The approach utilized in this study was to interview personnel with extensive experience working with AHU-VAV systems. These individuals all work in Philadelphia and were able to provide very helpful insights into their experiences with AHU-VAV faults in the field.

Experimental Data

In addition to using the ERS experimental data for the testing of fault detection algorithms, this data also provided some useful results with regard to the energy impact of faults. By simultaneously running two identical AHUs side-by-side with the same loads, it is possible to calculate the difference in energy consumption when one is artificially injected with various faults.

Energy Calculation Methods

To understand the energy impact of individual faults, four energy indices were calculated in this study:

- Electrical energy consumed by the return fan
- Electrical energy consumed by the supply fan
- Energy consumed by the heating coil
- Energy consumed by the cooling coil

For all of the different energy indices, the data provides energy usage data in one minute increments. The energy consumption values were calculated by averaging the energy consumption rate over the course of the test period. For example, then energy consumption during the course of an hour can be calculated using the relation

$$EN_{dt} = \frac{1}{60} \sum_{i=1}^n EN_{ins,i} \Delta t \quad (4-16)$$

where EN_{dt} is the accumulated energy usage (Btu or KW-h) over the hour, $EN_{ins,i}$ is the instantaneous energy consumption rate (Btu/hr or KW), Δt is the time interval between readings (1 min), and 60 is a time conversion factor, n is the total time and is 60 for hourly value.

The instantaneous electric power consumed by the fans and pumps ($PW_{ele,i}(t)$, Btu/hr or KW) is measured directly by sensors. The sum of the electric power for a time interval is computed using:

$$PW_{ele} = \int_{t_1}^{t_2} PW_{ele,i}(t) dt \quad (4-17)$$

where PW_{ele} (Btu or KW-h) is the accumulated power usage over a time period, t_1 and t_2 representing the initial and final times over which cumulative energy use over the period is taken. t_1 and t_2 have a unit of hour. In terms of discrete times with readings taken every minute, Eq. (4-17) for a time period of 24 h becomes:

$$PW_{ele} = \frac{1}{60} \sum_{i=1}^{1440} PW_{ele,i} \Delta t \quad (4-18)$$

where Δt is the time interval between readings (1 min). The instantaneous chilled water heat transfer rate for the AHU cooling coil ($q_{cc,i}$, Btu/hr or KW) is computed using (Gao et al., 2004)

$$q_{cc,i} = K_{cc} Q_{cc} (T_{ccmw} - T_{ccew}) \quad (4-19)$$

where K_{cc} is the property/unit factor for water, T_{ccew} and T_{ccmw} are the coil outlet and mixed water temperatures ($^{\circ}F$ or $^{\circ}C$), and Q_{cc} is the total volumetric water flow rate (gpm or m^3/s) evaluated at the location where mixed water temperature, T_{ccmw} , is measured. For chilled water, the property/unit factor is given by (Gao et al., 2004)

$$K_{cc} = K_{cc,r} [c_1 + c_2 (T_{ccew} - T_{w,r})] \quad (4-20)$$

where $K_{cc,r}$ is the reference property/unit factor for chilled water at the reference temperature of $T_{w,r}$ and c_1 and c_2 are curve-fit coefficients. Chilled water is a mixture of 15% ethylene glycol and water. The chilled water properties of density and specific heat are not sensitive to pressure for the conditions for which the tests were performed. The reference temperature for water is $T_{cw,r} = 40^\circ\text{F}$ (4.44°C) yielding $K_{cc,r} = 473 \text{ Btu/h-gpm-F}$ ($3956.23 \text{ kJ/m}^3\text{-C}$). The values of the curve-fit coefficients are $c_1 = 1$ and $c_2 = -0.0003 \text{ 1/}^\circ\text{F}$ (or $c_1 = 1.8$ and $c_2 = -0.00054 \text{ 1/}^\circ\text{C}$). Combining Eqs. (4-19) to (4-20) yields

$$q_{cc,i} = K_{cc,r} [c_1 + c_2(T_{c_{cew}} - T_{c_{w,r}})] Q_{cc} (T_{ccmw} - T_{c_{cew}}) \quad (4-21)$$

The three measured variables for the water heat transfer rate for the cooling coil are Q_{cc} , $T_{c_{cew}}$, and T_{ccmw} . The hourly sum of the water heat transfer rate can be determined using Eq.(4-16). Similar to the cooling coil energy calculation, the instantaneous hot water heat transfer rate for the heating coil is computed:

$$q_{hc,i} = K_{hc,r} [c_1 + c_2(T_{h_{cew}} - T_{h_{w,r}})] Q_{hc} (T_{h_{cmw}} - T_{h_{cew}}) \quad (4-22)$$

Where $K_{hc,r}$ is the reference property/unit factor for water, $T_{h_{cew}}$ and $T_{h_{cmw}}$ are the coil outlet and mixed water temperatures ($^\circ\text{F}$ or $^\circ\text{C}$), and Q_{hc} is the loop volumetric water flow rate (gpm or m^3/s) evaluated at the location where $T_{h_{cmw}}$, is sensed. The reference temperature for water is $T_{hw,r} = 120^\circ\text{F}$ (48.9°C) yielding $K_{hc,r} = 500 \text{ Btu/h-gpm-}^\circ\text{F}$ ($4181.81 \text{ kJ/m}^3\text{-}^\circ\text{C}$).

Summary of Findings from Experimental Data

Once all of the energy consumption values have been obtained, the difference in energy consumption between AHU-A and AHU-B can be calculated. This first section provides an overview of the delta of the airstream energy (i.e. energy from the fan and coil required to add or remove heat from the airstream). The next parts of this section address how these faults impact building energy consumption and the cost of operation.

Fault Energy Implications: Airstream Energy

The detailed results from the energy impact findings are included in the appendix, but a synopsis of the important results is included here. As part of the experiment, the fault energy impact of fault free data was included in the analysis. This provides a baseline of understanding the accuracy of this experimental methodology. The two AHUs were expected to differ by some small degree due to system and measurement noise, as well as the impossibility of making the two systems exactly identical. For reference, the fault-free system differences are included in

Table 4.12.

Table 4.12 Energy comparison of A and B systems at the ERS under fault free conditions

Date	Fault Description	AHU-A Minus AHU-B (kWh)					
		Fans	Cooling	Heat	Reheat	Net	Pct
01-29	Fault Free	-0.9	0.0	-3.6	-3.8	(8)	-6%
08-19	Fault Free	0.2	11.1	0.0	0.0	11	6%
08-25	Fault Free	-0.7	13.9	0.0	-0.2	13	8%
05-05	Fault Free	-0.5	11.6	0.1	0.5	12	10%
05-04	Fault Free	-0.9	10.6	1.1	0.4	11	13%
05-03	Fault Free	-0.9	6.3	0.2	-0.4	5	13%
02-17	Fault Free	-0.9	0.0	-15.1	-1.5	(18)	-16%
02-16	Fault Free	-0.6	0.0	-18.0	-0.3	(19)	-17%
05-02	Fault Free	-1.2	13.2	0.2	-0.1	12	20%

All of the data was taken from comparing two AHUs, each serving 4 VAV boxes from 8am to 6pm. The differences found from the two different AHUs span in magnitude from 6% to 20%, and from 5 kWh/day to 19 kWh/day. The average magnitude of difference is 12%, and the average difference is 3% more energy being used by AHU-A than by AHU-B (or 2.2 kWh/day). This provides some context with which to view the remaining results. Only those faults that exceed the highest fault-free differences from

Table 4.12 are included here. The first season evaluated was the summer season, with the important results summarized in Table 4.13.

Table 4.13 Summer fault energy impacts (airstream)

Date	Fault Description	AHU-A Minus AHU-B (kWh)					
		Fans	Cooling	Heat	Reheat	Net	Pct
09-03	Cooling Coil Valve Reverse Action	-1.1	140.2	156.7	1.0	297	146%
08-31	Cooling Coil Valve Stuck (15%)	-1.7	134.8	134.2	-0.7	267	157%
09-02	Cooling Coil Valve Stuck (65%)	-0.2	121.6	124.0	-0.3	245	126%
08-30	Heating Coil Valve Leaking (2- 2.0GPM)	-0.3	109.6	95.3	-0.6	204	135%
08-27	Cooling Coil Valve Stuck (Fully Closed)	23.4	-193.3	-0.2	0.0	(170)	-79%
08-29	Heating Coil Valve Leaking (2- 1.0GPM)	0.2	77.2	58.1	-0.6	135	86%
08-28	Heating Coil Valve Leaking (1- 0.4GPM)	3.4	50.1	28.6	-0.7	81	40%
08-23	RF complete failure	-1.7	54.6	-0.2	-0.3	52	34%
08-22	RF at Fixed Speed (30%)	-0.4	33.1	-0.5	0.0	32	18%
09-06	OA Damper Leak (55%)	-1.0	28.0	0.1	-0.3	27	17%
08-20	EA Damper Stuck (Fully Open)	1.0	21.3	-0.1	0.0	22	11%
08-24	Cooling Coil Valve Control Unstable	2.9	17.2	-0.1	-0.2	20	15%
09-07	AHU Duct Leaking (after SF)	0.3	17.2	-0.1	-0.2	17	11%

As can be readily observed, any problem with the cooling coil valve created significant additional energy, except when it was stuck closed resulting in energy savings. Following the cooling coil were problems with the heating coil leaking, that created a necessity for extra cooling in addition to the extra energy wasted for heating. Of course, this is only an issue when buildings are operating in a mode that requires simultaneous heating and cooling. If the boiler is turned off during the heat of the summer, of course the heating coil faults would not have an energy impact until the boiler is turned back on. The next season evaluated was the shoulder season, in this case the spring season, and the results are included in Table 4.14.

Table 4.14 Spring fault energy impacts (airstream)

Date	Fault Description	AHU-A Minus AHU-B (kWh)					
		Fans	Cooling	Heat	Reheat	Net	Pct
05-15	Cooling Coil Stuck (Fully Open)	-2.3	199.5	156.6	3.5	357	364%
05-16	Cooling Coil Stuck (50%)	-1.1	128.9	99.5	2.3	230	196%
05-06	Cooling Coil Stuck (Fully Closed)	20.0	-132.5	0.6	-1.9	(114)	-73%
05-30	OA Temperature Sensor Fault (-3 bias)	4.7	22.1	0.0	-0.4	26	15%
05-28	EA Damper Stuck (Fully Open)	3.7	20.3	-0.1	0.5	24	49%
05-19	RF Fixed Speed (80%)	4.3	19.1	0.0	0.3	24	24%
05-14	MA Damper/ Cooling Coil Control Unstable	-1.1	15.2	1.5	0.2	16	26%
05-09	EA Damper Stuck (Fully Open)	0.0	15.6	0.1	-0.6	15	23%
05-23	Air Filter Area Blocked 25%	-0.5	14.2	0.0	0.6	14	38%
05-08	OA Damper Stuck (40%)	8.5	7.9	-0.3	-1.9	14	17%
05-17	Heat and Cool Sequence Unstable	0.1	12.1	0.0	0.8	13	10%

The spring fault energy prioritization is similar to the summer fault table, in that the cooling coil faults are the most critical for energy consumption. This is followed by a variety of other faults, but the other faults are less critical than other seasons due to the relatively lower overall space conditioning loads during the shoulder seasons. The third season analyzed was the winter season, with the results included in

Table 4.15.

Of the faults tested in the winter, the majority of the major impacts were actually energy-saving faults. Once again, the cooling coil valve being stuck open leads the list of fault energy impacts but this is followed by a number of faults that save energy but create a hazardous indoor air environment. With the outdoor air damper or exhaust air damper fully closed, there is no way for the overall ventilation rate to meet minimum safety standards. The remaining faults in the winter were mostly related to the fouling or reduced capacity of the heating coil.

Table 4.15 Winter fault energy impacts (airstream)

Date	Fault Description	AHU-A Minus AHU-B (kWh)					
		Fans	Cooling	Heat	Reheat	Net	Pct
02-10	Cooling Coil Valve Stuck (Fully Open)	-2.3	198.0	130.7	38.9	365	230%
02-12	OA Damper Stuck (Fully Closed)	3.7	1.3	-132.7	-8.3	(136)	-73%
01-30	OA Damper Stuck (Fully Closed)	5.6	4.7	-112.0	-22.7	(124)	-58%
02-03	EA Damper Stuck (Fully Closed)	-1.6	0.0	-34.5	-6.0	(42)	-40%
02-05	Heating Coil Fouling (Stage 1)	4.4	0.0	-28.5	-4.7	(29)	-28%
02-09	Heating Coil Reduced Capacity 3	-0.9	0.0	-32.5	7.0	(26)	-23%
02-08	Heating Coil Reduced Capacity 2	-0.4	0.0	-21.4	-2.0	(24)	-27%
02-01	OA Damper Stuck (62%)	-1.3	0.0	23.6	-0.7	22	20%
02-07	Heating Coil Reduced Capacity 1	-0.7	0.0	-16.6	-2.8	(20)	-17%

Fault Energy Implications: Building Energy Consumption

The previous sub-section provides a baseline understanding of how much energy is wasted/saved by all of the faults tested at the airstream level, but it is important to take note of how this translates into overall building energy consumption. To do this required a number of assumptions to be made about typical primary building systems. The energy consumed at a building level is a function of the amount of energy consumed in the airstream and the efficiencies of the primary heating and cooling equipment. The assumptions used to perform the building energy consumption calculations are included in Table 4.16 below.

Table 4.16 Primary system efficiency assumptions

Primary System Efficiencies	
Chiller COP	4.0
Boiler Efficiency	80%
Fan Efficiency	100%

Using this data, the following tables provide an overview of how various faults will impact building consumption. Table 4.17 outlines the building energy consumption related to faults in the summer season.

Table 4.17 Summer fault energy impacts (building energy)

Date	Season	Fault Description	AHU-A Minus AHU-B				
			Fans	Chiller	Boiler	Net	Pct
09-03	3	Cooling Coil Valve Reverse Action	-1.1	35.1	195.9	230	342%
08-31	3	Cooling Coil Valve Stuck (15%)	-1.7	33.7	167.8	200	347%
09-02	3	Cooling Coil Valve Stuck (65%)	-0.2	30.4	155.0	185	285%
08-30	3	Heating Coil Valve Leaking (2- 2.0GPM)	-0.3	27.4	119.1	146	278%
08-29	3	Heating Coil Valve Leaking (2- 1.0GPM)	0.2	19.3	72.6	92	179%
08-28	3	Heating Coil Valve Leaking (1- 0.4GPM)	3.4	12.5	35.8	52	80%
08-27	3	Cooling Coil Valve Stuck (Fully Closed)	23.4	-48.3	-0.2	(25)	-36%
08-23	3	RF complete failure	-1.7	13.7	-0.2	12	23%
08-22	3	RF at Fixed Speed (30%)	-0.4	8.3	-0.6	7	12%
08-24	3	Cooling Coil Valve Control Unstable	2.9	4.3	-0.2	7	16%
09-06	3	OA Damper Leak (55%)	-1.0	7.0	0.2	6	12%
08-20	3	EA Damper Stuck (Fully Open)	1.0	5.3	-0.1	6	10%
09-07	3	AHU Duct Leaking (after SF)	0.3	4.3	-0.1	5	9%

The building energy consumption associated with faults in the spring season are documented in Table 4.18.

Table 4.18 Spring fault energy impacts (building energy)

Date	Season	Fault Description	AHU-A Minus AHU-B				
			Fans	Chiller	Boiler	Net	Pct
05-15	2	Cooling Coil Stuck (Fully Open)	-2.3	49.9	195.8	243	661%
05-16	2	Cooling Coil Stuck (50%)	-1.1	32.2	124.4	155	370%
05-06	2	Cooling Coil Stuck (Fully Closed)	20.0	-33.1	0.8	(12)	-23%
05-30	2	OA Temperature Sensor Fault (-3 bias)	4.7	5.5	0.0	10	19%
05-08	2	OA Damper Stuck (40%)	8.5	2.0	-0.4	10	30%
05-19	2	RF Fixed Speed (80%)	4.3	4.8	0.0	9	26%
05-28	2	EA Damper Fully Open	3.7	5.1	-0.1	9	46%
05-14	2	MA Damper/ Cooling Coil Control Unstable	-1.1	3.8	1.8	5	17%
05-09	2	EA Damper Stuck (Fully Open)	0.0	3.9	0.1	4	15%
05-17	2	Heat and Cool Sequence Unstable	0.1	3.0	0.0	3	7%
05-23	2	Air Filter Area Blocked 25%	-0.5	3.6	0.0	3	17%

The building energy consumption associated with faults in the winter season is itemized in Table 4.19.

Table 4.19 Winter fault energy impacts (building energy)

Date	Season	Fault Description	AHU-A Minus AHU-B				
			Fans	Chiller	Boiler	Net	Pct
02-10	1	Cooling Coil Valve Stuck (Fully Open)	-2.3	49.5	163.4	211	147%
02-12	1	OA Damper Stuck (Fully Closed)	3.7	0.3	-165.9	(162)	-89%
01-30	1	OA Damper Stuck (Fully Closed)	5.6	1.2	-140.0	(133)	-86%
02-03	1	EA Damper Stuck (Fully Closed)	-1.6	0.0	-43.1	(45)	-62%
02-09	1	Heating Coil Reduced Capacity 3	-0.9	0.0	-40.6	(42)	-40%
02-05	1	Heating Coil Fouling (Stage 1)	4.4	0.0	-35.6	(31)	-42%
02-01	1	OA Damper Stuck (62%)	-1.3	0.0	29.6	28	30%
02-08	1	Heating Coil Reduced Capacity 2	-0.4	0.0	-26.8	(27)	-32%
02-07	1	Heating Coil Reduced Capacity 1	-0.7	0.0	-20.8	(21)	-21%

Fault Energy Implications: Operational Costs

The above estimates can provide a good point of reference for the amount of primary energy consumed by various faults during different operating conditions. The final extension is to analyze the cost impacts associated with this additional energy consumption. The costs associated with the faults were calculated using typical prices paid by small-to-medium sized commercial and residential properties in Philadelphia during 2012. Since the incremental energy costs can vary significantly based upon market forces and the different types of service plans provided in Philadelphia, ranges of values were used for the utility cost estimates. The values utilized are included in Table 4.20, below.

Table 4.20 Utility cost estimates (Philadelphia, 2012)

Utility Costs				
Fuel	Low	Nominal	High	Units
Electricity	\$0.10	\$0.16	\$0.20	per kWh
Natural Gas	\$1.10	\$1.33	\$1.40	per ccf

Using this data, the summer daily cost impact of the faults itemized above was calculated and organized in Table 4.21.

Table 4.21 Summer fault impacts (daily cost)

Fault: Summer Season	Base Nominal	Low	Nominal	High	Pct
Cooling Coil Valve Reverse Action	10.72	218.89	265.99	281.06	2382%
Cooling Coil Valve Stuck (15%)	9.20	187.76	228.27	241.29	2380%
Cooling Coil Valve Stuck (65%)	10.33	173.48	210.94	222.99	1942%
Heating Coil Valve Leaking (2- 2.0GPM)	8.42	133.75	162.77	172.20	1833%
Heating Coil Valve Leaking (2- 1.0GPM)	8.21	81.79	99.66	105.52	1114%
Heating Coil Valve Leaking (1- 0.4GPM)	10.36	40.98	50.17	53.31	384%
Cooling Coil Valve Stuck (Fully Closed)	11.27	(2.71)	(4.25)	(5.26)	-138%
RF complete failure	7.99	0.96	1.63	2.09	-80%
OA Damper Leak (55%)	8.36	0.80	1.20	1.45	-86%
Cooling Coil Valve Control Unstable	7.21	0.54	0.94	1.22	-87%
EA Damper Stuck (Fully Open)	10.17	0.51	0.86	1.10	-92%
AHU Duct Leaking (after SF)	8.51	0.39	0.65	0.83	-92%
RF at Fixed Speed (30%)	9.44	0.08	0.41	0.68	-96%

The spring fault impact daily costs are organized in Table 4.22.

Table 4.22 Spring fault impacts (daily cost)

Fault: Spring Season	Base Nominal	Low	Nominal	High	Pct
Cooling Coil Stuck (Fully Open)	5.89	180.92	220.61	233.72	3648%
Cooling Coil Stuck (50%)	6.73	115.10	140.38	148.75	1987%
Cooling Coil Stuck (Fully Closed)	8.60	(2.75)	(3.83)	(4.45)	-145%
MA Damper/ Cooling Coil Control Unstable	4.19	2.04	2.58	2.80	-39%
EA Damper Fully Open	3.02	1.31	1.93	2.31	-36%
RF Fixed Speed (80%)	5.66	1.20	1.80	2.18	-68%
Heat and Cool Sequence Unstable	7.35	1.15	1.51	1.69	-79%
Air Filter Area Blocked 25%	10.18	0.99	1.34	1.53	-87%
OA Damper Stuck (40%)	5.27	(1.41)	(1.29)	(1.03)	-125%
OA Temperature Sensor Fault (-3 bias)	8.83	0.54	1.06	1.44	-88%
EA Damper Fully Open	2.17	0.45	0.56	0.59	-74%

The winter daily costs associated with various faults can be seen detailed in Table 4.23.

Table 4.23 Winter fault impacts (daily cost)

Fault: Winter Season	Base Nominal	Low	Nominal	High	Pct
Cooling Coil Valve Stuck (Fully Open)	8.38	10.86	14.97	17.25	79%
OA Damper Stuck (Fully Closed)	10.22	(5.83)	(6.89)	(7.13)	-167%
OA Damper Stuck (Fully Closed)	8.68	(4.58)	(5.27)	(5.33)	-161%
EA Damper Stuck (Fully Closed)	5.15	(1.78)	(2.21)	(2.38)	-143%
Heating Coil Reduced Capacity 3	6.65	(1.62)	(1.99)	(2.12)	-130%
Heating Coil Reduced Capacity 2	6.06	(1.05)	(1.29)	(1.37)	-121%
OA Damper Stuck (62%)	6.19	0.98	1.13	1.14	-82%
Heating Coil Reduced Capacity 1	6.39	(0.85)	(1.05)	(1.13)	-116%
Heating Coil Fouling (Stage 1)	5.21	(0.90)	(0.92)	(0.83)	-118%

Further detail regarding the building fault energy consumption and operational costs can be located in the appendix.

Preliminary Expert Interviews

As previously mentioned, understanding the overall impact of faults requires not only the rate of energy being wasted (or saved), but also requires some insight into the frequency at which various faults occur and at which they go undetected. One manner in which this insight can be gained is via interfacing with industry to gather experiential and anecdotal data regarding fault frequency and fault detection.

This interview process is currently ongoing, and some preliminary results have been compiled and included here. The primary focus is on fault prioritization and frequency, but there is also an added benefit of ensuring alignment of the overall AFDD goal with what is desired and required for commercial application. Some of this miscellany is included in the discussion following the more specific analysis of the fault occurrence probability data in this section.

Fault Prioritization and Frequency

As previously mentioned, there exists very little data on the frequency or probability of fault occurrence in AHU-VAV systems. One goal of this project is to provide additional insight into this current dearth of data. This information is very useful for two key reasons: prioritizing faults for AFDD strategies, and demonstrating the value of incorporating an AFDD tool into AHU-VAV systems. The energy (and associated cost) impacts of AHU-VAV systems operating in a faulty manner are often underestimated by the individuals tasked with maintaining, repairing, or managing them, so illuminating the true impact is a key step for widespread AFDD adoption for AHU-VAV systems.

As the interviews are still ongoing, the detailed results will not be published until the interviews are completed, however there have been consistent responses received about certain items, and some useful insights that have been included herein.

The most commonly occurring faults are typically air filter blockages and belt slippage. Replacing air filters and belts are a common part of maintenance for AHUs. Both of these faults can be detected by the PMPCA method when they start to impact system performance, but neither is the focus of the PMPCA method since they are generally part of routine maintenance. Air filter status is typically monitored by a separate DP sensor. A differential pressure switch was commonly used in the past, but now it is just as economical to use an analog pressure transmitter which allows for more flexibility.

Belt slippage is also a common problem, and especially with large AHUs the belts typically last only 3-4 years due to the length of the belts. Belts are inexpensive replacement parts, and once they start to slip they tend to fail relatively quickly afterwards.

The most common types of faults that don't fall under the category of maintenance items were reported as pertaining to dampers and then valves, in that order. Dampers are prone to leakage via seal degradation or via miscalibration. The miscalibration can occur at initial commissioning, during maintenance/repair activity, or from shaft slippage during operation. Other common valve faults include stuck bearings or broken actuator or linkages. Damper faults are an important fault for an AFDD strategy to effectively detect since they are typically only identified under extreme conditions, and thus the faults can go undetected for long periods of time.

The faults related to valves are primarily related to them becoming stuck, or some other problem with the actuation. As demonstrated in Section 9.1, leaking and stuck valves are some of the most significant faults with regard to their energy impact. Older valves can have seating issues that allows for some pass-through. The age at which this deterioration occurs is largely a function of the quality of the valves initially installed. Good valves can last 20 years with an indoor installation.

The next most commonly occurring faults were reported to be coil degradation faults. These faults consist of both exterior corrosion, in which the fins develop a "skin" on them, and interior fouling that reduces the flow through the coil. Both of these types of faults can eventually lead to reduced heat transfer capacity.

The interview subjects reported that sensor faults are less common than all of the previously discussed faults, with the exception of active sensors like relative humidity and CO₂ sensors. Assuming they are properly calibrated from the outset, temperature sensor failures are relatively rare, and when they fail, the failure is normally very significant (i.e. complete failure is more common than drifting).

Flow sensors that use differential pressure are notoriously unreliable at low flow rates, and comprise the most common problem found with the terminal units. Terminal units can also fail with problems to the actuator or on a longer timeframe with the controller (although often these units are combined into a single part in modern systems).

Other faults that are much rarer include control faults (e.g. schedule problems) and fan faults.

4.9. Conclusions and Recommendations

- From the literature and meetings with local industry personnel, it is evident that there exists a need for effective AFDD in AHU-VAV systems that is not being met by current commercially available products. Research interest in this area has increased significantly in recent years, yet there has been no extensive demonstration of a robust and effective solution to date.

- A dynamic fault simulation testbed is developed and experimentally validated, which allows for the simulation of 51 discrete faults during any seasonal operating condition specified by the user. Nearly all of these 51 faults can also be adjusted so different severities can be tested as well.
- The PMPCA method proposed herein shows promise for evolving into a commercially viable methodology. The results included in this paper demonstrate the successful ability to distinguish between faulty and fault-free system operation.
- The PMPCA method is in the process of being refined. During this refinement process, it has been found that the most important parameters are those pertaining to the creation of the PCA models, followed by the size of the window used for analysis, and other historical data considerations.
- At the current stage of refinement, the PMPCA method has been demonstrated to have a false alarm rate below 1%, with consistent detection of most faults. Further improvement is expected during the first quarter of BP3.
- Part of evaluating the benefit of an AFDD system for AHU-VAV systems is understanding the overall economic impact. The analysis conducted herein contains useful data and insights that can aid with quantifying accurate estimates of the value of effective AFDD for AHU-VAV systems.
- This coming year will bring final refinement of the detection method, and preparation of this method for the online demonstration. By the end of BP3, the online demonstration is expected to be in place. This will be a key step in testing the effectiveness of the method.
- Additionally, extensions of PCA fault detection methods have the potential to be used for diagnostic work. Experiments with this will commence this year, as well as review of existing diagnostic strategies that show promise.

5. Envelope Fault Diagnostics

5.1 Introduction

Analyzing building envelope faults helps to effectively address air leakage in and out of the building. This in turn helps to ensure acceptable indoor air quality and reduced energy consumption for heating or cooling. Many techniques have been developed to measure the air flow across the building envelope and characterize the envelope faults. Some of the commonly used techniques are:

- Tracer gas test
- Blower door test
- Theatrical smoke test
- Infrared (IR) Thermography

This report explains the objectives, advantages and disadvantages of each of these techniques.

A summary of the Blower door and IR thermography tests performed on Building 101 is also included in the latter section of this report.

The main goal of envelope fault characterization is to analyze air flow in and out of a building. It helps to identify sources of air leakage and thermal bridging which when addressed effectively help to ensure acceptable indoor air quality and also help reduce heating and cooling energy consumption.

Various techniques have been developed to measure how the air flows between the inside and the outside of a building, between different zones within the building as well as air flows through the mechanical systems.

Some of these techniques are:

- Tracer gas test
- Blower door test
- Theatrical smoke test
- Infrared (IR) Thermography

Each technique helps to analyze the air flows in different ways and has its own advantages and disadvantages.

- **The Tracer Gas test** helps to accurately quantify the air flow across a given boundary during normal operating conditions. However, it does not help to identify the exact sources of leaks. Also, the equipment required for this testing method is much more expensive compared to other techniques.
- **Blower Door Test** helps to measure the tightness of the building. It is a reliable and a cost effective way to compare the air leakage between two buildings.

In order to demonstrate the Blower Door test method and its applications, a summary of blower door tests performed on building 101 is included in a later section of this report. The goal of this test is to characterize the building air leakage.

- **Theatrical Smoke test**

Theatrical smoke is used for locating air leakage pathways or exact leak locations in the building envelope. The theatrical smoke test is often used in conjunction with a blower door test. The blower door

test often indicates how tight or how leaky the building is, but not the exact locations of the leaks. Hence, it needs to be used in conjunction with other tests such as theatrical smoke or IR tests to identify the leak sources. The theatrical smoke makes it easier to spot the leak locations. The equipment required for this test is inexpensive; however, it does require regular maintenance.

- **Infrared Thermography** is often done in conjunction with a Blower Door Test. While the Blower Door test identifies the air leakage locations in the building envelope, the IR thermography identifies the thermal bridges in the envelope. The two tests performed together help to identify potential retrofit solutions to reduce energy consumption within the space.

While the IR thermography and Theatrical smoke test both help to identify the exact leak sources, the theatrical smoke test has an advantage over the IR test. The IR test requires manipulation of the HVAC system to achieve a temperature differential of at least 10 F. However, while the smoke test method simply identifies the leak location, the IR thermography also identifies thermal bridges within the envelope.

An IR Thermography test was also conducted on Building 101 and the test results have been included in a later section of this report.

The various tests identified above, thus, help to analyze and characterize the envelope faults. These faults when addressed effectively can contribute to significant reduction in energy consumption of the building.

5.2 Literature review

Tracer Gas Test

The concept of the tracer gas leak test system is to trace escaped gases that exist at a low concentration in the atmosphere

While Blower door tests and duct pressurization tests help to identify leakage characteristics of the envelope and air distribution systems at elevated and uniform pressure differences, the tracer gas test accurately measures how much outside air actually enters the house under normal operating conditions. Thus, the Tracer gas methods are used to determine the air movement across a boundary during normal operating conditions. The boundary could be the building shell, a zone within the building or a room

However, tracer gas detection equipment is expensive compared to blower door testing and IR thermography. This serves as a disadvantage and is the reason why Tracer gas test is not as widely used as the blower door test although it gives the exact quantification of the air flow.

Test process

The tracer gas is injected into the room and mixed to a uniform concentration using the air handler or portable fans. The rate of decay in concentration of the tracer gas is used to calculate the air exchange rate due to infiltration. Thus, the flow of air across the boundary is determined by looking at the initial and final concentrations of the tracer gas and the time period between these concentrations.

Tracer gas test can be categorized as:

- Single Zone tests
- Multi Zone tests

Single Zone tests measure the net whole-building air exchange rates under a variety of operating conditions, while Multi Zone tests provide information as to how much outside air is distributed room to room inside the building.

Effective Tracer gas characteristics

- Detectable at low concentration
- Safe for humans
- Not naturally occurring
- Neutral buoyance in air.

Blower Door Test

A Blower Door is a diagnostic tool that measures the degree of a building's air-tightness. It identifies the leakage characteristics of the building envelope at elevated and uniform pressure differences.

It proves to be a reliable, highly accurate and cost-effective method for determining a building's air leakage performance. The number of air changes per hour at a standard pressure differential reveals the building envelope's air leakage profile.

Reasons for performing a Blower Door test:

- Helps to reduce energy consumption due to air leakage
- Avoid moisture or condensation problems
- Avoid uncomfortable drafts caused by cold air leakage from the outside

Although the Blower Door method does not give a measurement of actual ventilation during normal building operation, it is useful:

- To compare the leakage area of two different buildings
- To identify leakage sources within the building envelope
- To determine leakage reduction after an individual retrofit.

Blower Door method is also helpful in determining component leakage which helps to identify the distribution of leaks across the envelope. In this case, the building is divided into sections and the leakage is measured separately in each section. Multiple blower doors are used to simultaneously depressurize the test space as well as the adjacent spaces relative to outdoors. Thus, there is always a zero pressure difference between the test space and the adjacent spaces. This helps to ensure that there is no air leakage between the test space and the adjacent spaces. Thus, the air leakage measured for that space is indicative of the leaks associated from the space to outdoors.

Test process

A Blower Door is a powerful fan that is mounted into the frame of an exterior door. The fan pulls air out of the house, lowering the air pressure inside. The higher outside pressure then flows in through all unsealed cracks and openings.

Equipment for the test

Blower door consists of a frame and a flexible panel that fits in a doorway, a variable speed fan, a pressure gauge to measure the pressure differences inside and outside the home and an airflow manometer and hoses for measuring air flow.

- There are two types of Blower Doors-
- Calibrated
- Non-calibrated

A calibrated blower door has several gauges that measure the amount of air pulled out of the house by the fan. Non-calibrated blower doors, on the other hand, can only locate leaks in the envelope. This does not help determine the overall tightness of the building. The calibrated blower doors make it possible to quantify the amount of air leakage.

The Blower Door technique uses a parameter called the Effective Leakage Area which is considered the area of an opening which would provide the same air flow as the building shell when subjected to a given pressure differential.

Theatrical Smoke Test

Theatrical smoke is used for locating air leakage pathways or exact leak locations in building envelope.

The theatrical smoke test is often used in conjunction with a blower door test. The blower door test often indicates how tight or how leaky the building is but not the exact locations of the leaks. Hence, it needs to be used in conjunction with other tests such as theatrical smoke or IR tests to identify the leak sources. The theatrical smoke makes it easier to spot the leak locations.

Usually in a blower door test, the space being tested is depressurized; however, in the case of a theatrical smoke test, the space requires to be pressurized so that the smoke flows outside.

Test Process

The use of theatrical smoke to detect air leakage requires pressurization of the space to be tested. This is achieved with the help of Blower door tests. However, the leakage or air flow is not clearly visible with the blower door test.

Theatrical smoke is then introduced in the space. Due to pressurization technique, the smoke can be seen from the exterior, escaping from the space through various leaks in the envelope. This, thus, makes the leakage sites visible.

These tests should usually be conducted after a space has been insulated. It is easier to create a pressure difference inside and outside if the envelope is tight. The equipment required for theatrical smoke is pretty inexpensive, however, does require regular maintenance.

Thus, the results of a blower door test allow a prediction of how much air leakage there could be under typical environmental conditions. With the aid of theatrical smoke, air leakage can be visually identified.

Infrared Thermography

The IR thermography measures surface temperatures by using infrared video and still cameras. The images on the video or film record the temperature variations of the building's envelope, ranging from

white for warm regions to black for cooler areas. The highest temperatures in a thermographic image indicates highest amount of heat loss.

Thermographic inspections can be either interior survey or exterior survey. Interior scans are more common because warm air escaping from a building does not always move through the wall in a straight line. Heat loss detected in one area of the outside wall might actually have originated at some other location on the inside. Also, it is harder to detect temperature differences on the outside surface of the building during windy weather. Because of this difficulty, interior surveys are generally more accurate because they benefit from reduced air movement.

The main difference between IR thermography and a blower door test is that, IR thermography helps to identify thermal bridges in the envelope and likely locations for mold or mildew growth due to moisture problems. Blower door test on the other hand identifies air leakage locations in the building envelope.

Thermographic scans can be used in conjunction with Blower Door tests. The Blower Door test exaggerates the air leaking through the building envelope defects. Such air leaks appear as black streaks in the IR cameras.

While the IR thermography and Theatrical smoke test both help to identify the exact leak sources, the theatrical smoke test has an advantage over the IR test. The IR test requires manipulation of the HVAC system to achieve a temperature differential of at least 10 F. However, while the smoke test method simply identifies the leak location, the IR thermography also identifies thermal bridges within the envelope

Thus, the various tests listed above help in identifying and characterizing envelope faults. Effectively addressing these faults can contribute to significant reduction in energy consumption and increase in energy efficiency.

5.3. Envelope fault characterization methods and results

Conduct IR thermography test on Bldg. 101

Utilize Mark Group to conduct test

Mark Group performed the IR thermography on Building 101 with the main objective of

- Identifying air leakage spots
- Identifying locations where the existing insulation was no longer effective
- Identifying the locations in the existing structure which resulted in maximum heat loss.
- The IR test was performed on the exterior of the building.

The IR thermography conducted by Mark Group on Building 101 indicated that the building is basically in excellent shape; however, it does require a few improvements such as addressing cracks in the envelope or broken air seals at the soffit, windows, double doors, etc. in order to improve its energy performance.

The hypothesis on building inspection was that the building air leakage was concentrated around building's soffits and around the doors. The observations after the test confirmed the hypothesis to some extent. The air leakage spots as well as heat loss spots identified through the IR thermography include:

- Cracks in bricks where the pointing was no longer effective
- Building soffits without efficient air sealing or insulation

- Large arched windows due to ineffective air sealing
- Air gaps around door frames
- Underside of the large porch ceiling.
- Concrete foundation due to ineffective insulation.

Generate summary of results and validity of test to identify air leaks

Observations and Recommendation based on the IR Thermography Results:

1. Building Envelope – Brick Walls:

Cracks in building envelope due to degraded wall mortar result in leakage of conditioned air as well as water infiltration. This results in heat loss and deterioration of the structure affecting the overall energy consumption.

This issue can be addressed by re-pointing the cracks in the wall.



Figure 5.1 Heat loss through wall cracks

2. Heater/radiator:

Heaters located beneath the windows were observed to be conducting heat through exterior walls. This can be addressed by providing insulation behind the radiator.

3. Building Soffit – Ceiling and Roof:

- Ceiling Joists penetrations into the wall:

The junction between the third floor ceiling joists and the exterior walls have 1/8” to 1” gap around them which results in substantial heat loss through the soffit.

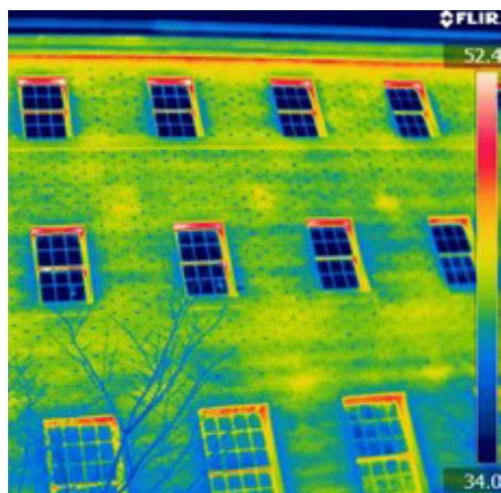


Figure 5.2 Heat loss through building soffit

- **Roof Joists penetrations into the wall**

A similar issue is observed with roof joists, which indicates that the junctions where the joists or other structural members meet the exterior wall are not effectively sealed against air infiltration.

This issue can be addressed by caulking or air sealing the gaps or cracks between the wall and ceiling. The penetrations of the roof joists and exterior wall can be effectively insulated with the help of closed cell spray foam.

- **Roof ridge**

The area where the insulation meets the roof ridge is not effectively air sealed. This results in heat loss through the roof ridge. This issue can be addressed by either repairing the existing insulation or by providing spray foam along the underside of the roof ridge in order to ensure complete air seal as well as effective insulation at junctions.

4. West-side Windows:

The IR thermography detected cracks in window frame and loose trim work for large arched windows on the West side of the building on the interior as well as exterior which were a source of air infiltration and heat loss. Cracks were also observed in the caulking around the small arched windows on the west side from the interior.

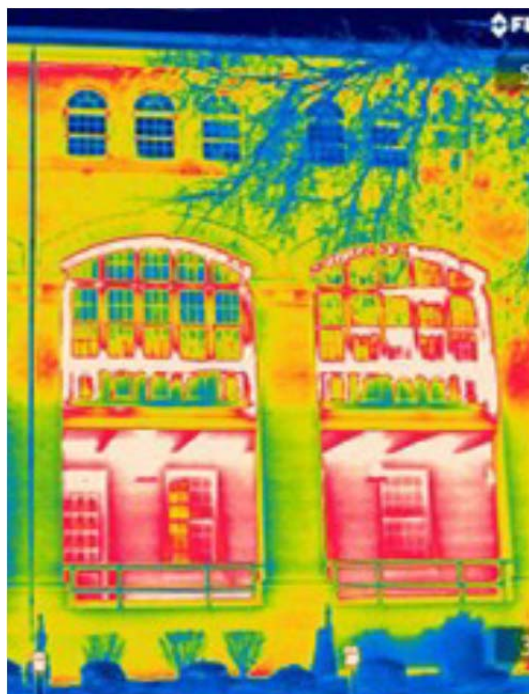


Figure 5.3 Heat loss through cracks in window frames

5. Doors and Windows:

The IR test detected gaps along the edges and the middle of double doors which contributed to heat loss. These issues could be resolved with the help of effective air sealing and weather stripping.

6. Covered Porch:

The IR thermography test identified the need of insulating the porch ceiling as heat loss was detected through the ceiling from the heated rooms above.

Summary

1. The IR Thermography test, thus, helped to identify source of air infiltration in the building envelope such as:
 - a) Window frames
 - b) Cracks in brick walls
 - c) Air gaps at the junctions where joists penetrate into the exterior wall
2. The IR test also helped to identify the parts of the roof where the insulation had become ineffective. This helps to analyze the need for putting in new insulation or repairing existing insulation.
3. Another major energy saving potential identified with the help of IR thermography is the need for new insulation to be installed in areas which contribute to major heat loss, such as, between the radiators and exterior walls, on the covered porch ceiling as well as effective insulation under the roof ridge.

5.4. Summarize blower door testing results for Bldg. 101

Obtain test summary report from appropriate person

Camroden Associates, Inc. visited building 101 on January 27, 28 and 29 of 2012. The focus of the visit was to characterize the building enclosure in terms of air leakage rates and leak locations. The building was inspected and several tests using calibrated fans and pressure difference data acquisition were conducted.

Generate summary of results to identify air leaks through the envelope in Bldg. 101

General observations from the various blower door tests conducted on Building 101 are:

- 1.8 ACH₅₀ air leakage rate for Building 101 which makes the building relatively air-tight for its size in comparison to historical test data for non-residential buildings.
- Air leakage sites are fairly well distributed around the building enclosure
- The air leakage through the fire dampers located in the basement is quite high in comparison to the total shell leakage
- Significant internal air leakage paths were observed indicating air leakage through the internal structure itself.
- Suite 210 in the North wing was observed to be leakier to the outside than the other north wing floors.
- Air leakage rate through outdoor air dampers was observed to be higher than leakage through the enclosure.

The table below indicates a detailed summary of the findings.

Table 5.1 Summary of the findings

Summary of Findings	
Building enclosure air leakage (excluding HVAC and smoke control damper leakage)	27,990 cfm at 50 pascals (1.8 ACH ₅₀ ; 0.32 cfm 50 per sq.ft of enclosure) 36,112 cfm at 75 pascals; (0.41 cfm 75 per square foot of enclosure) 5,600 cfm at 50 pascals is estimated to be through windows
Air leakage through smoke control dampers located in the basement	2,735 cfm at 50 pascals (in addition to 27,990 cfm ₅₀) 8cfm/sq.ft of damper face area (excluding a damaged damper)
Air leakage through outdoor air and make-up air dampers	4,534 cfm at 50 pascals (in addition to 27,990 cfm ₅₀) 54 cfm/sq.ft
Total enclosure air leakage including closed damper leakage	35,259 cfm ₅₀ (2.23 ACH ₅₀)
Suite 210 leakage:	
Total leakage	16,334 cfm ₅₀
Air leakage from 210 to the outside	4,879 cfm ₅₀
Air leakage to other interior spaces through HVAC distribution system	3,013 cfm ₅₀

Air leakage to other interior spaces through structure	8,442 cfm ₅₀
Interesting Observations	<ul style="list-style-type: none"> • The north wing basement and suite 210 run 10 – 20 pascals positive relative to the surrounding areas (the return damper in suite 210 does not appear to cycle open) • The south wing basement suite (Oxycool) runs around 70 pascals negative when the environmental chamber exhaust is operated • The smoke relief dampers in the ceiling of the core portion of the building are open all the time, creating a single zone condition with attic areas B, C and D • Exhaust fan 3 is installed backwards, apparently contrary to the drawings.

The main purpose of the project was to characterize the building enclosure air leakage.

Activities conducted

- The building enclosure, floor penetrations, stairwells, elevator shafts, utility chases and demising walls were inspected for intentional and unintentional gaps, holes and openings
- Pressure maps of the building were made using micro-manometers and smoke bottles. Pressure maps were made as the building was found and with the core of the building depressurized to -50 pascals.
- The air leakage rate of the building enclosure was measured using fan pressurization techniques, including total leakage to the exterior and exterior leakage for each floor. HVAC openings (motorized dampers on outdoor air and make-up air intakes) were closed and masked and exhaust fan motorized dampers were closed for initial test. Dampers remained closed but the intakes were unmasked for a subsequent test to determine how much air leakage there is through the mechanical system dampers to the exterior.
- The total leakage of suite 210 was measured. The leakage between suite 210 and outdoors, the leakage between suite 210 and other interior spaces through the floors and walls and through the air distribution system of the unit serving the north wing was measured in various tests.

Existing penetrations through the building enclosure

Foundation: The basement is day-lit with 3 to 4 feet of basement wall above grade and a concrete floor slab. The basement walls are un-insulated concrete and masonry. The basement contains mechanical equipment with the following penetrations in the enclosure:

- AHU 1, 2 and 3 serving the core and east wing, the south wing and the north wing respectively
- AHU serving the north wing basement suite
- 7 outdoor air and make-up air louvers (AHU1, AHU2, AHU3, AHU serving the north wing basement suite, AHU serving the south wing basement suite, make-up air for the boiler and make-up air for the hot water heaters.

- 2 exhaust louvers – one serving the environmental chamber in the south wing basement suite and one probable exhaust outlet serving the north wing basement suite.
- 6 fire control louvers in the basement wall.

Upper Walls: The walls from grade level to the wooden roof framing are heavy brick construction at least four wythe thick. The walls are un-insulated.

The penetrations in the wall include:

- 246 double hung windows
- 42 basement windows
- 13 arch top units with 5 double hung windows
- 6 double entry doors
- 6 single entry doors

Roofing System: The building is covered by a wooden frame roof system with a combination of low slope roof and pitched, hip roof. The low slope roof is covered by roofing membrane. The pitched roof is covered by shingles. Fiberglass batt insulation is located between the rafters. The attic is separated into five chambers which are well connected by large rectangular openings through the walls.

The roof is penetrated by:

- 3 exhaust fan outlets with backdraft dampers (EF 1, 2 and 4)
- 3 air inlets with motorized dampers (two are passive inlets serving the north and south wing attics; one is connected to a supply fan that is identified as exhaust fan # 3)
- 1 roof access hatch (wired to security)
- 4 curb mounted smoke relief hatches in the low slope roof.

5.5. Pressure Tests

Ten pressure tests were conducted for the building and for suite 210 in order to identify the air leakage through the enclosure.

Objectives of each test:

Test 1: To identify the leakage for the building envelope only.

Test 2: To identify the distribution of air leakage sites around the building enclosure.

Test 3: To identify leakage through fire control dampers in the basement.

Test 4 and 5: Core area depressurization- To identify leakage between each floor and zone.

Test 6: To identify the air leakage through outdoor air and make-up air dampers.

Test 7: To identify air leakage from suite 210 to outdoors.

Test 8: To identify air leakage from suite 210 (excluding the HVAC system) as if it were an individual building.

Test 9: To identify overall leakage through suite 210, including leakage through HVAC systems.

Test 10: To identify air leakage through windows.

Test 1:

The main purpose of test 1 was to identify the air leakage for building envelope. The air leakage rate of the building envelope was determined using calibrated orifice blower doors to exhaust air from the building.



Figure 5.4 Three fan blower door

Instruments used for the test:

- Multiple Model 3 Minneapolis Blower Doors manufactured by The Energy Conservatory (TEC)
- TEC DG-700 micro-manometers to measure indoor/outdoor pressure differences and blower door fan air flow volume.
- TECHLOG 2 data logging program to collect data from micro-manometers. It also provides computerized control of multiple Minneapolis Blower Door fans.

Building setup for the test:

- Whole building depressurization test
- All AHUs off
- All exhaust fans off
- All interior doors open except:
 - 110 inner and stairwell doors
 - Doors to secure suites in basement closed
 - Main mechanical room door
- All outdoor air intakes serving air handlers and make-up air intakes serving mechanical rooms closed and masked.
- All smoke inlet dampers in basement closed and masked
- Smoke relief dampers to attic open (these are always open)
- Exhaust fans 1 – 4 have gravity dampers at terminations on roof
- Make up air inlet through north wing roof motorized dampers closed.

Three blower doors are installed in each of the three exterior doorways – the north and south wing egress stairwell doors on the east side of the building and the west facing porch entry to the lobby. Exterior pressure taps were placed across all four azimuths of the building where the exterior walls meet grade. The locations for the fans and taps are given in the figure below. The reported pressure across the shell is the average of all four shell pressure measurements

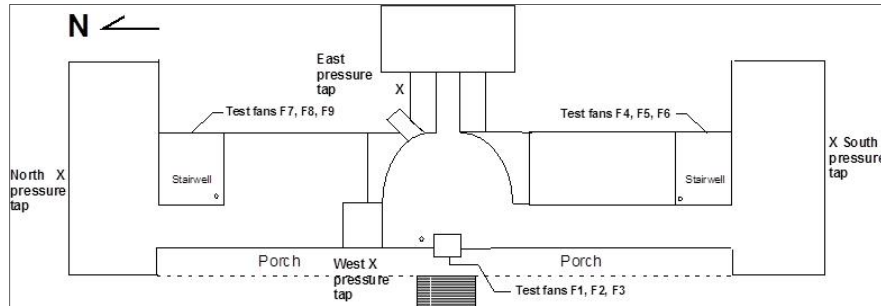


Figure 5.5 Location for blower door fans and pressure taps

Pressure differences were also collected between the central core and the 1st, 2nd and 3rd floors of the north wing and the 1st floor of the south wing. The internal pressure difference measurements serve two functions:

- They are used to assess and document single zone conditions during the whole building tests,
- They are used to provide series leakage data during tests to study inter-zonal leakage.

Results:

Air leakage metric includes a measurement of airflow at a particular induced indoor-outdoor pressure difference.

Table 5.2 Analysis results whole building depressurization test

Air leakage at 50 Pascals	27,990 cfm
Air leakage at 75 Pascals	36,112 cfm
95% confidence interval	0.7 %
Correlation coefficient squared (R^2)	0.999
Flow exponent (n)	0.628
Air leakage coefficient (C)	2,396.0 cfm/Pa ⁿ
Equivalent leakage area @ 10 Pa	2,991.4 sq. in.
Effective leakage area @ 4 Pascals	1,624.8 sq. in.
Whole building enclosure area	87,200 ft ²
Building Volume	948,297 ft ³
Cfm75/ft² enclosure (all six sides)	0.41
ACH₅₀	1.8

In comparison to the historical test data for non-residential buildings in terms of ACH₅₀, Building 101 is relatively air-tight for its size.

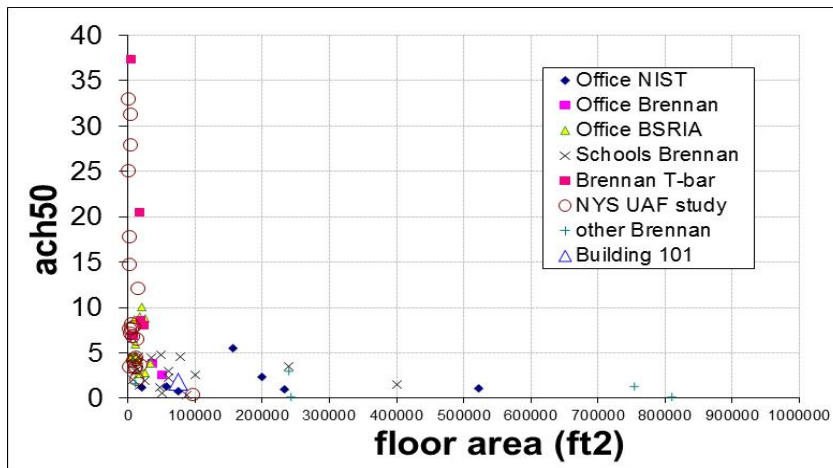


Figure 5.6 Historical test data for non-residential building in terms of ACH 50

Test 2:

Test 2 involves the same building setup as Test 1 except that all the doors between the north and south wings and the core of the building were closed. The test fan flows for each zone:

- North wing – 8,685 cfm
- Core – 9,520 cfm
- South wing 9,339 cfm

Total flow = 27,544 cfm

This test indicated that the air leakage sites are fairly well distributed around the building enclosure.

Test 3:

Test 3 uses the same building conditions as test 2, with 50 pascals indoor-outdoor shell pressure difference. All the fire control dampers located in the basement are unsealed.

Total test fan flow dampers unmasked = 30,279 cfm₅₀

Total test fan flow dampers masked = 27,554 cfm₅₀

Total basement fire damper leakage = 2,735 cfm at 50 pascals



Figure 5.7 Fire control dampers initially sealed with self-adhering duct mask

There are six, three foot by four foot openings with motorized dampers in closed position. One damaged damper came unsealed just before Test 3. The air leakage through this single damper appeared to be around 2,200 cfm_{50} . Unsealing the remaining dampers resulted in around an additional 500 cfm_{50} . For five dampers, the air leakage amounts to around 8 cfm_{50} per square foot of damper face area.

These damper leakage rates are, thus, observed to be quite high when compared to total shell leakage.

Test 4 and 5:

For test 4 the fans in the north and south stairwells were turned off and capped. For test 5 all the stairwell doors in both the north and south stairwells were closed. During the test the core portion of the building was depressurized by 25 pascals relative to the exterior of the building using the three fans in core porch doorway.

Results:

- Closing the stairwell doors in Test 5 did not have much impact on the pressure differences between the core and the north and south wing. This indicates that significant internal air leakage paths join each floor of the building and each zone of the building.
- The HVAC system joins each floor, but not each zone. This indicates that there are significant leakage sites through the internal structure itself.
- Also, air leakage to the outside from each floor of the South wing is fairly uniform; however, the suite 210 in the north wing is leakier to the outside than the other North wing floors.

Test 6

Test 6 was conducted in two parts with two fans running in each location. For the first part of the test, the outdoor air and make-up air dampers were masked while the indoor-outdoor average pressure difference was held at 50 pascals. The dampers were all unmasked for the second part of the test.

Unmasked: 34,096 cfm at 45.5 pascals

Masked: 29,824 cfm at 45.5 pascals

Total air leakage through the dampers is around 4,272 cfm at 45.5 pascals (4,534 cfm₅₀).

The area of dampers = ~84 sq.ft of face area (which includes 5 outdoor air dampers and 2 make-up air dampers).

This amounts to around 54 cfm₅₀ per square foot of damper.

Thus, the leakage through the outdoor air dampers is much high compared to the leakage through the enclosure



Figure 5.8 Outdoor air intake unmasked

Test 7:

A single fan door was set-up the entry door so it could be used to depressurize suite 210. All the core to wing doors and all the stairwell doors were open except those to suite 210. The test fans in the stairwells and building core were used to create a 50 pascal pressure difference between inside and outside. The single fan in suite 210 entry door was used create a near zero pressure difference between the interior of suite 210 and the surrounding areas. The air flow through the test fan in the suite door is then the air leakage between suite 210 and outdoors.

The result was 4,879 cfm at 50 pascals to produce a pressure difference of 50 pascals between suite 210 and the outdoors.

Test 8:

A three fan blower door was setup in the entry door to suite 210 with all diffusers and return grilles sealed. The total air leakage for the suite excluding that through the HVAC system to other floors is 13,321 cfm₅₀.

Test 9:

Test 9 uses the same setup as test 8, however, the supply diffusers and return grilles were unmasked. This test helps to measure the total air leakage for the suite including that through the HVAC system. The total leakage is 16,334 cfm₅₀.

This total air leakage from suite 210, 16,334 cfm₅₀ can be partitioned into three sets:

- Air leakage from suite 210 through the exterior enclosure to outside – 4,879 cfm_{50} .
- Air leakage from suite 210 to other interior spaces through HVAC distribution ductwork – 3,013 cfm_{50} .
- Air leakage through the interior structure from suite 210 to other interior spaces – 8,442 cfm_{50}

Test 10:

Window leakage was estimated through three windows on the west wall of suite 210.

The method used to test these windows was to seal the interior of the windows using 24 inch wide duct mask. This creates a cavity between the stretched plastic film and the prime window. A blower door setup in the suite entryway was used to pressurize the suite to around 50 pascals relative to outdoor air. A micro-manometer was used to measure the pressure differences between the indoor air and the cavity and between the indoor air and outdoor air. If the film makes a very good air seal and the windows are not perfectly airtight then nearly all the pressure drop is across the stretched plastic film. By cutting a one square inch holes in the film the air flow leaking through the window passes through the cut hole to the interior.

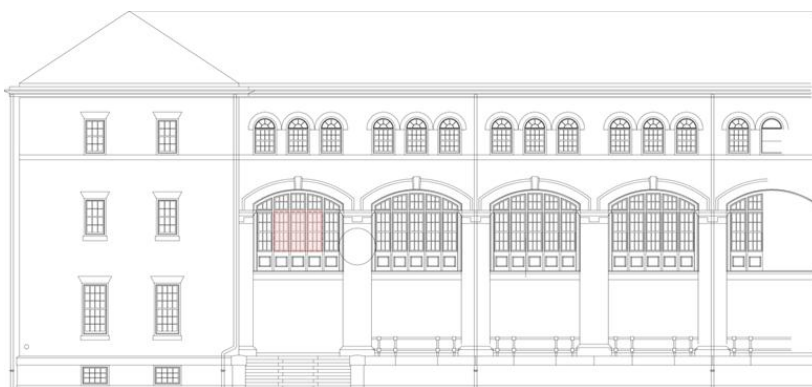


Figure 5.9 Large arched windows on the west side of the building

In this case, the pressure drop across the film is reduced and the pressure drop across the window increases. A regression analysis can be applied to the data and an estimate can be made for the value of flow at 50 pascals.

Total number of double hung windows in the building = 311

These windows are considered to be somewhat representative; thus, the leakage through the windows is assumed to be $311 \times 18 \text{ cfm}_{50} = 5,600 \text{ cfm}$ at 50 pascals.

5.6. Summary

The various tests performed help to characterize the building enclosure in terms of air leakage rates and leak locations. The observations and results of the tests indicate:

- 1.8 ACH_{50} air leakage rate for Building 101 which makes the building relatively air-tight for its size in comparison to historical test data for non-residential buildings.
- Air leakage sites are fairly well distributed around the building enclosure
- The air leakage through the fire dampers located in the basement is quite high in comparison to the total shell leakage

- Significant internal air leakage paths were observed indicating air leakage through the internal structure itself.
- Suite 210 in the North wing was observed to be leakier to the outside than the other north wing floors.
- Air leakage rate through outdoor air dampers was observed to be higher than leakage through the enclosure

The two reports – the Blower door test and the IR thermography performed on Building 101 discussed above help to diagnose and characterize faults in building envelope. While the Blower door test helped analyze the air leakage through the building envelope, through HVAC penetrations as well as through windows; the IR thermography test helped to identify the spots in the envelope which accounted for maximum heat loss through the envelope.

The IR thermography detected cracks in window frames on the west side of the building which were a source of air infiltration. This was confirmed through the Blower door tests which indicated an air leakage of 18cfm through the large arched windows. Both the IR Thermography as well as the Blower door test indicated that effective sealing of air gaps at points of penetrations in the exterior walls can help reduce energy consumption.

Thus, the results of the two tests complement each other and help to identify and analyze the faults in the building envelope. These faults when addressed effectively can contribute to significant reduction in energy consumption of the building.

6. Conclusions and Future Study

In BP2, the team members have successfully developed and demonstrated the effectiveness of the library of diagnostics decision support tools, which include diagnostics tools (for the RTU system, the AHU-VAV system, and the building envelop system) and the fault prioritization tools.

The diagnostics tools developed for the RTU system include the use of virtual sensors as a means of realizing a robust and low-cost approach to monitoring, detecting, and diagnosing faults. Various virtual sensors have been developed for vapor compression equipment. Existing data and laboratory tests were used to develop a FDD demonstration for refrigerant and air-side faults, including faulty economizer operation, heat exchanger fouling, and faulty refrigerant charge. A number of virtual sensors have been developed using RTU test data to enable a demonstration of diagnostics systems for RTUs. The RTU virtual sensors were shown to provide predictions that are within 10% of direct measurements. Some initial video demonstrations have been developed for RTU diagnostics.

In addition, a complete implementation for an FDD system has been developed and connected to data obtained from an RTU monitored in the field. The user interface incorporates integrated virtual sensors to provide diagnostic outputs and performance impacts of the fault(s). Health and economic status reports for equipment are generated using fault impact indices that measure degradation in system COP.

VRC, VRMF, and VAF sensors for three DX systems at Building 101 have been developed and demonstrated using data from Building 101. Although it was not possible to fully validate these sensors, the outputs did demonstrate the proper dependence on compressor and fan staging and did not deviate from normal behavior during the course of the evaluation.

Moreover, the impact of individual faults on capacity and energy efficiency was evaluated for air conditioners over a wide range of operating conditions. Based on the results of this study, refrigerant undercharging in the range of 25% can lead to an average reduction of 20% in cooling capacity. Furthermore, an undercharge of about 25% would cause an average penalty in a cost penalty of \$60 per year per ton of rated capacity for typical electricity rates. For evaporator fouling, a reduction of air flow rate by 50% decreased average capacity by 14%, whereas annual cost increases by \$24 per ton. For condenser fouling, a reduction of air flow rate by 50% decreased average capacity by 9%, whereas annual cost increased by \$80 per ton.

The diagnostics tools developed for the AHU-VAV system utilize machine learning techniques such as pattern matching and principle component analysis methods. The developed PMPCA technology does not require any fault data training and requires only 10-15 days fault-free training data (for each season). No requirement for customization for different AHU applications is needed. Three datasets, including a small office building experimental data from winter, summer, and shoulder seasons; a medium-sized office building experimental data from winter months; and data from the simulation testbed developed in this project, are used to assess the effectiveness of the developed diagnostics tools. The developed data-driven PMPCA method was shown to detect nearly 90% of the AHU faults from the three datasets described above, with an overall false-alarm rate of less than 1%.

Furthermore, a dynamic fault simulation testbed is developed and experimentally validated, which allows for the simulation of 51 discrete faults during any seasonal operating condition specified by the user. Nearly all of these 51 faults can also be adjusted so different severities can be tested as well. This testbed can now be used for comparison and analysis of AFDD strategies for this EEB HUB project, to identify the most effective AFDD methods as well as individual strengths and weaknesses of the methods.

Two building envelope diagnostics techniques, IR Thermography and Blower Door Testing, were chosen to be conducted on the EEB HUB headquarter building(101). A report was generated for each test to diagnose and characterize faults in the Building 101 envelope. While the Blower door test helped analyze air leakage through the building envelope via HVAC penetrations and windows, the IR thermography test helped to identify the spots in the envelope which accounted for maximum heat loss through the envelope. The IR Thermography Test detected cracks in window frames on the west side of the building which were a source of air infiltration. This was confirmed through the Blower Door Test which indicated an air leakage of 18cfm through the large arched windows. Both the IR Thermography as well as the Blower Door Test indicated that effective sealing of air gaps at points of penetrations in the exterior walls can help reduce energy consumption.

The fault prioritization tool chains include tool chains for design phase and tool chains for operation phase. The tool chains are developed using a generic model based approach that can be used for quantification of various faults and fault severities impact on energy consumption. A fault modeling library is developed in TRNSYS. In this study, it is also demonstrated that individual faults, as well as fault couplings are important. The coupling effect can boost the effect of individual faults significantly.

The development and prototyping of a scalable approach to quantify energy impact of faults during operational phase and to prioritize corrective actions are also completed. The current prototype can estimate energy impact of any damper and valve faults in an air-handling system. The prototype of the automated fault impact process is tested by comparing the results with the TRNSYS model for building 101.

These developed tools enable cost effective diagnostics solutions for existing buildings. Both existing literature and our study have demonstrated that these developed tools can help to reduce the HVAC system energy consumption by up to 30 percent. Therefore, this subtask directly support *the Hub's goal of "... reduce annual energy use in the commercial buildings sector in Greater Philadelphia by 20 percent by 2020."*

In the future, it would be desirable to further refine and extend the capabilities of the developed tools. For example, the developed decision making tools can be extended to include occupant comfort as additional performance indicator to limit the study only to the faults that could go undetected and cause significant energy performance degradation. More tests, especially field tests and demonstrations, need to be conduct to further assess the developed diagnosis tools and to accelerate the technology transfer and commercialization process.

Reference

1. ADM Associates, 2009, Market assessment and field M&V study for comprehensive packaged A/C systems program, SCE0286
2. Ahan, Y. C. Cheong., Y.G, and Lee, J. K., 2006, An Experimental Study of the Air-Side Particulate Fouling in Fin-and-Tube Heat Exchangers of Air Conditioners, *International Refrigerant and Air conditioning Conference*, No.20
3. Air conditioning and Refrigeration Institute (ARI), 2004, Standard 540: A method for presentation of compressor performance data, *Air-Conditioning and Refrigeration Institute*
4. ASHRAE. 2011 ASHRAE Handbook – Applications. Chapter 41. Atlanta: American Society of Heating, Refrigeration, and Air-Conditioning Engineers, Inc, 2011.
5. Basarkar M., Pang 4D., Wang L., Haves P., Hong T. 2011. Modeling and simulation of HVAC Results in EnergyPlus. Report: LBNL-5564E
6. Bendapudi, S. and J. E. Braun (2002). Development and Validation of a Mechanistic, Dynamic Model for a Vapor Compression Centrifugal Liquid Chiller, Report #4036-4, Deliverable for Research Project 1043-RP, ASHRAE, Atlanta, GA. .
7. Bin Chen, and J.E. Braun., 2001, Simple rule-based methods for fault detection and diagnostics applied to packaged air conditioners, *ASHRAE Transactions*, Vol. 107(1)
8. Blasnik, M., Downey, T., Proctor, J. and Peterson, G., 1996, “Assessment of HVAC Installations in New Homes in APS Service Territory”, Proctor Engineering Group Report for Arizona Public Service Company
1. Brambley, M., R. Pratt, D.P. Chassin, and S. Katipamula. “Automated diagnostics for outdoor air ventilation and economizers.” *ASHRAE Journal* 40(10), 1998.
2. Braun, J., 2003, Automated fault Detection and Diagnostics for vapor Compression Cooling Equipment, *Journal of solar energy engineering*, Vol. 125
3. Braun, J. E., Comstock, M. C., 1999, Development of analysis tools for the evaluation of fault detection and diagnostics for chillers. Deliverable for ASHRAE Research Project 1043-RP
4. Breuker, M. S. and Braun, J. E., 1998a, Evaluating the performance of a fault detection and diagnostic system for vapor compression equipment, *HVAC&R Research*, Vol. 4(4), p. 401-425
5. Breuker, M. S. and Braun, J. E., 1998b, Common faults and their impacts for rooftop air conditioner, *HVAC&R Research*, Vol. 4(3), p.303-318
6. California Energy Commission (CEC), 2003, Small HVAC system design guide, Available online: www.energy.ca.gov/pier/buildings
7. Carling, P. 2002. "Comparison of Three Fault Detection and Diagnosis Methods Based on Field Data of an Air Handling Unit," *ASHRAE Transactions*, 108 (1): pp. 904 – 921.
8. Castro, N. S., J. Schein, C. Park, M. A. Galler, S. T. Bushby, and J. M. House. 2003. Results from Simulation and Laboratory Testing of Air Handling Unit and Variable Air Volume Box Diagnostic Tools, NISTIR 6964, National Institute of Standards and Technology, Washington, DC.

9. Codes and Standards Enhancement Initiative (CASE). 2013 California Building Energy Efficiency Standards – Light Commercial Unitary HVAC. California Statewide Codes and Standards Team: November 2011.
10. Dexter, A. L., 1995, "Fuzzy Model Based Fault Diagnosis," IEE Proceedings – Control Theory Application, 142 (6), pp. 545 – 550.
11. Downey, T. and Proctor, J., 2002, What Can 13,000 Air Conditioners Tell Us?, In Proceedings of the ACEEE 2002, *Summer Study on Energy Efficiency in Buildings*, Vol. 1, p.53-68. Washington D.C.: American Council for an Energy-Efficient Economy
12. Energy Information Agency (EIA), 2003, Commercial Buildings Energy Consumption Survey 2003, Available online: <http://205.254.135.7/emeu/cbecs/cbecs2003>
13. Fernandez, N., Brambley, M.R., Katipamula, S., Self-Correcting HVAC Controls: Algorithms for Sensors and Dampers in Air-Handling Units. Pacific Northwest National Laboratory. December 2009.
14. Friedman, H. and Piette, M.A., Comparative Guide to Emerging Diagnostic Tools for Large Commercial HVAC Systems. LBNL Report 48629, Lawrence Berkeley National Laboratory. Berkeley, CA, May 2001.
15. Fukunaga, K., 1990, Introduction to statistical pattern recognition, Academic Press, West Lafayette, IN.
16. Goswami D. Y., 2002, Effect of refrigerant charge on the performance of air conditioning systems, *Fuel and Energy Abstracts*, Vol. 43(4)
17. Harms, T. M., 2002, "Charge Inventory System Modeling and Validation for Unitary Air Conditioners", Ph.D. Thesis, Herrick Labs 2002-13, Report No. 5288-2, Purdue University, West Lafayette, IN.
18. Haves, P., T. I. Salsbury, and J. A. Wright. 1996. "Condition Monitoring in HVAC Subsystems Using First Principles Models," ASHRAE Transactions, pp. 519 – 527.
19. Haves, P. 1997. Fault modelling in component-based HVAC simulation. Proceedings of Building Simulation 1997. Prague, Czech Republic, IBPSA
20. Hjortland, A. and Braun, J., General Outdoor Air Economizer Fault Detection and Diagnostics Assessment Method. International Refrigeration and Air Conditioning Conference at Purdue. July 16-19, 2012.
21. House, J. M., W. Y. Lee, et al. (1999). "Classification Techniques for Fault Detection and Diagnosis of an Air-Handling Unit." ASHRAE Transactions 105 (1).
22. Katipamula, S., R.G. Pratt, D.P. Chassin, Z.T. Taylor, K. Gowri, and M.R. Brambley. "Automated fault detection and diagnosis for outdoor-air ventilation systems and economizers: Methodology and results from field testing." ASHRAE Transactions 105: 555–567, 1999.
23. Katipamula, S. and Brambley, M. R., 2005, Methods for fault detection, diagnostics, and prognostics for vapor compression equipment Systems, A Review, Part I, *HVAR&R Research*, Vol. 11(1), p.3-25
24. Katipamula, Srinivas and Michael Brambley. "Automated Proactive Fault Isolation: A Key to Automated Commissioning." ASHRAE Transactions 113(2): 40-51, 2007.

25. Kim, W. H. and Braun, J. E., 2012a, Evaluation of the Impact of Refrigerant Charge on Air conditioner and Heat pump performance, *International Journal of Refrigeration*, Vol. 35, p. 1805-1814
26. Kim, W. H. and Braun, J. E., 2012b, Performance Evaluation of a Virtual Refrigerant Charge Sensor, *International Journal of Refrigeration*, In press
27. Lauritzen, S.L., 1992, Propagation of Probabilities, Means and Variances in Mixed Graphical Association Models, *Journal of the American Statistical Association*, Volume 87(420), pp 1098-1108.
28. Li, H. and Braun, J.E., 2003, An improved method for fault detection and diagnosis applied to packaged air conditioners, *ASHRAE Transactions*, Vol.109, Part 2
29. Li, H. and Braun, J. E., 2007a, Decoupling Features and Virtual Sensors for Diagnosis of Faults in Vapor Compression Air Conditioners. *International Journal of Refrigeration*, Vol. 30(3), pp 546-564
30. Li, H. and Braun, J. E., 2007b, A Methodology for Diagnosing Multiple-Simultaneous Faults in Vapor Compression Air Conditioners. *HVAC&R Research*, Vol. 13(2), p.369-395
31. Li, H. and Braun, J. E., 2009, Development, Evaluation, and Demonstration of a Virtual Refrigerant Charge Sensor. *HVAC&R Research*, Vol. 15(1), p.117-136
32. Li, S., 2009, A Model- Based Fault Detection and Diagnostic Methodology for Secondary HVAC Systems, Doctoral Thesis, Drexel University
33. Li, Y., Braun, J.E., and Groll, E.A., 2007, The impact of evaporator fouling and filtration on the performance of packaged air conditioners, *International Journal of Refrigeration*, Vol. 30, p.506-514
34. Messenger, M., 2008, Strategic Plan to Reduce the Energy Impact of Air Conditioners, *CEC-400-2008-010*
35. Norford, L. K., Wright, J. A., Buswell, R. A., and Luo, D. 2000. "Demonstration of Fault Detection and Diagnosis Methods in a Real Building," Final Report of ASHRAE 1020-RP, American Society of Heating, Refrigerating, and Air-Conditioning Engineers, Inc.: Atlanta, GA.
36. Payne, W. V., Kim, M. S., Yoon, S. H., and Domanski, P. A., 2008, Cooling mode fault detection and diagnosis method for a residential Heat Pump, *NIST Special Publication*, SP 1087
37. Rice, C. A., 1987, The Effect of Void Fraction Correlation and Heat Flux Assumption on Refrigerant Charge Inventory Predictions, *ASHRAE Transactions*, Vol. 93(1), p.341- 67
38. Rossi, T. M. and Braun, J. E., 1997, A statistical, rule-based fault detection and diagnostic method for vapor compression air conditioners, *HVAC&R Research*, Vol. 3(1), p.19–37
39. Schein, J., Bushby, S.T., House, J.M., & National Institute of Standards and Technology, Results from laboratory testing of embedded air handling unit and variable air volume box fault detection tools. U.S., 2003.
40. Seem, J.E., House, J.M., Integrated Control and Fault Detection of Air-Handling Units, *HVAC&R Research*, vol. 15, no. 1: p. 25-55, 2009.

41. Siegel, J. A. and Nazaroff, W. W., 2003, Predicting particle deposition on HVAC heat exchangers, *Atmospheric Environment*, Vol. 37, p. 5587-5596.
42. Taylor, Steven T., and C. Hwakong Cheng. "Economizer High Limit Controls and Why Enthalpy Economizers Don't Work." *ASHRAE Journal* 52.11 (2010): 12-28. Academic Search Premier. Web. 2 Jan. 2013.
43. U.S. Department of Energy, 2010, Energy efficiency trends in residential and commercial buildings, August
44. Alcala, C. F., & Joe Qin, S. (2011). Analysis and generalization of fault diagnosis methods for process monitoring. *Journal of Process Control*, 21(3), 322-330. doi: 10.1016/j.jprocont.2010.10.005
45. Bagajewicz, M. (2000). Design and Upgrade of Process Plant Instrumentation. Lancaster, PA: Technomic.
46. Bagajewicz, M. (2002). A Review of Techniques for Instrumentation Design and Upgrade in Process Plants. *The Canadian Journal of Chemical Engineering*, 80(February), 3-16.
47. Bishop, C. M. (2006). Pattern Recognition and Machine Learning. New York, Springer Science & Business Media.
48. Brambley, Michael R., Nick Fernandez, Weimin Wang, Heejin Cho, Hung Ngo and James Goddard. (Pacific Northwest National Laboratory) 2011. Self-Correcting Controls for VAV System Faults – Filter/Fan/Coil and VAV Box Sections. Fernandez et al., 2009a
49. Breuker, M. S., & Braun, J. E. (1999). Common faults and their impacts for rooftop air conditioners. *ASHRAE Transactions*, 105, PART 1/.
50. Bushby, S. T., Castro, N., Galler, M. A., Park, C., & House, J. M. (2001). Using the Virtual Cybernetic Building Testbed and FDD Test Shell for FDD Tool Development. In N. I. o. S. a. Technology (Ed.).
51. Castro, N. S., Schein, J., Park, C., Galler, M. A., & Bushby, S. T. (2003). Results from Simulation and Laboratory Testing of Air Handling Unit and Variable Air Volume Box Diagnostic Tools: National Institute of Standards and Technology.
52. Chen, Y., & Lan, L. (2009). A fault detection technique for air-source heat pump water chiller/heaters. *Energy and Buildings*, 41(8), 881-887. doi: 10.1016/j.enbuild.2009.03.007
53. Chen, Y., & Lan, L. (2010). Fault detection, diagnosis and data recovery for a real building heating/cooling billing system. *Energy Conversion and Management*, 51(5), 1015-1024. doi: 10.1016/j.enconman.2009.12.004
54. Cho, Y.-H., & Liu, M. (2010). Correlation between minimum airflow and discharge air temperature. *Building and Environment*, 45(7), 1601-1611. doi: 10.1016/j.buildenv.2010.01.008
55. Du, Z., & Jin, X. (2007a). Detection and diagnosis for multiple faults in VAV systems. *Energy and Buildings*, 39(8), 923-934. doi: 10.1016/j.enbuild.2006.09.015
56. Du, Z., & Jin, X. (2007b). Detection and diagnosis for multiple faults in VAV systems. *Energy and Buildings*, 39, 923-934.
57. Du, Z., & Jin, X. (2007c). Tolerant control for multiple faults of sensors in VAV systems. *Energy Conversion and Management*, 48(3), 764-777. doi: 10.1016/j.enconman.2006.09.007

58. Du, Z., Jin, X., & Wu, L. (2007). Fault detection and diagnosis based on improved PCA with JAA method in VAV systems. *Building and Environment*, 42(9), 3221-3232. doi: 10.1016/j.buildenv.2006.08.011
59. Du, Z., Jin, X., & Yang, X. (2009). A robot fault diagnostic tool for flow rate sensors in air dampers and VAV terminals. *Energy and Buildings*, 41(3), 279-286. doi: 10.1016/j.enbuild.2008.09.007
60. Fan, B., Du, Z., Jin, X., Yang, X., & Guo, Y. (2010). A hybrid FDD strategy for local system of AHU based on artificial neural network and wavelet analysis. *Building and Environment*, 45(12), 2698-2708. doi: 10.1016/j.buildenv.2010.05.031
61. Fernandez, N., Brambley, M. R., Katipamula, S., Cho, H., Goddard, J., & Dinh, L. (2009). Self-Correcting HVAC Controls. (PNNL-19074).
62. Galler, M., Bushby, S., & Sinai, N. (2011). Smart Building Automation and Control Testbed and Standards Retrieved 16/01/2012, from http://www.nist.gov/el/building_environment/mechsys/sbact.cfm
63. Ginestet, S., Marchio, D., & Morisot, O. (2008). Evaluation of faults impacts on energy consumption and indoor air quality on an air handling unit. *Energy and Buildings*, 40(1), 51-57. doi: 10.1016/j.enbuild.2007.01.012
64. Han, H., Gu, B., Hong, Y., & Kang, J. (2011). Automated FDD of multiple-simultaneous faults (MSF) and the application to building chillers. *Energy and Buildings*, 43(9), 2524-2532. doi: 10.1016/j.enbuild.2011.06.011
65. Hu, Y., Chen, H., Xie, J., Yang, X., & Zhou, C. (2012). Chiller sensor fault detection using a self-Adaptive Principal Component Analysis method. *Energy and Buildings*, 54, 252-258. doi: 10.1016/j.enbuild.2012.07.014
66. Katipamula, S., & Brambley, M. R. (2005a). Methods for fault detection, diagnostics, and prognostics for building systems - A review, Part I. HVAC and R Research, 11(Compendex), 3-25.
67. Katipamula, S., & Brambley, M. R. (2005b). Methods for fault detection, diagnostics, and prognostics for building systems - A review, Part II. HVAC and R Research, 11(Compendex), 169-187.
68. Kintner-Meyer, M. (2005). Opportunities of wireless sensors and controls for building operation. *Energy Engineering: Journal of the Association of Energy Engineering*, 102(5), 27-48.
69. Kintner-Meyer, M., & Brambley, M. R. (2002). Pros cons of wireless. *ASHRAE Journal*, 44(11), 54-56+58-61.
70. Kourti, T. (2005). Application of latent variable methods to process control and multivariate statistical process control in industry. *International Journal of Adaptive Control and Signal Processing*, 19(4), 213-246. doi: 10.1002/acs.859
71. Kwak, R.-Y., Takakusagi, A., Sohn, J.-Y., Fujii, S., & Park, B.-Y. (2004). Development of an optimal preventive maintenance model based on the reliability assessment for air-conditioning facilities in office buildings. *Building and Environment*, 39(10), 1141-1156. doi: 10.1016/j.buildenv.2004.01.029
72. Lee, S. H., & Yik, F. W. H. (2010). A study on the energy penalty of various air-side system faults in buildings. *Energy and Buildings*, 42(1), 2-10. doi: 10.1016/j.enbuild.2009.07.004

73. Lee, W.-Y., House, J. M., & Kyong, N.-H. (2004). Subsystem level fault diagnosis of a building's air-handling unit using general regression neural networks. *Applied Energy*, 77(2), 153-170. doi: 10.1016/s0306-2619(03)00107-7
74. Li, Mingyang. "Application of computational intelligence in modeling and optimization of HVAC systems." thesis, University of Iowa, 2009. <http://ir.uiowa.edu/etd/397>.
75. Li, S. (2009). *A Model-Based Fault Detection and Diagnostic Methodology for Secondary HVAC Systems*. Doctor of Philosophy, Drexel University, Philadelphia.
76. Ma, Z., & Wang, S. (2011). Online fault detection and robust control of condenser cooling water systems in building central chiller plants. *Energy and Buildings*, 43(1), 153-165. doi: 10.1016/j.enbuild.2010.09.003
77. Najafi, M., Auslander, D. M., Bartlett, P. L., Haves, P., & Sohn, M. D. (2012). Application of machine learning in the fault diagnostics of air handling units. *Applied Energy*, 96, 347-358. doi: 10.1016/j.apenergy.2012.02.049
78. Pakanen, J. E., & Sundquist, T. (2003). Automation-assisted fault detection of an air-handling unit; implementing the method in a real building. *Energy and Buildings*, 35, 193-202.
79. Pérez-Lombard, L., J. Ortiz, et al. (2008). "A review on buildings energy consumption information." *Energy and Buildings* 40(3): 394-398.
80. Qin, S. J., Valle, S., & Piovoso, M. (2001). On unifying multiblock analysis with application to decentralized process monitoring. *Journal of Chemometrics*, 15(9), 715-742.
81. Qin, J., & Wang, S. (2005). A fault detection and diagnosis strategy of VAV air-conditioning systems for improved energy and control performances. *Energy and Buildings*, 37(10), 1035-1048. doi: 10.1016/j.enbuild.2004.12.011
82. Ralston, P., DePuy, G., & Graham, J. H. (2004). Graphical enhancement to support PCA-based process monitoring and fault diagnosis. *ISA Transactions*, 43, 639-653.
83. Reddy, T. A. (2007). Application of a generic evaluation methodology to assess four different chiller FDD methods (RP-1275). *HVAC and R Research*, 13(5), 711-729.
84. Schein, J., Bushby, S. T., Castro, N. S., & House, J. M. (2006). A rule-based fault detection method for air handling units. *Energy and Buildings*, 38(12), 1485-1492. doi: 10.1016/j.enbuild.2006.04.014
85. Singhal, A., & Seborg, D. E. (2002). Pattern Matching in Multivariate Time Series Databases Using a Moving-Window Approach. *Industrial & Engineering Chemistry Research*, 41(16), 3822-3838.
86. Song, Y.-h., Akashi, Y., & Yee, J.-J. (2008). A development of easy-to-use tool for fault detection and diagnosis in building air-conditioning systems. *Energy and Buildings*, 40(2), 71-82. doi: 10.1016/j.enbuild.2007.01.011
87. Stoupe, D. E., & Lau, Y. S. (1989). Air conditioning and refrigeration equipment failures. *National Engineer*, 93(9), 14-17.
88. Sun, X., Marquez, J., & Chen, T. (2005). An Improved PCA Method with Application to Boiler Leak Detection. *ISA Transactions*, 44, 379-397.
89. Tan, H., & Dexter, A. (2006). Estimating airflow rates in air-handling units from actuator control signals. *Building and Environment*, 41(10), 1291-1298. doi: 10.1016/j.buildenv.2005.05.027

90. Venkatasubramanian, V., Rengaswamy, R., & Kavuri, S. N. (2003). A review of process fault detection and diagnosis. II. Qualitative models and search strategies. *Computers & Chemical Engineering*, 27(Copyright 2003, IEE), 313-326.
91. Venkatasubramanian, V., Rengaswamy, R., Kavuri, S. N., & Yin, K. (2003). A review of process fault detection and diagnosis. III. Process history based methods. *Computers & Chemical Engineering*, 27(Copyright 2003, IEE), 327-346.
92. Venkatasubramanian, V., Rengaswamy, R., Yin, K., & Kavuri, S. N. (2003). A review of process fault detection and diagnosis. I. Quantitative model-based methods. *Computers & Chemical Engineering*, 27(Copyright 2003, IEE), 293-311.
93. Wall, J., Guo, Y., Li, J., & West, S. (2011). A Dynamic Machine Learning-based Technique for Automated Fault Detection in HVAC Systems. *ASHRAE Transactions*.
94. Wang, H., Chen, Y., Chan, C. W. H., & Qin, J. (2011). A robust fault detection and diagnosis strategy for pressure-independent VAV terminals of real office buildings. *Energy and Buildings*, 43(7), 1774-1783. doi: 10.1016/j.enbuild.2011.03.018
95. Wang, H., Chen, Y., Chan, C. W. H., & Qin, J. (2012). An online fault diagnosis tool of VAV terminals for building management and control systems. *Automation in Construction*, 22, 203-211. doi: 10.1016/j.autcon.2011.06.018
96. Wang, H., Chen, Y., Chan, C. W. H., Qin, J., & Wang, J. (2012). Online model-based fault detection and diagnosis strategy for VAV air handling units. *Energy and Buildings*, 55, 252-263. doi: 10.1016/j.enbuild.2012.08.016
97. Wang, S., & Chen, Y. (2004). Sensor validation and reconstruction for building central chilling systems based on principal component analysis. *Energy Conversion and Management*, 45(5), 673-695. doi: 10.1016/s0196-8904(03)00180-8
98. Wang, S., & Jiang, Z. (2004). Valve fault detection and diagnosis based on CMAC neural networks. *Energy and Buildings*, 36(6), 599-610. doi: 10.1016/j.enbuild.2004.01.037
99. Wang, S., & Jin, X. (2000). Model-based optimal control of VAV air-conditioning system using genetic algorithm. *Building and Environment*, 35(6), 471-487. doi: 10.1016/s0360-1323(99)00032-3
100. Wang, S., & Qin, J. (2005). Sensor fault detection and validation of VAV terminals in air conditioning systems. *Energy Conversion and Management*, 46(15-16), 2482-2500. doi: 10.1016/j.enconman.2004.11.011
101. Wang, S., & Xiao, F. (2004a). AHU sensor fault diagnosis using principal component analysis method. *Energy and Buildings*, 36(2), 147-160. doi: 10.1016/j.enbuild.2003.10.002
102. Wang, S., & Xiao, F. (2004b). Detection and diagnosis of AHU sensor faults using principal component analysis method. *Energy Conversion and Management*, 45, 2667-2686.
103. Wang, S., & Xiao, F. (2006). Sensor Fault Detection and Diagnosis of Air-Handling Units Using a Condition-Based Adaptive Statistical Method. *HVAC and R Research*, 12(1), 127-150.
104. Wang, S., Zhou, Q., & Xiao, F. (2010). A system-level fault detection and diagnosis strategy for HVAC systems involving sensor faults. *Energy and Buildings*, 42(4), 477-490. doi: 10.1016/j.enbuild.2009.10.017

105. Weihua, L., Yue, H. H., Valle-Cervantes, S., & Qin, S. J. (2000). Recursive PCA for adaptive process monitoring. *Journal of Process Control*, 10(5), 471-486. doi: 10.1016/s0959-1524(00)00022-6
106. Wen, J. and S. Li (2010). Tools for Evaluating Fault Detection and Diagnostic Methods for Air-Handling Units. ASHRAE 1312-RP, American Society of Heating, Refrigeration and Air-Conditioning Engineers 1791 Tullie Circle, NE. Atlanta, GA 30329.
107. Wu, S., & Sun, J.-Q. (2011). Cross-level fault detection and diagnosis of building HVAC systems. *Building and Environment*, 46(8), 1558-1566. doi: 10.1016/j.buildenv.2011.01.017
108. Wu, S., & Sun, J. Q. (2011). A top-down strategy with temporal and spatial partition for fault detection and diagnosis of building HVAC systems. *Energy and Buildings*, 43(9), 2134-2139. doi: 10.1016/j.enbuild.2011.04.020
109. Xu, X., Xiao, F., & Wang, S. (2008). Enhanced chiller sensor fault detection, diagnosis and estimation using wavelet analysis and principal component analysis methods. *Applied Thermal Engineering*, 28(2-3), 226-237. doi: 10.1016/j.applthermaleng.2007.03.021
110. Yang, H., Cho, S., Tae, C.-S., & Zaheeruddin, M. (2008). Sequential rule based algorithms for temperature sensor fault detection in air handling units. *Energy Conversion and Management*, 49(8), 2291-2306. doi: 10.1016/j.enconman.2008.01.029
111. Yang, X.-B., Jin, X.-Q., Du, Z.-M., & Zhu, Y.-H. (2011). A novel model-based fault detection method for temperature sensor using fractal correlation dimension. *Building and Environment*, 46(4), 970-979. doi: 10.1016/j.buildenv.2010.10.030
112. Yang, X.-B., Jin, X.-Q., Du, Z.-M., Zhu, Y.-H., & Guo, Y.-B. (2013). A hybrid model-based fault detection strategy for air handling unit sensors. *Energy and Buildings*, 57, 132-143. doi: 10.1016/j.enbuild.2012.10.048
113. Yoo, C. K., & Lee, I.-B. (2006). Nonlinear multivariate filtering and bioprocess monitoring for supervising nonlinear biological processes. *Process Biochemistry*, 41(8), 1854-1863. doi: 10.1016/j.procbio.2006.03.038
114. Yu, Z., Haghghat, F., Fung, B. C. M., & Zhou, L. (2012). A novel methodology for knowledge discovery through mining associations between building operational data. *Energy and Buildings*, 47, 430-440. doi: 10.1016/j.enbuild.2011.12.018
115. Zhao, Y., Xiao, F., & Wang, S. (2013). An intelligent chiller fault detection and diagnosis methodology using Bayesian belief network. *Energy and Buildings*, 57, 278-288. doi: 10.1016/j.enbuild.2012.11.007
116. Zhu, Y., Jin, X., & Du, Z. (2012). Fault diagnosis for sensors in air handling unit based on neural network pre-processed by wavelet and fractal. *Energy and Buildings*, 44, 7-16. doi: 10.1016/j.enbuild.2011.09.043
117. 50PG Ultra High Efficiency Single Package Electric Cooling with Optional Electric Heat Commercial Rooftop Units with Puron, Carrier (<http://www.docs.hvacpartners.com/idc/groups/public/documents/techlit/50pg-06pd.pdf>)
118. 48HC High Efficiency Gas Heat/Electric Cooling Packaged Rooftop 3 to 12.5 Nominal Tons, Carrier (<http://www.docs.hvacpartners.com/idc/groups/public/documents/techlit/48hc-16si.pdf>)

Appendix 1

Test ID	Charge, %	IA flow, cfm	OA TDB, °F	IA TDB, °F	IA TWB, °F	Circuit	Comments
70% charge							
1	70%	2930	95	75	67	2	
2	70%	2930	95	80	67	2	
3	70%	2930	105	75	67	2	
4	70%	2930	105	80	67	2	
5	70%	2930	115	75	67	2	
6	70%	2930	115	80	67	2	
7	70%	2250	95	75	67	2	
8	70%	2250	95	75	67	1	
9	70%	2250	95	80	67	2	
10	70%	2250	105	75	67	2	
11	70%	2250	105	80	67	2	
12	70%	2250	115	75	67	2	
13	70%	2250	115	80	67	2	
70% Repeat Testing							
14	70%	2930	85	80	67	2	
15	70%	2930	95	80	67	2	
16	70%	2930	105	80	67	2	
17	70%	2930	115	80	67	2	
18	70%	2250	85	80	67	2	
19	70%	2250	95	80	67	2	
20	70%	2250	105	80	67	2	
21	70%	2250	115	80	67	2	
75% charge							
22	75%	2930	85	80	67	2	
23	75%	2930	95	80	67	2	
24	75%	2930	105	80	67	2	
25	75%	2930	115	80	67	2	
26	75%	2250	85	80	67	2	
27	75%	2250	95	80	67	2	
28	75%	2250	105	80	67	2	
29	75%	2250	115	80	67	2	
80% charge							
30	80%	2930	85	80	67	2	
31	80%	2930	95	80	67	2	
32	80%	2930	105	80	67	2	
33	80%	2930	115	80	67	2	
34	80%	2250	85	80	67	2	
35	80%	2250	95	80	67	2	
36	80%	2250	105	80	67	2	
37	80%	2250	115	80	67	2	
85% charge							
38	85%	2930	85	80	67	2	
39	85%	2930	95	80	67	2	
40	85%	2930	105	80	67	2	
41	85%	2930	115	80	67	2	
42	85%	2250	85	80	67	2	
43	85%	2250	95	80	67	2	
44	85%	2250	105	80	67	2	
45	85%	2250	115	80	67	2	
100% charge							
46	100%	2930	95	75	67	2	
47	100%	2930	95	75	67	1	
48	100%	2930	95	80	67	2	
49	100%	2930	95	80	67	1	
50	100%	2930	95	80	67	2	
51	100%	2930	95	80	67	1	
52	100%	2930	105	75	67	2	
53	100%	2930	105	75	67	1	
54	100%	2930	105	80	67	2	
55	100%	2930	105	80	67	1	
56	100%	2930	105	80	67	1	
57	100%	2930	115	75	67	2	
58	100%	2930	115	75	67	1	
59	100%	2930	115	80	67	2	
60	100%	2930	115	80	67	1	
61	100%	2250	95	75	67	2	
62	100%	2250	95	75	67	1	
63	100%	2250	95	80	67	2	
64	100%	2250	95	80	67	2	
65	100%	2250	95	80	67	1	
66	100%	2250	95	80	67	2	
67	100%	2250	95	80	67	1	
68	100%	2250	105	75	67	2	
69	100%	2250	105	75	67	1	
70	100%	2250	105	80	67	2	
71	100%	2250	105	80	67	2	
72	100%	2250	105	80	67	1	
73	100%	2250	105	80	67	1	
74	100%	2250	115	75	67	2	
75	100%	2250	115	75	67	1	
76	100%	2250	115	80	67	2	
77	100%	2250	115	80	67	2	
78	100%	2250	115	80	67	1	
79	100%	2250	95	80	67	2	Dry condition
80	100%	2250	95	80	67	2	Dry condition
81	100%	2250	95	80	67	2	Overnight
82	100%	2250	95	80	67	2	Overnight
100% charge retesting							
83	100%	2930	85	80	67	2	
84	100%	2930	95	80	67	2	
85	100%	2930	105	80	67	2	
86	100%	2930	115	80	67	2	
87	100%	2250	85	80	67	2	
88	100%	2250	95	80	67	2	
89	100%	2250	105	80	67	2	
90	100%	2250	115	80	67	2	
140% charge							
91	140%	2930	95	75	67	1	
92	140%	2930	95	80	67	1	
93	140%	2930	105	75	67	1	
94	140%	2930	105	80	67	1	
95	140%	2930	115	75	67	2	
96	140%	2930	115	80	67	1	
97	140%	2250	95	75	67	1	
98	140%	2250	95	80	67	1	
99	140%	2250	105	75	67	1	
100	140%	2250	105	80	67	1	
101	140%	2250	115	75	67	2	
102	140%	2250	115	80	67	1	

Appendix 2

1. Zone temperature sensor bias fault

Sensor bias fault was implemented by adding a positive or negative bias parameter into the sensor model, which would result in the sensor reading is higher or lower than the real temperature.

In this project, two temperature sensor bias faults were modeled and simulated. They are positive and negative 3OC (5.4 OF). Figure A2.1 shows the plot of west A room temperature sensor reading under sensor +3OC (5.4 OF) bias faulty condition. We can see clearly, at the faulty operation the room temperature sensor reading is 5.4 OF higher than that at normal condition. After the AHU system was turned on, the temperature started to decrease until it reached and kept at the cooling setpoint. However, the real zoom temperature at this faulty situation was kept at 66.6 OF, 5.4 OF lower than the cooling setpoint.

Figure A2.1 is the results for VAV damper position. In this plot, the VAV damper stays at 100% open for around one hour at faulty situation while under normal situation it doesn't. This is because at the faulty situation room temperature sensor reading is 5.4 OF higher than that at normal situation, and the air conditioning system need more cooling to decrease the room temperature to the design region. Therefore the damper stays at fully open for a while and then closes down to the minimal position when room temperature reaches to the cooling setpoint. Accordingly, the discharge air flowrate is plotted in Figure A2.2.

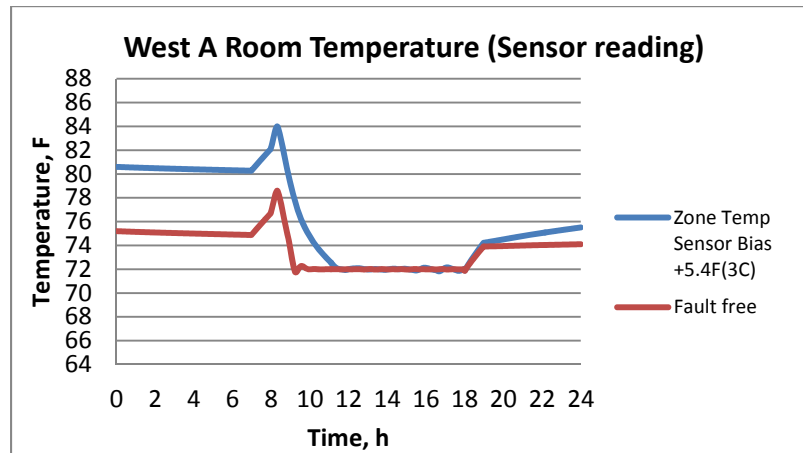


Figure A2.1. West A Room Temperature from EEB Model

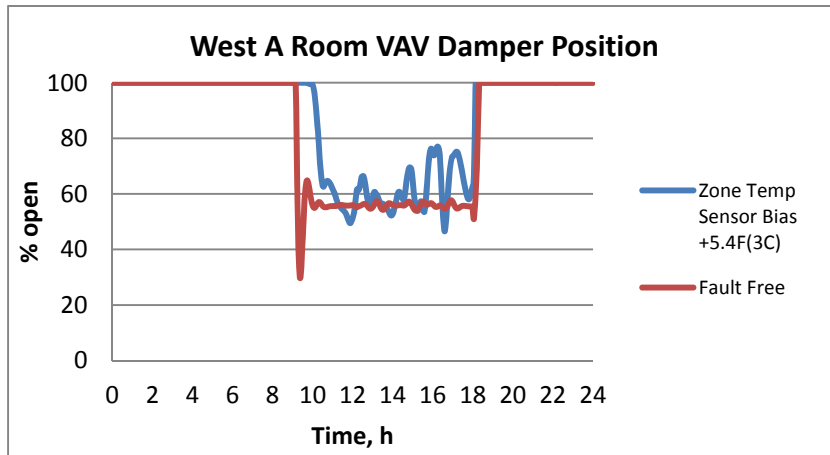


Figure A2.1. West A Room Damper Position from EEB Model

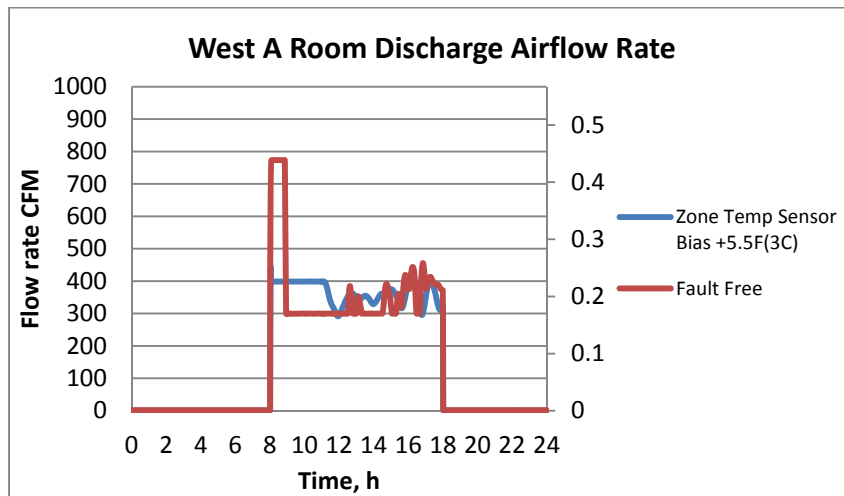


Figure A2.2. West A Room Discharge Airflow Rate EEB Model

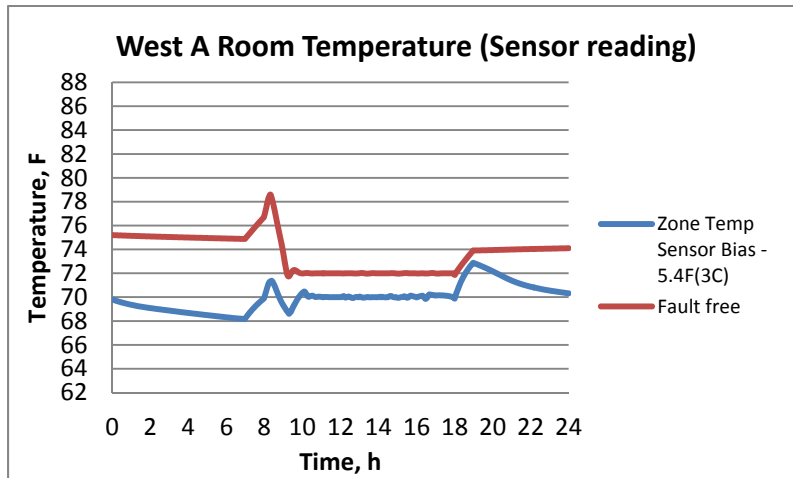


Figure A2.3. West A Room Temperature from EEB Model

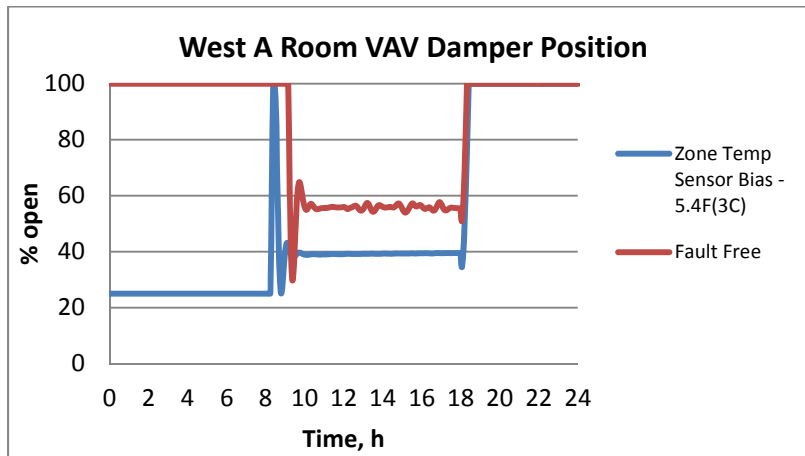


Figure A2.4. West A Room Damper Position from EEB Model

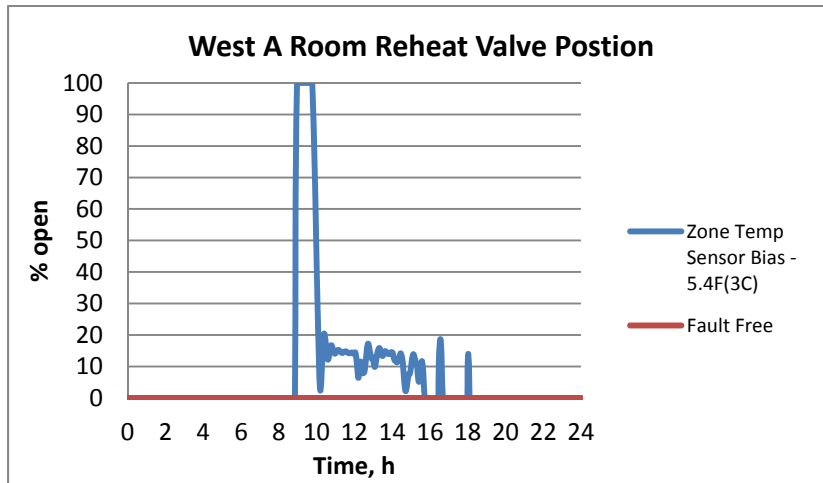


Figure A2.5. West A Room Reheat Coil Valve Position from EEB Model

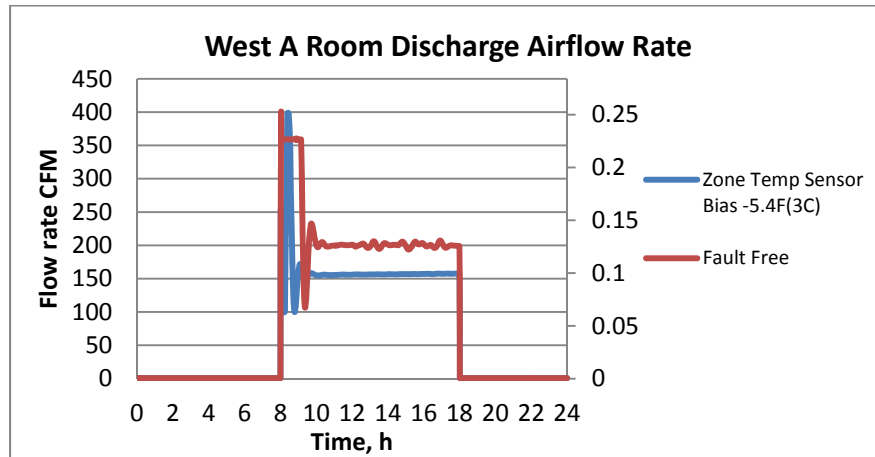


Figure A2.6. West A Room Discharge Airflow Rate from EEB Model

Oppositely, Figure A2.3, Figure A2.4, and Figure A2.5 are the West A room Temperature sensor reading, VAV damper position and reheat coil valve position results for zone temperature sensor -3°C (5.4°F) bias fault, respectively. Under faulty condition, the temperature sensor reading is 5.4°F lower than that at normal situation and the temperature is kept at the heating setpoint instead of cooling setpoint (Figure A2.3). However, the real zone temperature is around 75°F . The zone temperature increased 3-5 degree due to the solar radiation at early morning. Because the zone temperature sensor reading in the early morning dropped below heating setpoint, the VAV damper position was kept at the minimum position (Figure A2.4), and the reheat coil valve was opened to increase the zone temperature sensor reading (Figure A2.5).

Above all, the positive zone temperature sensor bias would increase the discharge airflow rate to maintain the sensor reading within the design region. This fault will increase the AHU energy consumption and decrease the thermal comfort. Because AHU has to handle more supply air and the real temperature is higher than the cooling setpoint. On the other hand, the negative zone temperature sensor

bias would decrease the discharge airflow rate (Figure A2.6), while increase the usage of reheat water. The change of energy consumption is hard to say. Because the energy consumption increase by reheat water increase and energy consumption decrease by discharge airflow rate decrease need detailed calculation. However, the real thermal comfort definitely decreases. Because the real zone temperature is lower than the heating setpoint.

2. Zone airflow rate sensor bias fault

Like zone temperature sensor bias fault, the airflow rate sensor bias fault was also implemented by adding a parameter into the airflow sensor model. Figure A2.7 and Figure A2.8 are the results for airflow sensor +50 CFM bias fault. Under the faulty condition, the discharge airflow sensor reading is 50 CFM higher than that in fault free situation. But the real discharge airflow is very close the 300CFM (Figure A2.7). In Figure A2.8, the VAV damper position at faulty situation is 10% larger than it under normal operation. Since the real discharge airflow rate, under fault situation, is close to it at normal operation, the zone temperature is close to that at normal operation (Figure A2.9).

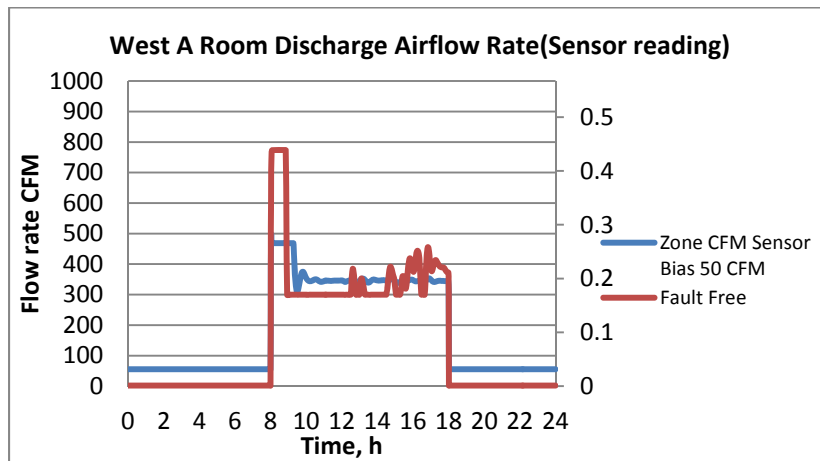


Figure A2.7. West A Room Discharge Airflow Rate from EEB Model

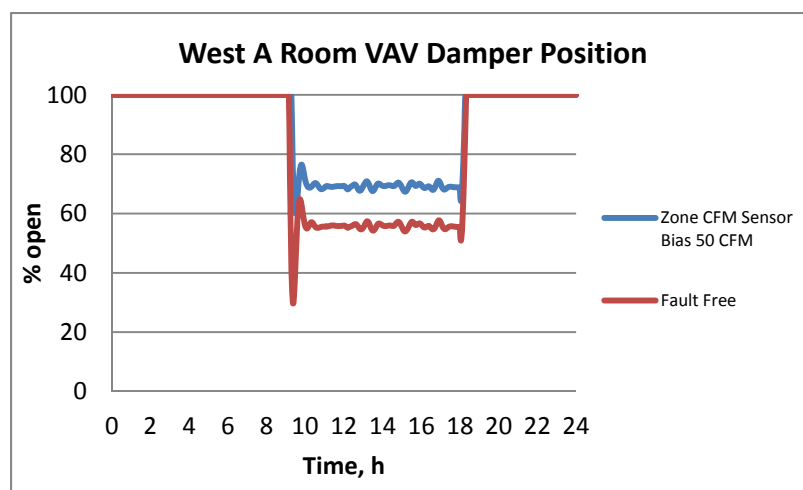


Figure A2.8. West A Room Damper Position from EEB Model

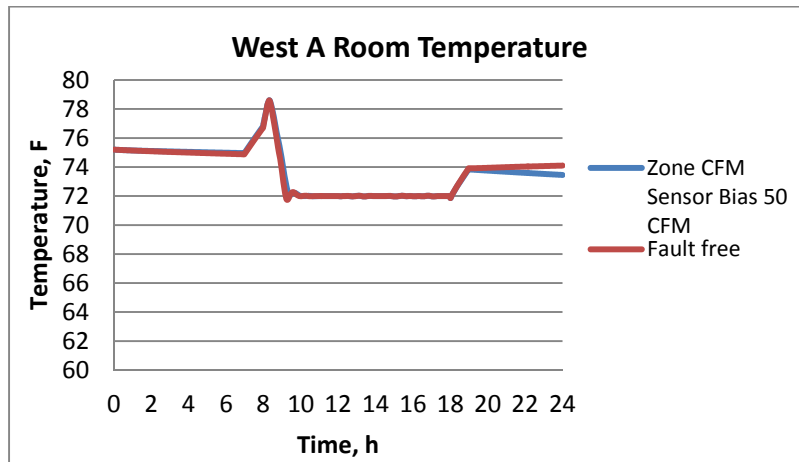


Figure A2.9. West A Room Temperature from EEB Model

Figure A2.10 and Figure A2.11 are the result of discharge airflow sensor reading and VAV damper position for airflow sensor -50 CFM bias fault. In contrast with results for airflow sensor +50 CFM bias, the discharge air is around 40 CFM than that under normal operation, and VAV damper position is 10% smaller than the position at fault free situation. Similar to the results of positive airflow sensor bias, the room temperature under negative airflow sensor bias is also very close to the normal airflow rate (Figure A2.12). What's more, in both positive and negative bias faulty situation, the reheat coil valve is always fully closed, because the room temperature never goes to below heating setpoint.

From the discussion, we can see, under certain range, the discharge airflow sensor bias will not affect the real discharge airflow, reheat water flow, and real room temperature. So in this range, the airflow sensor bias will not affect the energy consumption and indoor thermal comfort.

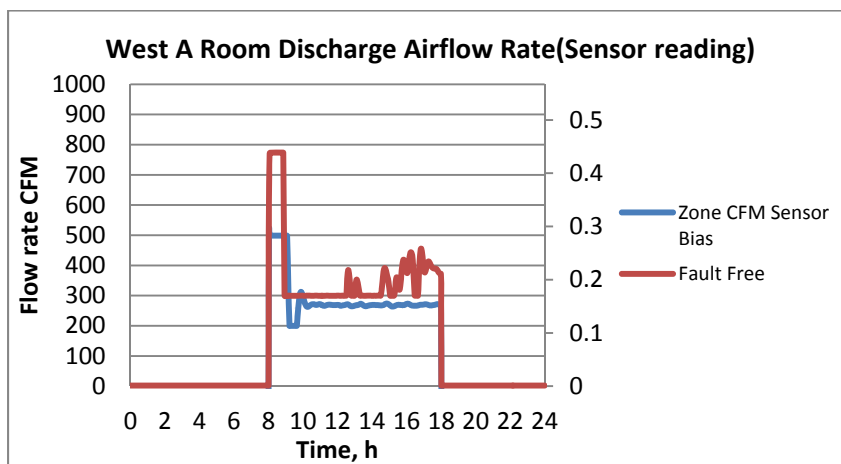


Figure A2.10. West A Room Discharge Airflow Rate from EEB Model

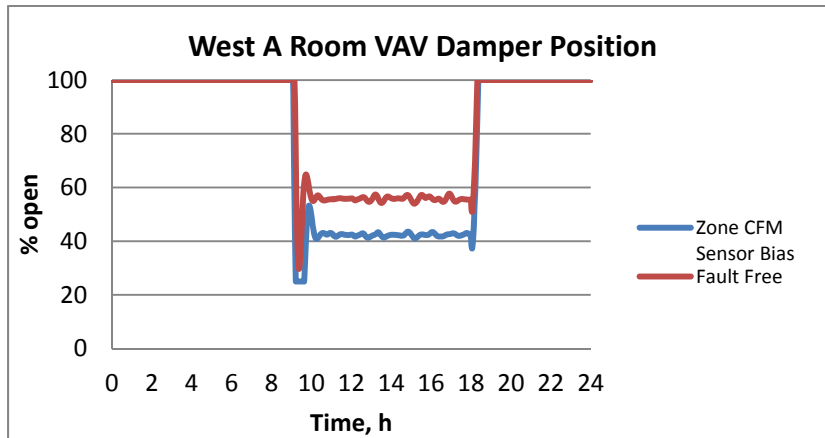


Figure A2.11 West A Room Damper Position from EEB Model

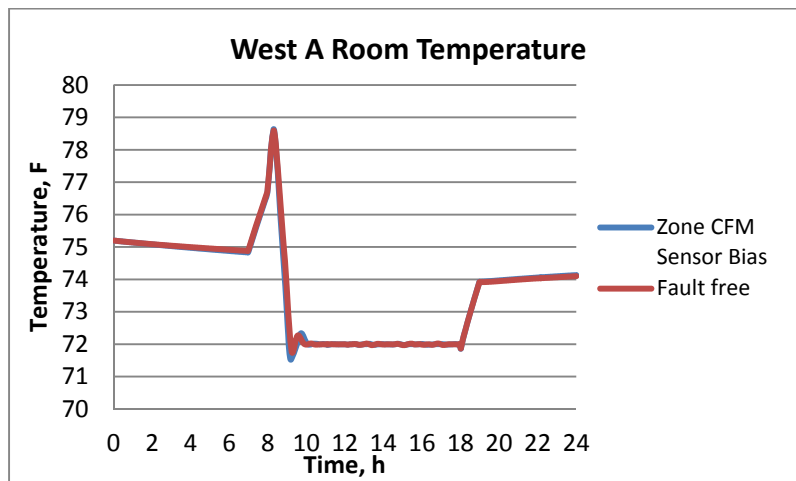


Figure A2.12. West A Room Temperature from EEB Model

3. Reheat Coil fouling

Two types of faults, namely, air side fouling fault, and water side fouling fault were modeled in this project. Reheat coil fouling has two aspect of impact on the system. Several studies in the literature discussed how to model coil faults. Bendapudi and Braun (2002) suggested that the heat exchanger fouling fault should be modeled by altering the heat-transfer coefficients. For the severest condenser fouling cases tested in their study, the water side heat transfer coefficient was reduced down to 55% of its fault free value. House et al (1999) also suggested that deposition of dirt and scale on a coil surface would increase the heat resistance. In this project, two variables, one for heat transfer coefficient and the other for flow resistance, were added into the reheat coil model.

Figure A2.13, Figure A2.17, Figure A2.18, and Figure A2.19 are the results for reheat coil air side fouling fault. In Figure A2.13, we can see that there are a litter bit difference between faulty simulation

and normal simulation at the early morning. The supply fan will adjust the rotation speed to maintain the room air temperature, which is shown in Figure A2.17. This reheat coil air side fouling fault increased the fan power (Figure A2.18 and Figure A2.19). In Figure A2.19 the plot is fan power under faulty situation minus the fan power at normal situation.

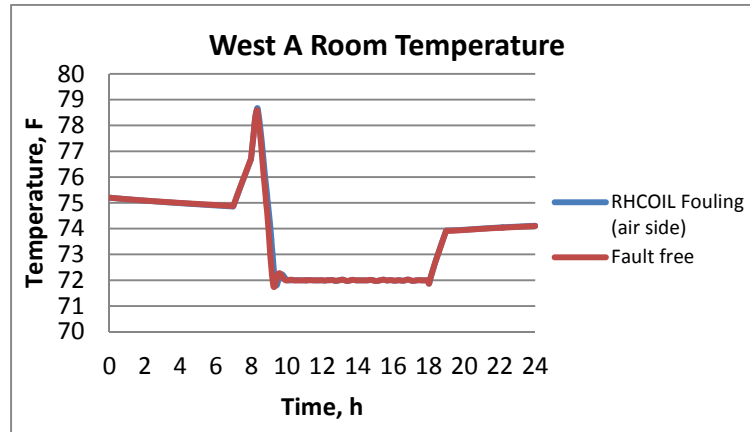


Figure A2.13. West A Room Temperature from EEB Model

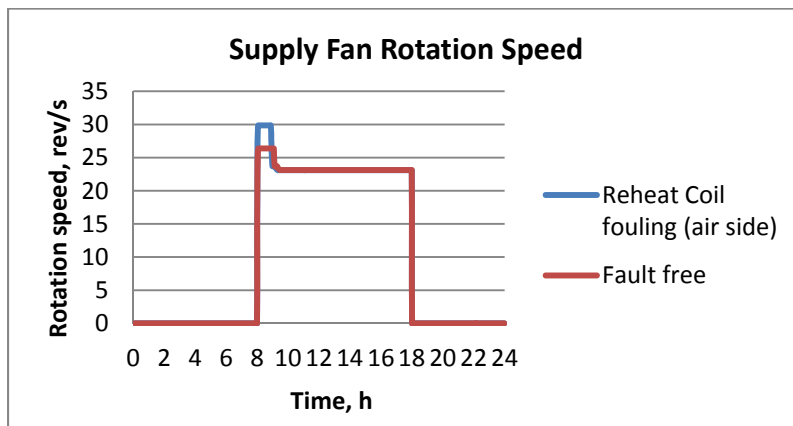


Figure A2.14. AHU Supply Fan Rotation Speed EEB Model

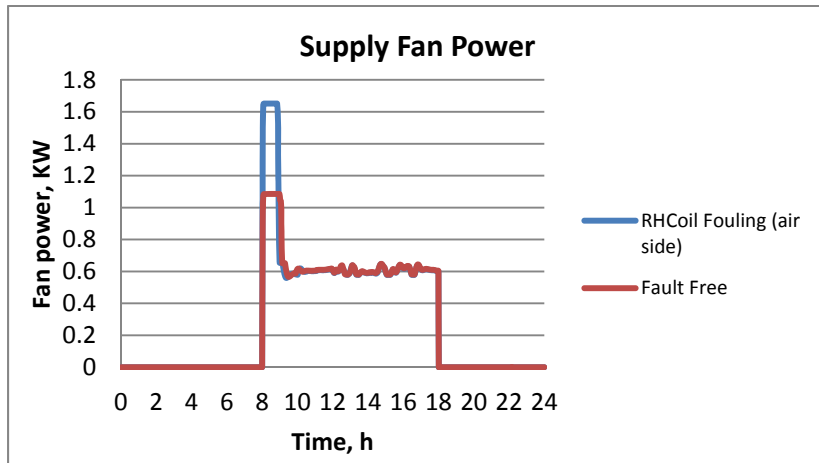


Figure A2.15 AHU Supply Fan Power EEB Model

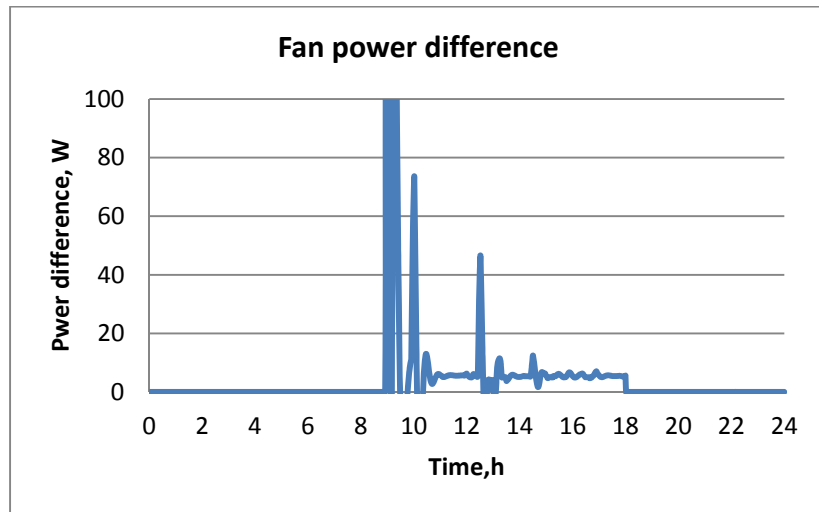


Figure A2.16. AHU Supply Fan Power difference

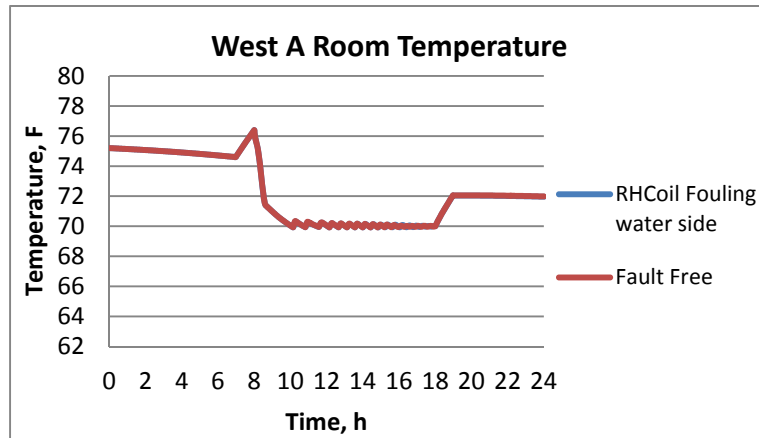


Figure A2.17. West A Room Temperature from EEB Model

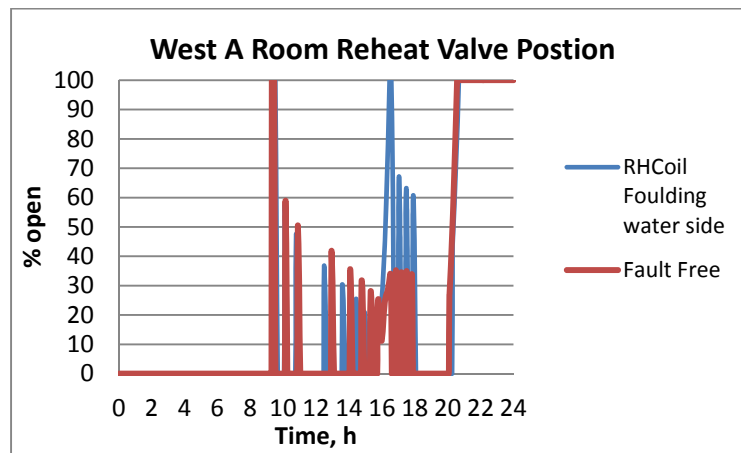


Figure A2.18. West A Room Reheat Valve Position from EEB Model

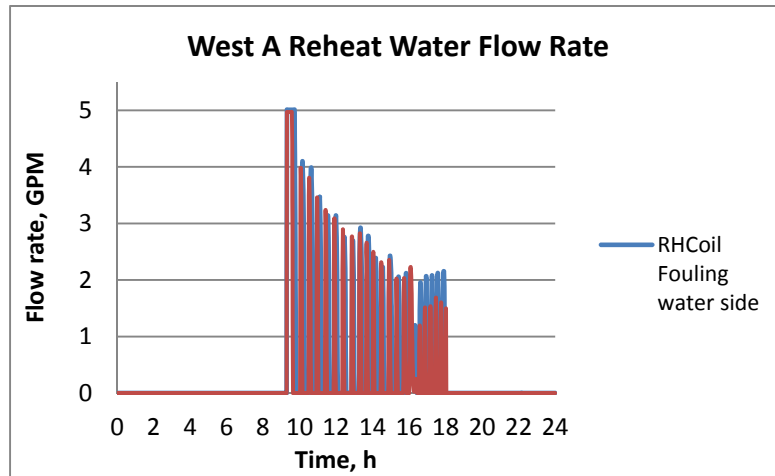


Figure A2.19. West A Room Reheat Water Flow Rate from EEB Model

Figure A2.19, Figure A2.18, and Figure A2.19 are results for reheat coil water fault under a cold day (Figure A2.20), when reheat coil valve is open. We can see that the reheat valve position is larger than that at normal operation. So does the reheat water flow rate. That is because the water side fouling will increase the water flow resistance and decrease the heat transfer coefficient, as we discussed before. Therefore, this reheat coil water side fouling fault increased the reheat water energy consumption. In this project, only the AHU and VAV terminal system were investigated, the results for reheat water pump energy was not calculated. However, from the analysis we did in this section, we can concluded that reheat water pump energy consumption was changed due to the change of reheat water flow rate.

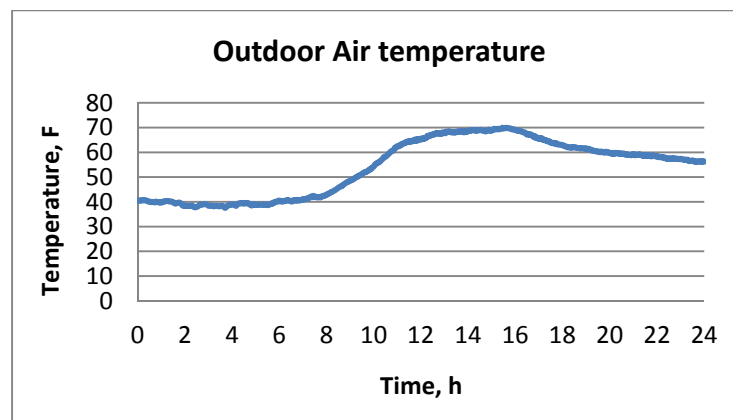


Figure A2.20. Outdoor Air Temperature of Valve Fault Simulation

4. VAV Damper Controller Unstable Fault

Controller unstable fault was implemented by adding parameter to increase the proportional band in the PID loop. Figure A2.21, Figure A2.22, and Figure A2.23 are the results of VAV damper position, discharge airflow rate and room temperature for VAV damper controller unstable fault, respectively. In

Figure A2.21 we can clearly see that the fluctuation of VAV damper position under this faulty situation is larger than that at normal operation. So does the discharge airflow rate (Figure A2.22). The room temperature doesn't change too much under this faulty operation (Figure A2.23), because the thermal capacitance of the room is large enough to smooth it.

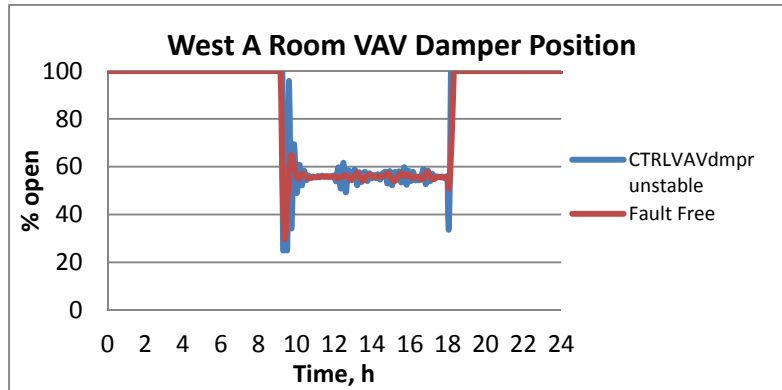


Figure A2.21. West A Room Damper Position from EEB Model

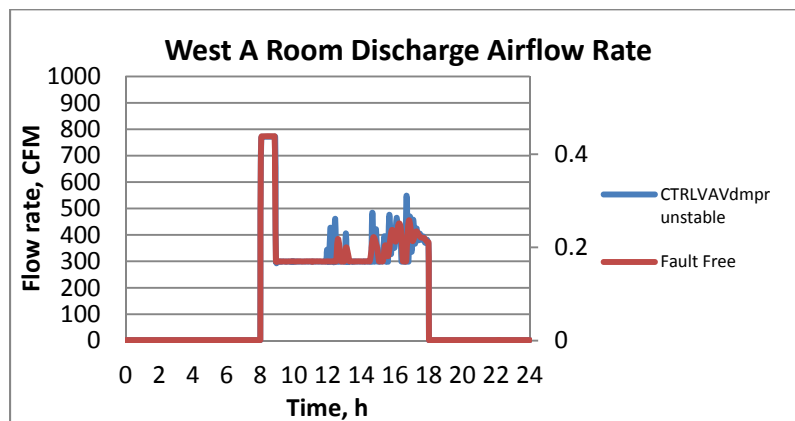


Figure A2.22. West A Room Discharge Airflow Rate from EEB Model

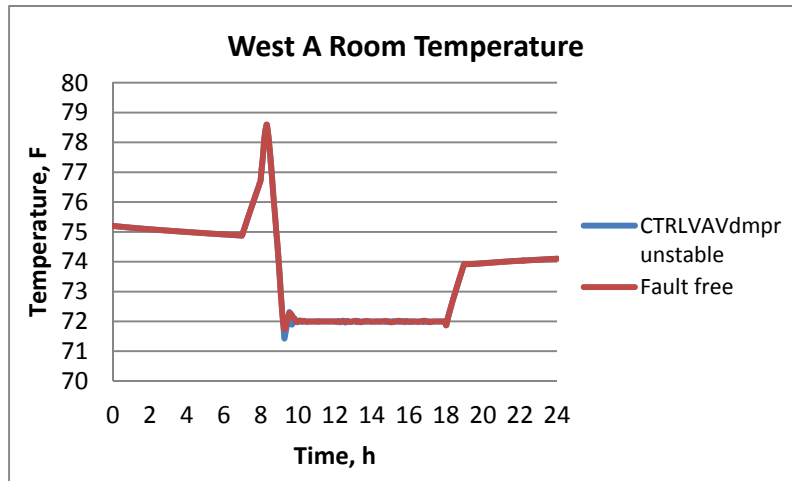


Figure A2.23. West A Room Temperature from EEB Model

5. Reheat Coil Valve Controller unstable Fault

In order to show the symptoms of reheat coil valve controller unstable fault, a cold day was chosen, because in a hot summer day, the reheat valve will never open.

In Figure A2.24 we can see that the fluctuation of reheat coil valve position under this faulty situation is larger than that at normal operation. The valve position can affect the reheat water flow rate and the discharge air temperature (Figure A2.26). Similar to the result in VAV damper controller unstable fault, the room temperature at faulty situation is very close to that at normal operation. However, this fault will change the reheat water flow rate and change the reheat water energy consumption.

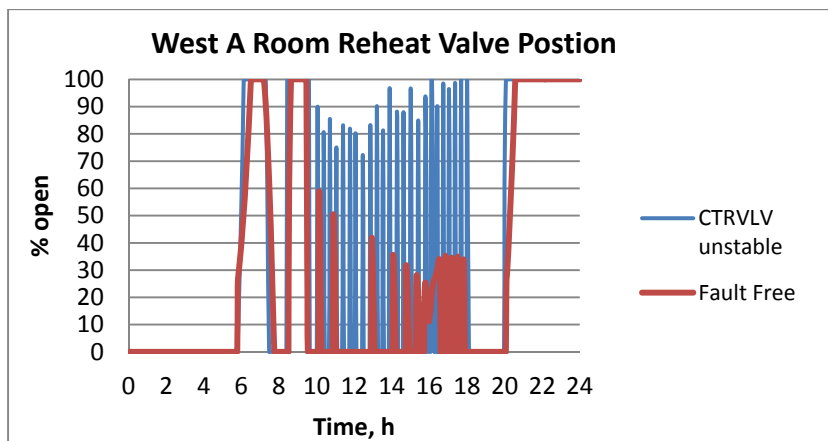


Figure A2.24. West A Room Reheat Valve Position from EEB Model

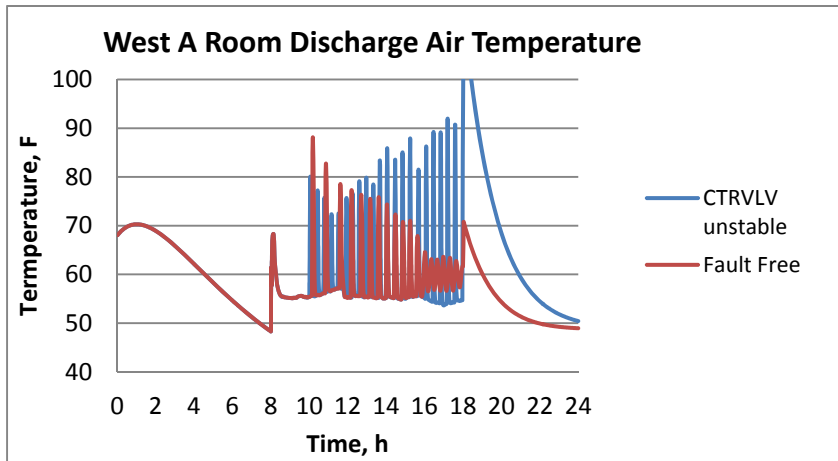


Figure A2.25. West A Room Discharge Air Temperature from EEB Model

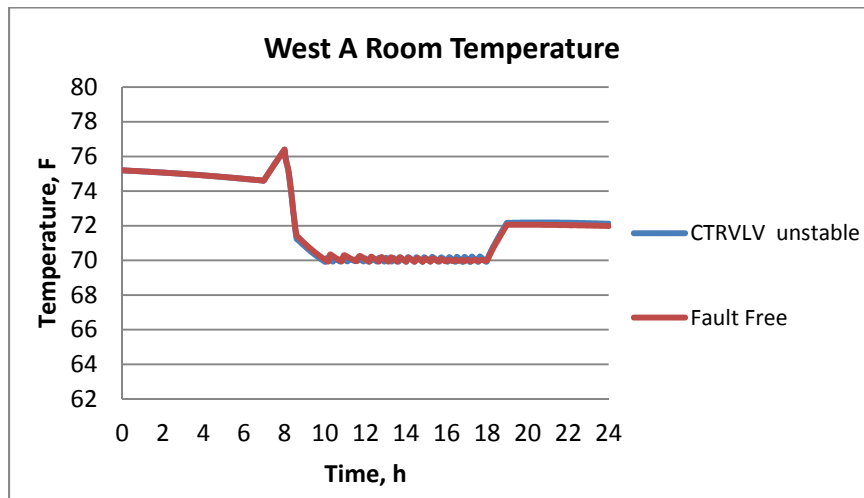


Figure A2.26. West A Room Temperature from EEB Model

Appendix 3

Fault Energy Impact Tables: Airstream Energy

TABLE A3.1: WINTER FAULT ENERGY IMPACTS (AIRSTREAM)

Date	Fault Description	AHU-A Minus AHU-B (kWh)					
		Fans	Cooling	Heat	Reheat	Net	Pct
02-10	Cooling Coil Valve Stuck (Fully Open)	-2.3	198.0	130.7	38.9	365	230%
02-12	OA Damper Stuck (Fully Closed)	3.7	1.3	-132.7	-8.3	(136)	-73%
01-30	OA Damper Stuck (Fully Closed)	5.6	4.7	-112.0	-22.7	(124)	-58%
02-03	EA Damper Stuck (Fully Closed)	-1.6	0.0	-34.5	-6.0	(42)	-40%
02-05	Heating Coil Fouling (Stage 1)	4.4	0.0	-28.5	-4.7	(29)	-28%
02-09	Heating Coil Reduced Capacity 3	-0.9	0.0	-32.5	7.0	(26)	-23%
02-08	Heating Coil Reduced Capacity 2	-0.4	0.0	-21.4	-2.0	(24)	-27%
02-01	OA Damper Stuck (62%)	-1.3	0.0	23.6	-0.7	22	20%
02-07	Heating Coil Reduced Capacity 1	-0.7	0.0	-16.6	-2.8	(20)	-17%
02-16	Fault Free	-0.6	0.0	-18.0	-0.3	(19)	-17%
02-17	Fault Free	-0.9	0.0	-15.1	-1.5	(18)	-16%
02-06	Heating Coil Fouling (Stage 2)	12.5	4.3	-29.7	-2.3	(15)	-18%
02-11	Cooling Coil Valve Stuck (20%)	-0.7	25.2	5.2	-17.5	12	7%
02-13	OA Damper Stuck (52%)	-0.2	0.0	-3.0	-8.1	(11)	-9%
02-15	OA Damper Stuck (62%)	-1.6	0.0	-5.1	-2.0	(9)	-6%
01-29	Fault Free	-0.9	0.0	-3.6	-3.8	(8)	-6%
01-31	OA Damper Stuck (52%)	-1.0	1.2	0.1	-7.8	(8)	-9%
02-02	EA Damper Stuck (Fully Open)	-0.4	0.0	-3.9	-1.1	(5)	-5%

TABLE A3.2: SPRING FAULT ENERGY IMPACTS (AIRSTREAM)

Date	Fault Description	AHU-A Minus AHU-B (kWh)					
		Fans	Cooling	Heat	Reheat	Net	Pct
05-15	Cooling Coil Stuck (Fully Open)	-2.3	199.5	156.6	3.5	357	364%
05-16	Cooling Coil Stuck (50%)	-1.1	128.9	99.5	2.3	230	196%
05-06	Cooling Coil Stuck (Fully Closed)	20.0	-132.5	0.6	-1.9	(114)	-73%
05-30	OA Temperature Sensor Fault (-3 bias)	4.7	22.1	0.0	-0.4	26	15%
05-28	EA Damper Fully Open	3.7	20.3	-0.1	0.5	24	49%
05-19	RF Fixed Speed (80%)	4.3	19.1	0.0	0.3	24	24%
05-14	MA Damper/ Cooling Coil Control Unstable	-1.1	15.2	1.5	0.2	16	26%
05-09	EA Damper Stuck (Fully Open)	0.0	15.6	0.1	-0.6	15	23%
05-23	Air Filter Area Blocked 25%	-0.5	14.2	0.0	0.6	14	38%
05-08	OA Damper Stuck (40%)	8.5	7.9	-0.3	-1.9	14	17%
05-17	Heat and Cool Sequence Unstable	0.1	12.1	0.0	0.8	13	10%
05-25	Air Filter Area Blocked 25%	0.9	11.3	0.0	0.7	13	7%
05-24	Air Filter Area Blocked 25%	-0.8	12.9	0.0	0.3	12	21%
05-02	Fault Free	-1.2	13.2	0.2	-0.1	12	20%
05-20	EA Damper Stuck (Fully Open)	-0.8	12.0	0.0	1.0	12	15%
05-05	Fault Free	-0.5	11.6	0.1	0.5	12	10%
05-10	EA Damper Stuck (Fully Closed)	-2.5	12.9	0.1	1.1	12	25%
05-13	MA Damper Unstable	-1.1	12.0	0.0	0.4	11	17%
05-04	Fault Free	-0.9	10.6	1.1	0.4	11	13%
05-12	RF Complete Failure	-4.5	13.7	0.1	0.8	10	12%
05-26	Air Filter Area Blocked 25%	-0.9	8.4	0.0	0.8	8	5%
05-18	RF Fixed Speed (20%)	-4.2	11.0	0.0	1.3	8	9%
05-22	Air Filter Area Blocked 10%	-1.0	12.3	0.0	-3.6	8	14%
05-07	OA Damper Stuck (Fully Closed)	4.8	-9.2	0.1	-2.0	(6)	-7%
05-29	OA Temperature Sensor Fault (+3 bias)	-1.7	8.4	0.0	-0.4	6	8%
05-27	EA Damper Fully Open	-1.4	6.7	0.0	0.9	6	28%
05-03	Fault Free	-0.9	6.3	0.2	-0.4	5	13%
05-11	EA Damper Stuck (40%)	-1.9	6.7	0.2	0.0	5	12%

TABLE A3.3: SUMMER FAULT ENERGY IMPACTS (AIRSTREAM)

Date	Fault Description	AHU-A Minus AHU-B (kWh)					
		Fans	Cooling	Heat	Reheat	Net	Pct
09-03	Cooling Coil Valve Reverse Action	-1.1	140.2	156.7	1.0	297	146%
08-31	Cooling Coil Valve Stuck (15%)	-1.7	134.8	134.2	-0.7	267	157%
09-02	Cooling Coil Valve Stuck (65%)	-0.2	121.6	124.0	-0.3	245	126%
08-30	Heating Coil Valve Leaking (2- 2.0GPM)	-0.3	109.6	95.3	-0.6	204	135%
08-27	Cooling Coil Valve Stuck (Fully Closed)	23.4	-193.3	-0.2	0.0	(170)	-79%
08-29	Heating Coil Valve Leaking (2- 1.0GPM)	0.2	77.2	58.1	-0.6	135	86%
08-28	Heating Coil Valve Leaking (1- 0.4GPM)	3.4	50.1	28.6	-0.7	81	40%
08-23	RF complete failure	-1.7	54.6	-0.2	-0.3	52	34%
08-22	RF at Fixed Speed (30%)	-0.4	33.1	-0.5	0.0	32	18%
09-06	OA Damper Leak (55%)	-1.0	28.0	0.1	-0.3	27	17%
08-20	EA Damper Stuck (Fully Open)	1.0	21.3	-0.1	0.0	22	11%
08-24	Cooling Coil Valve Control Unstable	2.9	17.2	-0.1	-0.2	20	15%
09-07	AHU Duct Leaking (after SF)	0.3	17.2	-0.1	-0.2	17	11%
08-25	Fault Free	-0.7	13.9	0.0	-0.2	13	8%
08-19	Fault Free	0.2	11.1	0.0	0.0	11	6%
09-09	AHU Duct Leaking (before SF)	-3.2	13.1	0.1	-0.4	10	7%
08-21	EA Damper Stuck (Fully Closed)	-1.6	-3.8	0.0	0.0	(5)	-2%
08-26	OA Damper Stuck (Fully Closed)	5.8	-2.2	-0.1	0.0	4	2%
09-08	AHU Duct Leaking (before SF)	-3.8	0.9	0.0	-0.4	(3)	-2%
09-04	Fault Free	0.0	0.0	0.0	0.0	0	N/A

Fault Energy Impact Tables: Building Energy Consumption

TABLE A3.4: WINTER FAULT ENERGY IMPACTS (BUILDING ENERGY)

Date	Season	Fault Description	AHU-A Minus AHU-B				
			Fans	Chiller	Boiler	Net	Pct
02-10	1	Cooling Coil Valve Stuck (Fully Open)	-2.3	49.5	163.4	211	147%
02-12	1	OA Damper Stuck (Fully Closed)	3.7	0.3	-165.9	(162)	-89%
01-30	1	OA Damper Stuck (Fully Closed)	5.6	1.2	-140.0	(133)	-86%
02-03	1	EA Damper Stuck (Fully Closed)	-1.6	0.0	-43.1	(45)	-62%
02-09	1	Heating Coil Reduced Capacity 3	-0.9	0.0	-40.6	(42)	-40%
02-05	1	Heating Coil Fouling (Stage 1)	4.4	0.0	-35.6	(31)	-42%
02-01	1	OA Damper Stuck (62%)	-1.3	0.0	29.6	28	30%
02-08	1	Heating Coil Reduced Capacity 2	-0.4	0.0	-26.8	(27)	-32%
02-06	1	Heating Coil Fouling (Stage 2)	12.5	1.1	-37.2	(24)	-38%
02-16	1	Fault Free	-0.6	0.0	-22.5	(23)	-22%
02-07	1	Heating Coil Reduced Capacity 1	-0.7	0.0	-20.8	(21)	-21%
02-17	1	Fault Free	-0.9	0.0	-18.9	(20)	-24%
02-11	1	Cooling Coil Valve Stuck (20%)	-0.7	6.3	6.5	12	9%
02-15	1	OA Damper Stuck (62%)	-1.6	0.0	-6.4	(8)	-5%
01-29	1	Fault Free	-0.9	0.0	-4.4	(5)	-5%
02-02	1	EA Damper Stuck (Fully Open)	-0.4	0.0	-4.9	(5)	-6%
02-13	1	OA Damper Stuck (52%)	-0.2	0.0	-3.7	(4)	-4%
01-31	1	OA Damper Stuck (52%)	-1.0	0.3	0.1	(1)	-1%

TABLE A3.5: SPRING FAULT ENERGY IMPACTS (BUILDING ENERGY)

Date	Season	Fault Description	AHU-A Minus AHU-B				
			Fans	Chiller	Boiler	Net	Pct
05-15	2	Cooling Coil Stuck (Fully Open)	-2.3	49.9	195.8	243	661%
05-16	2	Cooling Coil Stuck (50%)	-1.1	32.2	124.4	155	370%
05-06	2	Cooling Coil Stuck (Fully Closed)	20.0	-33.1	0.8	(12)	-23%
05-30	2	OA Temperature Sensor Fault (-3 bias)	4.7	5.5	0.0	10	19%
05-08	2	OA Damper Stuck (40%)	8.5	2.0	-0.4	10	30%
05-19	2	RF Fixed Speed (80%)	4.3	4.8	0.0	9	26%
05-28	2	EA Damper Fully Open	3.7	5.1	-0.1	9	46%
05-14	2	MA Damper/ Cooling Coil Control Unstable	-1.1	3.8	1.8	5	17%
05-09	2	EA Damper Stuck (Fully Open)	0.0	3.9	0.1	4	15%
05-25	2	Air Filter Area Blocked 25%	0.9	2.8	0.0	4	6%
05-17	2	Heat and Cool Sequence Unstable	0.1	3.0	0.0	3	7%
05-04	2	Fault Free	-0.9	2.6	1.4	3	9%
05-23	2	Air Filter Area Blocked 25%	-0.5	3.6	0.0	3	17%
05-07	2	OA Damper Stuck (Fully Closed)	4.8	-2.3	0.2	3	8%
05-05	2	Fault Free	-0.5	2.9	0.2	3	6%
05-24	2	Air Filter Area Blocked 25%	-0.8	3.2	0.0	2	11%
05-02	2	Fault Free	-1.2	3.3	0.2	2	9%
05-20	2	EA Damper Stuck (Fully Open)	-0.8	3.0	0.0	2	7%
05-22	2	Air Filter Area Blocked 10%	-1.0	3.1	0.0	2	9%
05-13	2	MA Damper Unstable	-1.1	3.0	0.0	2	7%
05-18	2	RF Fixed Speed (20%)	-4.2	2.8	0.0	(1)	-4%
05-26	2	Air Filter Area Blocked 25%	-0.9	2.1	0.0	1	2%
05-12	2	RF Complete Failure	-4.5	3.4	0.1	(1)	-3%
05-10	2	EA Damper Stuck (Fully Closed)	-2.5	3.2	0.2	1	4%
05-03	2	Fault Free	-0.9	1.6	0.2	1	5%
05-29	2	OA Temperature Sensor Fault (+3 bias)	-1.7	2.1	0.0	0	1%
05-27	2	EA Damper Fully Open	-1.4	1.7	0.0	0	2%
05-11	2	EA Damper Stuck (40%)	-1.9	1.7	0.2	(0)	0%

TABLE A3.6: SUMMER FAULT ENERGY IMPACTS (BUILDING ENERGY)

Date	Season	Fault Description	AHU-A Minus AHU-B				
			Fans	Chiller	Boiler	Net	Pct
09-03	3	Cooling Coil Valve Reverse Action	-1.1	35.1	195.9	230	342%
08-31	3	Cooling Coil Valve Stuck (15%)	-1.7	33.7	167.8	200	347%
09-02	3	Cooling Coil Valve Stuck (65%)	-0.2	30.4	155.0	185	285%
08-30	3	Heating Coil Valve Leaking (2- 2.0GPM)	-0.3	27.4	119.1	146	278%
08-29	3	Heating Coil Valve Leaking (2- 1.0GPM)	0.2	19.3	72.6	92	179%
08-28	3	Heating Coil Valve Leaking (1- 0.4GPM)	3.4	12.5	35.8	52	80%
08-27	3	Cooling Coil Valve Stuck (Fully Closed)	23.4	-48.3	-0.2	(25)	-36%
08-23	3	RF complete failure	-1.7	13.7	-0.2	12	23%
08-22	3	RF at Fixed Speed (30%)	-0.4	8.3	-0.6	7	12%
08-24	3	Cooling Coil Valve Control Unstable	2.9	4.3	-0.2	7	16%
09-06	3	OA Damper Leak (55%)	-1.0	7.0	0.2	6	12%
08-20	3	EA Damper Stuck (Fully Open)	1.0	5.3	-0.1	6	10%
08-26	3	OA Damper Stuck (Fully Closed)	5.8	-0.6	-0.1	5	9%
09-07	3	AHU Duct Leaking (after SF)	0.3	4.3	-0.1	5	9%
09-08	3	AHU Duct Leaking (before SF)	-3.8	0.2	0.0	(4)	-6%
08-19	3	Fault Free	0.2	2.8	0.0	3	5%
08-25	3	Fault Free	-0.7	3.5	0.0	3	5%
08-21	3	EA Damper Stuck (Fully Closed)	-1.6	-0.9	0.0	(3)	-4%
09-09	3	AHU Duct Leaking (before SF)	-3.2	3.3	0.2	0	0%

Fault Energy Impact Tables: Daily Operational Costs

TABLE A3.7: WINTER FAULT ENERGY IMPACTS (DAILY COSTS)

Fault: Winter Season	Base Nominal	Low	Nominal	High	Pct
Cooling Coil Valve Stuck (Fully Open)	8.38	10.86	14.97	17.25	79%
OA Damper Stuck (Fully Closed)	10.22	(5.83)	(6.89)	(7.13)	-167%
OA Damper Stuck (Fully Closed)	8.68	(4.58)	(5.27)	(5.33)	-161%
EA Damper Stuck (Fully Closed)	5.15	(1.78)	(2.21)	(2.38)	-143%
Heating Coil Reduced Capacity 3	6.65	(1.62)	(1.99)	(2.12)	-130%
Heating Coil Reduced Capacity 2	6.06	(1.05)	(1.29)	(1.37)	-121%
Cooling Coil Valve Stuck (20%)	8.08	0.81	1.20	1.44	-85%
OA Damper Stuck (62%)	6.19	0.98	1.13	1.14	-82%
Fault Free	6.93	(0.91)	(1.12)	(1.20)	-116%
Heating Coil Reduced Capacity 1	6.39	(0.85)	(1.05)	(1.13)	-116%
Fault Free	5.78	(0.80)	(1.00)	(1.08)	-117%
Heating Coil Fouling (Stage 1)	5.21	(0.90)	(0.92)	(0.83)	-118%
OA Damper Stuck (62%)	9.28	(0.40)	(0.54)	(0.62)	-106%
Heating Coil Fouling (Stage 2)	4.51	(0.04)	0.49	0.94	-89%
Fault Free	6.74	(0.26)	(0.35)	(0.40)	-105%
EA Damper Stuck (Fully Open)	5.83	(0.22)	(0.28)	(0.31)	-105%
OA Damper Stuck (52%)	6.89	(0.16)	(0.20)	(0.22)	-103%
OA Damper Stuck (52%)	4.10	(0.06)	(0.10)	(0.13)	-102%

TABLE A3.8: SPRING FAULT ENERGY IMPACTS (DAILY COSTS)

Fault: Spring Season	Base Nominal	Low	Nominal	High	Pct
Cooling Coil Stuck (Fully Open)	5.89	180.92	220.61	233.72	3648%
Cooling Coil Stuck (50%)	6.73	115.10	140.38	148.75	1987%
Air Filter Area Blocked 10%	3.83	(3.68)	(4.37)	(4.53)	-214%
Cooling Coil Stuck (Fully Closed)	8.60	(2.75)	(3.83)	(4.45)	-145%
MA Damper/ Cooling Coil Control Unstable	4.19	2.04	2.58	2.80	-39%
OA Damper Stuck (Fully Closed)	5.24	(1.79)	(2.07)	(2.10)	-139%
EA Damper Fully Open	3.02	1.31	1.93	2.31	-36%
RF Fixed Speed (80%)	5.66	1.20	1.80	2.18	-68%
EA Damper Stuck (Fully Closed)	3.45	1.38	1.70	1.82	-51%
Heat and Cool Sequence Unstable	7.35	1.15	1.51	1.69	-79%
RF Fixed Speed (20%)	5.57	1.26	1.47	1.50	-74%
Air Filter Area Blocked 25%	10.18	0.99	1.34	1.53	-87%
OA Damper Stuck (40%)	5.27	(1.41)	(1.29)	(1.03)	-125%
Air Filter Area Blocked 25%	2.94	0.92	1.23	1.39	-58%
Air Filter Area Blocked 25%	3.64	0.85	1.12	1.26	-69%
OA Temperature Sensor Fault (-3 bias)	8.83	0.54	1.06	1.44	-88%
RF Complete Failure	5.48	0.90	1.05	1.07	-81%
Air Filter Area Blocked 25%	7.93	0.73	0.92	1.01	-88%
MA Damper Unstable	4.12	0.57	0.77	0.87	-81%
EA Damper Fully Open	2.17	0.45	0.56	0.59	-74%
Fault Free	6.71	0.36	0.53	0.63	-92%
OA Temperature Sensor Fault (+3 bias)	4.83	(0.42)	(0.50)	(0.51)	-110%
Fault Free	4.13	0.33	0.48	0.57	-88%
Fault Free	5.30	0.29	0.41	0.49	-92%
EA Damper Stuck (Fully Open)	5.08	(0.32)	(0.30)	(0.25)	-106%
Fault Free	3.02	0.18	0.24	0.27	-92%
EA Damper Stuck (40%)	3.13	0.19	0.22	0.22	-93%
EA Damper Stuck (Fully Open)	4.33	(0.15)	(0.03)	0.09	-101%

TABLE A3.9: SUMMER FAULT ENERGY IMPACTS (DAILY COSTS)

Fault: Summer Season	Base Nominal	Low	Nominal	High	Pct
Cooling Coil Valve Reverse Action	10.72	218.89	265.99	281.06	2382%
Cooling Coil Valve Stuck (15%)	9.20	187.76	228.27	241.29	2380%
Cooling Coil Valve Stuck (65%)	10.33	173.48	210.94	222.99	1942%
Heating Coil Valve Leaking (2- 2.0GPM)	8.42	133.75	162.77	172.20	1833%
Heating Coil Valve Leaking (2- 1.0GPM)	8.21	81.79	99.66	105.52	1114%
Heating Coil Valve Leaking (1- 0.4GPM)	10.36	40.98	50.17	53.31	384%
Cooling Coil Valve Stuck (Fully Closed)	11.27	(2.71)	(4.25)	(5.26)	-138%
RF complete failure	7.99	0.96	1.63	2.09	-80%
OA Damper Leak (55%)	8.36	0.80	1.20	1.45	-86%
Cooling Coil Valve Control Unstable	7.21	0.54	0.94	1.22	-87%
EA Damper Stuck (Fully Open)	10.17	0.51	0.86	1.10	-92%
OA Damper Stuck (Fully Closed)	9.59	0.43	0.72	0.92	-92%
AHU Duct Leaking (after SF)	8.51	0.39	0.65	0.83	-92%
AHU Duct Leaking (before SF)	9.17	(0.41)	(0.63)	(0.78)	-107%
Fault Free	9.99	0.26	0.43	0.55	-96%
EA Damper Stuck (Fully Closed)	11.36	(0.26)	(0.41)	(0.52)	-104%
RF at Fixed Speed (30%)	9.44	0.08	0.41	0.68	-96%
Fault Free	8.55	0.23	0.39	0.50	-95%
AHU Duct Leaking (before SF)	7.69	0.18	0.22	0.23	-97%

Notes from Interviews: Subject 1 (Facility Manager)

Most common faults

1. Air filter blockage
 - a. Filter blockage can cause the DX coil to freeze
 - b. Filter sensors are now considered to be a good investment (pressure drop across the filter)
 - c. Older buildings are typically changed by knowing the typical schedule or from a no-heat/cooling call
2. Belts slipping (belts last 3-4 years typically)
 - a. Some units have multiple belts
 - b. Vibration and long belts may cause premature wear
 - c. Variable speed drives (VSD) – build a relationship between speed, amperage, and HP to find slippage?
 - d. Newer VSDs pass a lot of data back to the BMS
 - e. As belts wear, small pieces will come off and can even trigger a fire alarm
 - f. Belts are cheap
3. Damper leakage (function of quality of equipment as well)
 - a. Seals
 - b. Stuck bearings
 - c. Broken actuator / linkage
 - d. Only typically identified under extreme conditions
4. Valve passing (function of quality of equipment)
 - a. Drexel gets only high-performance valves
 - b. Large valves (butterfly valves) – expects 20 years of this valve installed indoors
 - c. Smaller valves (ball valves) – expects 20 years of this valve installed indoors
 - d. Typically identified through performance problems
5. Degradation in coil performance over time
 - a. Korman AHU – 21,000 cfm
 - b. Fins get a “skin” or corrosion on them.
 - i. Can be washed with a detergent, but only to a point – then they have to be replaced
 - c. (Delta T on the water side) versus (Delta t on the air side)
 - i. Thermistor sensors (\$40 per sensor) ... can be bought in matched sets for an extra \$10 - \$20 (from Kele sensors)
 - ii. Not likely to have chilled water in and out at the air handler – may buy extra sensors for this. Could use a flowmeter, or if single pump just look at where you are on the pump curve.
 - d. Plotting over time to see the degradation, and see how much energy is required to do the same job.

- e. Chiller may be running unloaded or overloaded, (i.e. not in the most efficient range of operation)
- f. Aside on full-plant optimization and chiller optimization
 - i. Fail more frequently than the motor bearings
6. Fan bearings
 - a. Typical length of life for fan bearings ~ 15 years
7. Motor bearings
 - a. Best way to diagnose bearing failure is vibration, but requires expensive equipment and expert analysis.
 - i. How expensive is this type of sensor now?
 - ii. Do they monitor this for chillers? (More “critical” piece of equipment b/c more expensive failure to repair)
 - iii. Previously often monitored by technicians who notice a difference in the noise the motor and fan are making
 1. Perhaps using acoustics could detect this... identify a grinding sound?
 2. Detect the slight increase in HP to overcome increased friction or too minor to detect?
 - b. Bearing failure could cause motor shaft damage... need to send out for a re-build or get a replacement. At the top of a building, this could be worthwhile
 - c. Cooling towers have vibration sensors built in to them

AHU Life Span

- d. Top quality = 50 years (replacing motors, belts, etc.)
- e. Lower quality ~ 20 years (rooftop location)

Sensor Faults

- Thermistor (2 wire) – reliable sensor (no need to upgrade to an RTD for the HVAC industry)
 - \$25 - \$30
 - 0.75 – 1 degree sensitivity
 - Tend to fail in a big way... don't go off by a degree, they go off by 20 degrees
- RTD sensor (3 wire)
 - \$60
 - Real extra cost is to run the extra wire and power supply
 - 0.1 degree sensitivity
- Flow switches are notoriously unreliable
 - They use a DP sensor
 - Only truly accurate flow sensor are magnetic sensors (\$5,000 sensor)
 - Paddle wheel, turbine wheel sensors are “crappy”
- DP sensor
 - Few hundred dollars
 - Generally good for 5 – 10 years

- Need to be maintained – small tubing gets blocked up
- RH sensors
 - \$300
 - Reliable for ~ 2 years... accuracy drifts off remarkably
 - Self-correcting to adjust for an offset error
 - Get what you pay for

Terminal Units (VAV)

- At low flow, the DP sensors are not accurate at all
 - May be better to reduce the size of VAV boxes to maintain higher velocity, or split one large box into two smaller boxes
 - Low-flow end gives headaches
 - 600 fpm gives the problem
- Damper motor failure (stuck damper)
 - VAV controller with motor on it (\$320)
 - Burns out, replace whole thing
 - Lower first cost
 - If separated, just replacing the motor is a 15 minute job (\$50 plus labor)
 - 4 - 10 years
 - Controllers last much longer (lots from the 1980's still running)
 - Controller failure
 - Output relays are most common failures
 - Open relay, close relay
 - Have them programmed to update less frequently, and added deadbands to minimize the amount of modulation
 - Now they last multiple years instead of 1 -2 years

False alarm rates

- Tied to the importance of the device
 - e.g. fire-system accepts more false alarms
 - Lots of false alarms on the filters? 1 in 100 activations can be false alarms or other method will be used
 - Accept a higher rate of false alarms for a chiller (chance of catastrophic \$100,000 repair), so maybe 10%
 - Keep investing money until it comes down to a lower rate
 - Wouldn't put a technician's time on getting the AHU false alarm rate returned
 - What do you alarm?
 - Boiler that doesn't start when temp is cold outside
 - Power failure in a building
 - Chiller output temp exceeds 49 deg F
 - Filter alarm -> "don't chirp at me" but let me know

- BMS systems have multiple levels of alarm
 - Lights up in red
 - Flashes
 - Beep/chirp
 - Continuous beeping/chirping
- High level = can't open the building that day

Notes from Interview: Subject 2 (Building Control Engineer)

FDD in General

1. Sees a great need for FDD
2. Lots of companies working on it
3. Looking for something to start testing with his customers

Data Acquisition

1. Terry discussed the difficulties with mapping the data to the AFDD platform.
 - Discussed the middleware platform that will allow us to “plug'n'play”

Discussion of how newer systems have increased sensor density, and may not require additional

AHU System Lifespan

- Mechanically about 20-30 years
- Often sees older ones that have been upgraded at some point
- Average lifespan is about 20-25 years (indoor, hydronic)
- Rooftop is shorter than that

Timing of problems

1. Often the building is not commissioned well at the outset. Increased the utility for third party commissioning companies.
 - a. E.g. When you mount a damper actuator on the unit – mount it, tighten the bolts a few degrees extra “closed” to get a good seal.
2. If it's commissioned well, you probably won't see stuff for a “couple years”

Most common AHU-faults

- Controls-side faults
 - People used to say 10 years, but they don't really fail a lot. TH has seen a lot of “old stuff out there”. If it is going to fail, will probably fail early on and overall he doesn't see a lot of electronic failure.
- **Dampers and valves** are the most common problem
 - Because they are mechanical

1. He would put **dampers first** because they are “more mechanical”.
 - a. They are:
 - i. exposed to the elements,
 - ii. get rusted up,
 - iii. stop moving,
 - iv. shafts slip (very common).
 - b. The way we attach to a damper now is not as good as we used to do it. Now we use a direct mount actuator. Years ago, there was a box with an arm and a crank and “all that”. But this method had its problems too, due to the U-bolt through the shaft.
 - i. If the U-bolt slips, then it will be wrong (out of calibration). Or people will move the U-bolt during maintenance and inadvertently take it out of calibration.
 - c. In TH’s opinion, the biggest energy waste in an AHU is either from the OA damper or MA damper
2. In terms of failure probabilities, **valves** come next (second)
 - a. Because they are mechanical system
 - b. They get stuck/ stop working
 - c. Actuation is more important than degradation
 - d. Seating issues in old valves. Tight close-off is a problem
3. **Coils** are next
 - a. Coils get fouled on the inside
 - b. Don’t cleaned on the outside
4. **Fans** are fairly simple
 - a. Biggest issue with fans? Belt tension
 - b. How long belts are slipping for? Tends to solve itself, since the belts seem to wear much faster once they start to slip.
 - c. Using, instead of a current switch.
 - d. Long time ago, was a pressure swith, then current switch (\$15)
 - e. Now an analog current sensor (\$30)
 - f. That can tell you a lot. When the belt starts to slip, you will see the current change.
 - g. Bearing failure? Don’t see it a lot. Definitely it’s there. Fan bearings more than motor bearings – take a little more abuse (because they are further apart, etc.)
5. **Schedule** problems
 - a. Should be picked up by the control algorithm, so not a problem
6. He doesn’t see a lot of **sensor** failure.
 - a. Characterized as a fairly rare occurrence
 - b. Just don’t see a lot of failure on sensors. Down the list quite a bit
 - c. Any active sensors like RH, CO2 degrade over time – the worst of the active sensors is RH. But RH is older, so we don’t know about CO₂ yet. So, yes, RH sensors are a problem.

- d. Weather station data? Yes, we have been doing that. We now advise our customers to not put in OA, O RH sensors.
 - i. One potential complication is when NOAA changes the IP address, because some systems can't use just a web address.
 - e. When temperature sensors fail, they fail badly.
 - i. TH: It is a bad idea to field-calibrate these sensors – more harm than good.
7. **Filter** statuses
- a. Used to be all DP switches, but never really worked correctly
 - b. Analog pressure transmitter is now just as cheap
 - c. DP depends on type of filter, RH in the air
 - d. Switch was too finicky – people just adjust them out
 - e. Now, best to use analog and just set a range specific to the system
 - f. Is the dirty filter a problem that is already solved?
 - i. Terry would agree that the filter situation is getting better.

Most Common Terminal Unit Faults

- 1. Main problems? Air flow measurement is the biggest problem
 - a. That's a big problem when that sensor goes bad, wastes a lot of energy.
 - b. Poor accuracy when the velocity goes down. Oversized boxes?
 - c. Need an accurate pressure transmitter as well
 - d. They are using Ebtron temperature flow-rate sensors. The cost has gone down enough that these aren't bad any more.
 - i. Ebtron trains their people – he can get me on the list for a three day event to learn about the sensor.
 - ii. Ebtron provides a pre-calibrated tube that is just plug'n'play
 - iii. Add in the time to install and calibrate, the ebtrons were actually a better deal. Sell a lot, so agreed that it is a better way of doing it.
 - iv. For a VAV unit (\$300)

General Comments on AFDD

- 1. PMPCA method: For retrofit applications, it could be a problem if you put something in during the middle of the unit's lifespan. *The algorithm won't pick up things that are already degraded.* Even with re-commissioning, there is a limit to what can be sensed (e.g. interior coil fouling).
- 2. Wiring vs. Wireless
 - a. Designed to be wireless (for union laborers), but still not less expensive overall
 - b. If you have a drop ceiling wired is always better
 - c. Wireless problems:
 - d. Still used for hard-to-get-to places
 - e. 25 year battery life

- f. Standard wireless protocols
- g. Jump right onto wi-fi is a new option, and often preferable
- 3. Front end considerations
 - a. What is the operator going to want to look at
 - b. Reasonable false alarm rate:
 - c. Ezenics – fault has to trigger for a long time. Wait long enough – will reduce false alarm rate
 - d. Finds fault prioritization to be murky:
 - i. Estimation of the energy-waste on a specific fault.
 - 1. Very difficult to estimate
 - e. If you get a lot of false alarms, they are going to stop using it.
 - f. Display the multi-trend for everything that relates to the fault.
 - g. Trigger to the BAS